

## INFORMATION TO USERS

This reproduction was made from a copy of a document sent to us for microfilming. While the most advanced technology has been used to photograph and reproduce this document, the quality of the reproduction is heavily dependent upon the quality of the material submitted.

The following explanation of techniques is provided to help clarify markings or notations which may appear on this reproduction.

1. The sign or "target" for pages apparently lacking from the document photographed is "Missing Page(s)". If it was possible to obtain the missing page(s) or section, they are spliced into the film along with adjacent pages. This may have necessitated cutting through an image and duplicating adjacent pages to assure complete continuity.
2. When an image on the film is obliterated with a round black mark, it is an indication of either blurred copy because of movement during exposure, duplicate copy, or copyrighted materials that should not have been filmed. For blurred pages, a good image of the page can be found in the adjacent frame. If copyrighted materials were deleted, a target note will appear listing the pages in the adjacent frame.
3. When a map, drawing or chart, etc., is part of the material being photographed, a definite method of "sectioning" the material has been followed. It is customary to begin filming at the upper left hand corner of a large sheet and to continue from left to right in equal sections with small overlaps. If necessary, sectioning is continued again—beginning below the first row and continuing on until complete.
4. For illustrations that cannot be satisfactorily reproduced by xerographic means, photographic prints can be purchased at additional cost and inserted into your xerographic copy. These prints are available upon request from the Dissertations Customer Services Department.
5. Some pages in any document may have indistinct print. In all cases the best available copy has been filmed.

**University  
Microfilms  
International**

300 N. Zeeb Road  
Ann Arbor, MI 48106



8318425

Rhoads, Charles Michael

MID-INFRARED FILTERS USING CONDUCTING ELEMENTS

*The Ohio State University*

PH.D. 1983

University  
Microfilms  
International 300 N. Zeeb Road, Ann Arbor, MI 48106





PLEASE NOTE:

In all cases this material has been filmed in the best possible way from the available copy. Problems encountered with this document have been identified here with a check mark .

1. Glossy photographs or pages \_\_\_\_\_
2. Colored illustrations, paper or print \_\_\_\_\_
3. Photographs with dark background
4. Illustrations are poor copy \_\_\_\_\_
5. Pages with black marks, not original copy \_\_\_\_\_
6. Print shows through as there is text on both sides of page \_\_\_\_\_
7. Indistinct, broken or small print on several pages
8. Print exceeds margin requirements \_\_\_\_\_
9. Tightly bound copy with print lost in spine \_\_\_\_\_
10. Computer printout pages with indistinct print \_\_\_\_\_
11. Page(s) \_\_\_\_\_ lacking when material received, and not available from school or author.
12. Page(s) \_\_\_\_\_ seem to be missing in numbering only as text follows.
13. Two pages numbered \_\_\_\_\_. Text follows.
14. Curling and wrinkled pages \_\_\_\_\_
15. Other \_\_\_\_\_

University  
Microfilms  
International



MID-INFRARED FILTERS USING CONDUCTING ELEMENTS

DISSERTATION

Presented in Partial Fulfillment of the Requirements for  
the Degree Doctor of Philosophy in the Graduate  
School of The Ohio State University

By

Charles M. Rhoads, B.S.E.E., M.Sc.

\*\*\*\*\*

The Ohio State University

1983

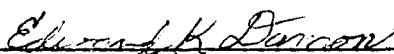
Reading Committee:

Professor Edward K. Damon

Professor Benedikt A. Munk

Professor Leon Peters, Jr.

Approved by:

  
\_\_\_\_\_  
Adviser  
Department of Electrical  
Engineering

# MID-INFRARED FILTERS USING CONDUCTING ELEMENTS

by

Charles M. Rhoads, Ph.D.

The Ohio State University, 1983

Professor Edward K. Damon, Adviser

Previous studies have shown that periodic arrays of antenna elements could be used to perform the common functions of filtering for electromagnetic (EM) waves. These previous studies have been largely confined to the microwave portion of the EM spectrum although filters with limited performance characteristics have been constructed and measured in the far-infrared. In this dissertation, measured results on band-pass and band-reject filters for the mid-infrared are reported. The frequencies involved are at least a factor of ten higher than any previously reported for the types of filters discussed. In addition to the measured data, calculations of the band-reject filter characteristics are presented. These calculated data were obtained using computer codes previously tested in the microwave regime. With some modifications to these codes the measured and calculated filter center frequencies are found to be in good agreement. In addition, techniques are presented to model the effect of metallic loss in the antenna elements. This effect is found to be important for filters designed to operate in the mid-infrared.

## ACKNOWLEDGMENT

The author wishes to thank his many friends and associates at the ElectroScience Laboratory for their support and guidance while enrolled as a graduate student at The Ohio State University. Professor David L. Moffatt deserves recognition as a past adviser. Many thanks must be extended to Professor Benedikt A. Munk for his numerous helpful discussions during the course of this study and for his technical review of this manuscript. A debt of gratitude is also owed to Professor Leon Peters, Jr. for his review of this manuscript and help throughout the years. Special recognition must be given to Professor Edward K. Damon for his advice and friendship in addition to his formal role as the author's dissertation adviser. The author would also like to thank Dr. Lee W. Henderson and Dr. Daniel J. Ryan for their technical assistance during this study and Mr. James Gibson, Mr. Robert Davis and Mrs. Sally Owens Eilts for their excellent work on the figures and text of this manuscript. In addition, Professor E.D. Wolf, Director, Mr. Brian Whitehead and Mr. Richard Tiberio of The National Research and Resource Facility for Submicron Structures at Cornell University are to be commended for their aid in the construction of the devices described in this study. Lastly, the author would like to express his gratitude and thanks to his family for their encouragement and support during his graduate studies.

This dissertation was sponsored under Project F33615-80-C-1072 between The Ohio State University Research Foundation and the Department of the Air Force, Wright-Patterson Air Force Base. The author would like to thank Dr. George Reinhardt of the Department of the Air Force for his critical review of the manuscript.

VITA

March 10, 1954 . . . . . Born - Hillsboro, Ohio  
1976 . . . . . B.S.E.E., The Ohio State  
University  
1978 . . . . . M.Sc., The Ohio State University  
1976-1983 . . . . . Graduate Research Associate,  
ElectroScience Laboratory,  
Department of Electrical  
Engineering, The Ohio State  
University.

PUBLICATIONS

"Transient Response Characteristics in Identification and Imaging",  
(co-authors, D.L. Moffatt, J.D. Young, A.A. Ksienski, and H.C. Lin),  
IEEE Trans. on Antennas and Propagation, Vol. AP-29, No. 2, March 1981.  
"Radar Identification of Naval Vessels", (co-author, D.L. Moffatt), IEEE  
Trans. on Aerospace and Electronic Systems, Vol. AES-18, No. 2, March  
1982.  
"Mid-Infrared Filters Using Conducting Elements", (co-authors, E.K.  
Damon, B.A. Munk), Applied Optics, Vol. 21, No. 15, August 1982.

FIELDS OF STUDY

Major Field: Electrical Engineering  
    Studies in Electromagnetics. Professors Robert G. Kouyoumjian and  
        David L. Moffatt  
    Studies in Communication Theory. Professor Claude E. Warren  
    Studies in Lasers/Optics. Professor John G. Meadors  
    Studies in Mathematics. Professor John T. Scheick

## TABLE OF CONTENTS

	Page
ACKNOWLEDGMENT	ii
VITA	iv
LIST OF TABLES	vi
LIST OF FIGURES	vii
Chapter	
I. INTRODUCTION	1
II. ANALYSIS OF PERIODIC SURFACE CHARACTERISTICS	5
A. GRID THEORY	6
B. PERIODIC SURFACE THEORY (PST)	12
III. SIMPLIFIED SURFACE DESIGN AND CONSTRUCTION	27
IV. MEASURED TRANSMITTANCE DATA AND SEM PHOTOGRAPHS	41
V. CALCULATION OF FILTER TRANSMITTANCE	83
VI. SUMMARY AND CONCLUSIONS	107
APPENDICES	
A. THE CONSTRUCTION OF MID-INFRARED PERIODIC SURFACES	112
B. MID-INFRARED MEASUREMENTS	135
C. MID-INFRARED PROPERTIES OF CALCIUM FLUORIDE	156
D. OHMIC LOSS IN PERIODIC SURFACES	167
E. MID-INFRARED DATA FOR ALUMINUM AND GOLD	210
REFERENCES	216



## LIST OF TABLES

TABLE	PAGE
3.1 CRITICAL DIMENSIONS FOR CROSSED-DIPOLES AND TRIPLES ON CALCIUM FLUORIDE NEAR $10 \mu\text{m}$	30
3.2 RESULTS OF FIRST CORNELL NRRFSS TRIP	34
3.3 RESULTS OF SECOND CORNELL NRRFSS TRIP	38
5.1 COMPARISON OF MEASURED AND CALCULATED RESONANT FREQUENCIES	91

## LIST OF FIGURES

Figure	Page
2.1. An inductive grid and its grid theory transmission line model.	7
2.2. A capacitive grid and its grid theory transmission line model.	9
2.3. A capacitive cross grid and its grid theory transmission line model.	11
2.4. Periodic array of linear elements in a skewed grid geometry.	13
2.5. Relationship between flat wire geometry and equivalent wire radius [37].	22
3.1. Shapes and critical dimensions.	29
3.2. Ideal, 120° symmetric tripole array.	32
3.3. Optical micro-photographs of liftoff results.	
4.1. SEM photograph of short chrome-gold tripoles on substrate #1.	50
4.2. Measured transmittance data for substrate #1.	51
4.3. SEM photograph of short aluminum tripoles on substrate #5.	52
4.4. SEM photograph of long aluminum tripoles on substrate #5.	53
4.5. Measured transmittance data for the tripoles on substrate #5.	54
4.6. SEM photograph of short aluminum crossed dipoles on substrate #5.	55
4.7. SEM photograph of long aluminum crossed dipoles on substrate #5.	56
4.8. Measured transmittance data for the crossed-dipoles on substrate #5.	57
4.9. Measured transmittance data for the crossed-dipoles for substrate #5, showing substrate etalon behavior.	58

Figure	Page
4.10. SEM photograph of short fat aluminum dipoles on substrate #7.	59
4.11. SEM photograph of long narrow aluminum dipoles on substrate #7.	60
4.12. SEM photograph of short narrow aluminum dipoles on substrate #7.	61
4.13. Measured transmittance data for substrate #7.	62
4.14. SEM photograph of short fat aluminum dipoles on substrate #10.	63
4.15. SEM photograph of long narrow aluminum dipoles on substrate #10.	64
4.16. SEM photograph of short narrow aluminum dipoles on substrate #10.	65
4.17. Measured transmittance data for substrate #10.	66
4.18. SEM photograph of short fat aluminum dipoles on substrate #11.	67
4.19. SEM photograph of long narrow aluminum dipoles on substrate #11.	68
4.20. SEM photograph of short narrow aluminum dipoles on substrate #11.	69
4.21. Measured transmittance data for substrate #11.	70
4.22. SEM photograph of short fat chrome dipoles on substrate #12.	71
4.23. SEM photograph of long narrow chrome dipoles on substrate #12.	72
4.24. SEM photograph of short narrow chrome dipoles on substrate #12.	73
4.25. Measured transmittance data for substrate #12.	74
4.26. SEM photograph of substrate #8.	75

Figure	Page
4.27. SEM photograph of substrate #8.	76
4.28. SEM photograph of substrate #8.	77
4.29. Measured transmittance data for substrate #8.	78
4.30. SEM photograph of substrate #9.	79
4.31. SEM photograph of substrate #8.	80
4.32. SEM photograph of substrate #9.	81
4.33. Measured transmittance data for substrate #9.	82
5.1. Computer code current modes for general dipoles, tripoles and crossed-dipoles.	84
5.2. The relationship between measured element length, $l_m$ , and tip corrected element length, $l_t$ .	87
5.3. Calculated transmittance data for substrate #1.	88
5.4. Calculated transmittance data for substrate #5.	89
5.5. Calculated transmittance data for substrate #5.	92
5.6. Calculated transmittance data for substrate #5.	95
5.7. Calculated transmittance data for substrate #7.	98
5.8. Calculated transmittance data for substrate #10.	99
5.9. Calculated transmittance data for substrate #11.	100
5.10. Calculated transmittance data for substrate #12.	101
5.11. Measured transmittance data for the tripole arrays on substrate #5 using the low f# measurement system.	102
5.12. Calculated transmittance data for substrate #5 including the aluminum loss model.	103

Figure	Page
5.13. Calculated transmittance data for substrate #5 including the aluminum loss model.	104
5.14. Calculated transmittance data for substrate #5 including surface loss.	105
5.15. Calculated transmittance data for substrate #5 including surface loss.	106
A.1. Laser interference pattern system.	113
A.2. Interference fringes in Kodak type 1a spectroscopic plate.	114
A.3. Limits for various techniques in high resolution lithography [5].	116
A.4. Long tripoles on S#1 showing liftoff failure caused by line lengthening due to proximity effect.	118
A.5. Pattern formation by liftoff.	120
A.6. First stages of etch processing for metal pattern formation.	122
A.7. The wet etching process.	124
A.8. Effects of wet etch undercutting, substrate #4.	125
A.9. Simplified schematic diagram of apparatus for reactive ion etching (RIE).	127
A.10. Defects in chrome slots due to surface scratches in CaF <sub>2</sub> .	129
A.11. Multi-level resist process.	131
A.12. Multi-level resist at the start of argon-ion milling.	132
A.13. Results of multi-layer resist patterning of long narrow slots.	133
B.1. Illustration of two measurements required for FTS.	137
B.2. Optical Fourier transform spectroscopy (FTS) system.	139
B.3. Practical beam splitter construction.	142

Figure	Page
B.4. Effects of phase error.	147
B.5. f2 transmission measurement system.	150
B.6. Relation between cone angle and f#.	153
B.7. f8 transmission measurement system.	155
C.1. Transmission by a dielectric slab in free space.	160
C.2. Measured transmittance data for calcium fluoride.	161
C.3. Approximate extinction coefficient for CaF <sub>2</sub> .	163
C.4. Calculated transmittance data for calcium fluoride.	165
D.1. Placement of equivalent loss components.	169
D.2. Local element coordinate system geometry and dipole dimensions.	170
D.3. Example of a sine or cosine mode showing effect of effective length on the distribution.	171
D.4. Slot geometry and electric field direction.	176
D.5. Relationship between the local slot coordinates $\hat{p}$ , $\hat{p}'$ , $\hat{y}$ and the array coordinates $\hat{x}$ , $\hat{y}$ , $\hat{z}$ .	178
D.6. Loss regions for thin slots, showing dimensions and effective reflection coefficients.	179
D.7. Radiating elements in a stratified media.	183
D.8. Geometry of a thick slot.	198
D.9. Modelling the effect of the thick slot walls using image theory.	199

Figure	Page
D.10. Model geometry to obtain the interior slot fields.	200
D.11. Definition of the region for the interior pattern factor.	202
E.1. Extinction coefficient data for aluminum.	212
E.2. Reflectance data for aluminum and gold [79].	213
E.3. Calculated surface resistance of aluminum and gold.	214
E.4. Calculated skin depths of aluminum and gold.	215

## CHAPTER I

### INTRODUCTION

Many studies [1-4,6-13] have shown that periodic arrays of antenna elements could be used to perform the common functions of filtering (both bandpass and bandstop) for propagating wave systems. Most of these studies have been limited to frequencies in the microwave and frequency regimes. It is the purpose of this dissertation to show that these low frequency techniques can be applied to the analysis and construction of filters designed to operate at frequencies in the mid-infrared. The ultimate aim is to increase the design flexibility of filters for this frequency regime to enable the construction of surfaces with controllable off-normal characteristics. This is quite important since many times filters must be placed in optical trains at various angles or in positions where the optical beam is convergent or both. Obtaining stable frequency characteristics for such purposes can be quite difficult when using standard, multi-layer, dielectric filters since the operation of the filters depends on the phase delays between various surfaces. These phase delays, as well as the reflection



coefficients at the surfaces, change with incidence angle resulting in changes in the filter characteristics.

It has been shown [7,8,10] that the filter characteristics of surfaces consisting of infinite arrays of resonant elements can be designed for center frequencies which are stable with incidence angle. The reason for this is that the resonance locations of the elements do not change with aspect angle. In addition, by proper design of the dielectric layers around the resonant elements (accounting for resonance shifts due to dielectric loading), the filters can be designed for constant bandwidth with incidence angle. Resonant surfaces have also been built for use in the far-infrared regime where the elements are somewhat smaller (generally the higher the resonant frequency the smaller the dimensions of the elements). At these higher frequencies, the elements have typically been very simple fat dipoles (square metal elements) or fat slots (square holes in metal) [1-4,17-20]. Unfortunately, these far-infrared surfaces have been designed using a very simplified theory which cannot predict the filter performance at oblique incidence angles and is thus unsatisfactory.

The main thrust of this study will be to show that advanced filters for the mid-infrared frequency regime (roughly the wavelength region from 5 microns to 15 microns) can be designed, built and actually measured.

The rest of this dissertation will be organized as follows. In Chapter II, two theories for design of periodic surfaces or grid

structures will be reviewed and the most appropriate examined in detail. This review is quite tutorial in nature and presents the strengths and weaknesses of each technique.

In Chapter III, a simplified version of the more complete theory will be used to design periodic surfaces for the mid-infrared regime. In addition, this chapter presents actual results of constructing filters based on these simple designs using the techniques of electron-beam (e-beam) lithography. Two appendices are included in support of Chapter III. In Appendix A, the techniques for constructing the extremely small antenna elements are presented. These techniques include a laser interferometric system which was inadequate for pattern generation and the description of an e-beam pattern generation facility which was finally used. Appendix C provides information about the substrate material, calcium fluoride ( $\text{CaF}_2$ ), which was chosen to provide physical support for the periodic surfaces.

In Chapter IV, measured transmittance data are presented for the filters described in Chapter III. The measurement system for this frequency range relies on the methods of Fourier transform spectroscopy (FTS). A detailed description of the actual system used including a derivation of the FTS process is provided in Appendix B. Included with the measured data in Chapter IV are scanning electron microscope (SEM) photographs of all the filter surfaces which were successfully built. These photos are used to obtain the actual dimensions of the antenna elements for detailed modelling of the filter characteristics.

Modelling of the filter surfaces is done in Chapter V using computer codes which were developed for the microwave frequency regime. The necessary modifications to these codes to account for the dispersive nature of the  $\text{CaF}_2$  substrate material are pointed out as well as several other modifications to account for properties of the mid-infrared materials. The required model for  $\text{CaF}_2$  is obtained in Appendix C. An important property in this frequency range is the resistive loss in the metal surfaces. Techniques for modelling this loss for an arbitrary metal are presented in Appendix D. This analysis requires a knowledge of the surface resistance of the metal. Data of this type are presented in Appendix E for some of the metals used in this study.

In Chapter VI, a summary of this study is given. Included in this section are recommendations for future studies as well as additional information which will be needed.

## CHAPTER II

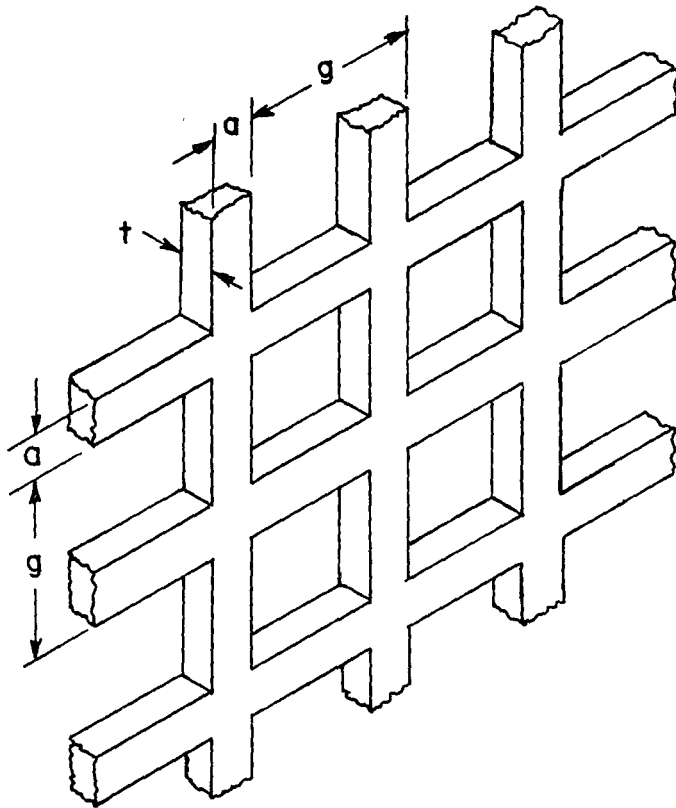
### ANALYSIS OF PERIODIC SURFACE CHARACTERISTICS

In this section, two techniques are presented for modelling the characteristics of infinite periodic surface structures. The first will be referred to as grid theory (GT) or Ulrich's theory after its prime developer [1-4]. This theory is a specialization of more complete results presented by Marcuvitz [5]. As a result, Ulrich's theory is an approximation which is reasonably valid only at low frequencies (below array first resonance) and at normal incidence. For these reasons, it will not be extensively discussed. A much more complete and accurate theory has been developed by Munk and co-workers [6-13]. This theory will be referred to as periodic surface theory (PST). PST is capable of handling frequencies above resonance and off-axis effects. For these reasons, PST has been used for the design and analysis of the filters constructed during this study, and will therefore be treated in greater detail than grid theory.

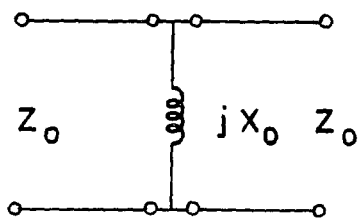
## A. GRID THEORY

This theory, as developed by Ulrich, is based on low frequency models for scattering by one-dimensional (1d) wire grids. The original models developed by Ulrich are in essence simplifications of models presented by Marcuvitz [5] and others for scattering by 1d grids. Marcuvitz's results are obtained by evaluating the scattering by a wire grid via integral equation techniques [14,15] and retaining the first two diffraction modes. These results are for both polarizations and various incidence angles. Ulrich's models are obtained from those of Marcuvitz by making two assumptions and several approximations. The first assumption is that all rays are incident normal to the grid surface which results in a considerable simplification of the model formulas. The second assumption is that the grid is essentially transparent for the H-field polarized parallel to the grid (i.e., the ideal polarizer). By crossing two such identical grids at 90°, a polarization insensitive surface is obtained. The resulting surface is shown in Figure 2.1 with its lumped circuit model useful for low frequencies and normal incidence. Due to the model used, this surface is referred to in grid terminology as an "inductive grid" (in PST terminology a "slot array"). For arrays consisting of flat strips in free space, the shunt impedance used to model the surface is given by [1]

$$X_o/Z_o = \ln \left( \csc \left( \frac{\pi a}{2g} \right) \right) g/\lambda \quad (2.1)$$



(a). Inductive grid (fat slot array) in free space.



(b). Transmission line model showing shunt impedance.

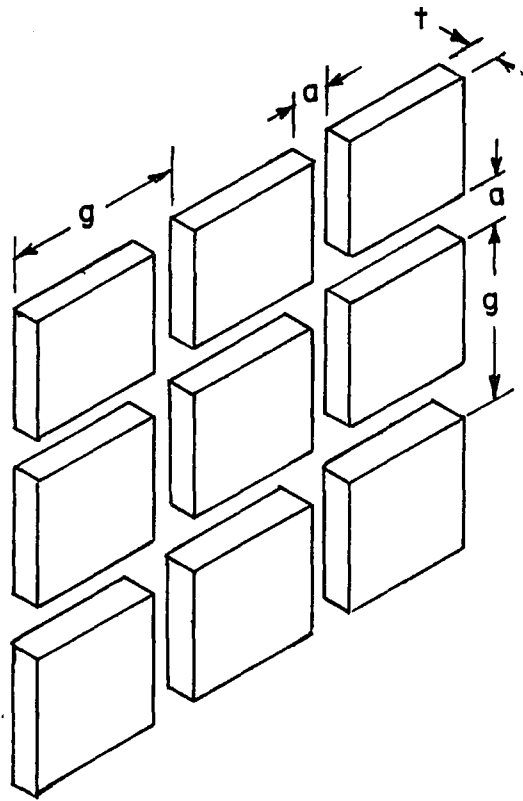
Figure 2.1. An inductive grid and its grid theory transmission line model.

for the case  $t \ll a \ll g \ll \lambda$  where  $Z_0$  is the impedance of free space. Typically, these restrictions are relaxed and Equation (2.1) is used over very broad regions. Using these results, the grid transmittance and reflectance are given by

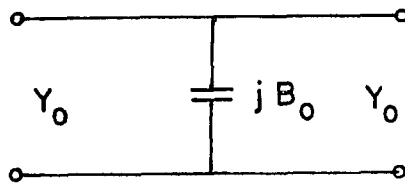
$$T = 1 - R = \frac{4(X_0/Z_0)^2}{1+4(X_0/Z_0)^2} \quad . \quad (2.2)$$

In addition to the inductive grid of Figure 2.1(a), Ulrich also defines the complement of this surface as a capacitive grid (PST fat dipole elements), an example of which is shown in Figure 2.2(a). This surface is the electrical dual of that in Figure 2.1(a). The utility of these models is easily seen since multiple arrays may be modelled by series connected transmission lines of suitable impedance with appropriately placed shunt impedances. Unfortunately, these simple models do not adequately describe the arrays in their resonance region where they exhibit their most interesting characteristics. In addition, the Ulrich theory using more advanced or complicated models [2,3] can not adequately treat problems of grating lobes, off-axis effects and the effects of mutual coupling for arrays on thin substrates. Finally, grid theory has problems predicting the properties of skewed arrays which are sometimes useful. For these reasons it was decided to use periodic surface theory (PST) which is based on the radiation properties of conducting elements in (possibly) sandwiched dielectric media.

It should be pointed out that even with all these deficiencies, grid theory has been used with fair success. Most applications have



(a). Capacitive grid (fat dipole array) in free space.

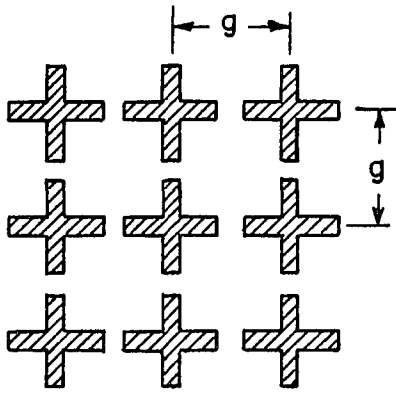


(b). Transmission line model with shunt admittance.

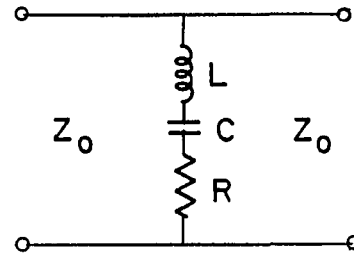
Figure 2.2. A capacitive grid and its grid theory transmission line model.



used the grids as partial reflector/transmitters in Fabry-Perot etalon [16] arrangements well below array resonance. Ulrich, et al., [17] have used grid etalons for tunable far-infrared laser output couplers and Muehlner and Weiss [18] have used similar etalon arrangements for far-infrared sky temperature measurements. In addition, several recent papers have been published concerning the use of grids in the near-millimeter to far-infrared regimes. Whitcomb and Keene [19] have built low-pass filters for sub-millimeter astronomy and Timusk and Richards [20] have built bandpass filters to operate in the near-millimeter range. Finally, Tomaselli, et al., [21] have constructed filters with bandpass characteristics for the far-infrared. The latter two articles [20,21] are interesting since they form relatively high-Q resonant structures by overlaying inductive and capacitive grids to form crossed-dipoles and crossed-slots. For more complicated surfaces such as these, the equivalent circuit for the surface impedance is typically a resonant tank consisting of a series/parallel combination of a capacitor and an inductor. In addition, if any metal loss is to be modelled, a resistance may be added to the tank circuit. The model for a capacitive cross grid (crossed-dipoles) is shown in Figure 2.3 along with a relative transmission curve. Note that this model is still only useful in the non-diffraction region,  $g > \lambda$  and normal incidence.



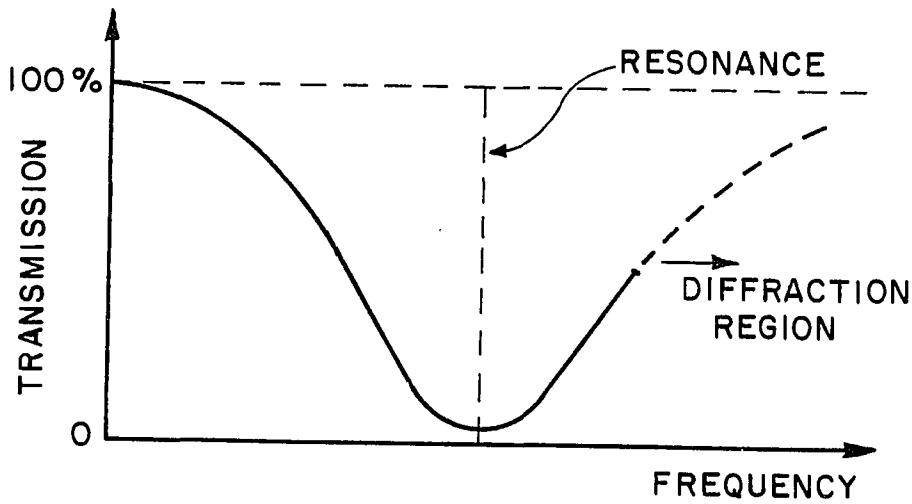
(a)



(b)

(a). Capacitive cross grid structure (crossed dipoles).

(b). Equivalent circuit.



(c)

(c). Relative transmission curve.

Figure 2.3. A capacitive cross grid and its grid theory transmission line model.

## B. PERIODIC SURFACE THEORY (PST)

The analysis of infinite arrays via PST begins with the assumption that an array in an infinite, homogeneous, lossless medium is illuminated by a plane wave propagating in an arbitrary but specified direction. The lossless medium condition is imposed to insure a uniform incident field in the plane of the array. This condition is removed by the introduction of stratified media, in which case the only requirement is incidence from a lossless halfspace. Typically, the analysis is done for metallic elements (dipoles, etc.) with the solution for slot elements obtained via duality [22]. Thus, we write the incident electric field as

$$\vec{E}^i(\vec{R}) = \vec{E}^i e^{-j\beta\vec{R}\cdot\hat{S}} \quad (2.3)$$

where  $\hat{S}$  is the unit vector in the direction of plane wave propagation and is given by

$$\hat{S} = \hat{x}S_x + \hat{y}S_y + \hat{z}S_z \quad (2.4)$$

It is further assumed that the array elements are located in the plane  $y=0$  with the reference element at the origin as shown in Figure 2.4. As a consequence of Floquet's theorem and the regular array structure, the current distribution on each element is identical to all the other elements except for a linear phase shift which matches that of the incident plane wave. Thus, assuming linear elements, the current on element  $(q,m)$  at  $x=qD_x$  and  $z=mD_z+q\Delta_z$  is simply

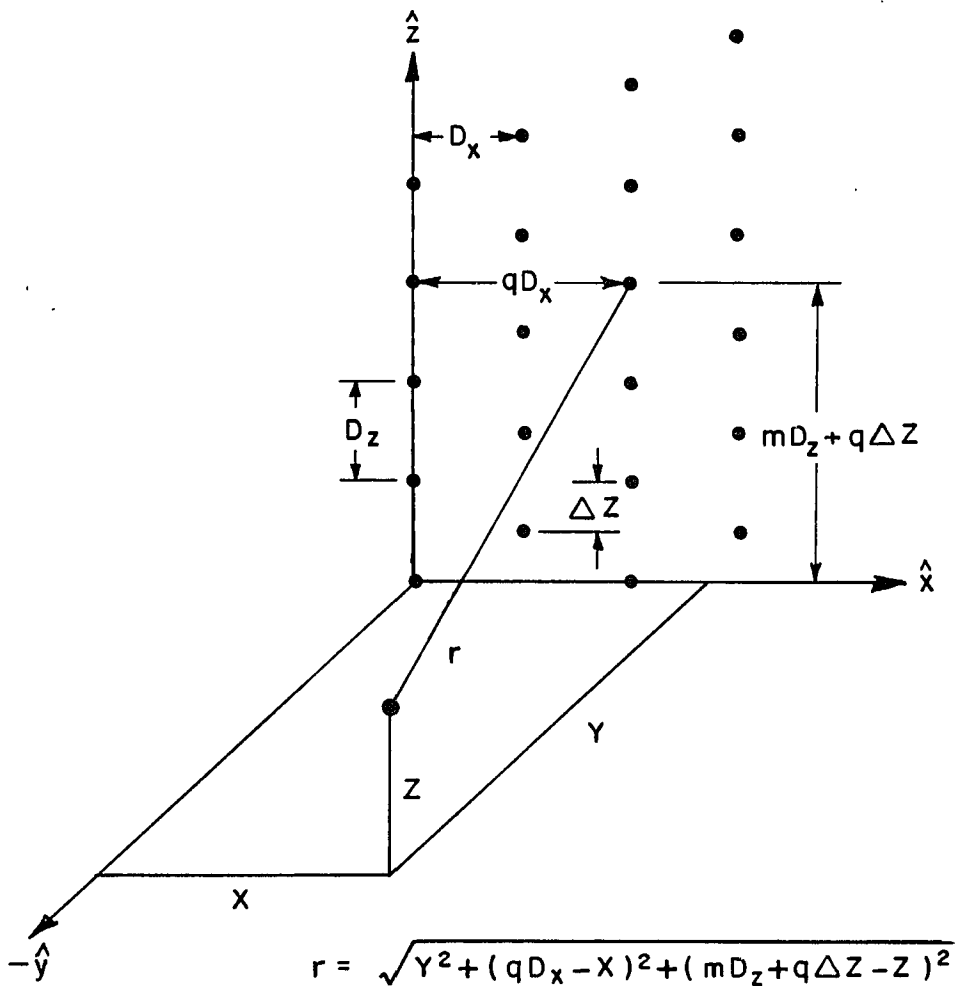


Figure 2.4. Periodic array of linear elements in a skewed grid geometry. The reference element is at the coordinate origin [23].

$$I_{qm}(\ell) = I(\ell)e^{-j\beta S_x(qD_x)}e^{-j\beta S_z(mD_z+q\Delta_z)} \quad (2.5)$$

To find the field of this array, we first find the field of an array of Hertzian dipoles with current  $I$ , length  $dp$ , and orientation  $\hat{p}$  having the same grid structure, i.e.,

$$\bar{I}_{qm} = \hat{p} I dp e^{-j\beta S_x(qD_x)}e^{-j\beta S_z(mD_z+q\Delta_z)} \quad (2.6)$$

Using Plane Wave Spectrum (PWS) techniques developed in [9], Kornbau [23] has shown that the vector potential from such an array of Hertzian dipoles is given by:

$$d\bar{A}(\bar{R}) = \hat{p} \frac{u I dp}{2j\beta D_x D_z} \sum_k \sum_n \frac{e^{-j\beta \bar{R} \cdot \hat{r}_\pm}}{r_y} \quad (2.7)$$

where

$$\hat{r}_\pm = \hat{x}r_x \pm \hat{y}r_y + \hat{z}r_z \quad (2.8)$$

and

$$r_x = S_x + k \frac{\lambda}{D_x} - n \frac{\Delta_z \lambda}{D_x D_z} \quad (2.9)$$

$$r_z = S_z + n \frac{\lambda}{D_z}$$

$$r_y = \sqrt{1 - r_x^2 - r_z^2} \quad .$$

In Equation (2.8), the "+" is used in the region  $y > 0$  and the "-" for  $y < 0$ . The resulting electric field is given by [24]

$$d\vec{E}(\vec{R}) = I \, dp \, \frac{Z_c}{2D_x D_z} \sum_k \sum_n \frac{e^{-j\beta\vec{R}\cdot\hat{r}_\pm}}{r_y} \vec{e}_\pm, \quad (2.10)$$

where

$$\begin{aligned} \vec{e}_\pm &= [\hat{p} \times \hat{r}_\pm] \times \hat{r}_\pm \\ &= [(\hat{r}_\pm \cdot \hat{p}) \hat{r}_\pm - \hat{p}] \end{aligned} \quad (2.11)$$

and  $Z_c$  in the medium characteristic impedance given by

$$Z_c = \sqrt{\mu/\epsilon}. \quad (2.12)$$

Equation (2.10) is specialized for the reference element at the origin; however, it is pointed out [25] that moving the reference to  $\vec{R}'$  moves the field point  $\vec{R}$  in Equation (2.10) to  $(\vec{R}-\vec{R}')$  yielding

$$d\vec{E}(\vec{R}) = I \, dp \, \frac{Z_c}{2D_x D_z} \sum_k \sum_n \frac{e^{-j\beta(\vec{R}-\vec{R}')\cdot\hat{r}_\pm}}{r_y} \vec{e}_\pm. \quad (2.13)$$

In Equation (2.13) the "+" on  $\hat{r}_\pm$  is used for  $y > y'$  and the "-" for  $y < y'$ .

Finding the field of an array of elements is now a routine matter of integrating Equation (2.13) over the limits of the reference element. This process is usually simplified by defining coordinates which are local to the element. For a linear element (i.e., a straight,

one-dimensional current source), identified as element (1) via superscripts, a convenient choice is

$$\bar{R}' = \bar{R}^{(1)} + \hat{p}^{(1)}_p, \quad a^{(1)} < p < b^{(1)}$$

where "a(1)" and "b(1)" are the endpoints of the reference elements in local coordinates and  $\bar{R}^{(1)}$  is a reference point in global coordinates on the reference element. The resulting field of this array of linear elements is

$$E^{(1)}(R) = \frac{Z_c}{2D_x D_z} \sum_k \sum_n \frac{e^{-j\beta(R-R^{(1)}) \cdot \hat{r}_{\pm}}}{r_y} \bar{e}_{\pm}^{(1)} \int_{a^{(1)}}^{b^{(1)}} I^{(1)}(p) e^{j\beta p \hat{p}^{(1)} \cdot \hat{r}_{\pm}} dp. \quad (2.15)$$

For reasons which will become obvious, this is usually recast in the following form

$$\bar{E}^{(1)}(\bar{R}) = I(\bar{R}^{(1)}) \frac{Z_c}{2D_x D_z} \sum_k \sum_n \frac{e^{-j\beta(R-R^{(1)}) \cdot \hat{r}_{\pm}}}{r_y} \bar{e}_{\pm}^{(1)} p^{(1)} \quad (2.16)$$

where

$$p^{(1)} = \frac{1}{I^{(1)}(\bar{R}^{(1)})} \int_{a^{(1)}}^{b^{(1)}} I^{(1)}(p) e^{j\beta p \hat{p}^{(1)} \cdot \hat{r}_{\pm}} dp \quad (2.17)$$

is called the array element pattern factor or simply the pattern factor. Note that this pattern factor should not be confused with the pattern factor for an isolated element even though the two are quite similar [25].

Several important results may be drawn from Equations (2.16) and (2.17). The most important observation is that the scattered field from the array may be considered to consist of a doubly infinite sum of plane waves. Depending on  $r_y$  (Equation (2.9)), the plane waves either propagate ( $r_y$  real) or are evanescent ( $r_y$  imaginary) in nature. Normally, only the principal rays (i.e.,  $\hat{r}$  evaluated for  $k=0=n$ ) are propagating and represent the directly transmitted and reflected fields. Note that only propagating waves yield real energy transfer, whereas the evanescent waves represent stored energy near the array. Later, when transmittance and reflectance coefficients are calculated, they will involve only the  $k=0=n$  terms. Higher order modes which become propagating are termed grating lobes and typically represent uncontrolled energy loss [34]. Thus one of the chief concerns in the design of periodic surfaces is the prevention of grating lobes.

The problem in using the preceding analysis is that the element currents on a periodic surface are unknown and must be determined as part of the filter characterization. A solution is obtained by expanding the current on each reference element in some basis set (called current modes) as in Harrington's moment method [26]. A similar method based on Rumsey's reaction formulation [27] has been used by Richmond [28] to model the scattering by thin wire structures. A requirement of all these formulations is a knowledge of the voltage induced in an antenna element due to an incident field.



It is now assumed that a linear antenna element with orientation  $\hat{p}^{(2)}$  when excited at position  $\bar{R}^{(2)}$  supports a transmitting current distribution  $I^{(2)}t(p)$ . If this element is subjected to an incident plane wave identical in form to Equation (2.3), it has been shown [29,30] that a voltage

$$V(\bar{R}^{(2)}) = \bar{E}^i \cdot \hat{p}^{(2)} \frac{1}{I^{(2)}t(\bar{R}^{(2)})} \int_{a^{(2)}}^{b^{(2)}} I^{(2)}t(p) e^{-j\beta[\bar{R}^{(2)} + \hat{p}^{(2)}p] \cdot \hat{s}} dp \quad (2.18)$$

will be induced at the terminals at position  $\bar{R}^{(2)}$ . Equation (2.18) may be rewritten as

$$V^{(2)}(\bar{R}^{(2)}) = \hat{p}^{(2)} \cdot \bar{E}^i(\bar{R}^{(2)}) P^{(2)}t \quad (2.19)$$

where

$$P^{(2)}t = \frac{1}{I^{(2)}(\bar{R}^{(2)})} \int_{a^{(2)}}^{b^{(2)}} I^{(2)}t(p) e^{-j\beta \hat{p}^{(2)} \cdot \hat{s} p} dp \quad (2.20)$$

which is quite similar to Equation (2.17) except for the exponent sign change. Equation (2.20) is also referred to as a pattern factor but again should not be confused with the normal pattern factor of an isolated element. The analysis now proceeds by allowing the scattered field from elements #1 to illuminate linear antenna element #2. This produces a terminal voltage in element #2 due to the currents in array #1. If we find the ratio of this terminal voltage to the terminal

current in array #1, then we define a quantity called the mutual impedance which is given by [29,31]

$$\begin{aligned}
 Z^{21} &= - \frac{V^{(2)}(\bar{R}^{(2)})}{I^{(1)}(\bar{R}^{(1)})} \\
 &= - \frac{Z_c}{2D_x D_z} \sum_k \sum_n \frac{e^{-j\beta(\bar{R}^{(2)} - \bar{R}^{(1)}) \cdot \hat{r}_{\pm}}}{r_y} \hat{p}^{(2)} \cdot \hat{e}_{\pm}^{(1)} t_p^{(2)} t_p^{(1)} \quad (2.21)
 \end{aligned}$$

It is important to point out that  $P^{(1)}$  should be evaluated for the current distribution which is actually on the array elements when excited by the incident field. This is usually called the scattering current distribution which is typically modelled using the receiving current distribution. For this reason  $P^{(1)}$  is often times called the receiving pattern factor. Note that element #2 is typically the reference element of another array, and that this process can be extended to any number of elements.

Thus, just as in Richmond's thin wire formulation, PST finds the scattered fields of elements by modelling the element currents with linear current modes (different distributions for receiving and transmitting). The next step involves forming the square impedance matrix which relates the terminal input current of each array mode to the terminal voltage of all the reference element modes (this includes the so called self-impedances). Next, the actual terminal voltages due to the incident field are found via Equations (2.19) and (2.20). Thus we have the system of equations,

$$\begin{bmatrix} V^{(1)}(\bar{R}^{(1)}) \\ V^{(2)}(\bar{R}^{(2)}) \\ \vdots \\ V^{(N)}(\bar{R}^{(N)}) \end{bmatrix} = \begin{bmatrix} Z^{11} & Z^{12} & \dots & Z^{1N} \\ Z^{21} & Z^{22} & \dots & Z^{2N} \\ \vdots & \vdots & \ddots & \vdots \\ Z^{N1} & Z^{N2} & \dots & Z^{NN} \end{bmatrix} \begin{bmatrix} I^{(1)}(\bar{R}^{(1)}) \\ I^{(2)}(\bar{R}^{(2)}) \\ \vdots \\ I^{(N)}(\bar{R}^{(N)}) \end{bmatrix} \quad (2.22)$$

where the unknowns are the mode current amplitudes. This system of equations is then inverted to yield the mode amplitudes. Finally, Equation (2.16) is used to find the scattered fields using the receiving distribution for each mode with the proper mode amplitude. Note that if there are any equivalent impedances to account for loaded elements [32, 33] or ohmic loss [33] (Appendix D), they should be added to the self-impedance terms before the impedance matrix is inverted. It should also be pointed out that any such load impedances should be calculated using the receiving current mode distribution since it is this mode which will be used to find the scattered fields.

A comment concerning evaluation of Equation (2.21) for the self impedances (diagonal matrix terms) should be made. For these terms, it would seem that we should let the exponent  $(\bar{R}^{(2)} - \bar{R}^{(1)})$  vanish; however, this has been found to yield invalid results. The problem arises due to modelling the element current distributions with filament currents which have zero radii. Better results have been obtained using the concept of equivalent wire radius by allowing the transmitting and receiving modes to be displaced laterally (i.e., in the  $\hat{x}$  or  $\hat{z}$

directions) by such a radius. In past microwave regime calculations in which the conductors have been very thin, an equivalent radius of  $1/4$ , the element width has been used satisfactorily. For the optical elements to be shown the thickness to width ratios are commonly 1:3 or greater and thus a better wire radius model is required. Such a model was obtained from the Microwave Engineers Handbook and Buyer's Guide [37] and is given in Figure 2.5.

The last major portion of PST is a modification of the preceding formulas to account for the presence of stratified dielectric layers. This is a very important modification since dielectric layers are always used to support metallic elements and are usually found with slot elements. Furthermore, the proper design of the layers (i.e., dielectric constants and thicknesses) has been found to have a stabilizing effect on surface bandwidth characteristics [34,35]. The utility of the PWS technique is apparent in that the effect of stratified dielectric layers can be handled using simple Fresnel reflection coefficients. The cumulative effect of multiple dielectric layers, including multiple internal reflections is embodied in a quantity called the "T" factor (or Transformation function) the derivation of which is straightforward but nontrivial [36]. For this reason, the form of the T factor will not be rederived here.

A major property of the T factor is that it is polarization sensitive and just as with reflection and transmission coefficients, it is typically broken up into two parts; one for orthogonal polarization and the other for parallel polarization. Here, orthogonal and

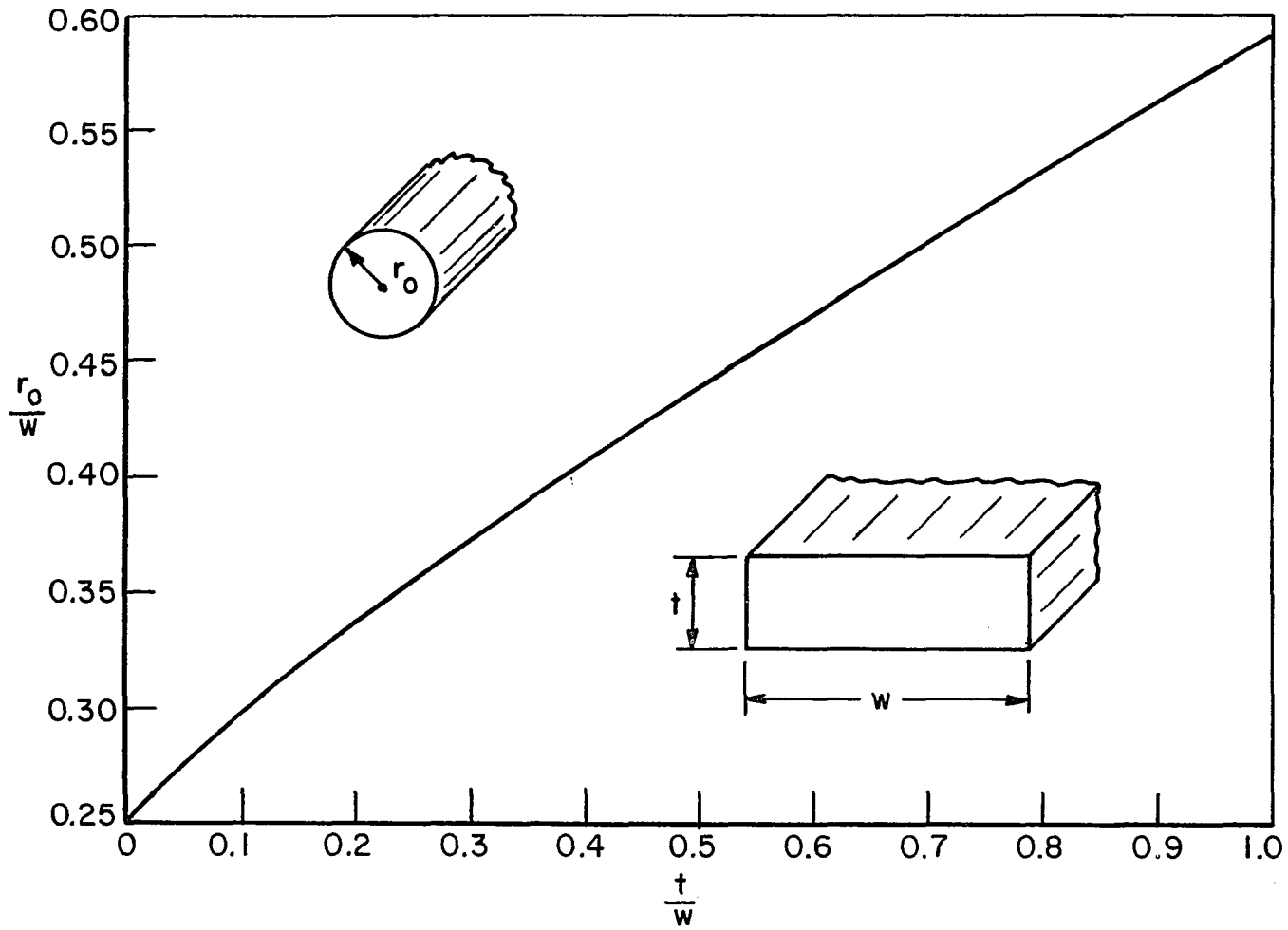


Figure 2.5. Relationship between flat wire geometry and equivalent wire radius [37].

parallel are defined with respect to the plane of incidence. In addition it should be pointed out that these surfaces will in general depolarize the incident fields producing cross-polarized scattered components. For this reason, we usually introduce scattering matrices for the reflected and transmitted fields which are defined as

$$\begin{bmatrix} \perp E^r \\ \parallel E^r \end{bmatrix} = \begin{bmatrix} \perp S_{\perp}^r & \perp S_{\parallel}^r \\ \parallel S_{\perp}^r & \parallel S_{\parallel}^r \end{bmatrix} \begin{bmatrix} \perp E^i \\ \parallel E^i \end{bmatrix} \quad (2.23)$$

and

$$\begin{bmatrix} \perp E^t \\ \parallel E^t \end{bmatrix} = \begin{bmatrix} \perp S_{\perp}^t & \perp S_{\parallel}^t \\ \parallel S_{\perp}^t & \parallel S_{\parallel}^t \end{bmatrix} \begin{bmatrix} \perp E^i \\ \parallel E^i \end{bmatrix} \quad (2.24)$$

The elements of these scattering matrices are complex-valued since they must account for magnitude as well as phase information. The phase reference point is usually taken to be the coordinate origin. Note that the main diagonal elements of the scattering matrices by assumption contain terms which account for the directly transmitted and reflected fields (independent of any periodic arrays).

Using these scattering matrix elements, the calculated transmittance (and reflectance) can now be defined. The percent transmittance is defined as the ratio of transmitted power to incident power times 100 or

$$T_{\%} = 100 \left[ \frac{P_{out}}{P_{in}} \right] . \quad (2.25)$$

Assuming the output and input media are identical this can be rewritten as

$$T_{\%} = 100 \left[ \frac{|_{\perp}E^t|^2 + |_{\parallel}E^t|^2}{|_{\perp}E^i|^2 + |_{\parallel}E^i|^2} \right] . \quad (2.26)$$

Since our ultimate goal is a comparison with measured data, it is assumed that there is equal energy in the two incident polarizations due to the nature of the measurement radiation source used (Appendix B). In addition, it is assumed that the two polarizations are uncorrelated so that any cross product terms resulting in interference effects are negligible. With these assumptions, the transmittance can be written as

$$T_{\%} = 100 \left[ \frac{|_{\perp}S_{\perp}^t|^2 + |_{\perp}S_{\parallel}^t|^2 + |_{\parallel}S_{\perp}^t|^2 + |_{\parallel}S_{\parallel}^t|^2}{2} \right] \quad (2.27)$$

and similarly the reflectance as

$$T_{\%} = 100 \left[ \frac{|_{\perp}S_{\perp}^r|^2 + |_{\perp}S_{\parallel}^r|^2 + |_{\parallel}S_{\perp}^r|^2 + |_{\parallel}S_{\parallel}^r|^2}{2} \right] . \quad (2.28)$$

In Ulrich's grid theory, the effects of metal loss can be accounted for by the inclusion of a series of parallel loss resistance (see Figure 3(b)). Even though this resistance is usually very small, its effects

may become quite noticeable since it tends to limit the filter insertion loss at resonance for bandstop designs. Unfortunately, this resistance cannot be readily calculated and must be determined empirically from measured data and curve fitting techniques. As mentioned before in PST the effects of metal loss can be modelled analytically using effective resistances which are included in the self impedance terms. A perturbation method for doing this was developed by Munk [38] for the case of small losses in metallic elements such as dipoles. This technique is reviewed in Appendix D with enhancements for elements on lossy substrates. In addition, techniques for modelling loss effects in slot arrays are presented.

It should be pointed out that the PST techniques for modelling metal loss require a knowledge of the metal surface resistance,  $R_s$ ; if the metal has reasonably good conductivity (i.e., small skin depth) the surface resistance can be modelled with knowledge of reflectance data at normal incidence. Reflectance data of this type is presented in Appendix E for several metals in the near infrared regime. At normal incidence, the reflectance,  $R$ , of a good conductor is

$$R = 100 \left[ \frac{R_s - Z_0}{R_s + Z_0} \right]^2 \quad (2.29)$$

where  $Z_0$  is the impedance of free space ( $\sim 377$  ohms). Solving Equation (2.29) for  $R_s$  yields



$$R_s = Z_0 \left[ \frac{1 - \sqrt{R/100}}{1 + \sqrt{R/100}} \right] \quad (2.30)$$

where the negative principal square root has been used since a surface with 100% reflectance has zero surface resistance. Calculated transmittance data is included in Chapter V showing the effects of metal loss on periodic surface performance.

## CHAPTER III

### SIMPLIFIED SURFACE DESIGN AND CONSTRUCTION

Due to the many uncertainties in the construction of the mid-infrared periodic surface elements, it was decided to forego any detailed preliminary designs for this initial study. Instead, rather simple surfaces encompassing dipoles, tripoles and crossed-dipoles (and their complementary slots) were designed according to first order theory. Thus, the actual procedure of theory, construction and measurement consisted of the following six part process:

1. Selection of resonant frequencies (wavelengths)
2. First order design dimensions
3. Construction of the surfaces
4. Measurement of filter characteristics
5. SEM photographs to obtain actual element dimensions
6. Calculation of filter characteristics.

The selection of desired resonant frequencies was somewhat arbitrary but constrained by substrate effects and construction techniques. Once calcium fluoride ( $\text{CaF}_2$ ) was selected as the substrate material (see

Appendix C) a lower frequency limit of about  $1000 \text{ cm}^{-1}$  was set due to dielectric resonance absorption. Construction techniques limited the smallest elements which could be built. When coupled with the index of  $\text{CaF}_2$ , element size placed a high frequency limit at approximately  $2000 \text{ cm}^{-1}$ . Within this region the rather arbitrary frequencies of  $1100 \text{ cm}^{-1}$  ( $9 \mu\text{m}$ ) and  $1400 \text{ cm}^{-1}$  ( $7 \mu\text{m}$ ) were chosen. These frequencies were felt to be sufficiently far enough apart to see appreciable filter effect differences but not so far that both response regions could not be viewed on one data plot. Actually, the  $1100 \text{ cm}^{-1}$  resonance location was chosen to be near the  $\text{CaF}_2$  infrared absorption edge (Appendix C) so that these effects could be studied. These data should thus allow the validation of previous computer codes which could account for dielectric loss but had not been tested against measured data. On the other hand, the  $1400 \text{ cm}^{-1}$  resonance is far enough from the absorption edge that the substrates can be considered lossless for the  $1 \text{ mm}$  flats which were used.

The desired surfaces are to be resonant at some free-space wavelength  $\lambda_0$  (either  $7 \mu\text{m}$  or  $9 \mu\text{m}$ ). According to Munk, et al [39], the resonant frequency (but not bandwidth) of a single array of elements is a perturbation of the resonance of an isolated element. Thus, to first order we shall consider an isolated element in the design of these surfaces. For elements such as dipoles, tripoles and crossed-dipoles, the designs become particularly easy.

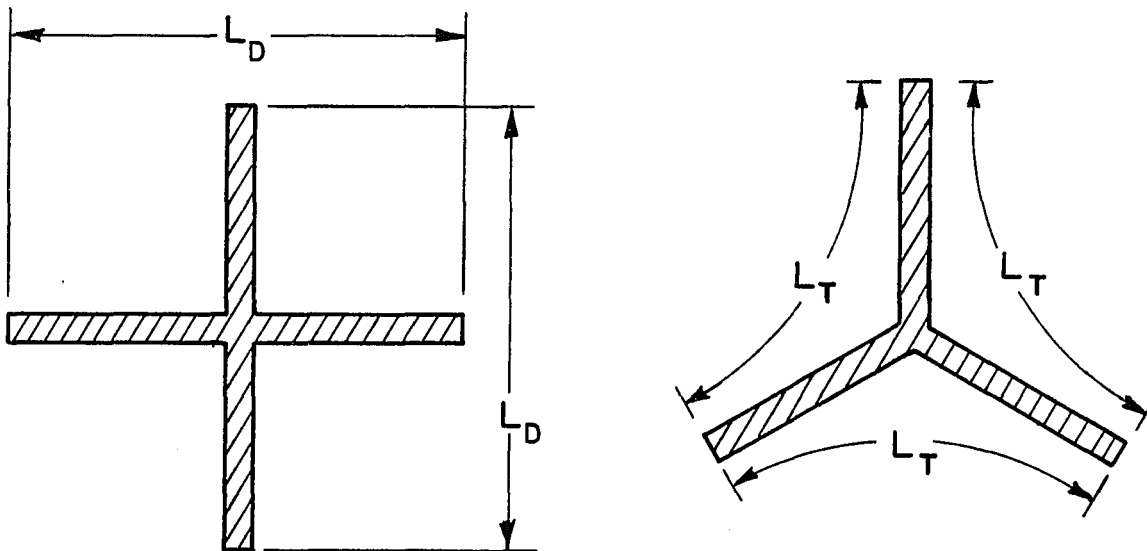
The first resonance of a crossed-dipole (or simple dipole), as shown in Figure 3.1, is given by

$$L_D \approx 0.5 \left( \frac{\lambda_0}{N_{\text{eff}}} \right) \quad (3.1)$$

and for a tripole by

$$L_T \approx 0.55 \left( \frac{\lambda_0}{N_{\text{eff}}} \right) \quad (3.2)$$

In Equations (3.1) and (3.2),  $N_{\text{eff}}$  is the effective index of refraction "seen" by the elements and is given by



(a)

(a). Crossed-dipoles.

(b)

(b). Tripoles.

Figure 3.1. Shapes and critical dimensions.

$$N_{\text{eff}} = \sqrt{\frac{\epsilon_1 + \epsilon_2}{2}}, \quad (3.3)$$

where  $\epsilon_1$  and  $\epsilon_2$  are the relative permittivities of the media on each side of the array. Using an approximate value of 1.3 for the index of  $\text{CaF}_2$  (nominal 10  $\mu\text{m}$  value) we obtain the dimensions in Table 3.1.

Using the values in Table 3.1 as guidelines, attempts were made with the aid of the National Research and Resource Facility for Submicron Structures (NRRFSS) to construct patches of these elements on  $\text{CaF}_2$ . The principles of construction and terminology are explained in Appendix A. Two trips were made to the NRRFSS with patches

TABLE 3.1

CRITICAL DIMENSIONS FOR CROSSED-DIPOLES AND TRIPLES  
ON CALCIUM FLUORIDE NEAR 10  $\mu\text{m}$

$\lambda_0$ ( $\mu\text{m}$ )	$L_D$ ( $\mu\text{m}$ )	$L_T$ ( $\mu\text{m}$ )
7	3.0	3.3
9	3.9	4.3

placed on six substrates during each trip. To maintain reasonable E-beam exposure time, the largest patch was limited to a 3mm x 3mm area, resulting in an average exposure time of approximately 70 minutes. Due to this small patch size and the 25 mm diameter of the substrates, typically two or more patches were placed on each substrate. Usually, a patch of nominal 9  $\mu\text{m}$  resonant elements and a patch of nominal 7  $\mu\text{m}$  resonant elements were placed on the same substrate. For the sake of brevity, the elements designed to be resonant at a 9  $\mu\text{m}$  wavelength have been referred to as long as compared to the elements designed to be resonant at 7  $\mu\text{m}$  which are referred to as short. Thus, the distinctions long tripoles or short crossed-slots.

For the first set of substrates, the chosen element shapes were tripoles and crossed-dipoles. The initial designs called for the tripoles to be in a skewed grid geometry having 120° symmetry. Thus, the top grid angle (TGA) defined by Kornbau [40] was to be 60° and all leg angles were to be 120° as shown in Figure 3.2. However, it was found that for the EBMF (see Appendix A) unit used, the preferred drawing directions were for horizontal lines, vertical lines and lines having a 2:1 slope (or 1:2 slope). Using the 2:1 slopes resulted in leg angles of 117° rather than 120° which was felt to be sufficiently accurate for these initial studies. Typically, surface patches were put down in pairs of similar long and short elements (i.e., only factors affecting element length would change). Thus, a given substrate might have a 3mm x 3mm patch of short tripoles and a 3mm x 3mm patch of long

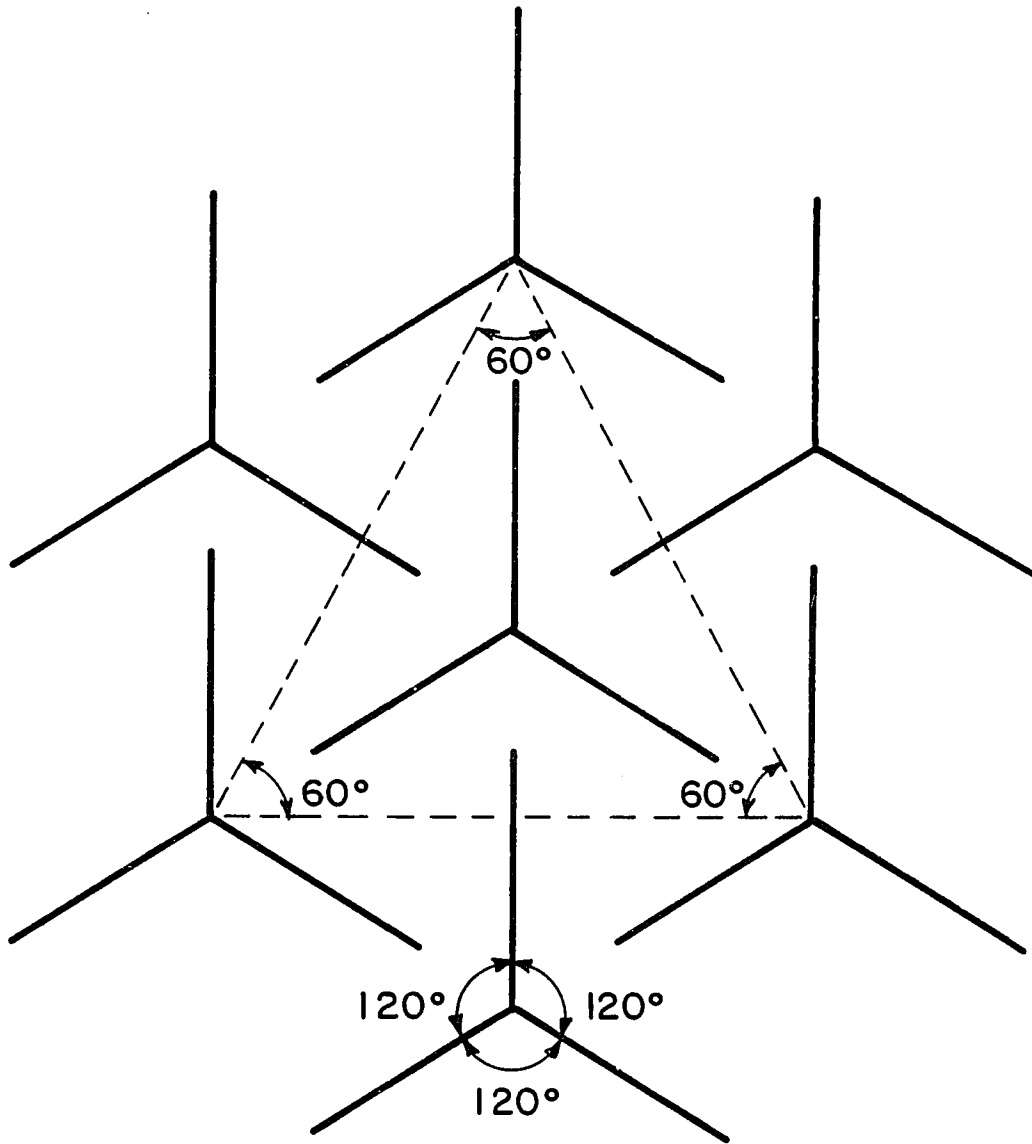


Figure 3.2. Ideal, 120° symmetric tripole array.

tripoles. For such a pair of similar patches, the factors defining the array spacing ( $D_x, D_z, \Delta_z$ ) were held constant as were the element leg angles (measured from the x-axis in the direction of the z-axis). Since the elements are on the same substrate, the metal thicknesses and type of metal are essentially identical.

The results of the first NRRFSS trip are summarized in Table 3.2. This set of substrates yielded a total of five patches which were of sufficient quality to obtain measured data. These patches were the short tripoles on substrate #1 and all four patches on substrate #5. This trip was a very successful learning experience especially concerning the construction techniques. Two points about this should be quickly made. The first is that wet etching is totally unacceptable for forming elements useful in the mid-infrared (see Appendix A), as evidenced by substrates #2 through #4. The second point is that when using the liftoff technique, it is better to slightly overdevelop the resist than to underdevelop. If the resist is underdeveloped, then poor adhesion may occur during metallization resulting in elements which partially break free from the substrate. This caused the appearance of the small tripoles on substrate #6 as illustrated in Figure 3.3(b). These may be compared to the small tripoles on substrate #5 (Figure 3.3(a)) which turned out very well.

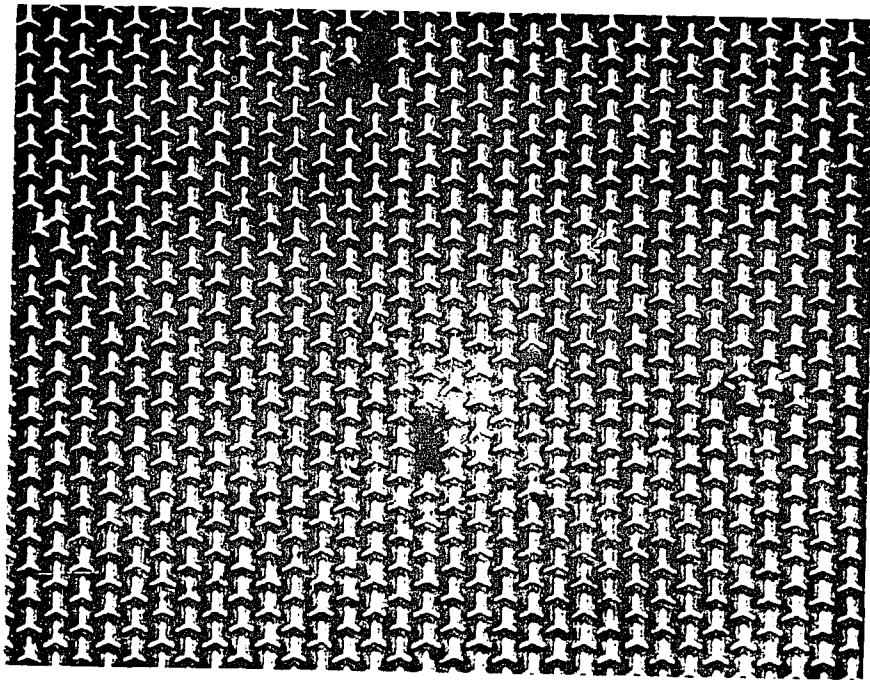
During the second trip to the NRRFSS, the only elements constructed were straight dipoles and straight slots. The reasons for this were two-fold. First of all the construction techniques for straight dipoles



TABLE 3.2

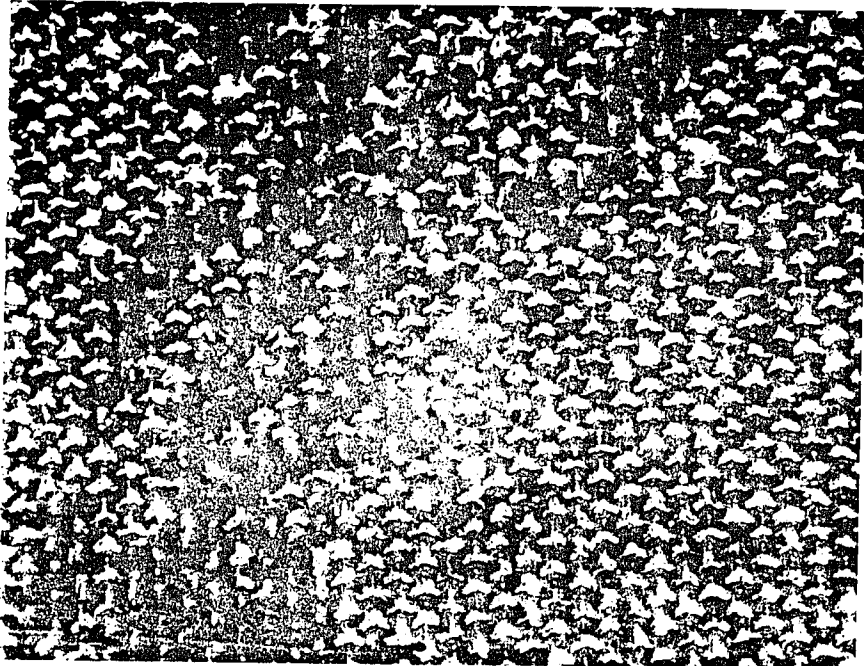
## RESULTS OF FIRST CORNELL NRRFSS TRIP

Substrate (CaF <sub>2</sub> )	Patterns	Metal & thickness (microns)	Construction technique	Comments
1	short tripoles long tripoles	gold on (0.0100) chrome (0.0900) ----- (0.1000)	liftoff	Small tripoles are excellent. Large tripoles show bridging due to proximity effect.
2	short crossed-slots long crossed-slots	aluminum (0.1400)	wet etch, NaOH	All patterns show undercutting and severe over etching.
3	short crossed-slots long crossed-slots	chrome (0.1400)	wet etch, Cyantek	All patterns show undercutting.
4	short crossed-slots long crossed-slots	aluminum (0.1400)	wet etch, NaOH	All patterns show undercutting.
5	short tripoles long tripoles short crossed-dipoles long crossed-dipoles	aluminum (0.1400)	liftoff	All patterns are excellent.
6	short tripoles long tripoles short crossed-dipoles long crossed-dipoles	chrome (0.1400)	liftoff	Liftoff did not turn out due to insufficient development.



(a). Substrate #5. Results of liftoff with good development.  
( $M \approx 1290$ ).

Figure 3.3. Optical micro-photographs of liftoff results.



(b). Substrate #6. Results of resist underdevelopment.  
( $M \approx 1290$ ).

Figure 3.3. (Continued).

are much simpler than for three or four legged elements. This resulted in a considerable reduction of E-beam exposure time, which due to equipment problems was at a premium. The second reason is that during the computer analysis stage, only one current mode is required to model dipoles resulting in a  $1 \times 1$  impedance matrix. For a tripole array requiring two independent current modes, the impedance matrix is of dimension  $2 \times 2$ . Since generation of the impedance matrix elements has been found to be the most time consuming portion of PST analysis, the resulting computer time savings are obvious.

The results of the second NRRFSS trip are summarized in Table 3.3. It was decided that on this trip, each substrate would have three patches exposed. The first two patches were to be dipoles formed using a fairly narrow electron beam. One patch was to be long dipoles and the other short dipoles. The third patch was to be short dipoles having a much greater element width. The purpose was to study the effect of element width on filter bandwidth. These latter elements will henceforth be referred to as "fat" as compared to the prior two patch elements which are referred to as "narrow". A fourth patch of long fat dipoles would have been desirable but was eliminated as an E-beam time saving measure.

Two different techniques were tried as a means of forming the fat elements. The first technique relied on slowing the clock speed on the E-beam deflection electronics to slow the writing speed. This was done while keeping the beam current the same as for the narrow elements. Since the beam current was fixed, the beam spot sizes for all these

TABLE 3.3

## RESULTS OF SECOND CORNELL NRRFSS TRIP

Substrate (CaF <sub>2</sub> )	Patterns	Metal & thickness (microns)	Construction technique	Comments
7	short fat dipoles short narrow dipoles long narrow dipoles	aluminum (0.1350)	liftoff	All patterns are excellent. However, the attempt to draw fatter lines using a slower EBMF clock has produced no appreciable difference.
8	short fat slots short narrow slots long narrow slots	chrome (0.1400)	multi-level resist	All patterns are good although there is some line broadening. Increasing EBMF beam current produces much better fat lines.
9	short fat slots short narrow slots long narrow slots	aluminum (0.1400)	multi-level resist	Same exposure as Substrate # 8. All patterns are good although there is some line broadening.
10	short fat dipoles short narrow dipoles long narrow dipoles	aluminum (0.1400)	liftoff	Same exposure as Substrate # 8. All patterns are excellent.
11	short fat dipoles short narrow dipoles long narrow dipoles	aluminum (0.0360)	liftoff	Same exposure as Substrate # 8. All patterns are excellent.
12	short fat dipoles short narrow dipoles long narrow dipoles	chrome (0.1400)	liftoff	Same exposure as Substrate # 8. All patterns are excellent.

elements were identical and only the exposure (typically expressed in Coulombs/cm<sup>2</sup>) was increased. This was tried on substrate #7 with disappointing results since little appreciable differences in element widths were observed. The second technique tried proved quite successful and was used on substrates #8 through #12. In this technique, the fat elements were obtained by doubling the clock speed while quadrupling the beam current. Note that this effectively doubles the exposure. It should be further noted that it is not the change in exposure which caused the elements to be fatter but a larger E-beam spot size due to space charge effects. This effect is explained in greater detail in Appendix A.

Substrates #8 through #12 were exposed using nearly identical ERMF parameters so as to obtain nearly identical element dimensions. For metallic elements (both aluminum and chrome) excellent results were obtained for all metal thicknesses. The slot elements on substrates #8 and #9 are acceptable but some line growth has been observed. The results for the multi-level resist technique are probably satisfactory for this initial study but future work using reactive ion etching (RIE) should be better.

The last element parameter which was varied was the metal thickness. For substrate #11, an aluminum thickness of 0.0360 microns was obtained. This was chosen to be only slightly greater than a skin depth (see Appendix E) for aluminum at wavelengths near the array resonances. A slot array for such a metal thickness would have been

desirable, but was not obtained due to time limitations. Such a slot array could have been used to check low frequency filter rejection.

## CHAPTER IV

### MEASURED TRANSMITTANCE DATA AND SEM PHOTOGRAPHS

In this chapter, measured transmittance data and SEM photographs are presented for all of the good filter patches discussed in the previous chapter. These include the small tripole patch on substrate #1 and all patches on substrate #5 and on substrates #7 through #12. The sets of data will be generally grouped into metallic elements and slot elements. Within these groups, the data will be presented on a substrate by substrate bases. The only exception to this rule is substrate #5 which is further divided into tripole and crossed-dipole data sets. Within these groups, the data will be organized as a set of SEM photographs of similar element patches followed by a plot of the measured transmittance of those patches. The SEM photographs were taken with near normal viewing angle and as such, the contrast is not very high. Tilting the substrates would have improved the contrast and element visibility but would have distorted the element dimensions. Included on each data plot is a measured response of unmodified  $\text{CaF}_2$  for reference purposes. It should also be pointed out that along with each



SEM photograph of the metal elements, two sets of numeric data are presented. The first set of array data was obtained from the EBMF input data and is considered very accurate. DX and DZ are the PST grid spacings and DDZ is the grid skewing factor. The X and Z offset values are somewhat meaningless here but are used to describe array shifting when there is more than one set of elements to a given filter. Since the values (DX, DZ and DDZ) are considered very accurate due to careful adjustment of the EBMF, they were actually used to calibrate the dimensions on the SEM photographs. Once calibrated, the SEM photographs were used to obtain the actual element dimensions of leg length and width. The leg angles are given in degrees from the x-axis in the z-axis direction and were also obtained from the EBMF input data. The element or metal thickness values were obtained by carefully monitoring the metallization process.

All the transmittance data with one exception were obtained using the high f# measured system described in Appendix D. The exception is the high resolution data of Figure 4.9 which is included to illustrate the etalon behavior of the CaF<sub>2</sub> substrates. (For the sake of convenience, all figures for Chapter IV will be grouped together at the end of the chapter). The high resolution data were taken with the low f# system using a resolution of approximately 0.031 cm<sup>-1</sup> after which sixteen data points were averaged yielding a plotted resolution of 0.482 cm<sup>-1</sup>. This is adequate to see the approximate 3.1 cm<sup>-1</sup> ripple in Figure 4.9. Using the high f# system, data were taken using a resolution of

0.964  $\text{cm}^{-1}$  of which eight points were averaged to yield a plotted resolution of 7.71  $\text{cm}^{-1}$ . The averaging was done to lower the data noise level and thus improve the data appearance. As a last word about the data collection procedure, it should be stated that all the measured responses are for normal incidence. Note that the incidence is not truly normal since a convergent optical beam is used in the measurement system which has a finite beam average angle as explained in Appendix D. Also note that the use of a convergent optical beam will partially destroy the coherence of the multiply reflected beams within the substrate. This partial loss of coherence is pointed out since it has probably lowered the ripple amplitude seen in Figure 4.9 and this effect will be important in the presentation of the calculated data.

The SEM photograph of the short tripoles on substrate #1 is presented in Figure 4.1. As stated before, the long tripoles on this substrate were destroyed because of improper liftoff. As a result, only one curve is displayed in Figure 4.2 in addition to the  $\text{CaF}_2$  transmittance curve. The filter effect seen in Figure 4.2 is quite pronounced with a null depth of about 10.8 dB. This is fairly typical of all the crossed-dipole and tripole arrays which have null depths between 9 dB and 11 dB. In addition, the resonance location is at approximately 8.4 microns rather than 7.0 microns as desired. This is also fairly typical of the short crossed-dipoles and short tripoles in that the resonance locations occur at slightly longer wavelengths than predicted by first order theory. However, the converse is found to be

true for the long crossed-dipoles and long tripoles. For these elements, the resonance locations occur at slightly shorter wavelengths than the desired 9.0 microns. The reasons for these occurrences can be partially explained since the element dimensions differ slightly from those in Table 3.1. Since we were not trying to design for precise resonance locations, this is not viewed as a severe problem.

An interesting feature in the data from the first set of substrates (corresponding to those in Table 3.2) is the bandwidth effect which can be seen by comparing Figures 4.5 and 4.8. It has been pointed out [41] that the bandwidth of a periodic surface is roughly proportional to the inverse product of  $D_x$  and  $D_z$ . Thus, spreading the array out narrows the filter response and vice versa. Even though the element types change considerably between Figures 4.5 and 4.8, (i.e., tripoles and crossed-dipoles) it is felt that these data also support the bandwidth-spacing dependence.

A last interesting feature of the data from the first set of substrates is the appearance of small nulls which may be attributed to second order resonances. In Figure 4.2, such a null may be seen at approximately  $2250 \text{ cm}^{-1}$  for the short chrome-gold tripoles on substrate #1. Similar nulls can be seen in Figure 4.5 for the aluminum tripoles on substrate #5. Note that the second resonances do not occur at twice the first resonance frequency. This can be attributed to the dispersive nature of the  $\text{CaF}_2$  with an index of refraction which is slightly increasing with frequency (see Appendix C) with a resulting

drop in the second resonance frequency. Interestingly enough, the second resonance nulls are not seen in Figure 4.8 for the substrate #5, crossed-dipole data. At this time, there is no apparent reason for this discrepancy in the crossed-dipole data since the second resonance effect is also seen for the straight dipoles which will now be discussed.

For reasons discussed in Chapter III, it was decided that during the second trip to the NRRFSS only dipole or straight slot elements would be constructed. It was anticipated that such elements when measured would show only a 3 dB null for dipoles and a minimum 3 dB insertion loss for straight slots. The reason is that straight elements can only intercept one polarization in our randomly polarized measurement system or one half of the total power. To improve this, attempts were made to build a simple, straight line array polarizer which would have improved the measurement dynamic range. Unfortunately, all attempts at this failed. With the resulting limitations in mind, the last set of substrates will be discussed.

On substrates #7 through #12, three sets of elements (three filter patches) were constructed. In addition to the long and short elements on the previous set, a patch was added which was to have had a fatter line width. Thus, the added distinctions of fat or narrow to describe the element shapes. In Figures 4.10 - 4.12 are shown respectively, the short fat dipoles, long narrow dipoles and short narrow dipoles on substrate #7. The technique of using a slower writing speed to create the fat elements did not work too well. For this reason, the width was

increased on later elements by using a higher beam current. To save time on later substrates, the exposure technique was changed quite a bit. As a result, the data on substrate #7 cannot be easily compared to later substrates. Nonetheless, good transmittance measurements were obtained on this substrate and are presented in Figure 4.13. It is interesting to point out that even though little difference can be seen in the widths of the short elements, there are obvious differences in bandwidths. As expected, the fatter dipoles show a more broadband filter characteristic. On Figure 4.13, also note that second resonance effects are visible as mentioned previously.

On substrates #8 through #12, the exposure and development parameters were identical to within practical limits. Data on the dipole elements is shown in Figures 4.14 through 4.25. From the SEM photographs, it can be seen that the difference in widths between the narrow and fat elements is significant (almost a factor of two). In addition, note that the fat elements are slightly longer than the corresponding short elements due to the larger E-beam radius. No attempt was made to keep the "short" dipoles the same length. From Figure 4.17 it can again be seen that the dipole elements behave as expected. The bandwidth of the fat element is again greater than for the narrow elements as in Figure 4.13 for substrate #7. However, in Figure 4.17, the fat elements in addition to having a greater bandwidth also have a slightly higher resonant frequency. This is consistent with data on substrates #9 through #12 but is opposite to that on substrate #7 with regard to the center frequency for the short element resonances.

More interesting comparisons occur between substrates #10 and #11. The major difference between these substrates is the thickness of the aluminum layer used. On substrate #10, the aluminum was chosen to be 0.140 microns thick which is approximately 6 skin depths (see Appendix E). On substrate #11, only 0.036 microns of aluminum were used. This latter thickness is approximately 1.5 skin depths. The interesting fact is that the performance of the two sets of filters is almost identical except the thinner elements (substrate #11) all resonate at a lower frequency than do the thicker elements (substrate #10). Observations of Figures 4.17 and 4.21 show that the null depths are quite comparable, however, the system dynamic range is probably insufficient to see much difference. The use of a polarizer would probably have yielded better data for this comparison. Two dimensional elements intercepting both polarizations would also have been better.

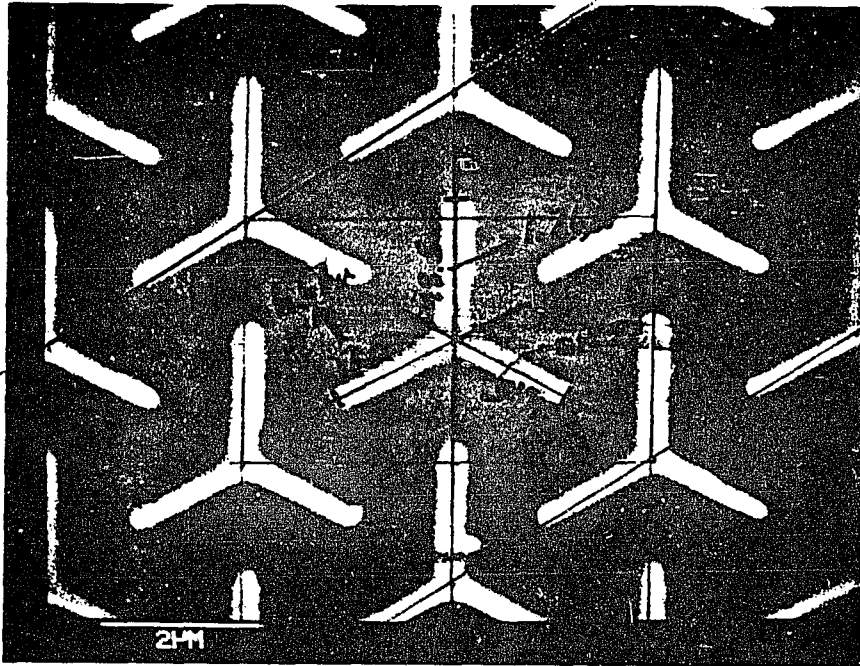
Similar comparisons can be drawn between substrates #10 and #12. Here, the only difference is the type of metal used. It was hoped that the chrome on substrate #12 would be much lossier than the aluminum on substrate #10. Expected results for lossy materials would be lessened resonant characteristics. Thus it was hoped that the chrome dipoles would not show as great an insertion loss at resonance as the aluminum dipoles. However, this conclusion can not be reached by comparison of the data in Figures 4.17 and 4.25. Again, the use of a polarizer or two dimensional elements would have yielded better data for comparison.

A major accomplishment of the second NRRFSS visit was the construction of the slot arrays on substrates #8 and #9. The identical exposure-development process was used on these substrates as was used on substrates #10, #11 and #12 in construction of the dipole arrays. The multi-level resist process developed at the NRRFSS and explained in Appendix A was used to build the slots as opposed to the liftoff process for the dipoles. By comparing the SEM photographs in Figures 4.26 through 4.32 with those in Figures 4.14 through 4.24, it can be seen that some line growth has resulted. Thus, the slot elements are larger than their dipole counterparts. It is believed that reactive ion etching (RIE, see Appendix A) could have produced better elements but this technique was not available.

The slot arrays were again measured in transmittance using the high f# measurement system. The results for substrate #8 (slots in chrome) are presented in Figure 4.29. The results for substrate #9 (slots in aluminum) are presented in Figure 4.33. In these figures it can again be seen that the fat elements have a broader bandpass than the narrow elements, as expected. In addition, the fat elements resonate at a slightly higher frequency as was observed in the data for substrates #10, #11 and #12. The two different metals were again used to hopefully study metal loss effects; however, the two sets of data are again almost identical. The only major difference appears to be a greater transmittance for the long slots in aluminum than for the long slots in chrome. Since the aluminum covered substrate was broken near the long

slot patch prior to the measurement, this increase is probably due to leakage around the patch and not through it.





ARRAY DATA

X OFFSET = 0.00  
 Z OFFSET = 0.00  
 DX = 2.680  
 DZ = 3.120  
 DDZ = 1.560

ELEMENT DATA

LEG #	ANGLE	LENGTH	WIDTH	THICKNESS
1	90.000	1.800	0.340	0.100
2	206.570	1.660	0.250	0.100
3	333.430	1.600	0.250	0.100

Figure 4.1. SEM photograph of short chrome-gold tripoles on substrate #1. EBMF input array data and measured element data.

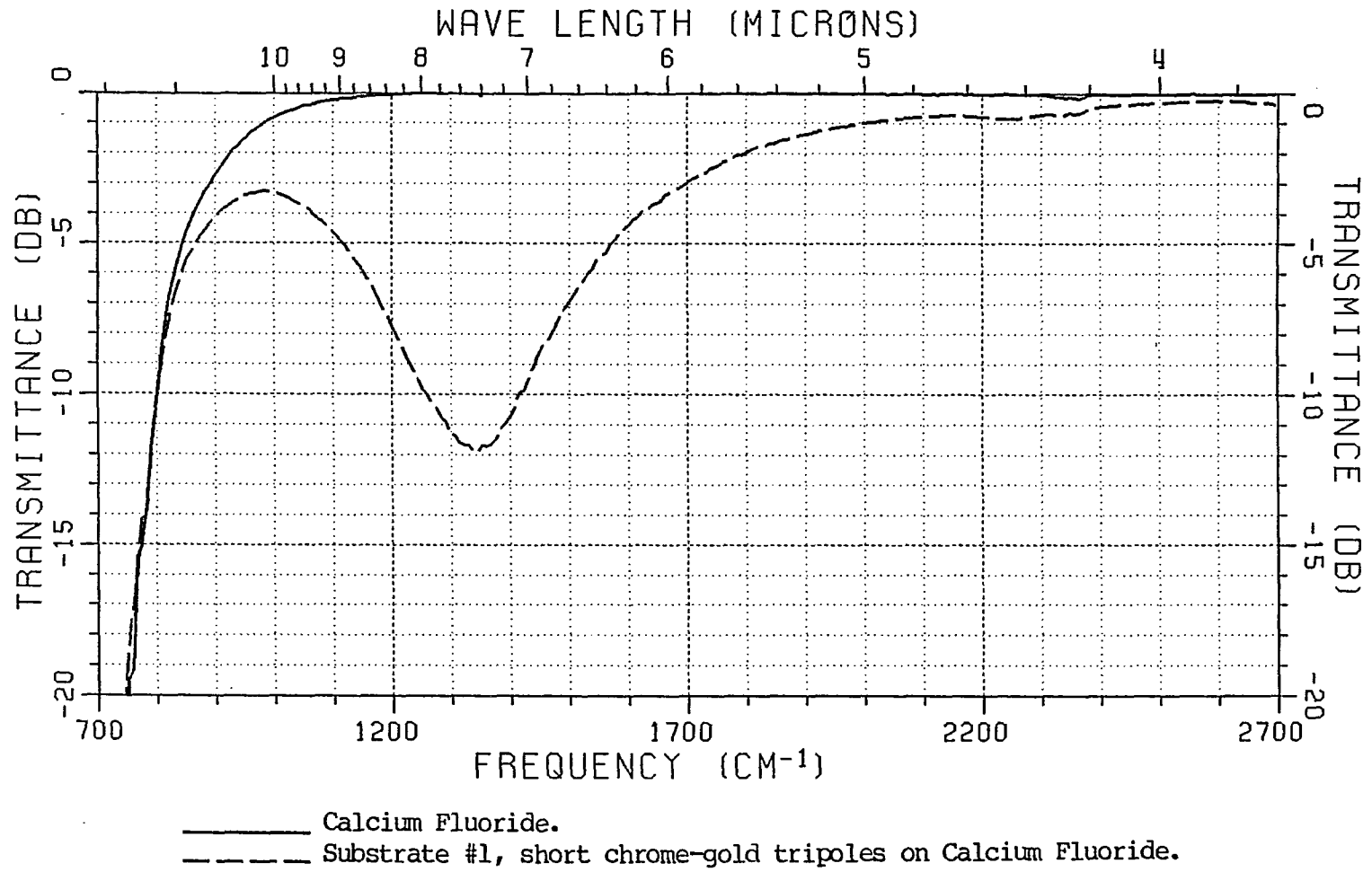
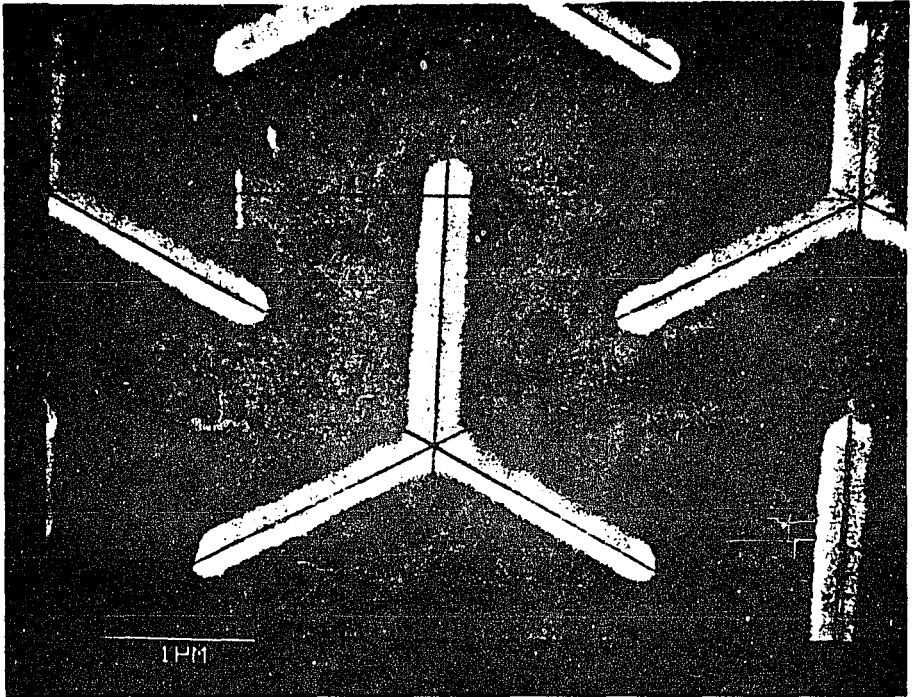


Figure 4.2. Measured transmittance data for substrate #1.



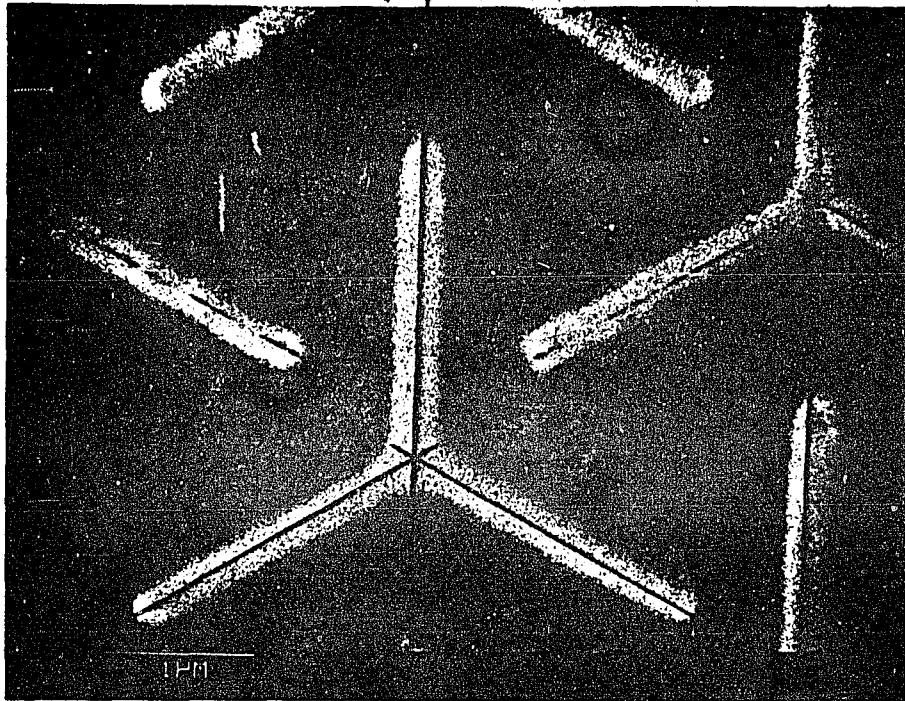
ARRAY DATA

X OFFSET = 0.00  
 Z OFFSET = 0.00  
 DX = 2.640  
 DZ = 3.300  
 DDZ = 1.650

ELEMENT DATA

LEG #	ANGLE	LENGTH	WIDTH	THICKNESS
1	90.000	1.860	0.320	0.140
2	206.570	1.760	0.290	0.140
3	333.430	1.710	0.270	0.140

Figure 4.3. SEM photograph of short aluminum tripoles on substrate #5. EBMF input array data and measured element data.



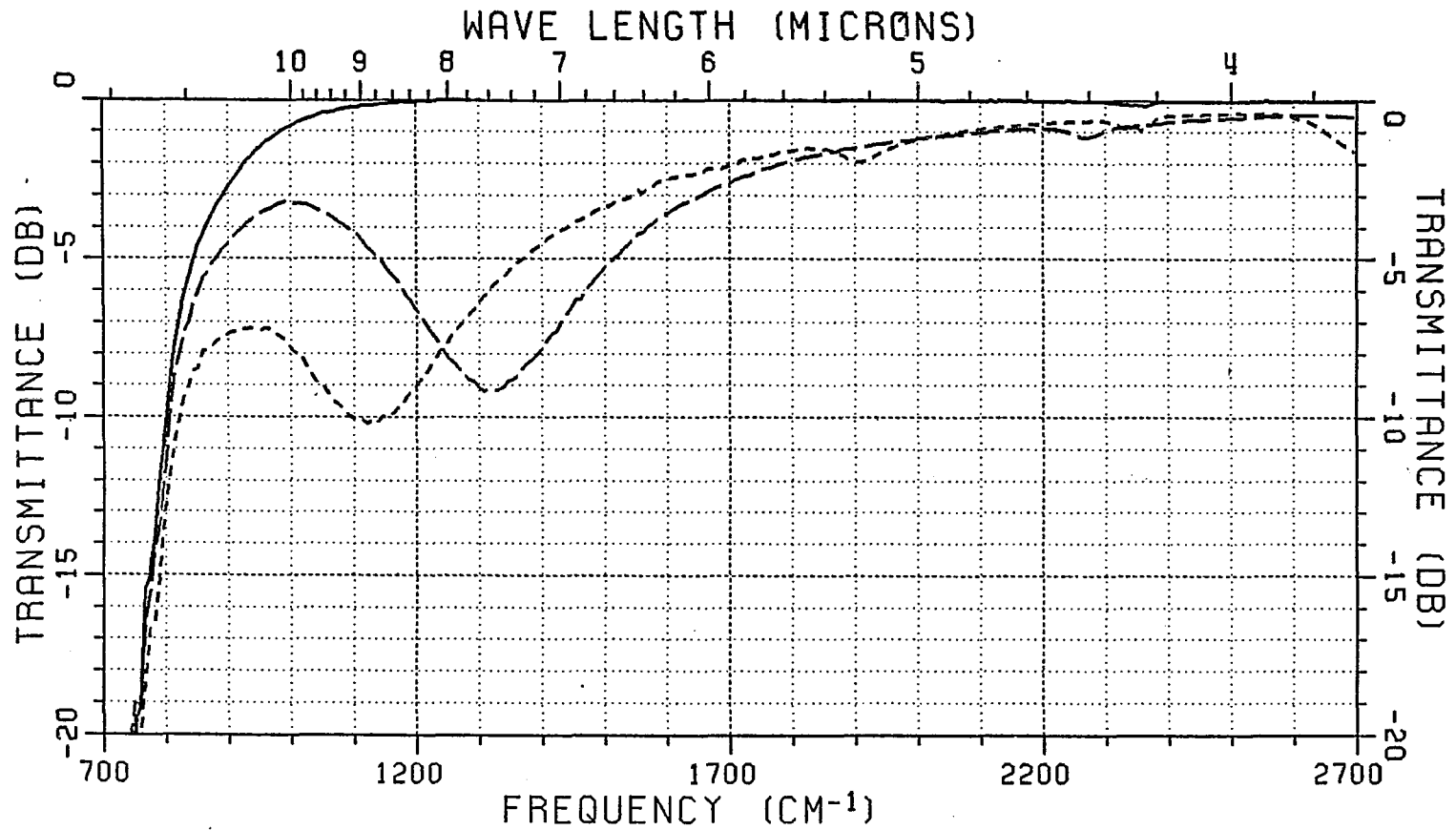
ARRAY DATA

X OFFSET = 0.00  
Z OFFSET = 0.00  
DX = 2.640  
DZ = 3.300  
DDZ= 1.650

ELEMENT DATA

LEG #	ANGLE	LENGTH	WIDTH	THICKNESS
1	90.000	2.100	0.290	0.140
2	206.570	2.130	0.240	0.140
3	333.430	2.100	0.240	0.140

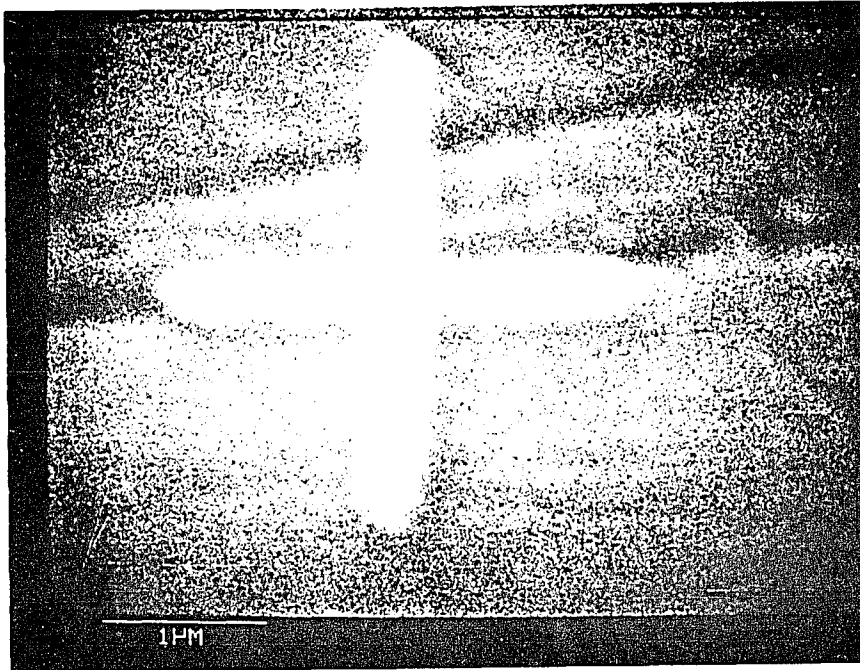
Figure 4.4. SEM photograph of long aluminum tripoles on substrate #5. EBMF input array data and measured element data.



- Calcium Fluoride.
- - - Substrate #5, short aluminum tripoles on Calcium Fluoride.
- · - · Substrate #5, long aluminum tripoles on Calcium Fluoride.

Figure 4.5. Measured transmittance data for the tripoles on substrate

#5.



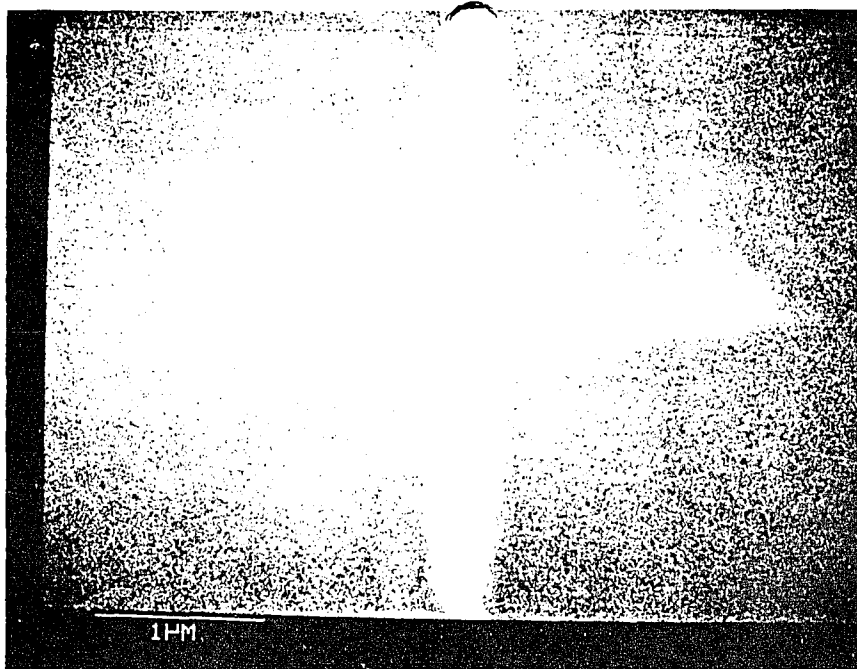
ARRAY DATA

X OFFSET = 0.00  
 Z OFFSET = 0.00  
 DX = 4.500  
 DZ = 4.500  
 DDZ = 0.000

ELEMENT DATA

LEG #	ANGLE	LENGTH	WIDTH	THICKNESS
1	0.000	1.370	0.350	0.140
2	90.000	1.430	0.350	0.140
3	180.000	1.370	0.350	0.140
4	270.000	1.430	0.350	0.140

Figure 4.6. SEM photograph of short aluminum crossed dipoles on substrate #5. EBMF input array data and measured element data.



ARRAY DATA

X OFFSET = 0.00  
 Z OFFSET = 0.00  
 DX = 4.500  
 DZ = 4.500  
 DDZ = 0.000

ELEMENT DATA

LEG #	ANGLE	LENGTH	WIDTH	THICKNESS
1	0.000	1.690	0.310	0.140
2	90.000	1.760	0.310	0.140
3	180.000	1.690	0.310	0.140
4	270.000	1.760	0.310	0.140

Figure 4.7. SEM photograph of long aluminum crossed dipoles on substrate #5. EBMF input array data and measured element data.

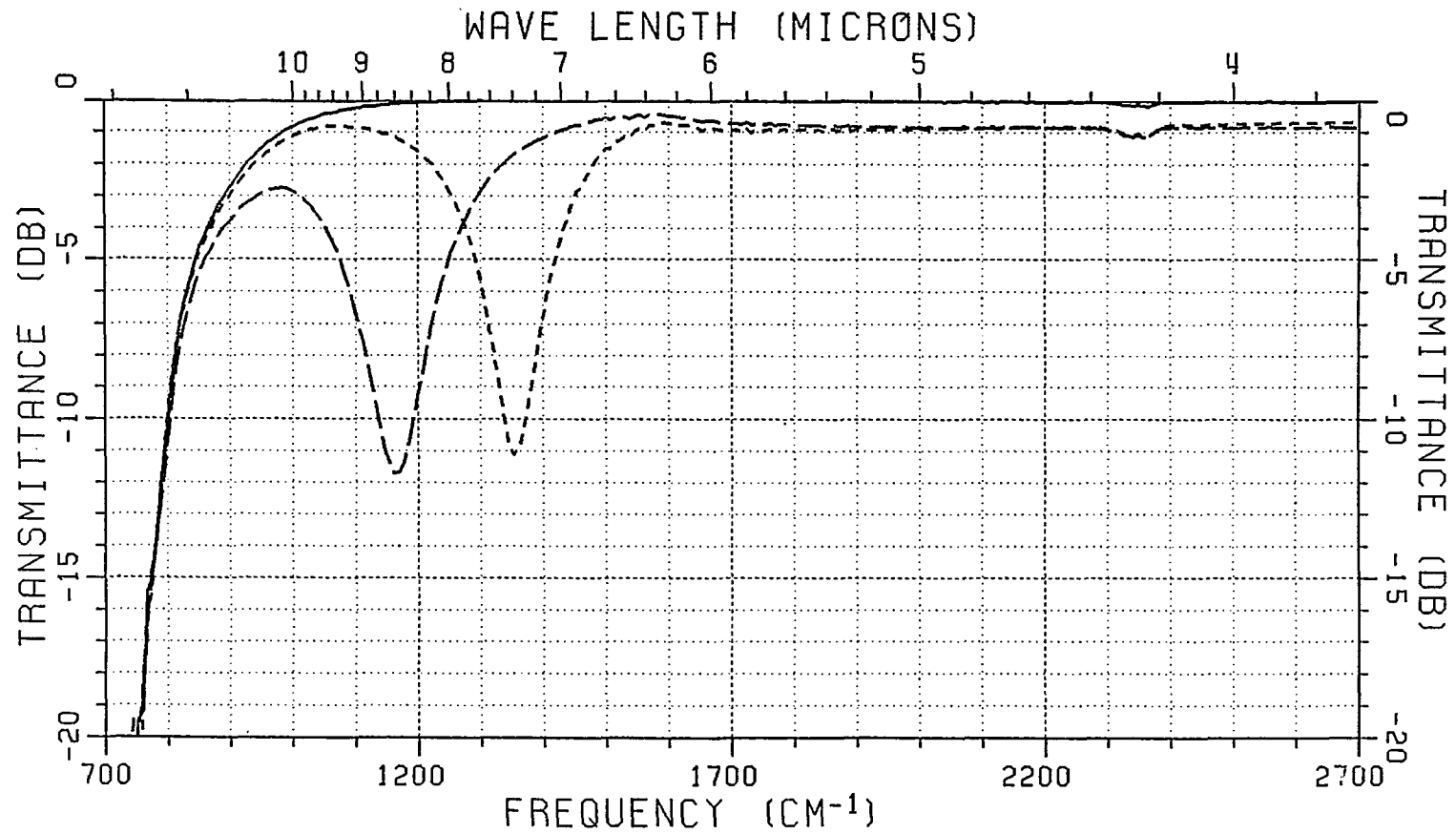
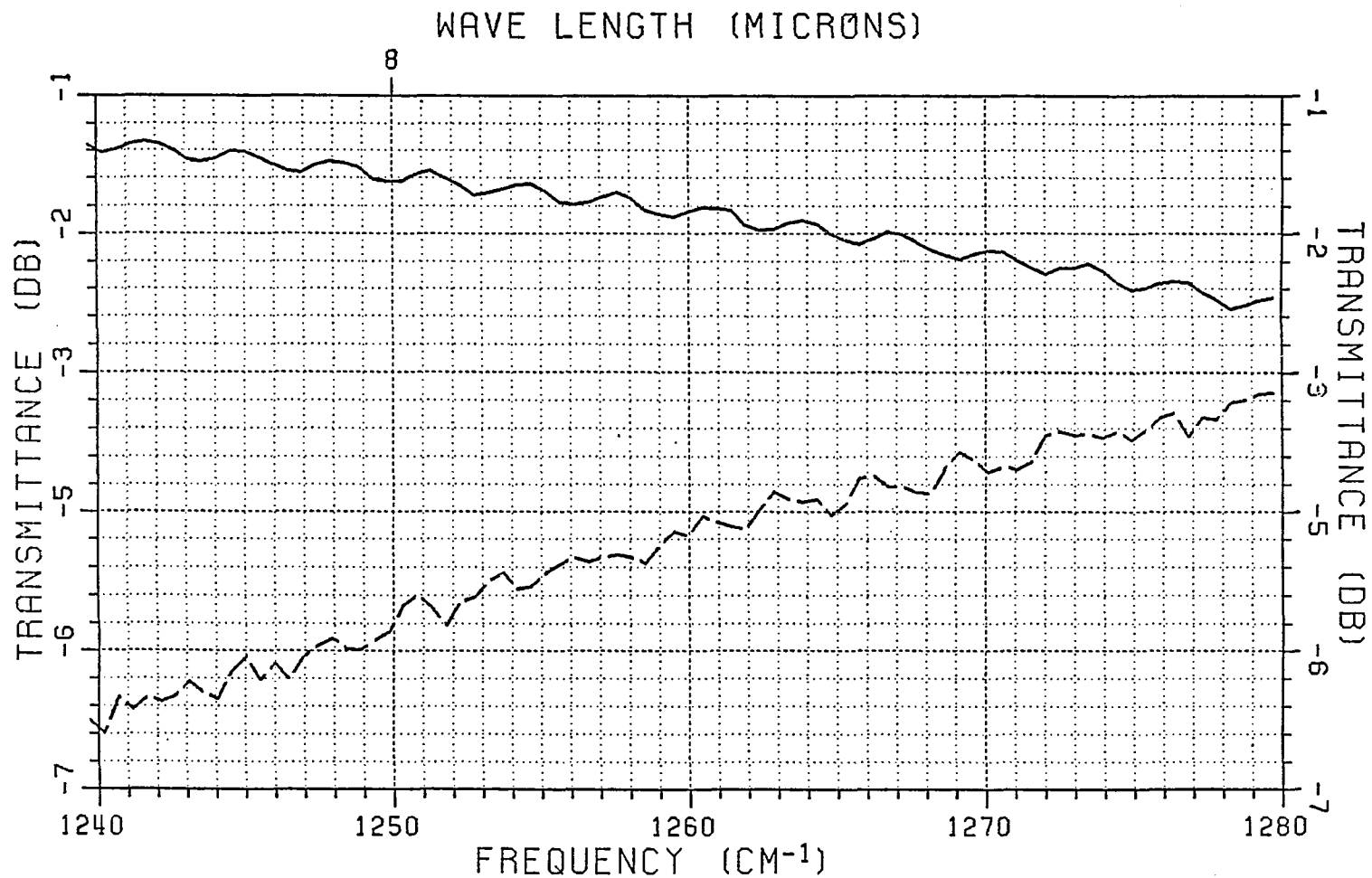


Figure 4.8. Measured transmittance data for the crossed-dipoles on substrate #5.

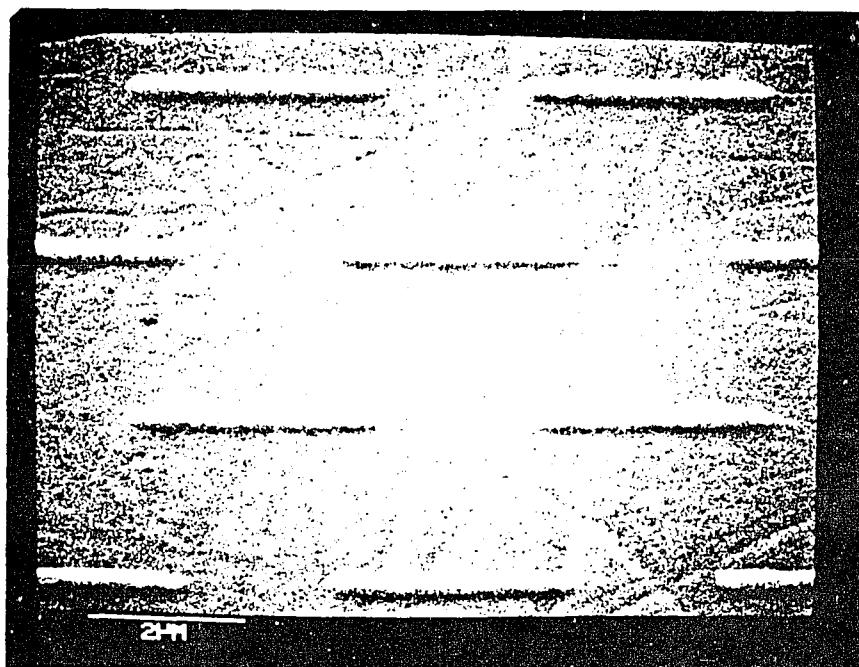




— Substrate #5, short aluminum crossed-dipoles on Calcium Fluoride.  
 - - - Substrate #5, long aluminum crossed-dipoles on Calcium Fluoride.

Figure 4.9. Measured transmittance data for the crossed-dipoles for

substrate #5, showing substrate etalon behavior.



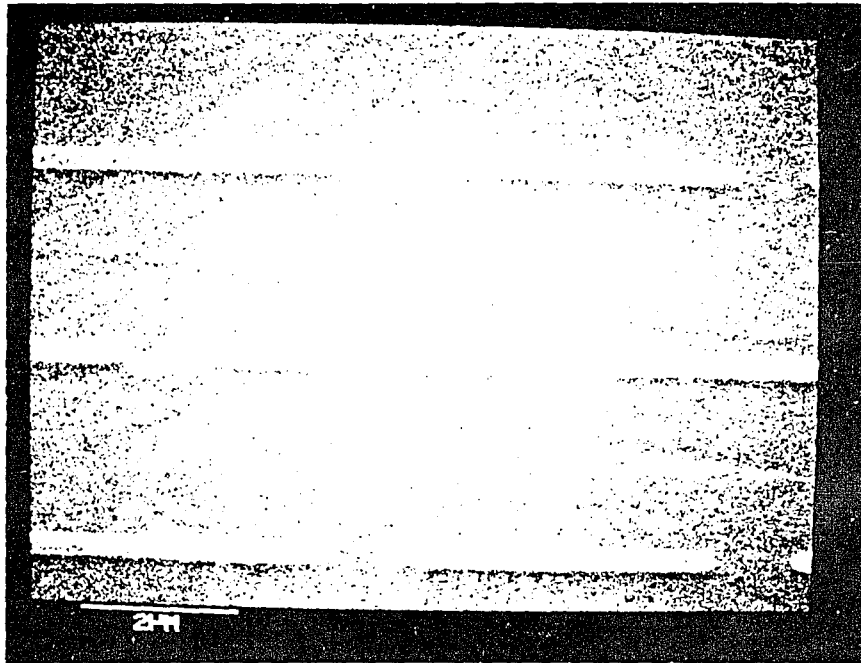
ARRAY DATA

X OFFSET = 0.00  
Z OFFSET = 0.00  
DX = 2.500  
DZ = 5.000  
DDZ = 2.500

ELEMENT DATA

LEG #	ANGLE	LENGTH	WIDTH	THICKNESS
1	90.000	1.560	0.270	0.135
2	270.000	1.560	0.270	0.135

Figure 4.10. SEM photograph of short fat aluminum dipoles on substrate #7. EBMF input array data and measured element data.



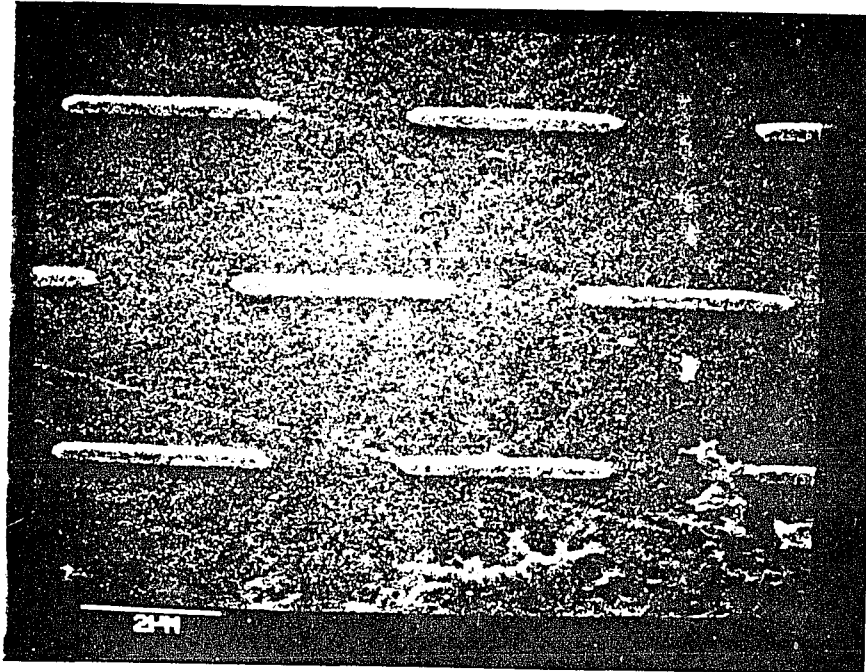
ARRAY DATA

X OFFSET = 0.00  
 Z OFFSET = 0.00  
 DX = 2.500  
 DZ = 5.000  
 DDZ = 2.500

ELEMENT DATA

LEG #	ANGLE	LENGTH	WIDTH	THICKNESS
1	90.000	2.000	0.260	0.135
2	270.000	2.000	0.260	0.135

Figure 4.11. SEM photograph of long narrow aluminum dipoles on substrate #7. EBMF input array data and measured element data.



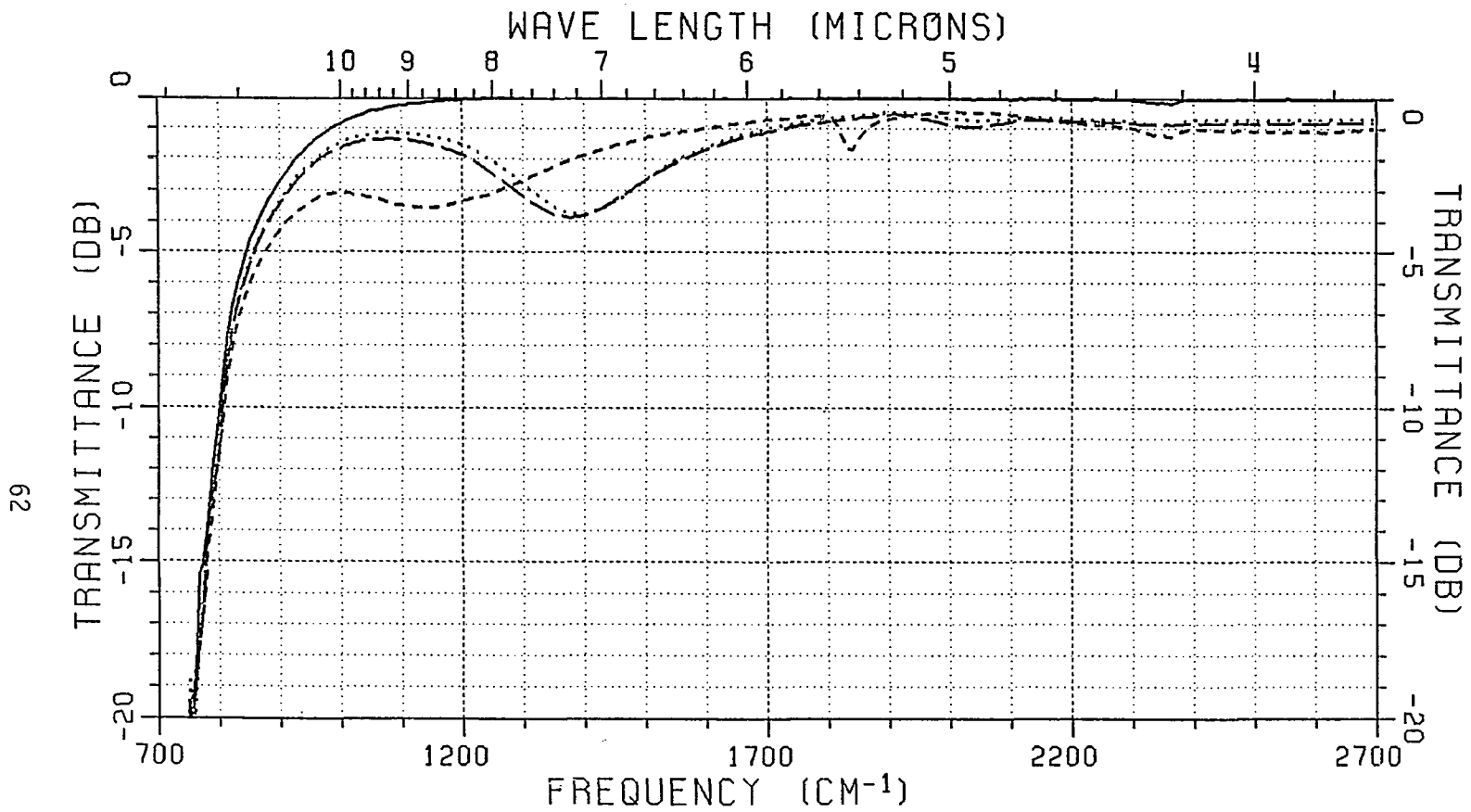
ARRAY DATA

X OFFSET = 0.00  
 Z OFFSET = 0.00  
 DX = 2.500  
 DZ = 5.000  
 DDZ = 2.500

ELEMENT DATA

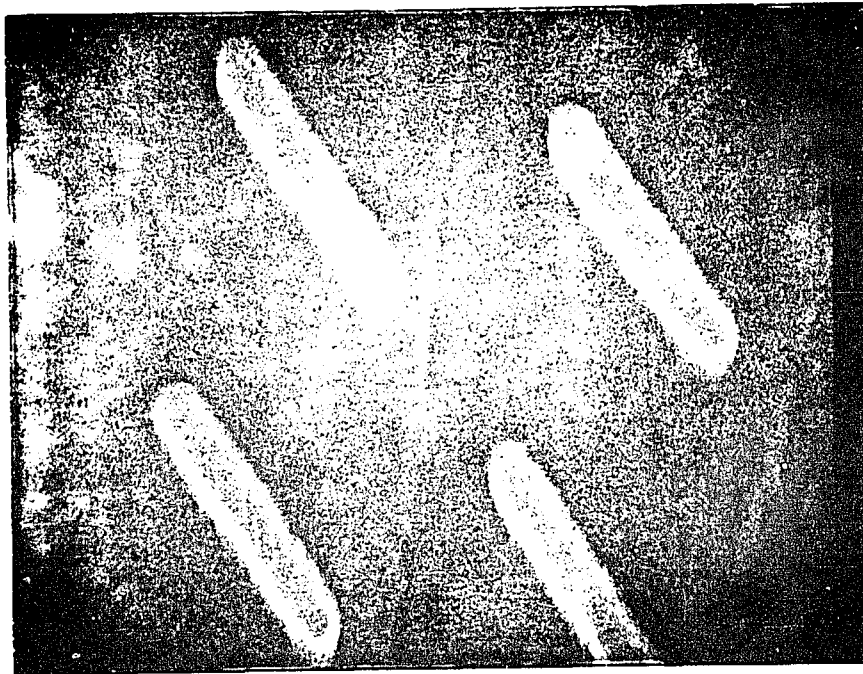
LEG #	ANGLE	LENGTH	WIDTH	THICKNESS
1	90.000	1.520	0.260	0.135
2	270.000	1.520	0.260	0.135

Figure 4.12. SEM photograph of short narrow aluminum dipoles on substrate #7. EBMF input array data and measured element data.



- Calcium Fluoride.
- Substrate #7, short fat aluminum dipoles on Calcium Fluoride.
- - - - - Substrate #7, long narrow aluminum dipoles on Calcium Fluoride.
- ..... Substrate #7, short narrow aluminum dipoles on Calcium Fluoride.

Figure 4.13. Measured transmittance data for substrate #7.



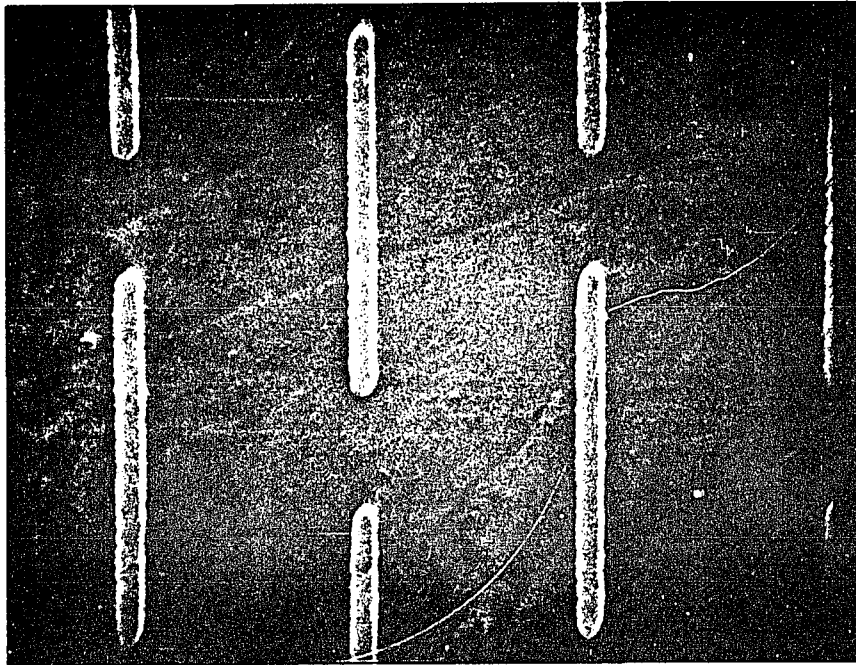
ARRAY DATA

X OFFSET = 0.00  
Z OFFSET = 0.00  
DX = 2.500  
DZ = 5.000  
DDZ = 2.500

ELEMENT DATA

LEG #	ANGLE	LENGTH	WIDTH	THICKNESS
1	90.000	1.555	0.540	0.140
2	270.000	1.555	0.540	0.140

Figure 4.14. SEM photograph of short fat aluminum dipoles on substrate #10. EBMF input array data and measured element data.



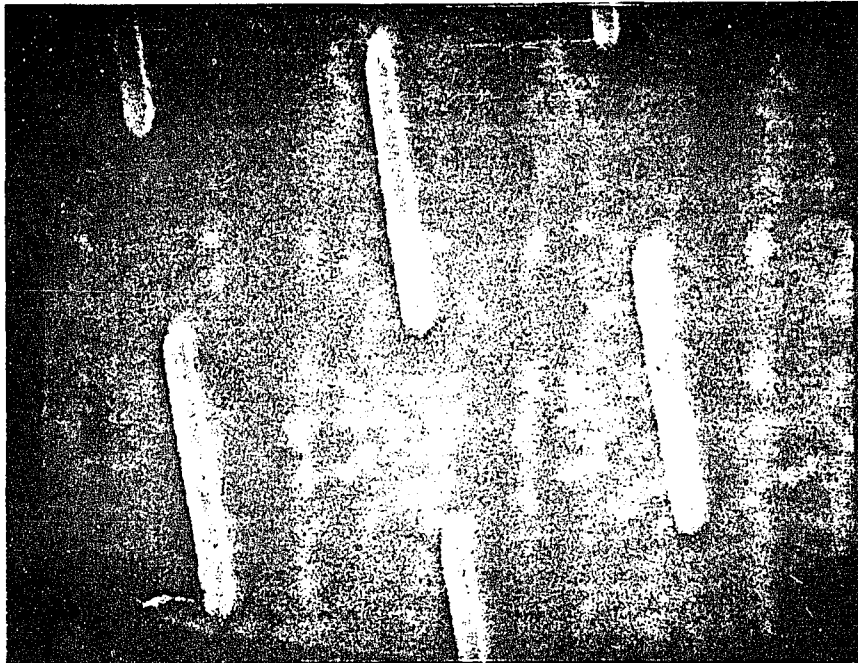
ARRAY DATA

X OFFSET = 0.00  
Z OFFSET = 0.00  
DX = 2.500  
DZ = 5.000  
DDZ = 2.500

ELEMENT DATA

LEG #	ANGLE	LENGTH	WIDTH	THICKNESS
1	90.000	1.905	0.290	0.140
2	270.000	1.905	0.290	0.140

Figure 4.15. SEM photograph of long narrow aluminum dipoles on substrate #10. EBMF input array data and measured element data.



ARRAY DATA

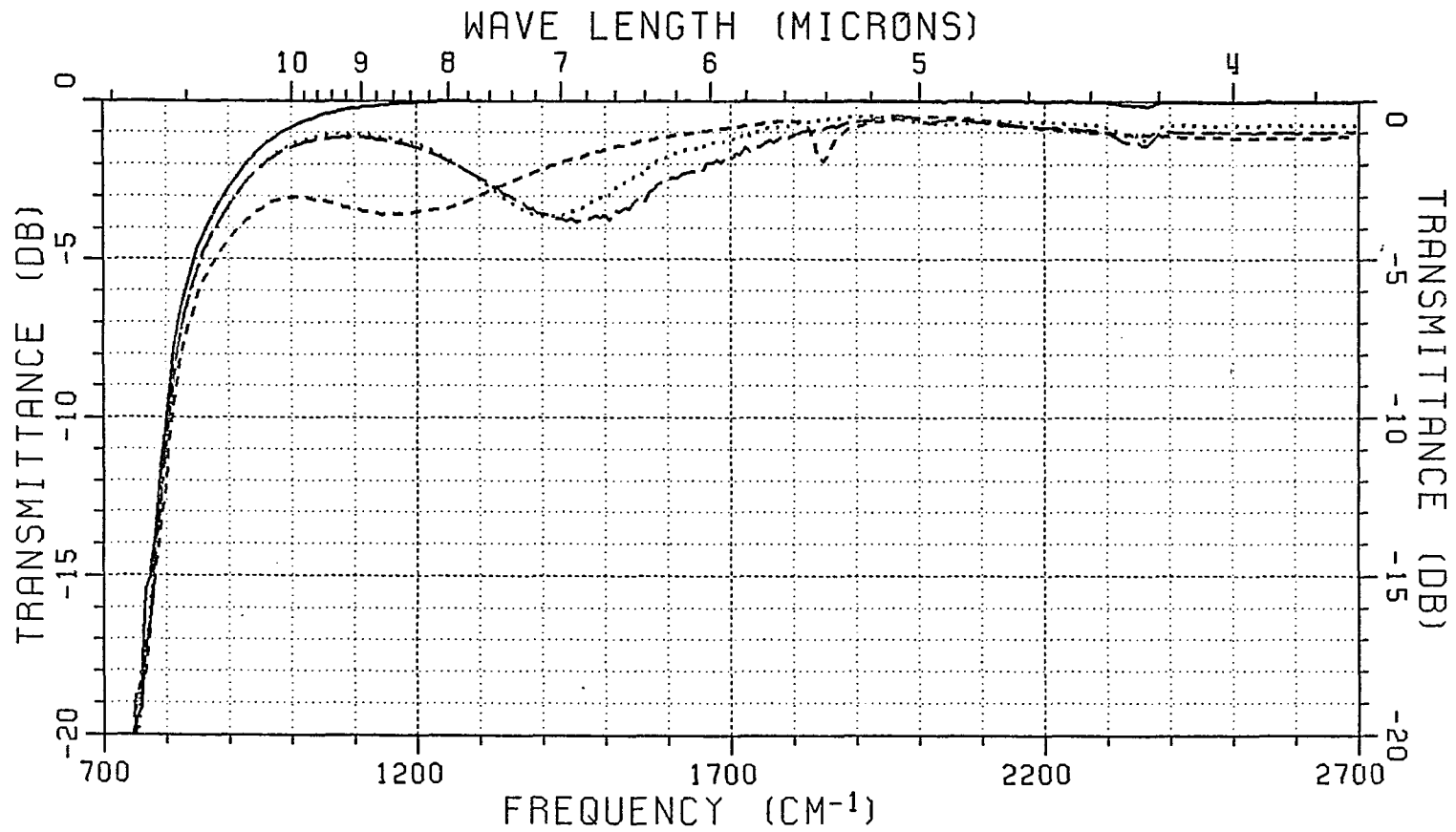
X OFFSET = 0.00  
Z OFFSET = 0.00  
DX = 2.500  
DZ = 5.000  
DDZ = 2.500

ELEMENT DATA

LEG #	ANGLE	LENGTH	WIDTH	THICKNESS
1	90.000	1.475	0.310	0.140
2	270.000	1.475	0.310	0.140

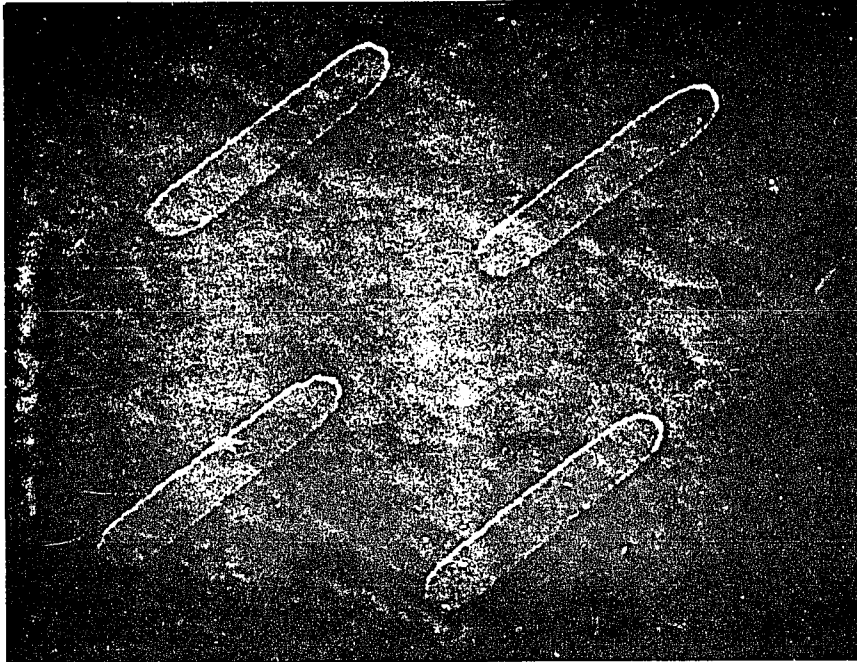
Figure 4.16. SEM photograph of short narrow aluminum dipoles on substrate #10. EBMF input array data and measured element data.





- Calcium Fluoride.
- Substrate #10, short fat aluminum dipoles on Calcium Fluoride.
- ..... Substrate #10, long narrow aluminum dipoles on Calcium Fluoride.
- ..... Substrate #10, short narrow aluminum dipoles on Calcium Fluoride.

Figure 4.17. Measured transmittance data for substrate #10.



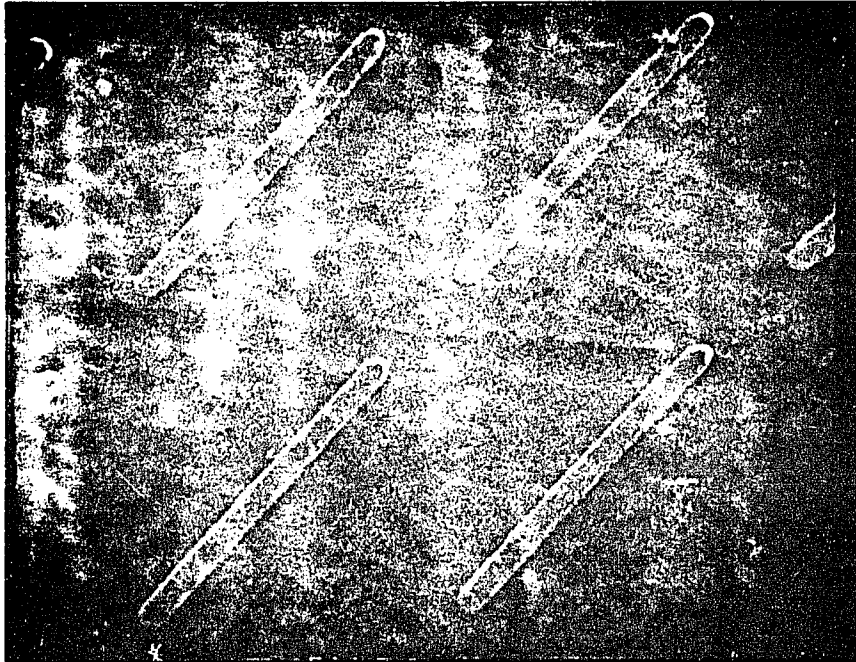
ARRAY DATA

X OFFSET = 0.00  
Z OFFSET = 0.00  
DX = 2.500  
DZ = 5.000  
DDZ = 2.500

ELEMENT DATA

LEG #	ANGLE	LENGTH	WIDTH	THICKNESS
1	90.000	1.535	0.540	0.036
2	270.000	1.535	0.540	0.036

Figure 4.18. SEM photograph of short fat aluminum dipoles on substrate #11. EBMF input array data and measured element data.



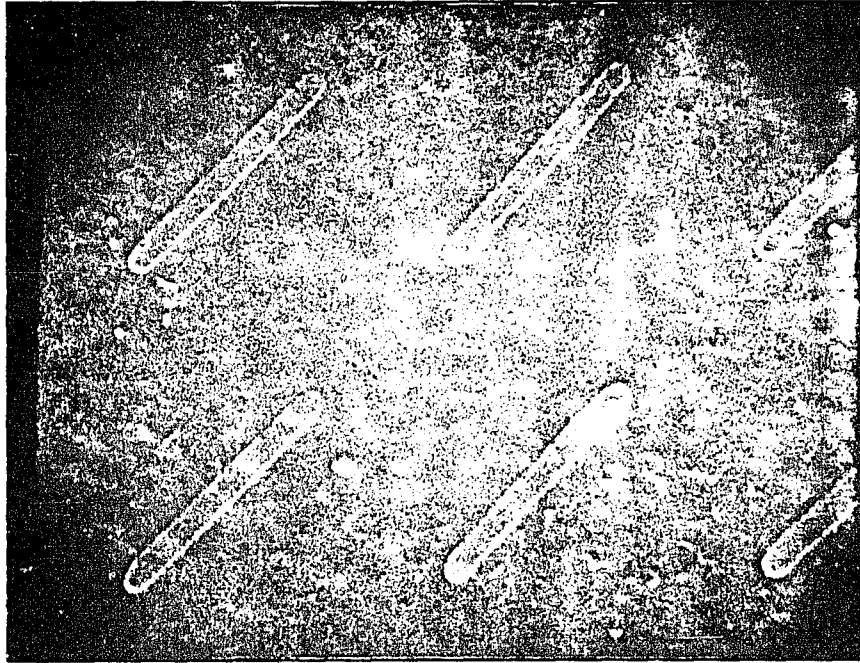
ARRAY DATA

X OFFSET = 0.00  
Z OFFSET = 0.00  
DX = 2.500  
DZ = 5.000  
DDZ = 2.500

ELEMENT DATA

LEG #	ANGLE	LENGTH	WIDTH	THICKNESS
1	90.000	1.925	0.290	0.036
2	270.000	1.925	0.290	0.036

Figure 4.19. SEM photograph of long narrow aluminum dipoles on substrate #11. EBMF input array data and measured element data.



ARRAY DATA

X OFFSET = 0.00  
Z OFFSET = 0.00  
DX = 2.500  
DZ = 5.000  
DDZ = 2.500

ELEMENT DATA

LEG #	ANGLE	LENGTH	WIDTH	THICKNESS
1	90.000	1.495	0.320	0.036
2	270.000	1.495	0.320	0.036

Figure 4.20. SEM photograph of short narrow aluminum dipoles on substrate #11. EBMF input array data and measured element data.

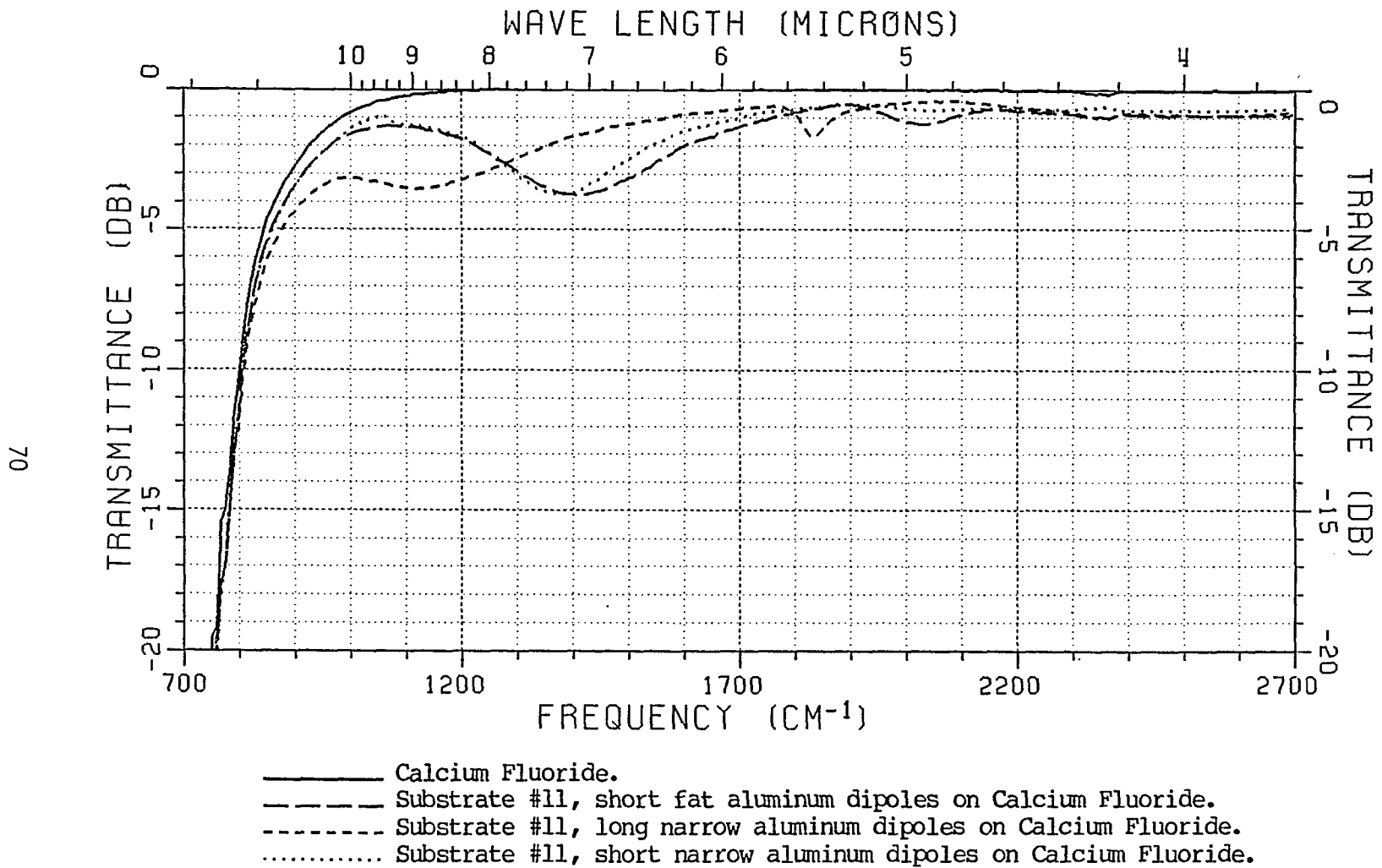
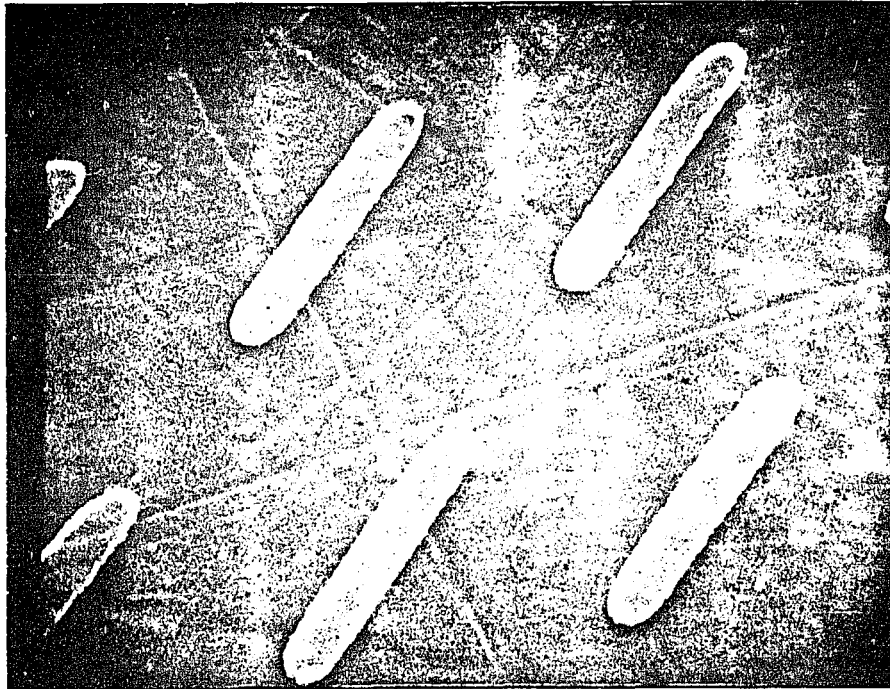


Figure 4.21. Measured transmittance data for substrate #11.



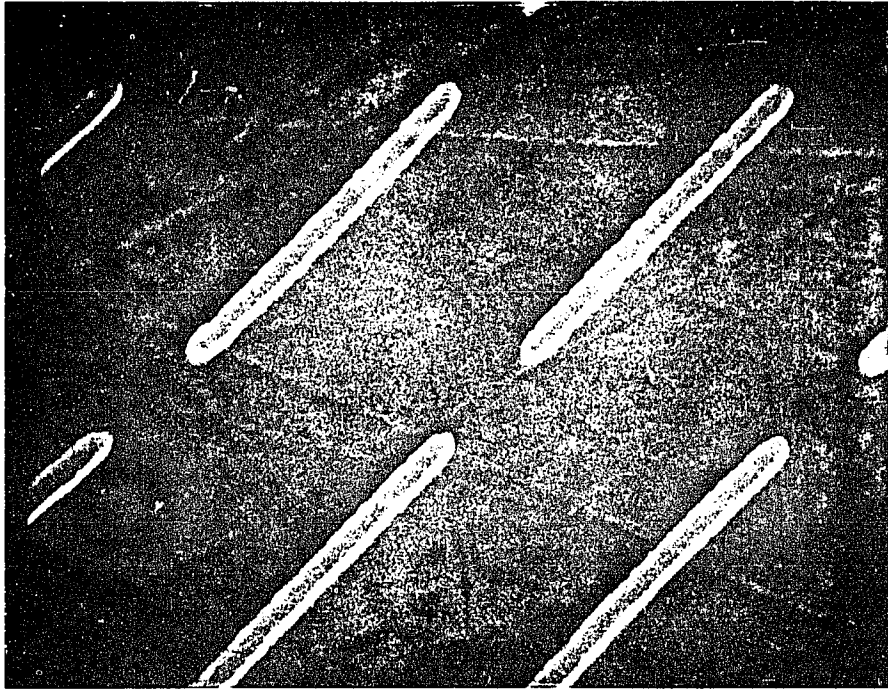
ARRAY DATA

X OFFSET = 0.00  
Z OFFSET = 0.00  
DX = 2.500  
DZ = 5.000  
DDZ = 2.500

ELEMENT DATA

LEG #	ANGLE	LENGTH	WIDTH	THICKNESS
1	90.000	1.530	0.520	0.140
2	270.000	1.530	0.520	0.140

Figure 4.22. SEM photograph of short fat chrome dipoles on substrate #12. EBMF input array data and measured element data.



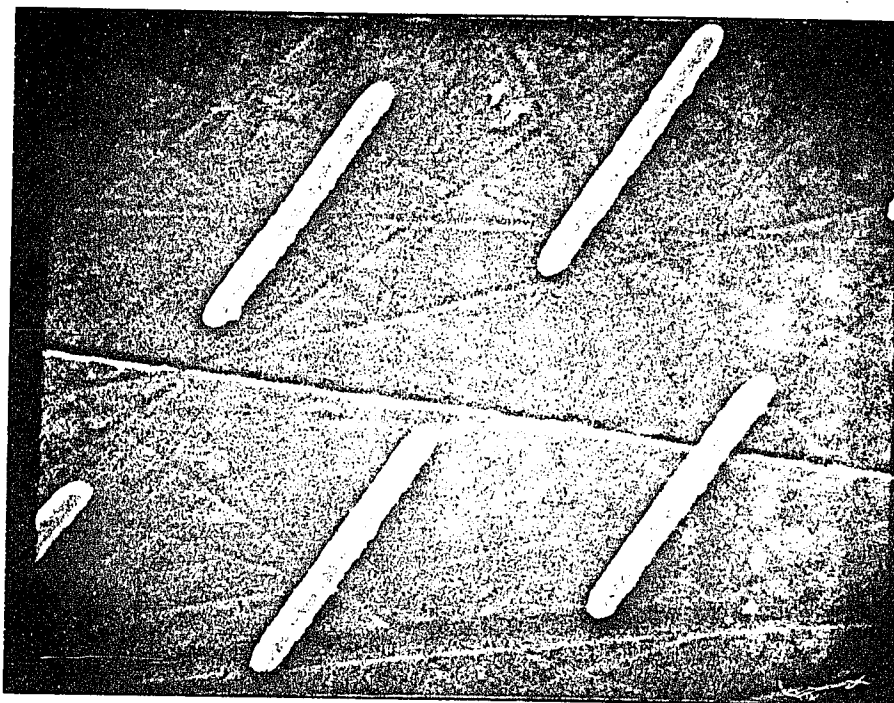
ARRAY DATA

X OFFSET = 0.00  
Z OFFSET = 0.00  
DX = 2.500  
DZ = 5.000  
DDZ = 2.500

ELEMENT DATA

LEG #	ANGLE	LENGTH	WIDTH	THICKNESS
1	90.000	1.945	0.300	0.140
2	270.000	1.945	0.300	0.140

Figure 4.23. SEM photograph of long narrow chrome dipoles on substrate #12. EBMF input array data and measured element data.



ARRAY DATA

X OFFSET = 0.00  
Z OFFSET = 0.00  
DX = 2.500  
DZ = 5.000  
DDZ = 2.500

ELEMENT DATA

LEG #	ANGLE	LENGTH	WIDTH	THICKNESS
1	90.000	1.510	0.310	0.140
2	270.000	1.510	0.310	0.140

Figure 4.24. SEM photograph of short narrow chrome dipoles on substrate #12. EBMF input array data and measured element data.



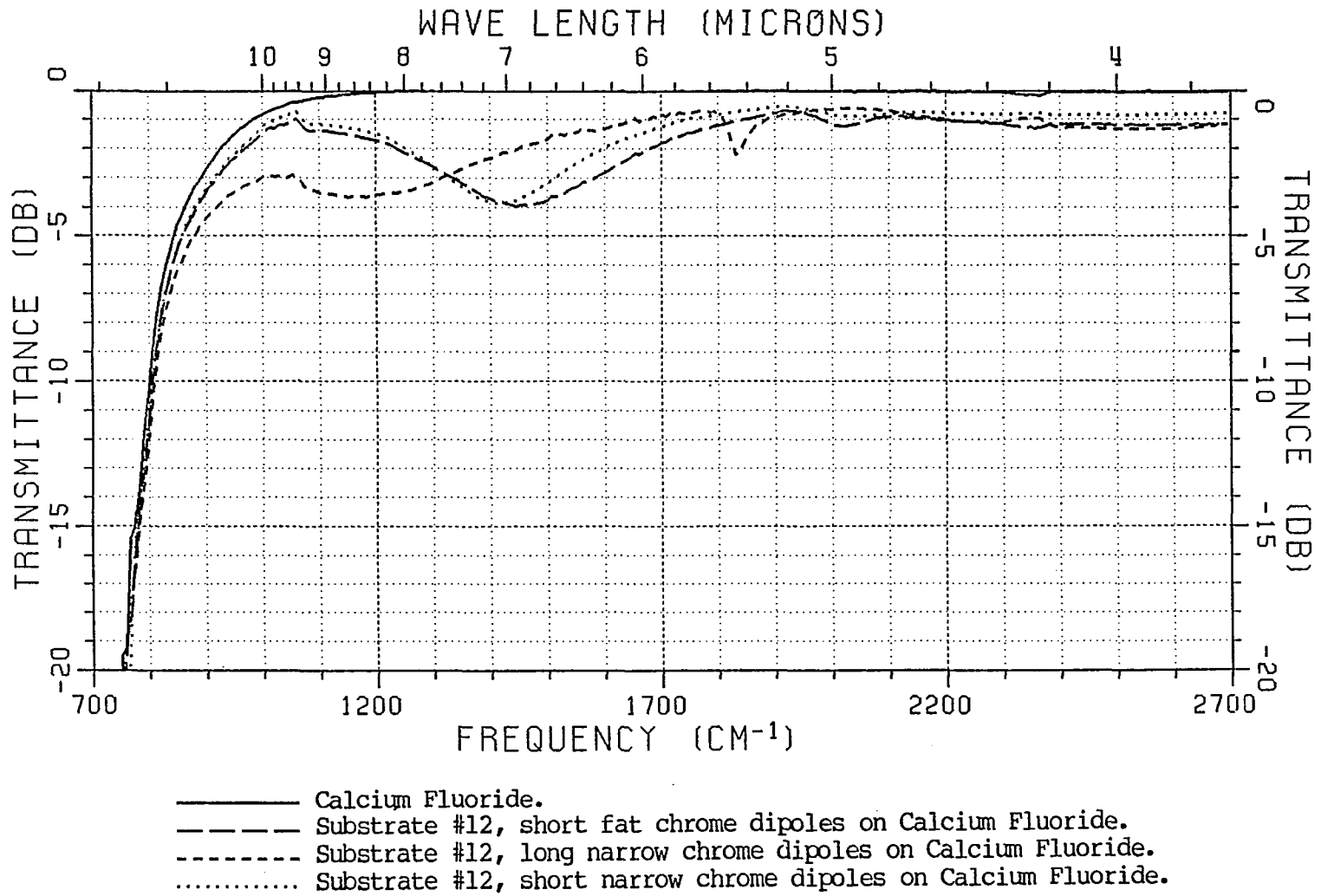


Figure 4.25. Measured transmittance data for substrate #12.

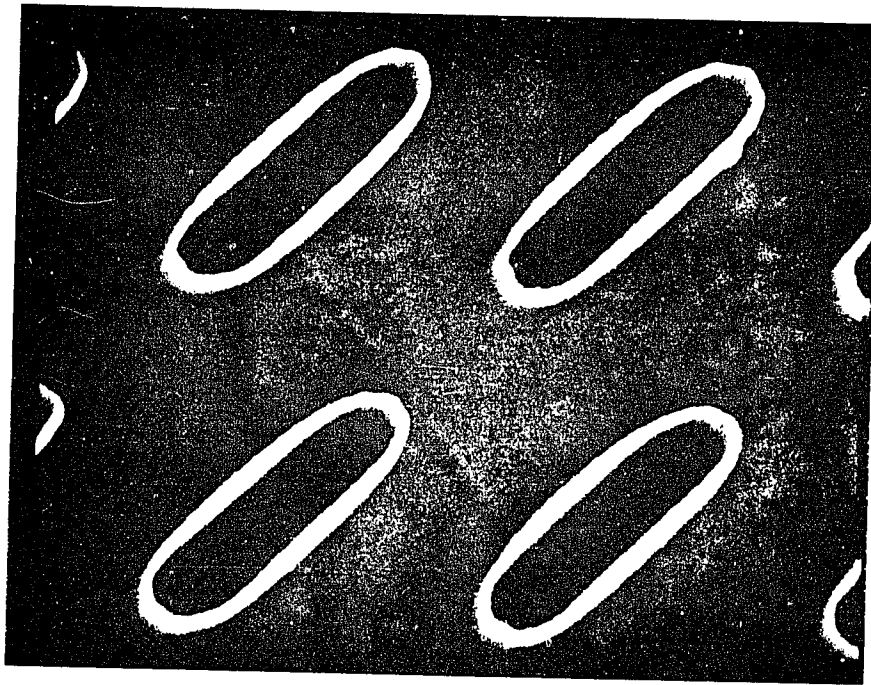


Figure 4.26. SEM photograph of substrate #8.  
Short fat slots in chrome.

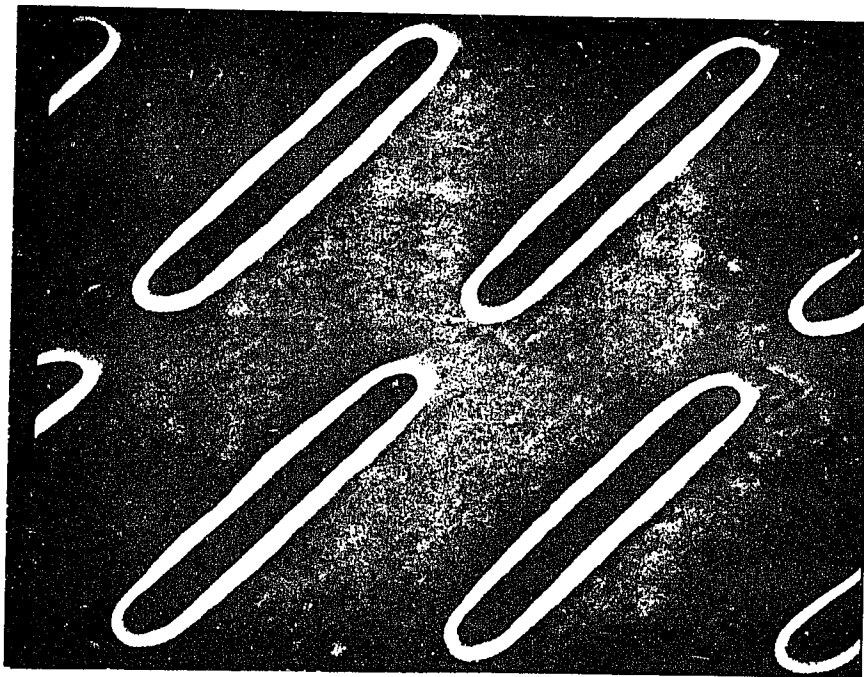


Figure 4.27. SEM photograph of substrate #8.  
Long narrow slots in chrome.

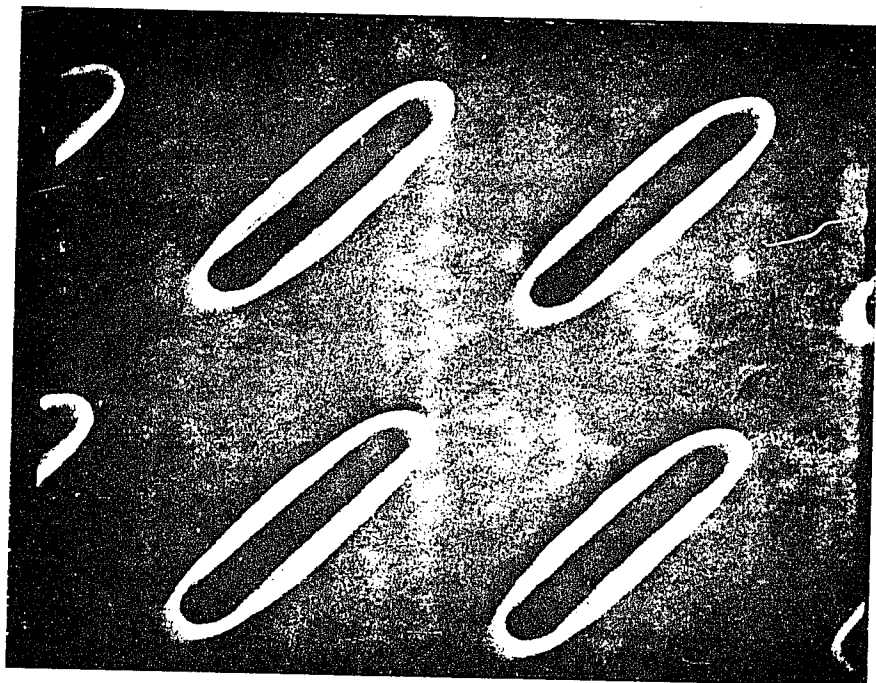


Figure 4.28. SEM photograph of substrate #8.  
Short narrow slots in chrome.

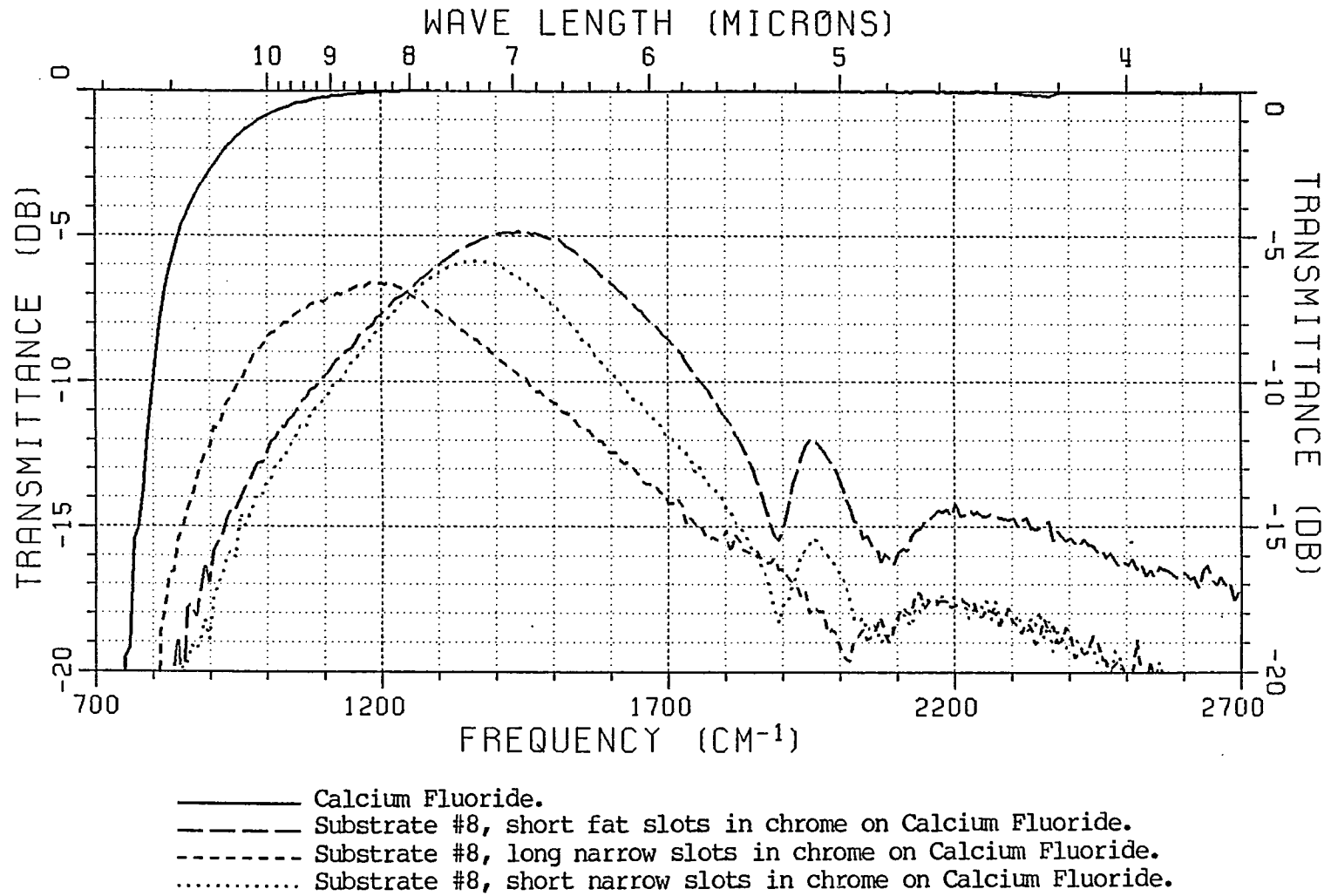


Figure 4.29. Measured transmittance data for substrate #8.

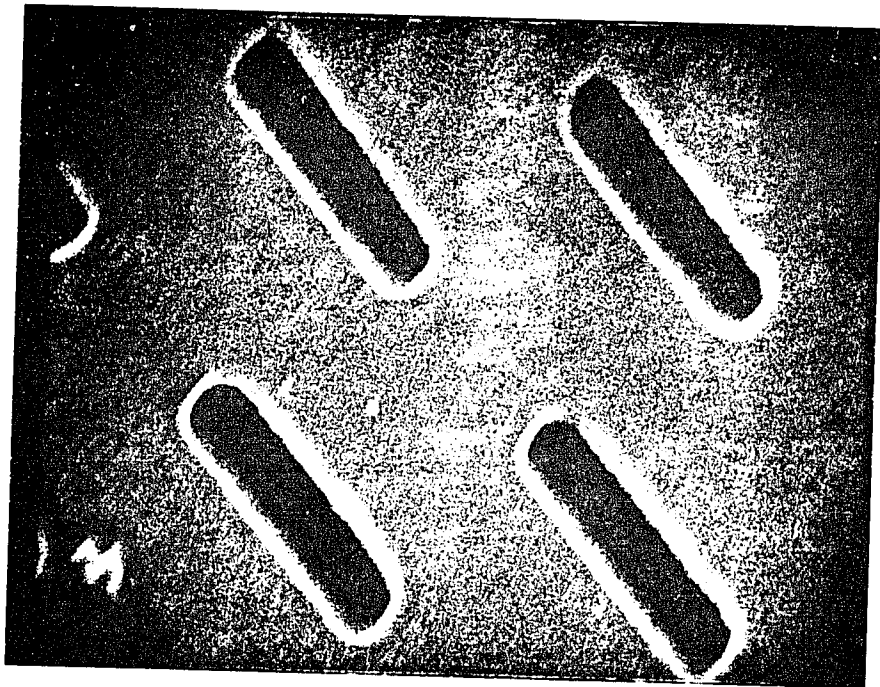


Figure 4.30. SEM photograph of substrate #9.  
Short fat slots in aluminum.

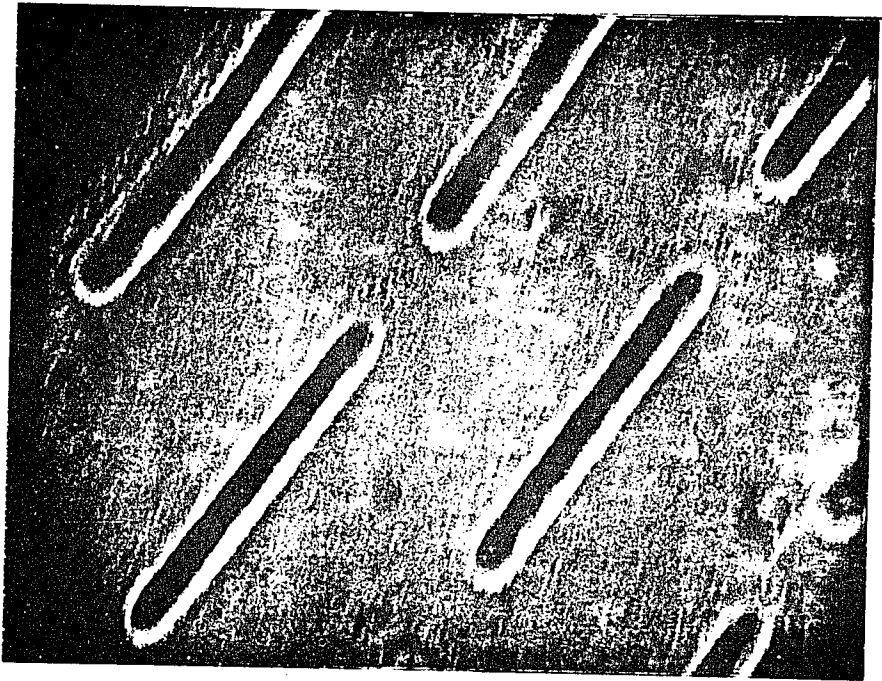


Figure 4.31. SEM photograph of substrate #8.  
Long narrow slots in aluminum.

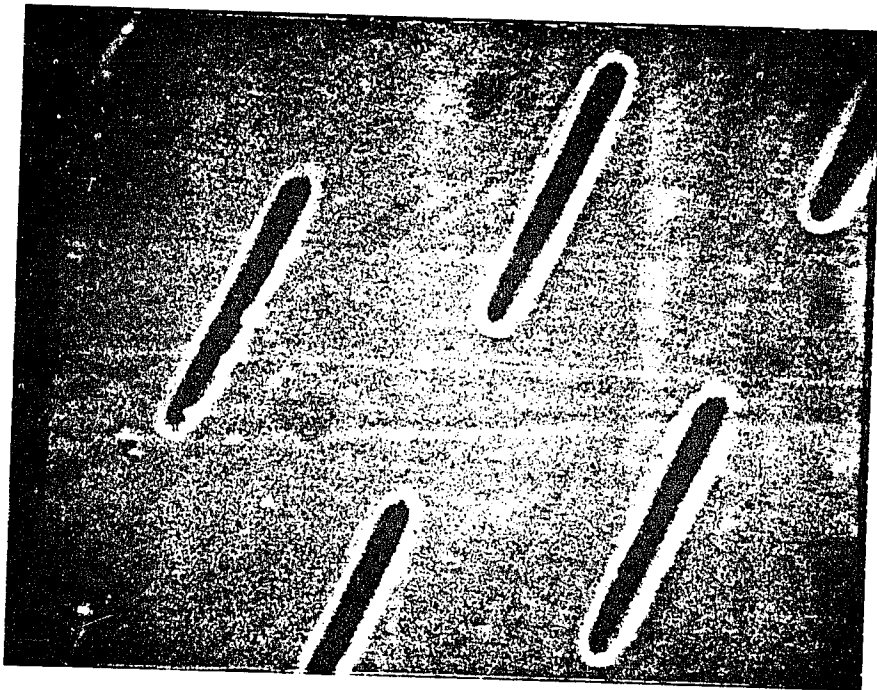


Figure 4.32. SEM photograph of substrate #9. Short narrow slots in aluminum.



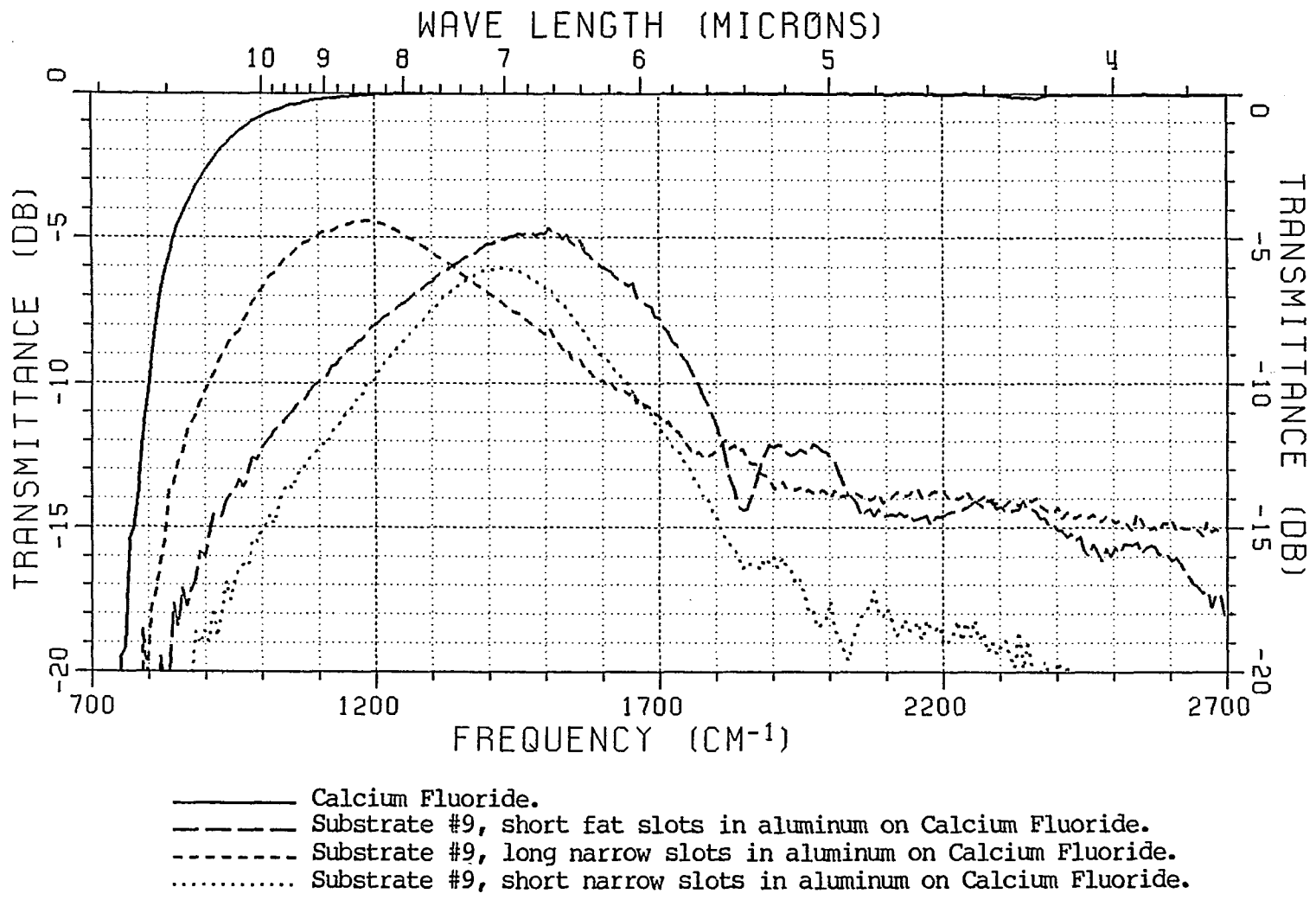


Figure 4.33. Measured transmittance data for substrate #9.

## CHAPTER V

### CALCULATION OF FILTER TRANSMITTANCE

Using the results of Periodic Surface Theory (PST) discussed in Chapter III, many computer codes have been written to analyze the performance of periodic arrays of resonant elements. Most of these codes have been used to validate PST in the microwave region. Thus, the results of this study represent an attempt to validate these theories at frequencies nearly a thousand times higher than previously used. One particular code was obtained [42] which was very convenient and efficient for modelling three legged elements (i.e., tripoles). This code was modified to handle general N-legged elements, where the leg junctions have a common connection point. Examples are dipoles (both straight and bent), tripoles and crossed-dipoles. For elements of this type, having N legs, the minimal complete set of modal currents must have N-1 modes. The modes used in this code are shown in Figure 5.1 for dipoles, tripoles and crossed-dipoles. In general, the M<sup>th</sup> mode flows from leg M to leg M+1 as shown in Figure 5.1.

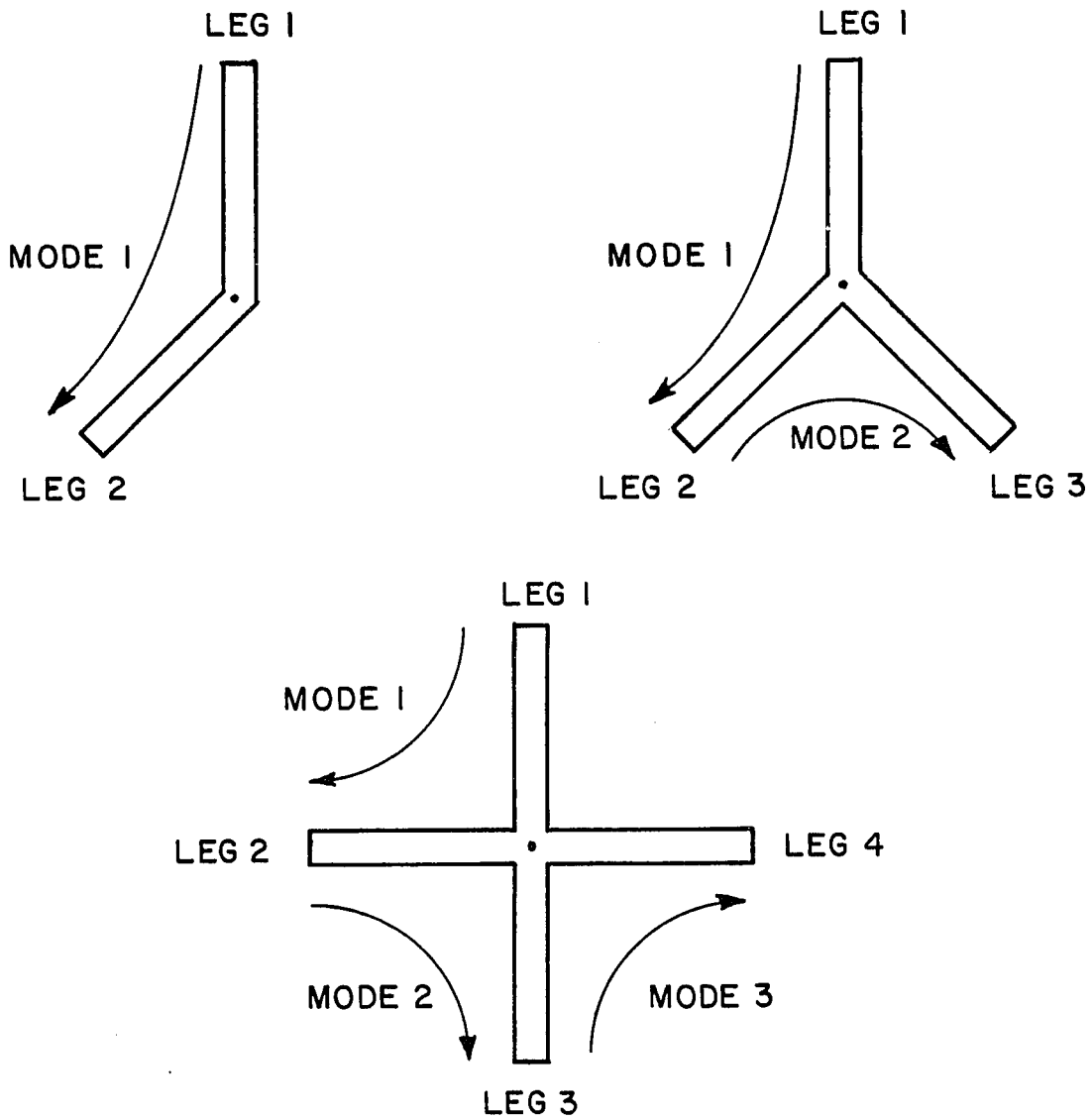


Figure 5.1. Computer code current modes for general dipoles, tripoles and crossed-dipoles.

The current modes used to model the element currents were the piecewise sinusoids discussed in Appendix D. For the transmitting and receiving modes respectively, the sine and cosine mode were used. This combination has been found to yield the best overall agreement with measured results in previous studies [42,43]. To model the effects of charge buildup at the ends of the elements, the concept of effective length was used [44] which can also be seen in Appendix D. Using these modes and effective length, the currents are typically well modelled until the mode length is about  $0.7 \lambda_0$ . Thus, these are low frequency models. It should be pointed out that in the plots to follow the calculations have been extended beyond this point. Note that these current modes are basically filament currents. The use of effective length also accounts for any width and thickness effects on the current distribution. Width and thickness are also taken into account when finding the effective wire radius which is used in calculation of the self-impedance terms in the mutual impedance matrix.

A major feature of the selected code was the ability to account for substrate or dielectric loss. This is of prime importance for the  $\text{CaF}_2$  substrate in the frequency range of interest and is generally important for most usable infrared materials. The model obtained in Appendix C for  $\text{CaF}_2$  dielectric loss was added to the code. While this model is not extremely accurate below  $1000 \text{ cm}^{-1}$ , it is felt to be good enough for the purposes of this study. The resulting calculated transmittance curves for the  $\text{CaF}_2$  substrates (1 mm thick) are presented in almost all data plots in this section and in Appendix C.

Using the element and array dimensions presented with the SEM photographs in the previous chapter, the transmittance characteristics of the dipoles, tripole and crossed-dipole filters were modelled. It was found that all the calculated resonance locations were lower in frequency than those in the measured data. To partially account for this, the element lengths were shortened by a process called tip correction. The tip correction was done to account for the rounded ends on the elements caused by drawing with a round E-beam spot. This process shortens the lengths of the round tip elements so that they will have the same areas as elements with square tips. This is shown in Figure 5.2, where the tip corrected element length,  $\ell_t$ , is related to the measured length and width (respectively,  $\ell_m$  and  $w_m$ ) by

$$\ell_t = \ell_m - w_m \left( \frac{4-\pi}{8} \right) \quad . \quad (5.1)$$

The resulting transmission curves for all the metal element patches are illustrated in Figures 5.3 through 5.10. Note that no mention is made of any metal type in these figures since the model assumes the elements to be perfectly conducting. All these plots with one exception were obtained from calculated data in which the frequency sampling interval was  $50 \text{ cm}^{-1}$ . Due to the etalon behavior of the relatively thick substrates as shown in Figure 5.4, this data is quite coarse and jumps around a great deal due to the high frequency etalon ripple. In Figure 5.4, the frequency sampling interval is  $0.35 \text{ cm}^{-1}$  which is 200 times more dense than the other figures. The high resolution data for the

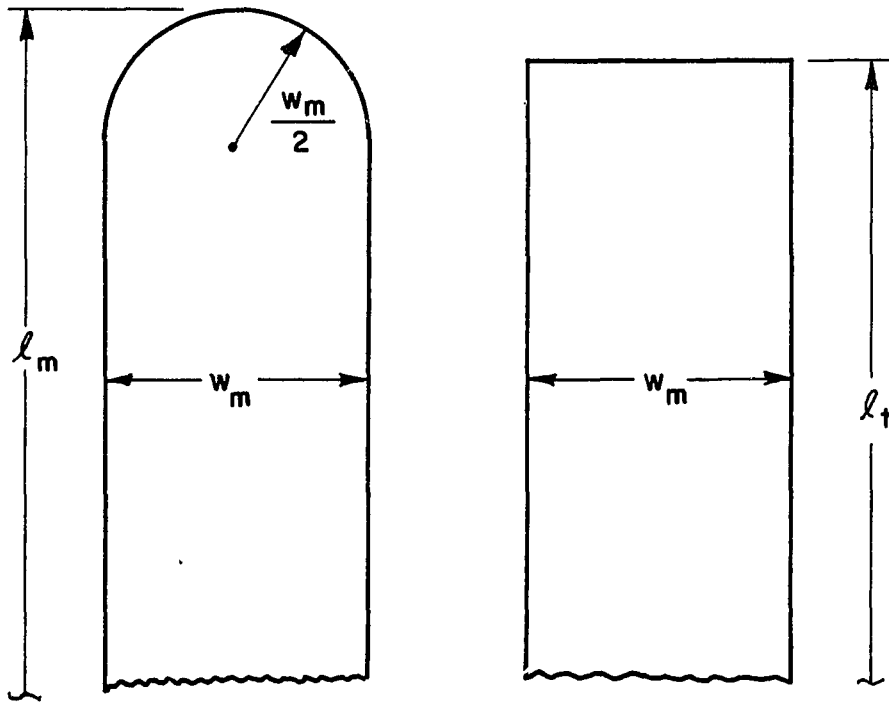


Figure 5.2. The relationship between measured element length,  $l_m$ , and tip corrected element length,  $l_t$ .

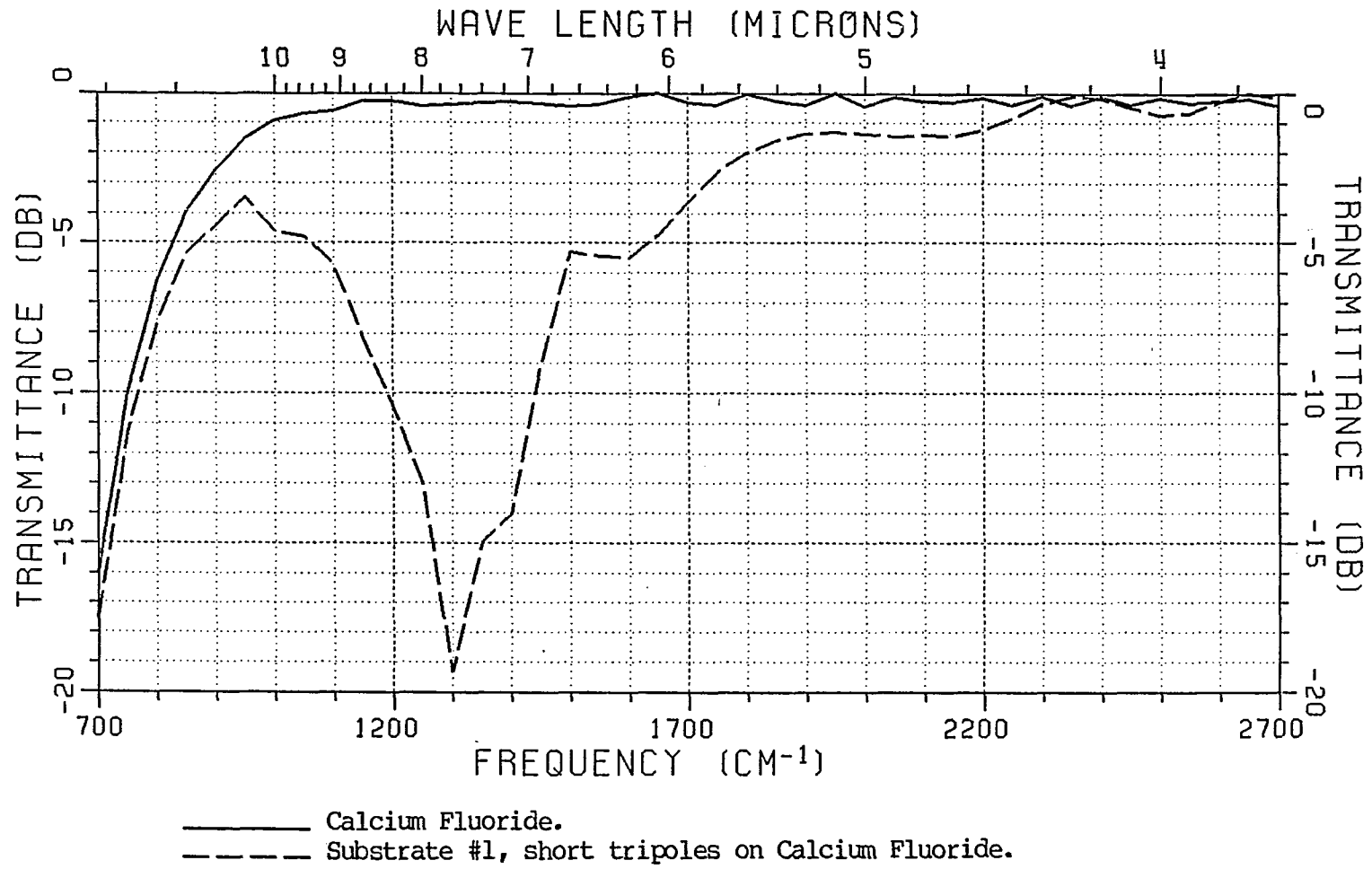


Figure 5.3. Calculated transmittance data for substrate #1.

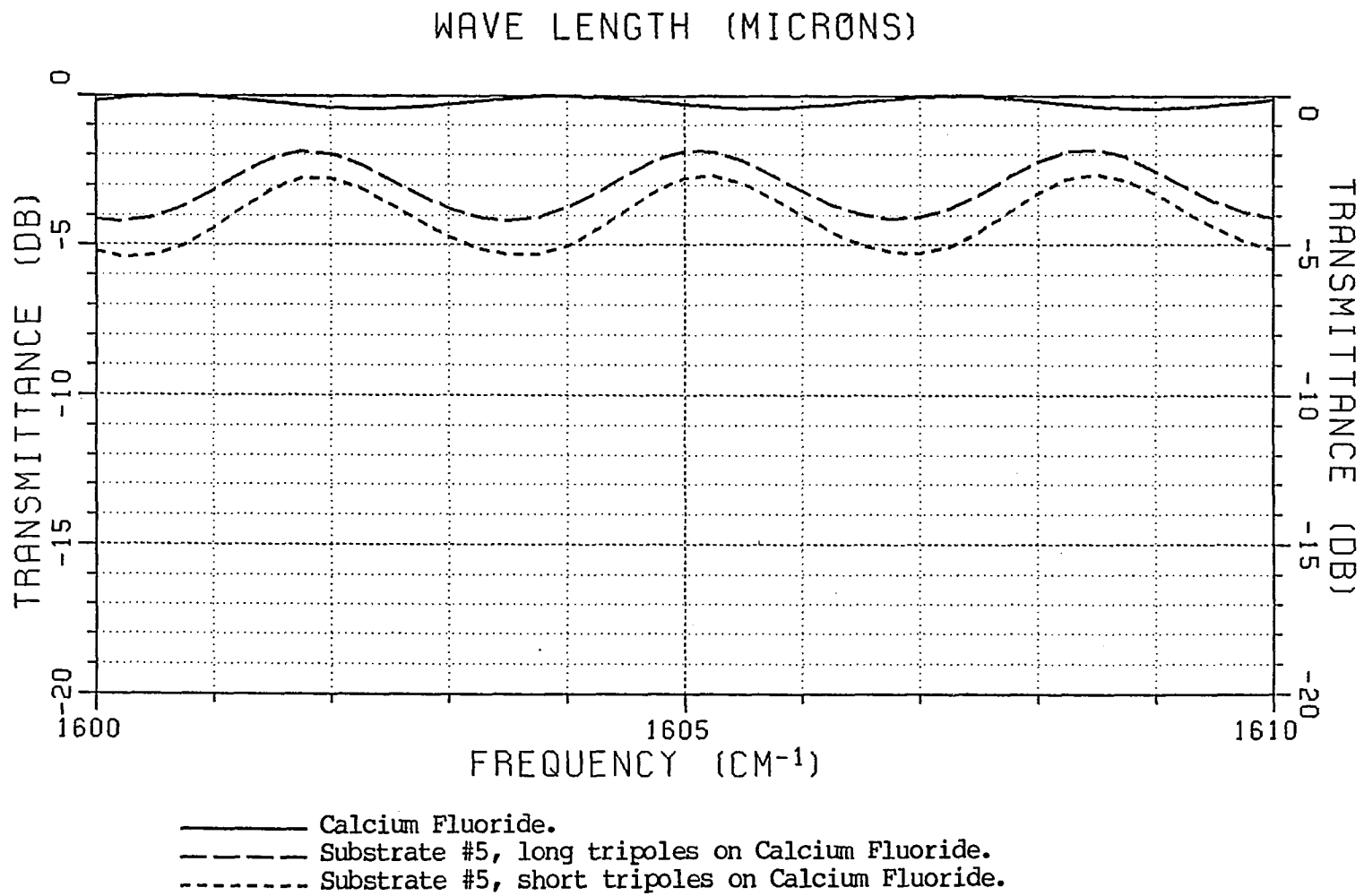


Figure 5.4. Calculated transmittance data for substrate #5. High resolution data showing etalon effect.



long tripoles in Figure 5.4 is also repeated in Figure 5.5 as a set of error bars at 1605  $\text{cm}^{-1}$ . Thus, to have obtained very accurate plots which could be smoothed for comparison with the previous measured data would have required excessive computer time. Instead, this data was taken as is and used to estimate the resonance location using a linear least mean square fit technique. Using this approach, the minimum calculated transmittance point in the region from 1000  $\text{cm}^{-1}$  to 1700  $\text{cm}^{-1}$  was found and the nearest five calculated points (i.e.,  $\pm 100 \text{ cm}^{-1}$  from the course minimum) in dB were fit to the quadratic

$$T_{\text{dB}}(\nu_i) = A_0 + A_1\nu_i + A_2\nu_i^2 \quad , \quad (5.2)$$

The resonant frequency,  $\nu_{\text{min}}$ , was then approximated as

$$\nu_{\text{min}} = -\frac{A_1}{2A_2} \quad . \quad (5.3)$$

The results of applying this process to the calculated data sets are presented in Table 5.1 for both the non tip-corrected and tip-corrected cases. In addition, the resonance locations for the measured data set from Chapter IV are also presented in Table 5.1. For consistency and to minimize noise effects, the measured resonance locations were found by a similar least mean square technique. For the measured data, all points in the range of  $\pm 100 \text{ cm}^{-1}$  from the minimum transmittance location were included in the processing. This process was done on the smoothed data. Along with each calculated resonant frequency is given a percentage error figure  $\bar{e}$ , defined as

TABLE 5.1

## COMPARISON OF MEASURED AND CALCULATED RESONANT FREQUENCIES

Substrate (CaF <sub>2</sub> )	Patterns	Measured Resonant Frequency (cm <sup>-1</sup> )	Calculated Resonant Frequency (cm <sup>-1</sup> ) (non-tip corrected)	Calculated Resonant Frequency (cm <sup>-1</sup> ) (tip corrected)
1	short tripoles	1341	1297 (-3.3%)	1304 (-2.8%)
5	short tripoles	1318	1262 (-4.3%)	1278 (-3.8%)
	long tripoles	1126	1102 (-2.1%)	1108 (-1.6%)
	short crossed-dipoles	1355	1282 (-5.4%)	1298 (-4.2%)
	long crossed-dipoles	1164	1101 (-5.4%)	1115 (-4.2%)
7	short fat dipoles	1378	1344 (-2.5%)	1348 (-2.2%)
	long narrow dipoles	1138	1031 (-9.4%) worst	1066 (-6.3%) worst
	short narrow dipoles	1394	1349 (-3.2%)	1353 (-2.9%)
10	short fat dipoles	1452	1362 (-6.2%)	1398 (-3.7%)
	long narrow dipoles	1163	1100 (-5.4%)	1105 (-4.9%)
	short narrow dipoles	1411	1344 (-4.8%)	1392 (-1.4%)
11	short fat dipoles	1407	1346 (-4.4%)	1384 (-1.6%)
	long narrow dipoles	1120	1097 (-2.1%) best	1103 (-1.5%)
	short narrow dipoles	1378	1344 (-2.5%)	1367 (-0.8%) best
12	short fat dipoles	1455	1374 (-5.6%)	1407 (-3.3%)
	long narrow dipoles	1160	1094 (-5.7%)	1099 (-5.3%)
	short narrow dipoles	1418	1345 (-5.2%)	1368 (-3.5%)
8	short fat slots	1436		
	long narrow slots	1195		
	short narrow slots	1365		
9	short fat slots	1495		
	long narrow slots	1183		
	short narrow slots	1420		

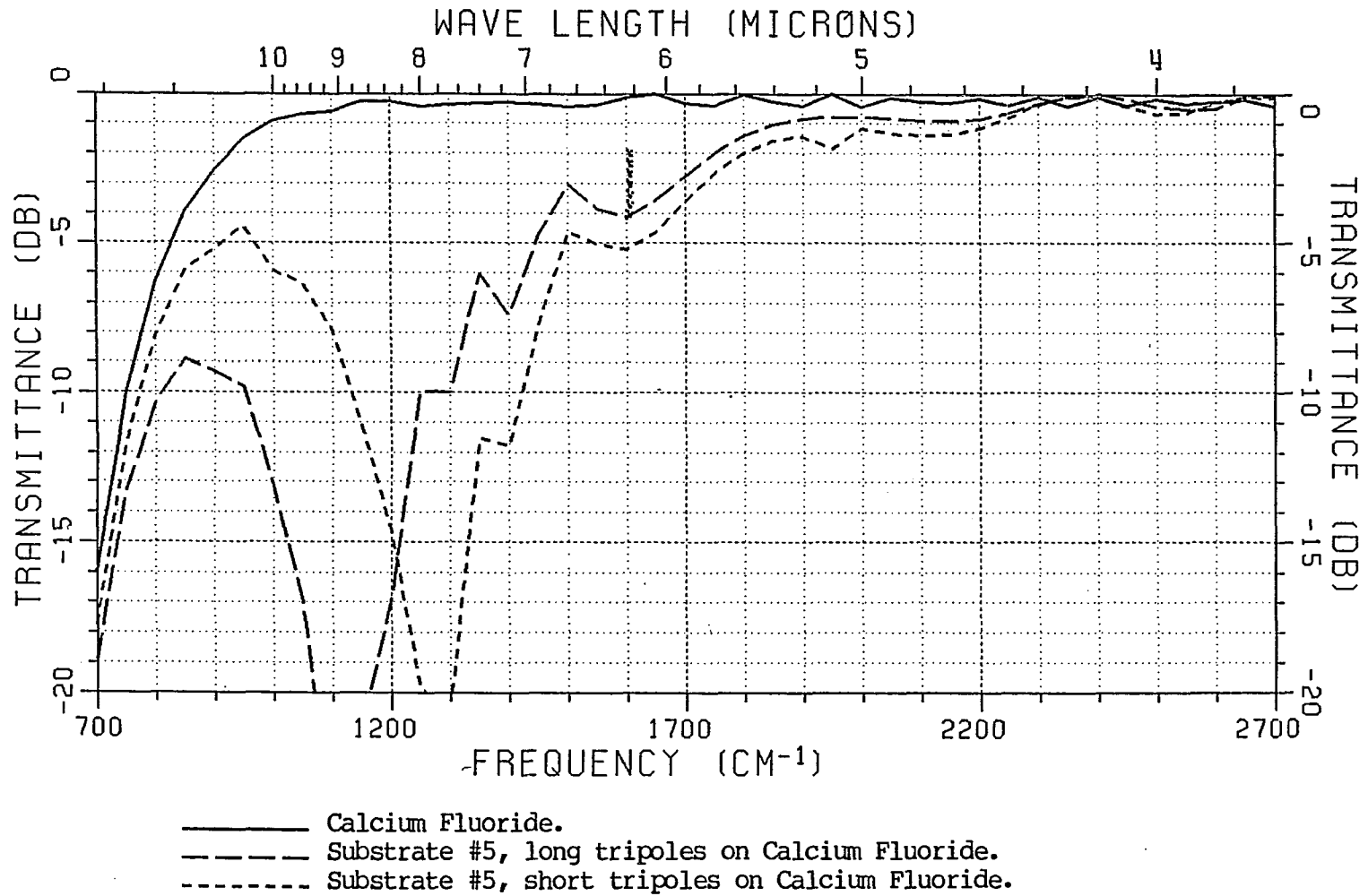


Figure 5.5. Calculated transmittance data for substrate #5.

$$\bar{e} = 100 \left( \frac{\nu_{\text{calculated}} - \nu_{\text{measured}}}{\nu_{\text{measured}}} \right) . \quad (5.4)$$

For the non tip-corrected data, the error range is -9.4% to -2.1% and for the tip-corrected data, -6.3% to -0.8%. The latter is considered very good given the quality of the SEM photographs in Chapter IV. As pointed out earlier, the resonance locations obtained using the non tip-corrected data are all lower than the measured resonance locations, as indicated by all negative errors in Table 5.1. This is also the case for the tip-corrected data. These results are probably due to some systematic error, the most likely one being mismeasurement of the element dimensions (primarily length but also width). There are two possible causes of this error. The first is a slight difference between the model element shape and the actual element shape. This could be caused by nonrectangular element cross sections yielding effects similar to the tip-correction mechanism. The second cause could be ERMF deflection electronics which are slightly out of calibration. Since the average errors are only -4.6% for the non tip-corrected cases and -3.1% for the tip-corrected cases, either is a possibility.

Several other comments should be made concerning the calculated data. The first is that the calculated data show many of the same effects as the measured data. In general, for the dipole elements, the fat elements are both broader in bandwidth than the narrow elements and resonate at a slightly higher frequency. The only exception to this is

substrate #7 on which the fat dipoles resonate at a slightly lower frequency than do the narrow elements. This is true for both the measured and calculated data. In addition, comparison of Figures 5.5 and 5.6 show that the calculated tripole data for substrate #5 is more broadband than the sparser crossed-dipole elements on the same substrate. Again, this was pointed out for the measured data.

The major difference which can be seen in comparing the calculated data to the measured data is the null depths of the filters for the tripole and crossed-dipole elements. These differences are hard to see for the dipole elements due to the previously mentioned dynamic range problems caused by interaction with only one polarization. There are several possible reasons for the lack of null depth in the measured data. One possibility is a loss of instrument response caused by the use of a focused beam. This possibility was ruled out since deeper nulls were obtained with the earlier low  $f\#$  measurement system than with the later high  $f\#$  system. An example of data obtained using the low  $f\#$  system is presented in Figure 5.11 for the aluminum tripoles on substrate #5. The problems with this system are fairly obvious since a passive device cannot exhibit gain (i.e., transmittance greater than 0 dB). The second major possibility limiting null depth is leakage around the arrays during the measurement process. However, two beam limiting apertures were used to prevent such leakage and it is felt that this technique was effective. The last major possibility is metal loss or imperfections incurred during storage between the two sets of

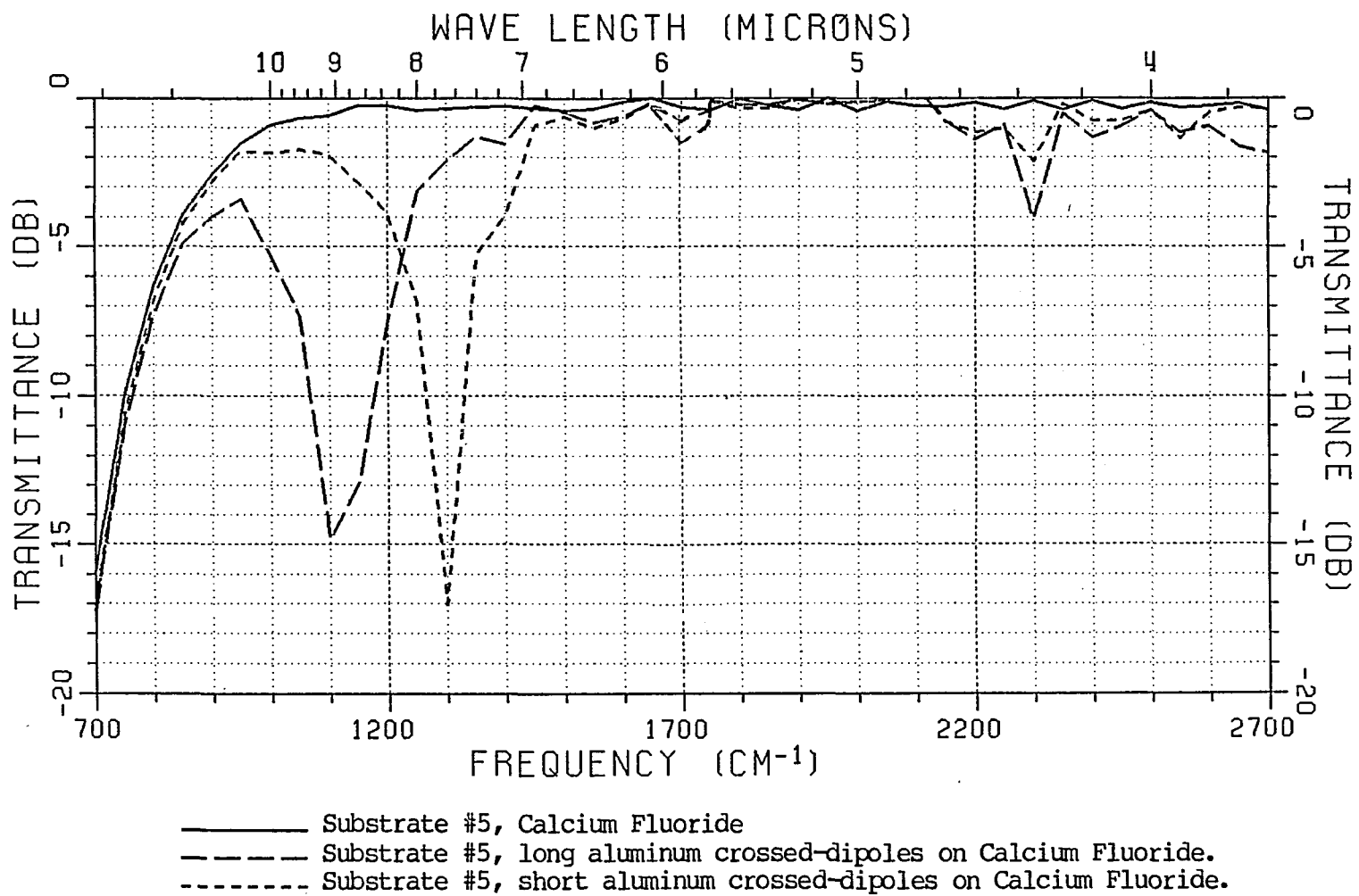


Figure 5.6. Calculated transmittance data for substrate #5.

measurements. Techniques to model such loss are presented in Appendix D and were tried for the tripole and crossed-dipole models of the elements on substrate #5. These results will now be discussed.

Using the lossy element analysis in Appendix D, the aluminum elements on substrate #5 were modelled to see if better agreement between experiment and theory could be obtained. The required surface resistance data was obtained as described in Appendix E. The cosine current mode was used to model the receiving current distribution as explained in Appendix D. The results of this analysis are presented in Figures 5.12 and 5.13 for the tripole and crossed-dipole elements, respectively. Note that the frequency region of interest has been reduced to  $900\text{ cm}^{-1}$  to  $1600\text{ cm}^{-1}$ . As can be seen by comparing Figures 5.12 and 5.13 to Figures 5.5 and 5.6, the inclusion of the aluminum loss model has very little effect. This is not surprising since the model data for the aluminum is based on the high reflectance data for clean, fresh films. For films which have aged slightly (due to oxidation and abrasion), the reflectivity is known to drop. To see what effect such aging would have, the approximate  $2\Omega$  surface resistance (see Figure E.3) of the aluminum was increased to  $5\Omega$ . The results presented in Figures 5.14 and 5.15 show that this loss better models the measured data shown in the previous chapter. Note that for a  $5\Omega$  surface resistance, the reflectance is still approximately 95% which is visually indistinguishable from a freshly coated surface. Even if the surface resistance approaches  $10\Omega$ , the reflectance will be nearly 90%, however,

severely degraded filter performance could be expected. For this reason, it may be necessary to provide a dielectric coating for protection of the fresh metal films if deep nulls (or low insertion loss for slots at resonance) are desirable. This could be further advantageous in providing an extra dielectric layer as a parameter for designing even better filter characteristics. Better characteristics may include both improved off-axis performance [45,46] and greater null depth for a given filter bandwidth.

One last point should be made concerning the addition of loss to the periodic surface analysis. It was noticed in all cases tested that increasing the surface loss resistance raised the calculated filter resonant frequencies. In some cases (the long elements and  $R_s=20\Omega$ ) the calculated resonant frequencies were even greater than the measured resonant frequencies; however, for these cases, the overall filter responses were highly degraded and as a result are not presented.



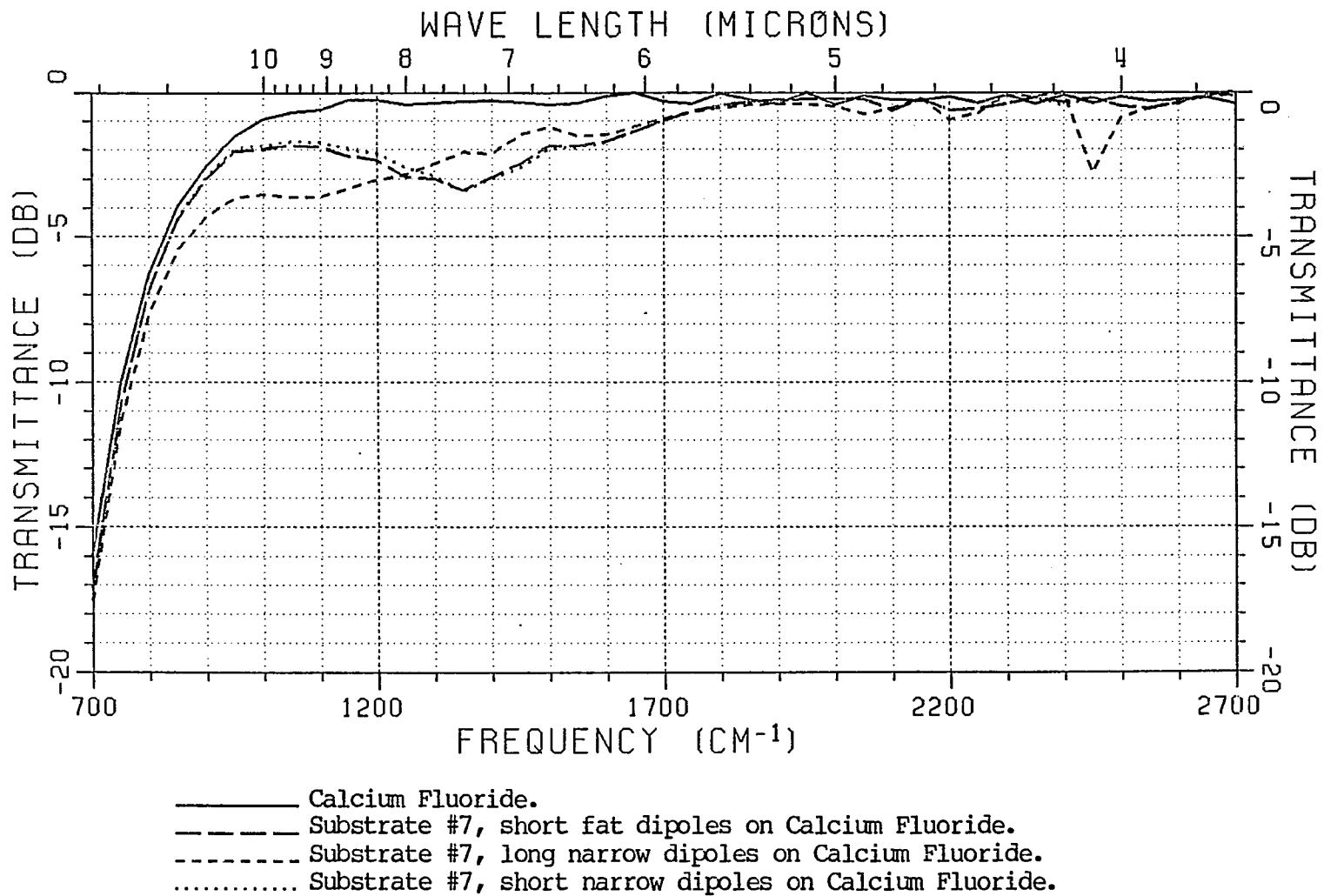
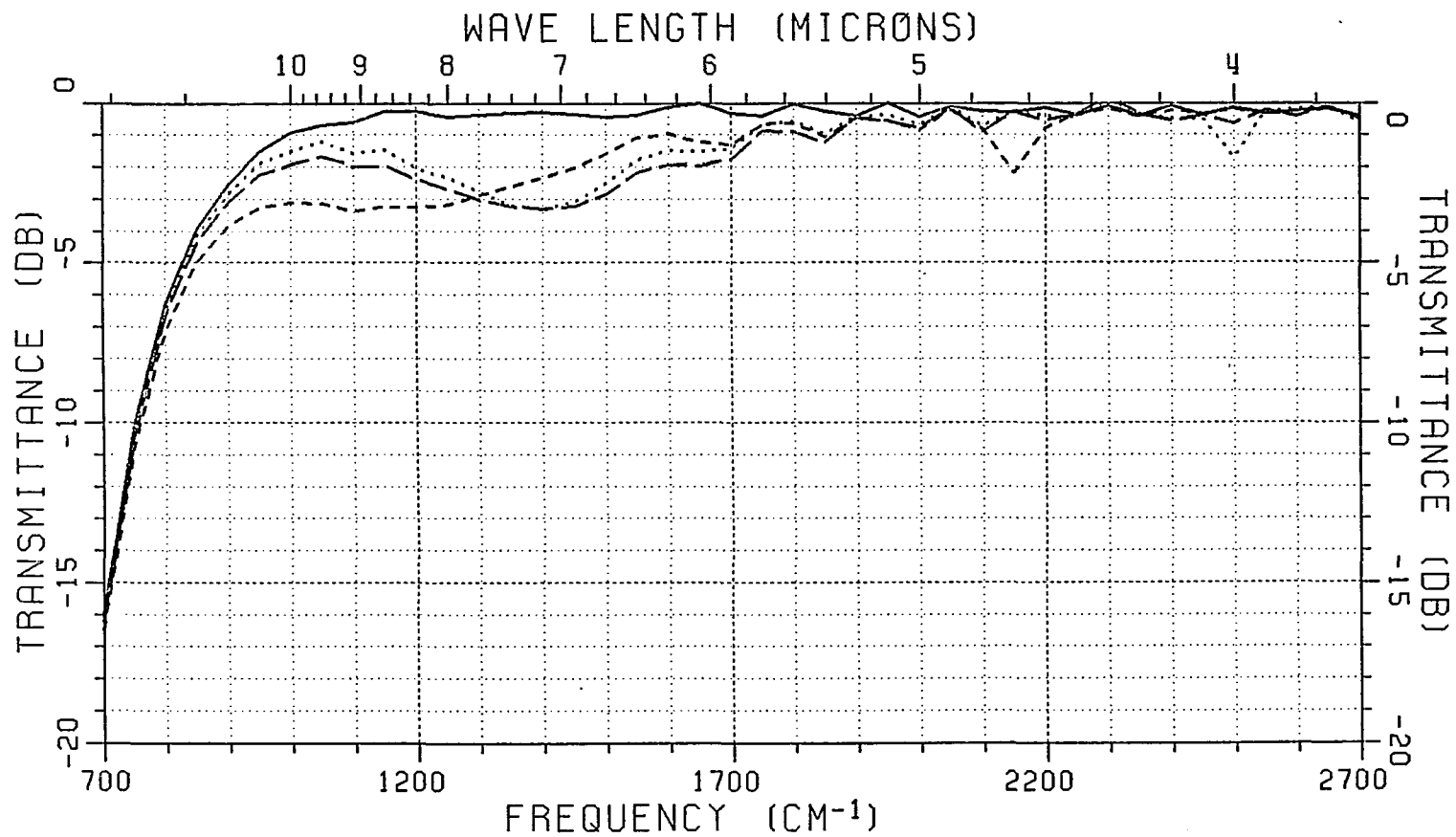


Figure 5.7. Calculated transmittance data for substrate #7.



- Calcium Fluoride.
- Substrate #10, short fat dipoles on Calcium Fluoride.
- · - · - Substrate #10, long narrow dipoles on Calcium Fluoride.
- ..... Substrate #10, short narrow dipoles on Calcium Fluoride.

Figure 5.8. Calculated transmittance data for substrate #10.

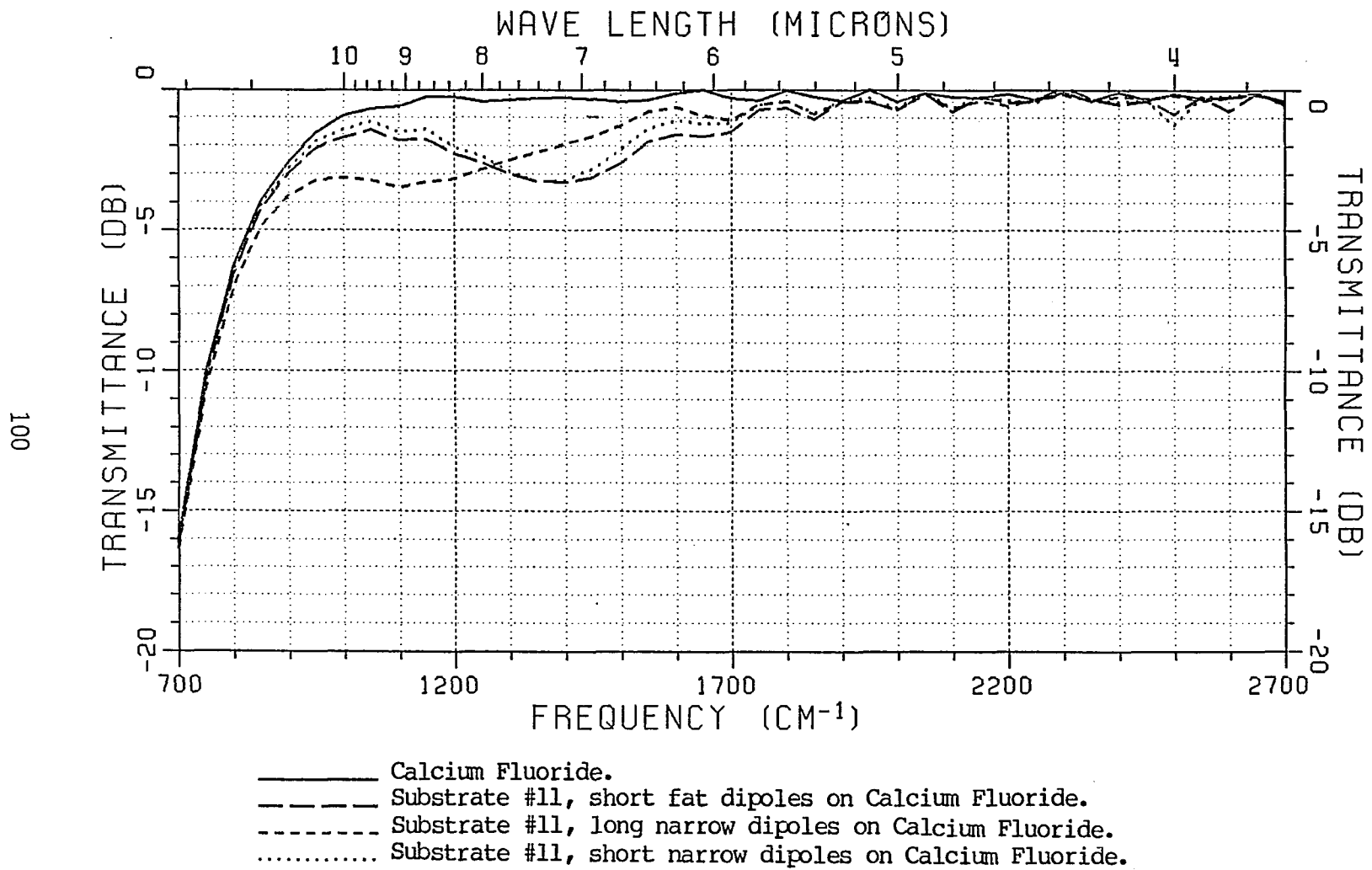


Figure 5.9. Calculated transmittance data for substrate #11.

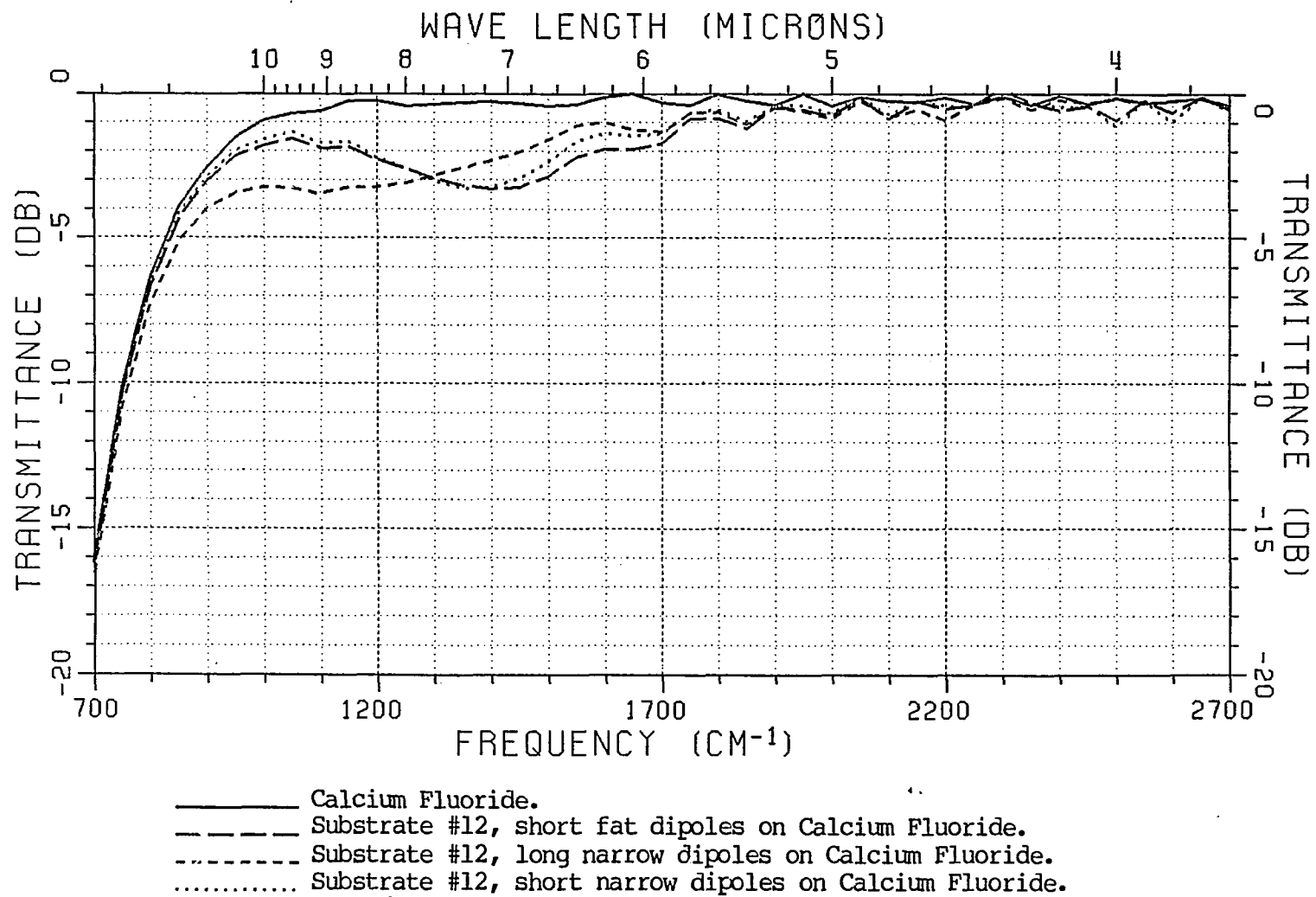
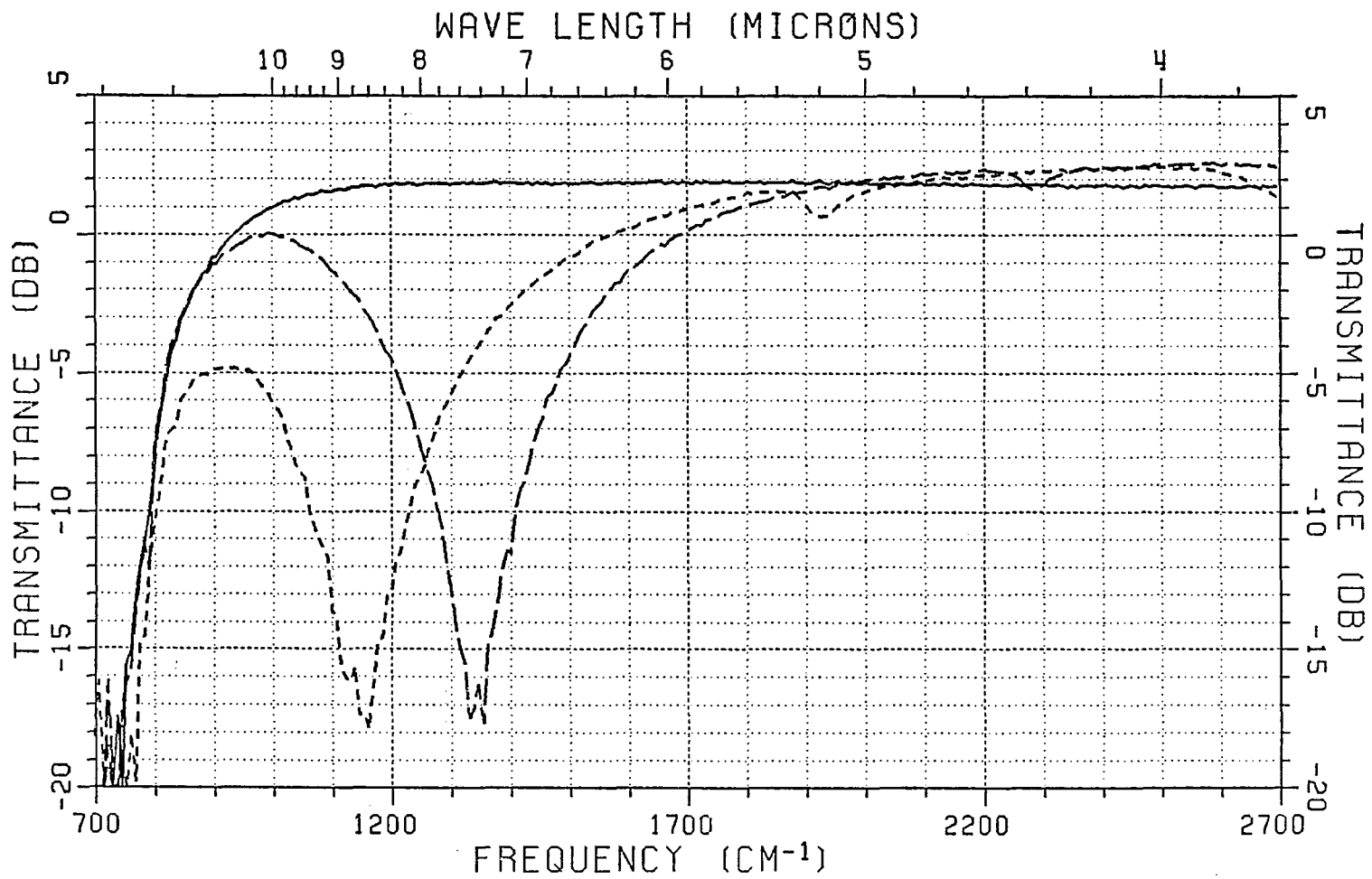


Figure 5.10. Calculated transmittance data for substrate #12.



- Substrate #5, Calcium Fluoride
- Substrate #5, short aluminum tripoles on Calcium Fluoride.
- · - · - Substrate #5, long aluminum tripoles on Calcium Fluoride.

Figure 5.11. Measured transmittance data for the tripole arrays on substrate #5 using the low f# measurement system.

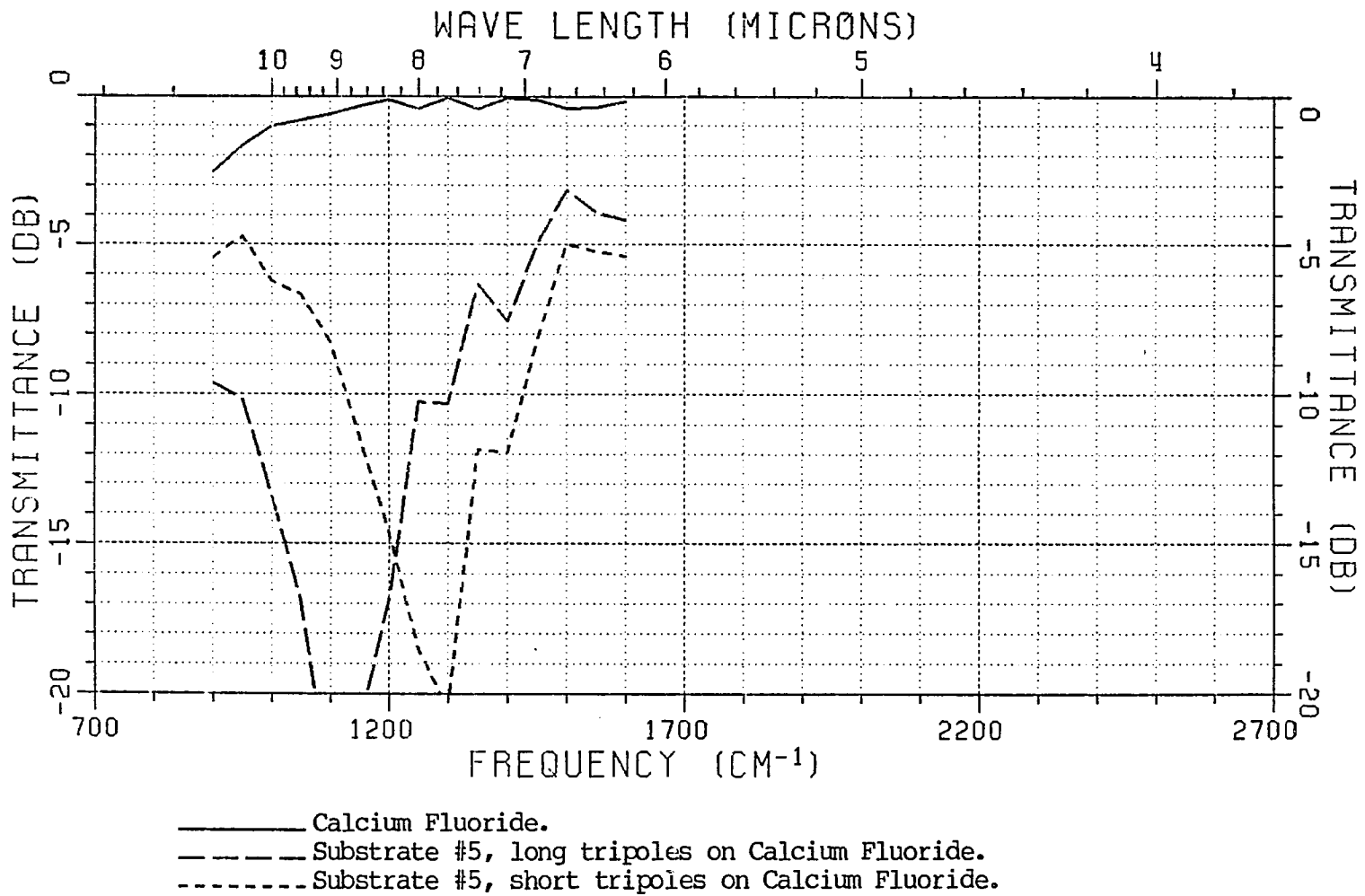


Figure 5.12. Calculated transmittance data for substrate #5 including the aluminum loss model.

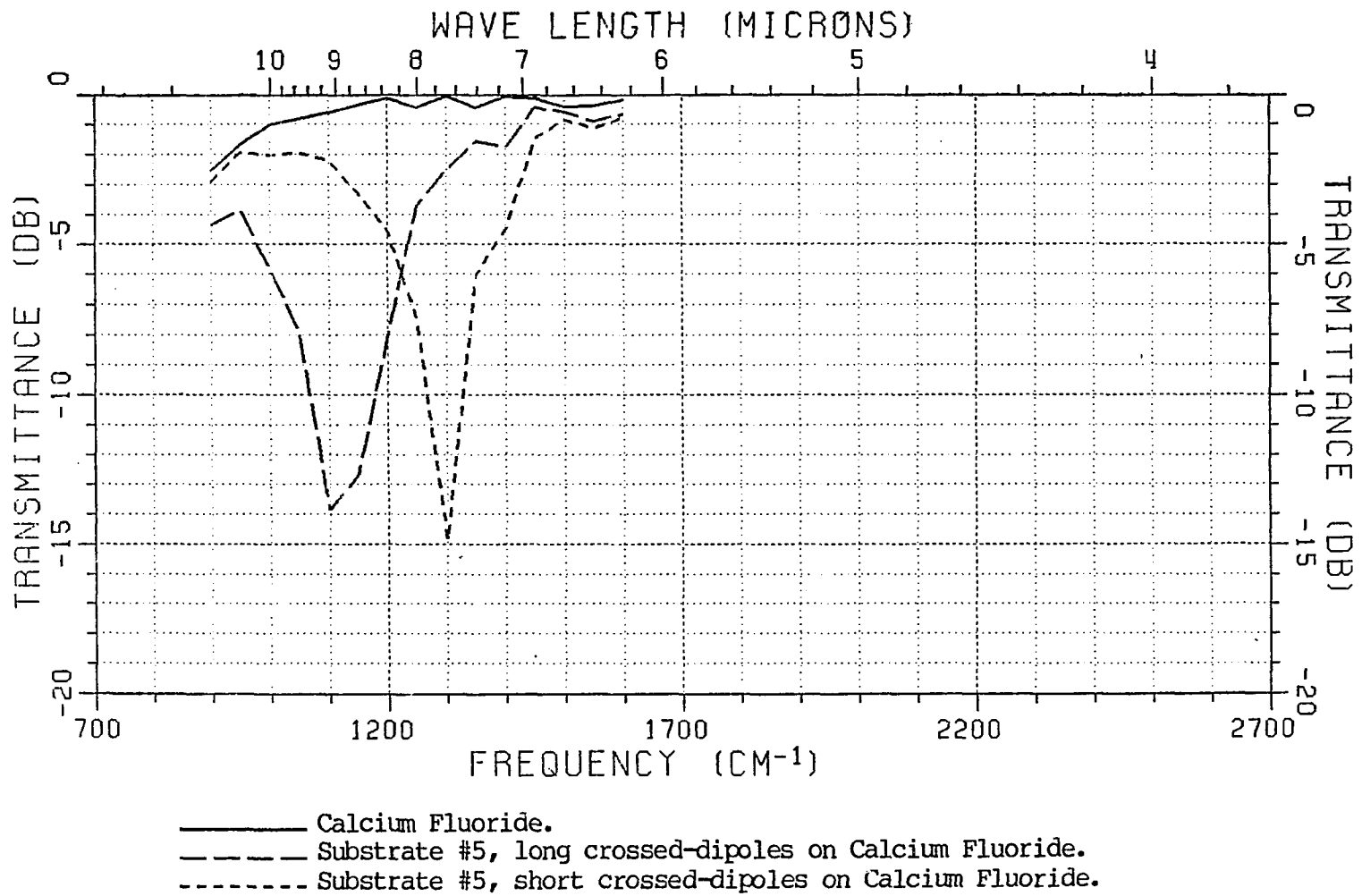
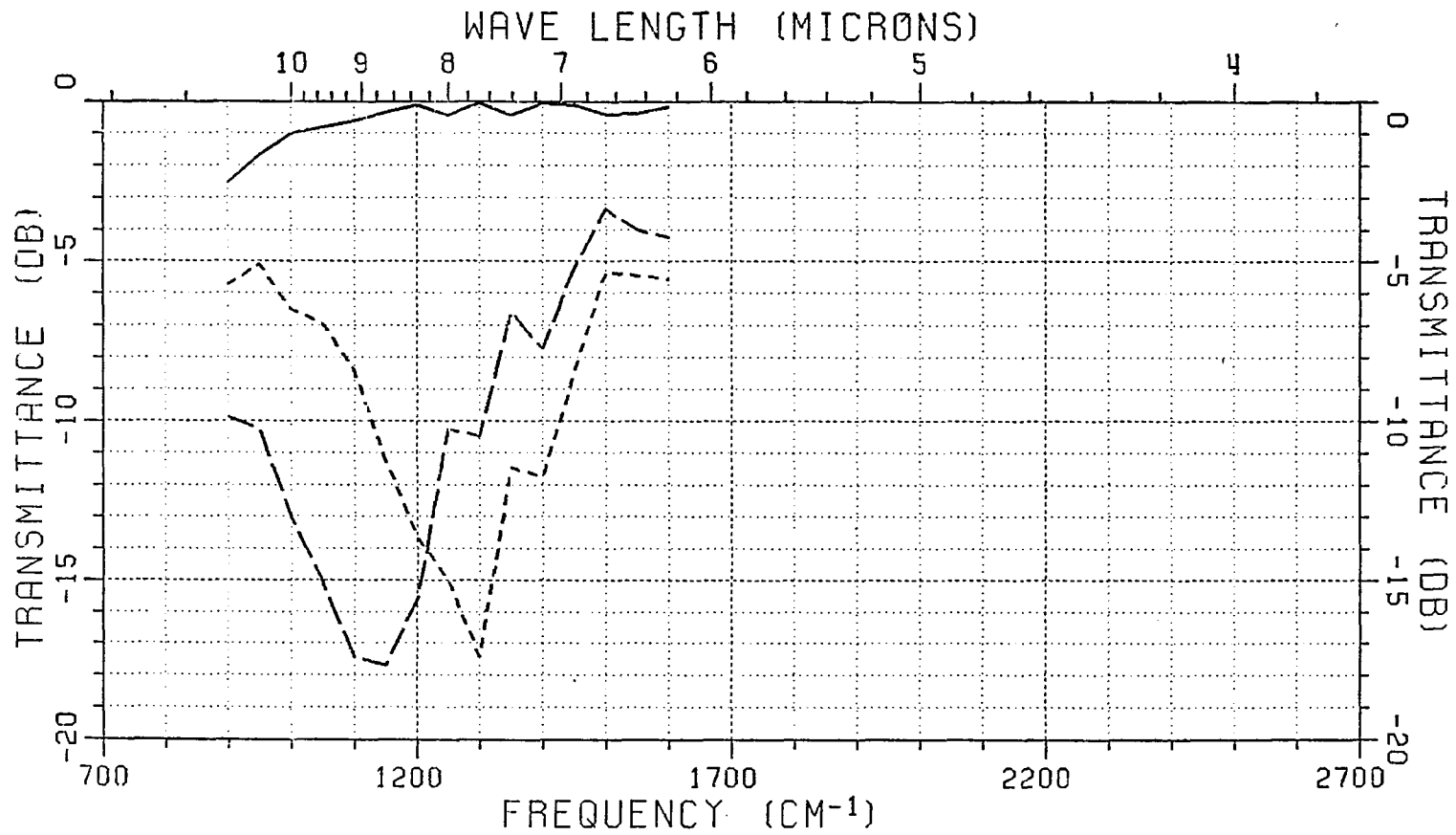


Figure 5.13. Calculated transmittance data for substrate #5 including the aluminum loss model.



————— Calcium Fluoride.  
 - - - - - Substrate #5, long tripoles on Calcium Fluoride.  
 - - - - - Substrate #5, short tripoles on Calcium Fluoride.

Figure 5.14. Calculated transmittance data for substrate #5 including surface loss.  $R_s = 5\Omega$ .



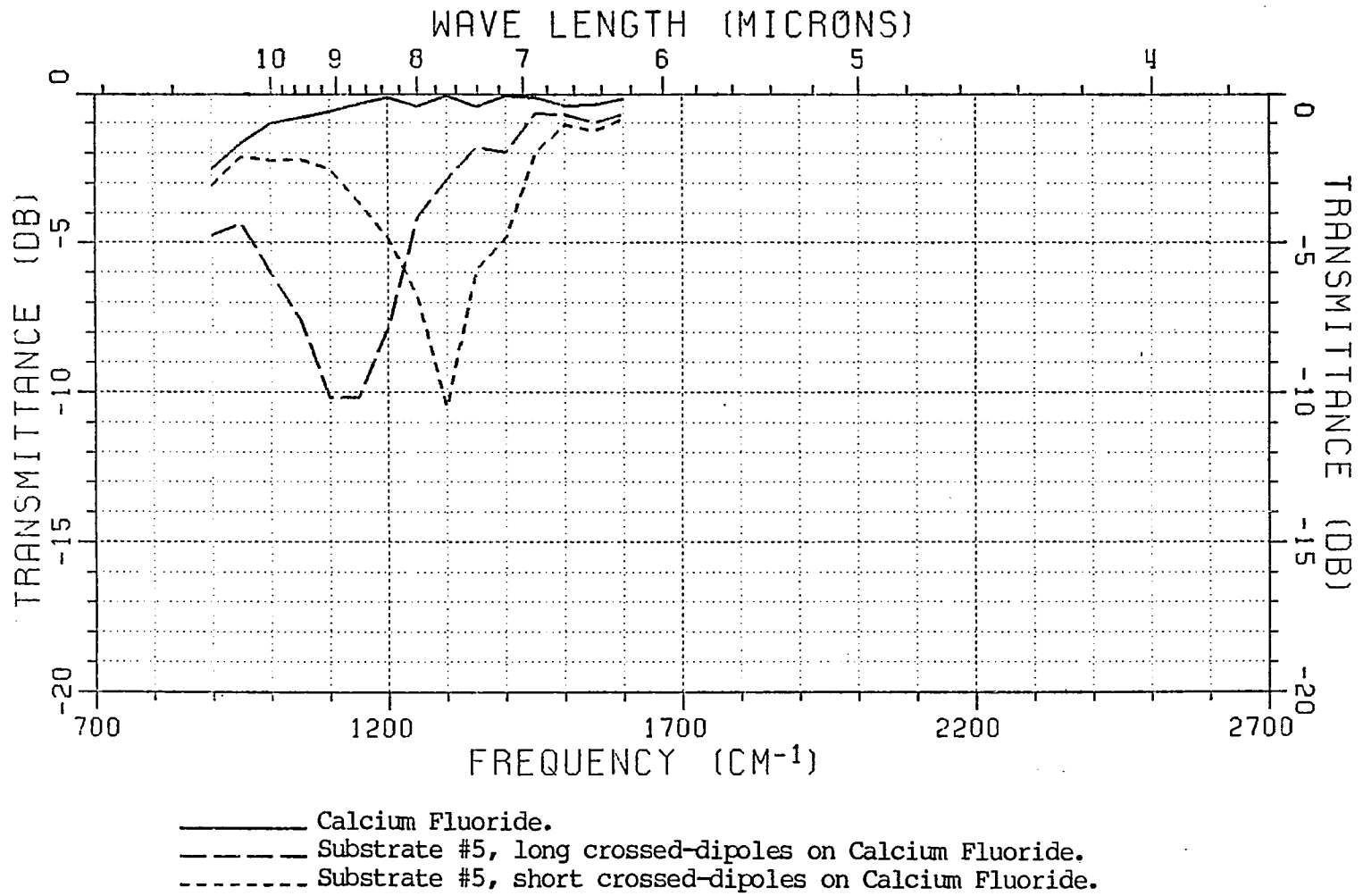


Figure 5.15. Calculated transmittance data for substrate #5 including surface loss.  $R_s = 5\Omega$ .

## CHAPTER VI

### SUMMARY AND CONCLUSIONS

In past studies, infinite, periodic arrays of antenna elements (both metallic and slots) have found applications in the microwave frequency regime. These surfaces, which can be designed to have bandpass or bandstop filter characteristics, are of interest due to their stable characteristics when scanned to angles other than normal incidence. The concept of stability implies small changes in filter center frequency and bandwidth when the incidence angle and/or polarization of the incident electromagnetic field change.

The results of this study show that the theories tested in the microwave regime may also be used to design filters for the mid-infrared regime. The ultimate goal is the construction of mid-infrared filters which have more stable characteristics than current filters constructed of simple, multi-layered dielectrics. In fact, mid-infrared filters have been designed via first order resonance theory for isolated elements and constructed using the techniques of electron-beam lithography. Several different types of elements have been built

including dipoles, tripoles and crossed-dipoles. In addition to the metallic elements such as straight dipoles, straight slots have also been built. The limits of currently available lithography have been discussed as well as the techniques for forming the metallic elements and slots. It has been shown that wet etching is unsatisfactory for the formation of slot elements; however, it is expected that the development of techniques such as reactive ion etching (RIE) and other dry etching techniques will be capable of producing high quality geometries.

The filter patches which were successfully constructed were measured in transmission using the techniques of infrared Fourier transform spectroscopy. Due to the small areas of the filter patches (approximately 3mm x 3mm), a focused optical beam was used to maximize the energy incident on the sample areas and hence increase the measurement signal to noise ratio. Initial measurements using approximately f2 lens optics showed that the surfaces did indeed exhibit the desired filter characteristics. Unfortunately the large cone angle for f2 optics (about 28°) does not yield a very good approximation to a plane wave. Final measured data for comparison with calculated plane wave data were taken using approximate f8 reflective optics with a cone angle of 7°. The reported data were obtained almost exclusively with the f8 system.

The last major portion of this study is a comparison of the measured data with calculations obtained using a computer code which had been tested in the microwave region. The original code was modified

to handle the effects of the lossy, dispersive calcium fluoride substrates on which the filter patches were constructed. Additional modifications were made to account for the thickness of the elements (the elements in this study had rather large aspect ratios) and effects caused by the rounded ends on the elements. Using dimensions obtained from detailed SEM photographs of the filter elements, transmittance curves were calculated for all the metallic element patches which were measured. This resulted in seventeen sets of data which were qualitatively compared on the basis of filter center frequency. The maximum error was found to be 6.8% and the minimum error only 0.8%. The average error for all seventeen data sets was only 3.1% which is considered excellent given the quality of the SEM photographs.

It was found that the measured transmission null depths for the tripoles and crossed-dipoles did not agree very well with the calculated data. It was postulated that metallic loss effects in the measured data which were not included in the calculated data caused the discrepancy. Using a perturbation analysis, a model for the surface loss in metal elements was developed and added to the computer code. When published data on aluminum films was incorporated into this model the results were found to differ only slightly from the original lossless calculations. However, it was shown that only a small increase in the surface resistance (less than a factor of three from the published aluminum data) produced results comparable to those in the measured data for the aluminum elements. This increase in surface resistance is in fact quite

believable since the published aluminum data were for fresh films and the final measurements on the aluminum patches occurred after sufficient time for some surface oxidation.

Due to the introductory nature of this study, the scope has been quite narrow. As a result, there are many areas for future work. One particular area of interest is in the study of other periodic surfaces geometries which could include both different element types and multilayered arrays. Future element types of interest could include loaded elements; however, even for the frequencies used in this study the construction of loaded elements would require better lithographic techniques. In addition to the loaded elements, multi-legged slots would also be of interest. For these purposes, the study of RIE and other micro-machining techniques would be invaluable. Multi-layered surfaces consisting of both multi-layered dielectrics and staggered metallic arrays should also be investigated as methods for both increasing and decreasing the filter bandwidths and controlling resonant frequency insertion loss.

As a practical matter, filter patches with larger areas should be constructed so that the off-axis characteristics of the filters may be verified. This would also provide methods for constructing larger filter patches for use in real optical systems. Practical problems such as these bring up other problems related to the electron beam process. The main problems are the slow speed of the electron beam exposure process and the lack of quality high resolution replication techniques

for the 0.25  $\mu\text{m}$  line widths obtained in this study. However, this area of technology is rapidly advancing due to the need for these techniques in the area of micro-electronics. Thus, the area of high frequency periodic surfaces may greatly benefit from the VLSI (very large scale integrated) circuit and VHSIC (very high speed integrated circuit) programs. Advances in these areas should make even higher frequency periodic surfaces possible. Currently work has even progressed to the point where contracts are being let for construction of ion beam lithography machines [47] having a 0.07  $\mu\text{m}$  (or 700Å) linewidth capability. This is two to three times finer than the linewidths produced by the e-beam machine used in this study.

In addition to the aforementioned improvements in analytical techniques and construction techniques, the study of infrared periodic surfaces would be greatly aided by improved data on materials in this frequency regime. For dielectrics, accurate data on index and extinction coefficient are needed and not generally available. For metals, data on the loss characteristics of the materials is largely unavailable or sporadic in nature. In addition, the effects of aging as it relates to increases in surface loss needs to be studied and techniques for minimizing these losses developed.

## APPENDIX A

### THE CONSTRUCTION OF MID-INFRARED PERIODIC SURFACES

The construction of the arrays of resonant conducting elements which comprise the periodic surfaces has proven to be a formidable task. The reason for this is that at the design wavelengths in question (i.e., 5 to 10  $\mu\text{m}$ ), the techniques of optical lithography which have been used with great success in the microwave and far infrared regions [48,49], can no longer resolve the required dimensions for high-Q elements such as thin dipoles or tripoles. Elements such as these are desirable since they are most easily packed (especially the tripoles) which delays the onset of grating lobes. Initially we abandoned such high-Q elements and attempted to build elements which would have been at best fat dipoles.

A laser interferometric system (Figure A.1) was used to expose Kodak type 1a spectroscopic plates to form simple patterns of alternating light and dark lines. These patterns were to be used as masks to expose a photo resist on our substrates which would have been used to form metal lines on the surface. The mask would have been

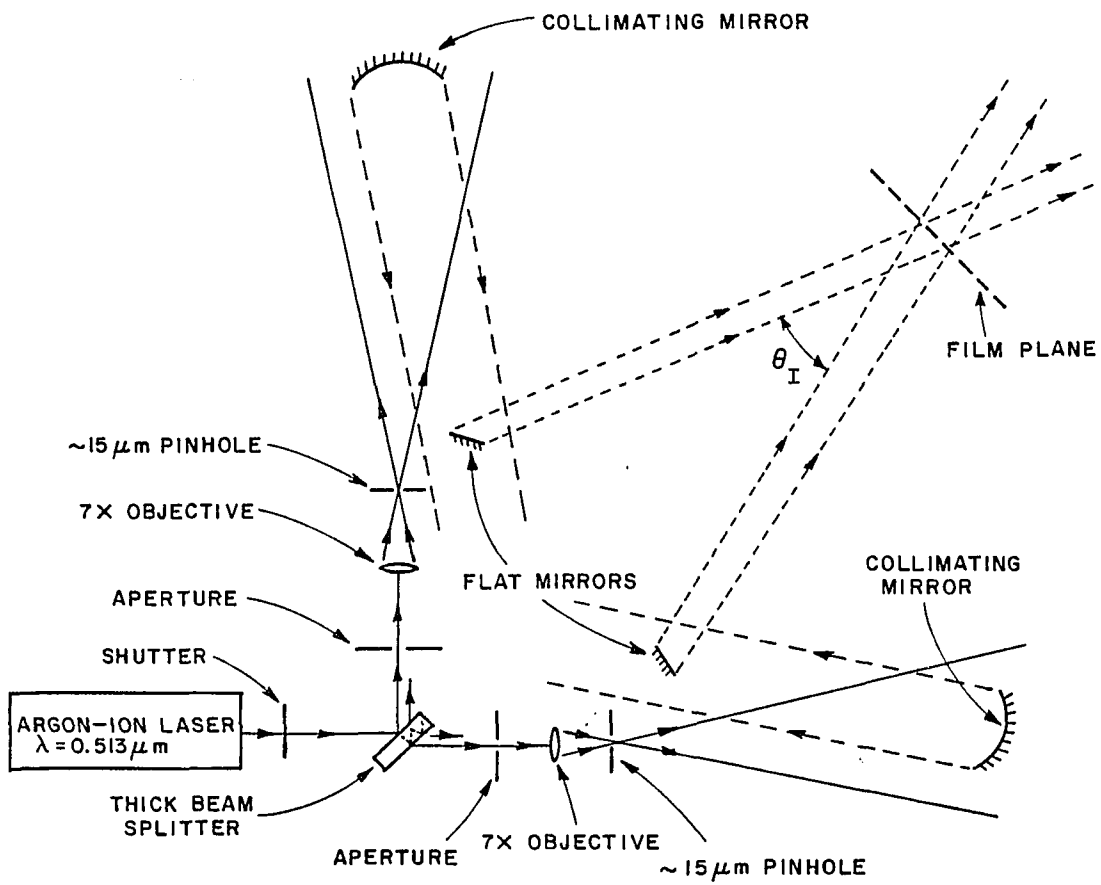


Figure A.1. Laser interference pattern system.



rotated and the process repeated to leave islands of metal. This turned out to be impractical since masks of high enough quality could not be produced. The lines produced were of the correct spacing (approximately 3  $\mu\text{m}$  as shown in Figure A.2) but the patterns were grainy and did not have sufficient contrast to produce good metal lines. It is not known whether the poor pattern quality was due to equipment problems such as aberrations from the mirrors and lenses or due to interference fringes in the photographic emulsion. These problems were not attacked since this technique was abandoned when the resources of the National Research and Resource Facility for Submicron Structures (NRRFSS) at Cornell University became available.

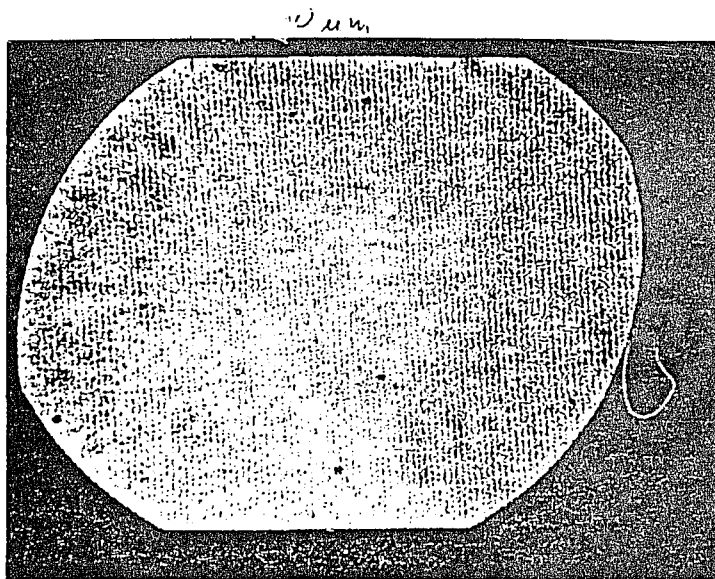


Figure A.2. Interference fringes in Kodak type 1a spectroscopic plate.  
Line separation is  $\approx 3 \mu\text{m}$ .

The NRRFSS is a unique research facility with equipment including a Cambridge EBMF 2-150 electron beam pattern generator, with a quoted resolution of 0.2  $\mu\text{m}$  or better [50]. It was decided to use the resources of this facility since it enabled the construction of the more desirable tripoles and cross-dipoles. The rest of this section will give a brief overview of the electron beam microfabrication (EBMF) techniques and related processes used at the NRRFSS for constructing the periodic surfaces. The capabilities and limitations of each technique will be briefly discussed as they relate to the results obtained.

#### A. ELECTRON BEAM MICRO-FABRICATION (EBMF)

The EBMF technique is somewhat similar to optical lithography in that a pattern is generated in a resist by an exposure-development process. Once this resist pattern is created it may be used to create a similar pattern or its complement in some desired material which in our case is a metal. The advantage of EBMF is that it is inherently capable of creating finer patterns in the resist. In optical lithography, the resist pattern is created by illuminating a mask consisting of clear and opaque areas and allowing this to shadow cast the image onto the resist. The limiting factors to resolution (i.e., minimum quality feature size or line width) are diffraction effects from the mask and reflection effects within the resist. Typically, this limits the resolution to linewidths greater than 2  $\mu\text{m}$  (see Figure A.3 [51]). The EBMF technique uses a focused beam of electrons to directly draw the pattern in a

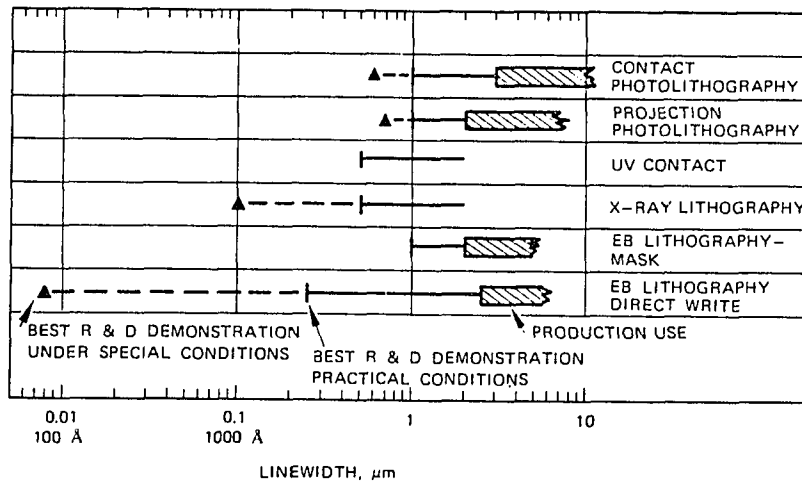


Figure A.3. Limits for various techniques in high resolution lithography [52].

resist [53,54]. It should be noted that the EBMF is essentially a scanning electron microscope (SEM) in which the beam steering electronics are capable of a vector scan mode in addition to raster scan mode. Typically, the beam steering and blanking are done under computer control. Due to the high energy of the electrons and associated short wavelength, the SEM and EBMF are capable of extremely small spot sizes. In the EBMF, spot sizes under 0.1 μm are usually not realized since very high beam currents are needed for realistic exposure times. The resulting space charge effects of the intense e-beam near the focus tends to limit the spot size due to electron repulsion. Another limiting factor is electron scattering in the resist due to

electron-molecule collisions. For these reasons, the equipment at NRRFSS is typically capable of generating 0.2  $\mu\text{m}$  lines although slight improvements are possible if great care is used and long exposure times are permissible.

The electron resist scattering process is also responsible for another problem in the EBMF process called the proximity effect. This effect becomes important when two lines are drawn close together resulting in the widely scattered electrons causing overexposure along the line edges. Thus, in regions where the lines are in close proximity, they broaden or lengthen and appear to grow towards each other. This may cause a problem (see Figure A.4) if we attempt to pack the resonant elements too close together to improve off-axis scan characteristics or bandwidth.

In e-beam lithography, there are two basic types of resists used: positive and negative. Their use is much the same as standard optical resists. The positive resists consist of polymer chains of high molecular weight, an example of which is polymethylmethacrylate (PMMA). The exposure process breaks the polymer links resulting in low weight molecules. The development process is essentially a controlled process of dissolving away the low weight molecules and leaving the high weight molecules. Thus, for positive resists, the unexposed material remains on the surface. For negative resists, this process is reversed in that the unexposed resists consist of low weight polymers with the exposure process causing chain cross linking to yield high molecular weights.

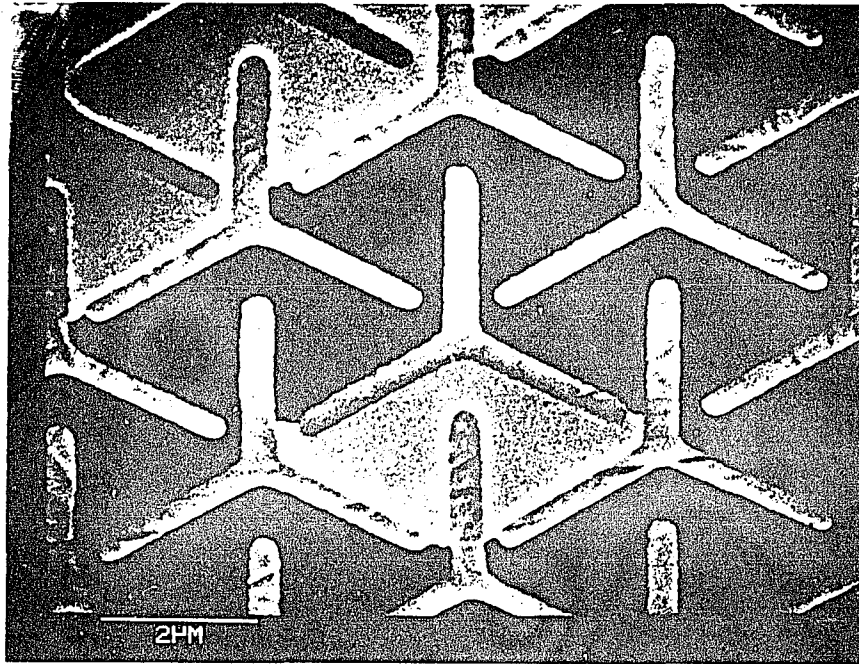


Figure A.4. Long tripoles on S#1 showing liftoff failure caused by line lengthening due to proximity effect.

Again, the development process removes the low molecular weight material with the result for negative resists being that the exposed material remains on the surface.

The preceding discussion was quite short to have covered such a complex group of chemical reactions. The main result to be drawn is that the process of molecular chain breakage (positive resists) is a more controlled process than chain linkage (negative resists) with the result that positive resists generally are capable of greater resolution than negative resists. For this reason, the work reported in this dissertation was done exclusively with the positive resist PMMA, since

it is the choice for fine work having a resolution limit of 0.1  $\mu\text{m}$ . In addition, PMMA is compatible with the techniques of liftoff and etching (wet and dry) which will now be discussed.

## B. LIFTOFF

The liftoff technique illustrated in Figure A.5 is used to fill in metal in a patterned resist layer. Once the resist has been patterned on a substrate and then developed to selectively expose the substrate, the resist side is coated with a metal layer (typically) by vacuum evaporation. Due to the electron scattering process during exposure, the sides of the developed resist tend to overhang the substrate. Thus, as the metal deposits on the surface, a natural separation occurs yielding a break in the metal layers on the substrate and on the resist. The entire substrate is now immersed in a solvent (an example for PMMA would be warm acetone) which dissolves the resist. It is important at this point to keep a flow of solvent on the surface so that the unwanted metal does not redeposit. The liftoff technique is thus very useful for making thin or narrow lines of metal. The main limitation of the liftoff technique is that the resist must be thicker than the desired metal layer. Usually a ratio of resist to metal thickness of 3:2 is sufficient to provide for successful metal edge breakage. The liftoff technique is not very good for making patterns in which the entire substrate is largely covered with metal due to the long exposure times required to do the patterns when filling in with the narrow e-beam. Instead, when using a positive resist to form small non-metal regions,

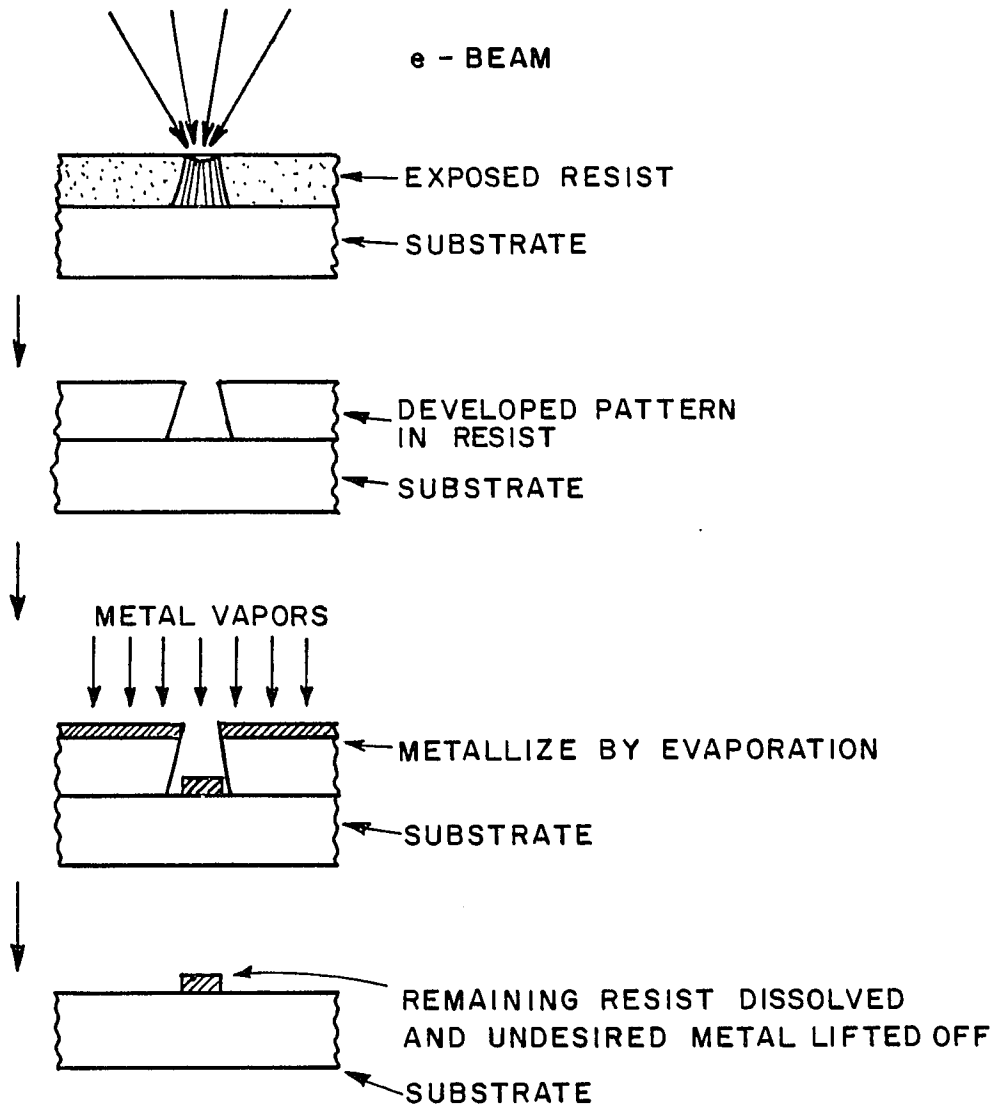


Figure A.5. Pattern formation by lift-off.

it is more practical to use an etching process to selectively remove the unwanted metal.

### C. ETCHING

In the etching process, the desired metal thickness is applied to the substrate and then the resist is applied and patterned (refer to Figure A.6). At this point, some material is brought into contact with the metal-resist side of the substrate to selectively remove the metal. Depending on the type of material used to remove the metal, the general etching process may be divided into two more specific cases, each of which has its advantages and limitations. The broad classes to be discussed here are (1) wet etching and (2) dry etching. The latter includes the two subclasses (a) plasma etching and (b) ion-milling.

#### 1. Wet Etching

Wet etching is the oldest of the pattern formation techniques and is the mainstay of the printed circuit board and large size integrated circuit technologies. This is due to its relative simplicity and low cost. Wet etching is accomplished by simply putting the substrate in a chemical bath which reacts with the metal. At this stage the requirements for the resist are fairly simple in that it must not react with the etchant. As long as the width of the metal line to be removed is much larger than the metal thickness, there are few problems. Problems arise, though, in micro-electronic work (which is similar to ours) when these dimensions become comparable. This is due to the



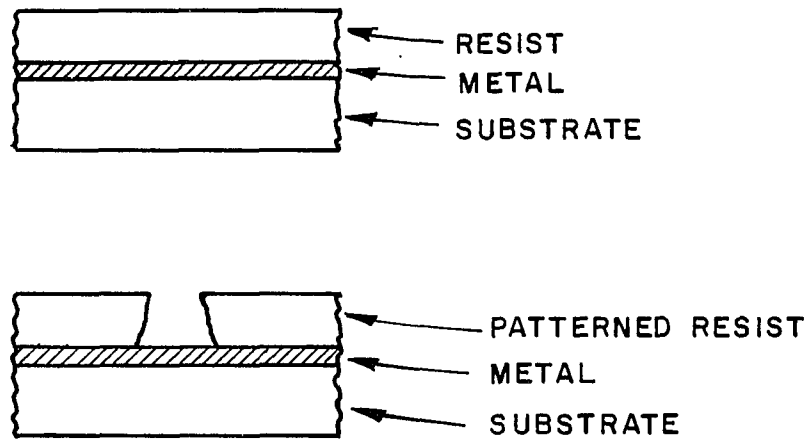


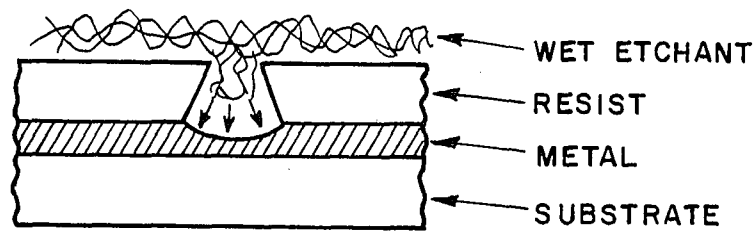
Figure A.6. First stages of etch processing for metal pattern formation.

isotropic or "equal in all directions" nature of the wet etch process which results in the undercutting of the metal beneath the resist. This is illustrated in Figure A.7. The results of undercutting are shown in Figure A.8 for an array of crossed slots in chrome. Note that the undercutting has not only caused the slots to broaden (which will raise the filter bandwidth) but has also caused the slots to lengthen (which will lower the filter center frequency).

## 2. Dry Etching

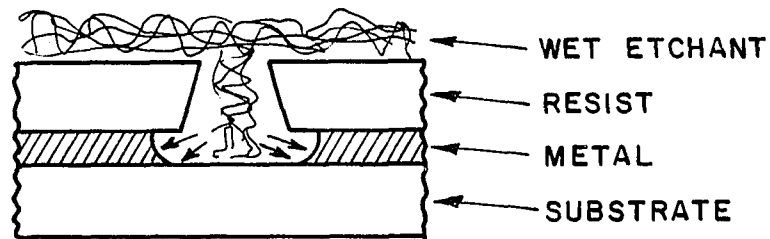
Another technique which has received considerable attention is the dry etching method known as plasma etching. In this method, the substrate is surrounded by an ionized cloud of a material which reacts with the metal layer. Common reactive species for metals are chlorine ions and fluorine ions produced by electrically decomposing carbon tetrachloride and carbon tetrafluoride, respectively. In addition, ionized oxygen as the reactive species is quite useful for general cleaning purposes such as removing resist which has been overheated or burned and will no longer dissolve in a solvent. The advantage of plasma etching is that it is not necessary to wet the surface to be etched. This can be a problem with some of the more viscous wet etchants when very small feature sizes are desired. Unfortunately plasma etching suffers from the same problem of isotropic etching that plagues wet etching, the result being undercutting.

Thus, to obtain good patterns on a surface by selectively removing material, it is necessary to use a technique which is anisotropic or



(a)

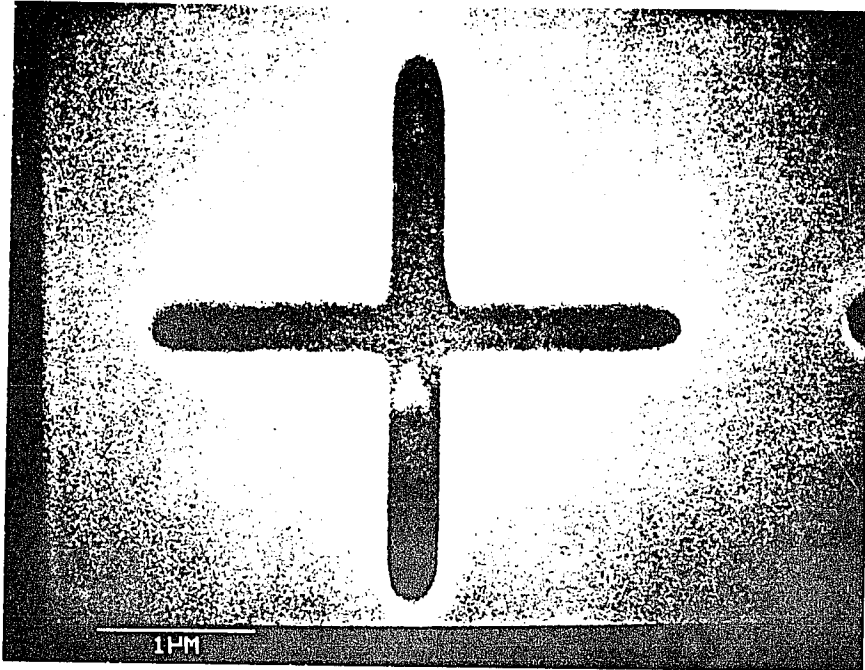
(a) Initial stages.



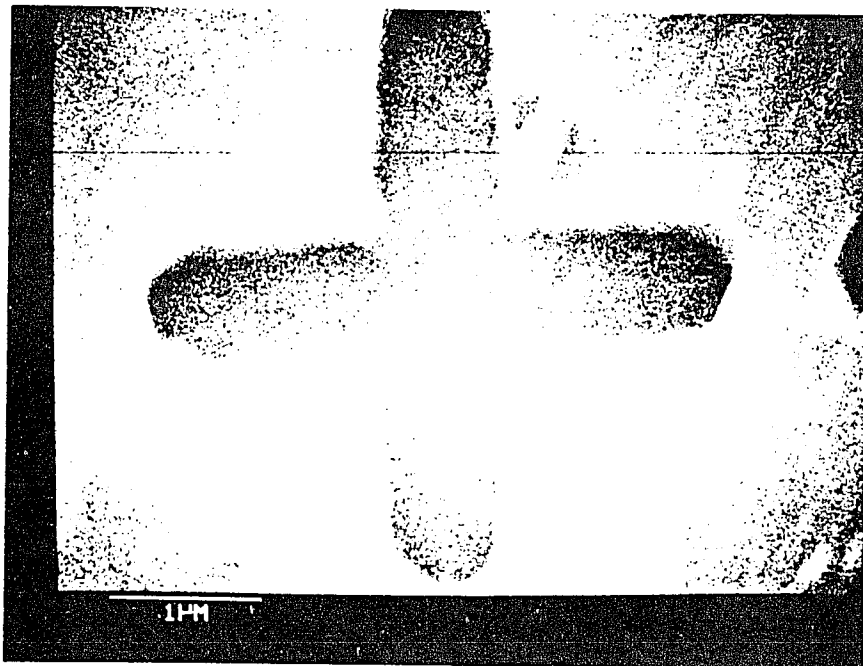
(b)

(b) Advanced stages showing undercutting.

Figure A.7. The wet etching process.



(a) Resist pattern.



(b) Final metal pattern showing line growth.

Figure A.8. Effects of wet etch undercutting, substrate #4.

has some preferential etching direction. This can be accomplished using two methods, one called reactive ion etching (RIE) and the other known as ion-milling. RIE is an advanced form of plasma etching which makes use of the ionized nature of the plasma cloud to accelerate the reactive ions toward the substrate thus giving them a preferred direction. The acceleration is produced by applying a bias field to the plasma cloud as shown in Figure A.9. This figure illustrates the bias arrangement for the case in which the reactive ions have a negative charge as is the case for chlorine and fluorine. The important parameters for RIE are the bias potential which controls the degree of anisotropy and differential etch rates between the resist and metal. It should be noted that the bias cannot usually become too high or the incident ions will actually bump or mill the surface resulting in a process called sputtering or ion-milling. This is a problem under normal RIE circumstances since the resist is usually softer in a mechanical sense than the underlying metal. If the resist can be made very thick (a problem if very fine lines are desired due to electron scattering) so as to overcome the differential etch rate problem between the resist and metal, then the ion-milling or sputtering can be a useful etching method. Often this is done using nonreactive ions such as argon. This can be advantageous since care in handling the reactive species is not necessary and since if there is no chemical etching there is also no undercutting.

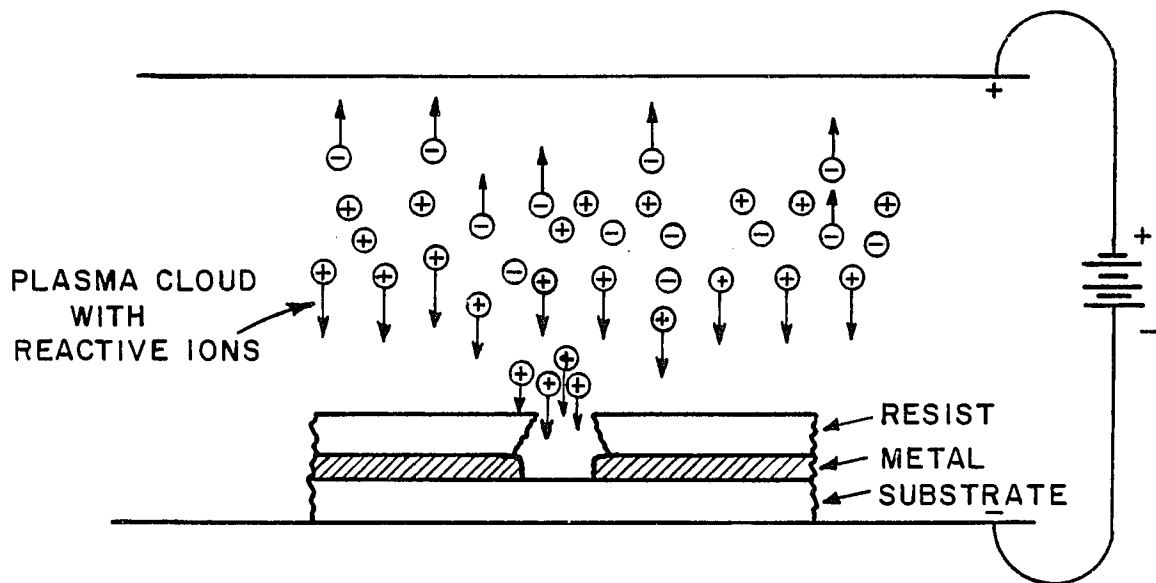


Figure A.9. Simplified schematic diagram of apparatus for reactive ion etching (RIE).

#### D. TECHNIQUES ACTUALLY USED AT THE NRRFSS

The facilities at the NRRFSS are fairly extensive and most methods in high resolution lithography are either currently available or under development. For construction of dipoles or similar elements, the liftoff technique was used exclusively with excellent results. Metal lines with widths as small as  $0.2 \mu\text{m}$  and as large as  $0.54 \mu\text{m}$  were made. The resulting length to width ratios for the dipoles were in the approximate range of 6:1 to 15:1. This range was good enough to show pronounced effects of element width on filter bandwidth.

Several etching techniques were tried for the construction of slots. RIE would have been the favored technique for this purpose but unfortunately this equipment was not yet working and the process well characterized during our visits to the NRFSS. Wet etching was attempted with the line growth results previously illustrated. In addition severe problems due to scratches in the calcium fluoride surfaces were noticed. This is shown in Figure A.10 for the case of chrome etched in Cyantek (a commercial chrome etching) as evidenced by the long scars running through the metal.

Plasma etching of the aluminum and chrome surfaces would have been desirable but the use of chlorine was not possible during our visits. The only plasma etchants then available were fluorine and oxygen, neither of which would etch aluminum or chrome. The last possibility was the use of an argon-ion mill. The only problem with this last technique is the low differential etch rate between the resist we used

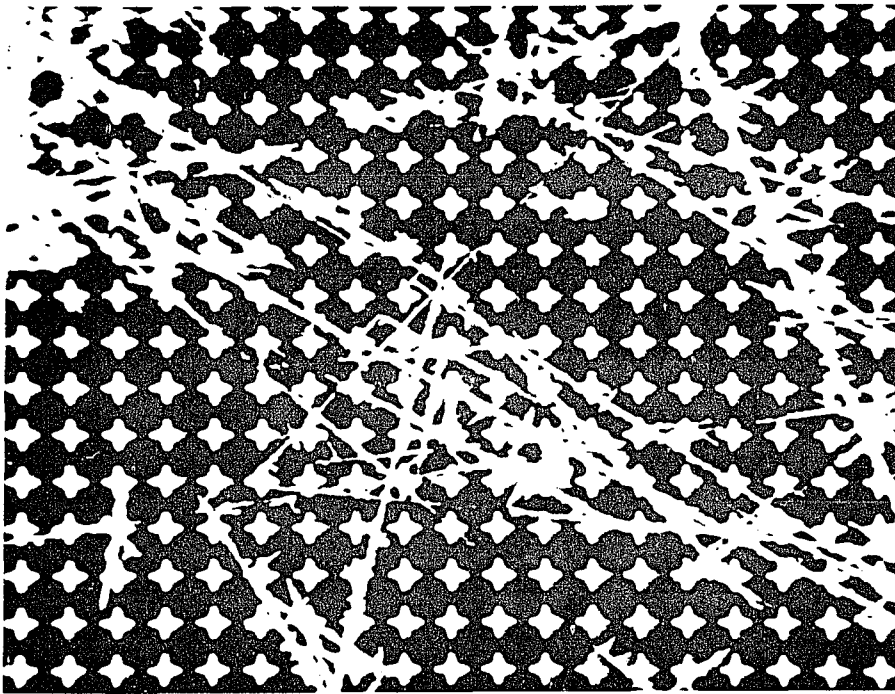


Figure A.10. Defects in chrome slots due to surface scratches in  $\text{CaF}_2$ .  
Substrate #3, back lighting, magnification  $\approx 1300$ .



(i.e., PMMA) and the two metals. To overcome this problem, a multi-level resist technique was developed by Mr. Brian Whitehead of the NRRFSS, which yielded satisfactory straight slots although not as good as expected using RIE.

The multi-level resist technique for ion-milling consisted of putting two additional layers between the metal layer and the resist layer to act as buffers for the milling process. This multiple layering is indicated in Figure A.11. The upper additional layer was a very thin evaporated coating of germanium which is patterned through the PMMA by plasma etching in disassociated carbon tetrafluoride. The underlying additional layer was a thick coating of Shipley AZ-1350J (a commercial high quality photo resist) which was baked at approximately 100°C for at least two hours. At this point, the photo-resist is simply a thick, relatively speaking, plastic layer useful only for buffering purposes. The photo-resist layer was patterned using an oxygen plasma etch. The results of the multi-level system just prior to ion-milling are shown in Figure A.12. Note that the oxygen plasma etch not only patterns the photo resist but also removes the PMMA.

The results using the multi-level resist technique with argon ion-milling of the metal surfaces for chrome (substrate #8) and aluminum (substrate #9) are shown in Figure A.13. It should be noted that the chrome slots are wider than the aluminum slots which may be attributed to the longer milling time required for the chrome. Milling time was determined by visual inspection under a microscope at approximately x1300 magnification when using transmitted light. The broadening of

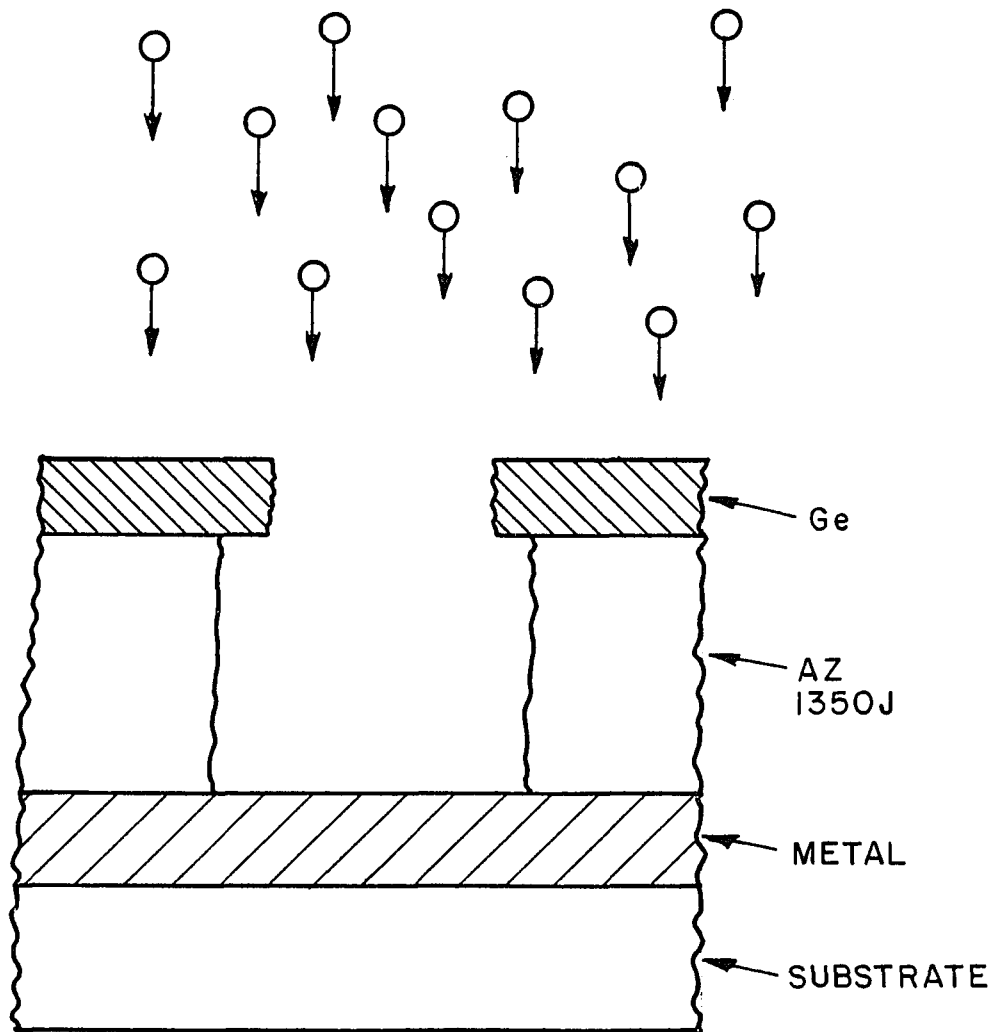
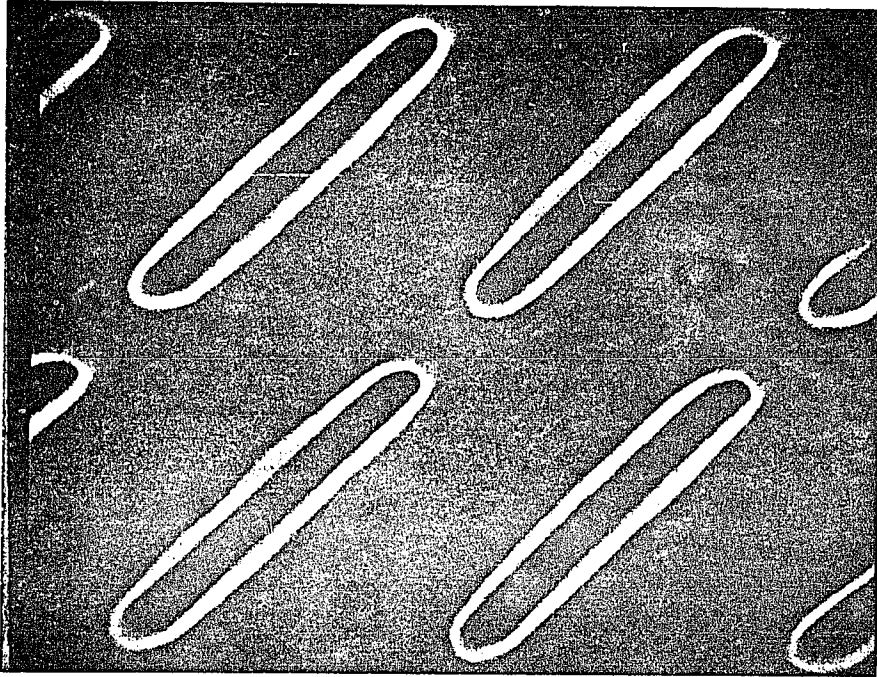
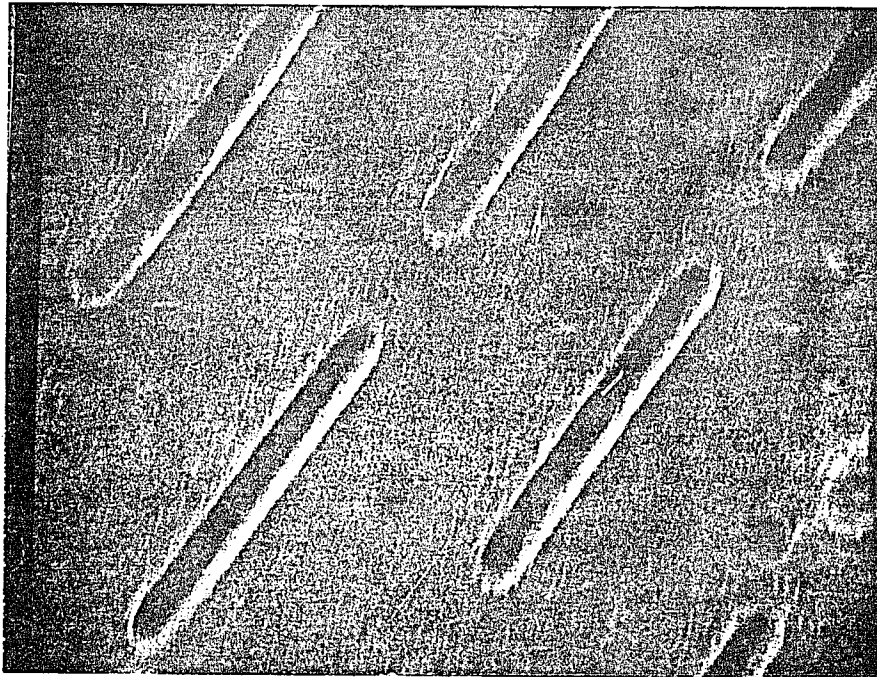


Figure A.12. Multi-level resist at the start of argon-ion milling.



(a) Chrome on S#8.



(b) Aluminum on S#9.

Figure A.13. Results of multi-layer resist patterning of long narrow slots.

the slots indicates that the multi-level resist was not completely successful in preventing line growth but is still better than wet etching (see Figures A.8 and A.10). These results were deemed sufficient as they were the best we could obtain, but future work using RIE as it becomes available should yield better results.

The use of all these different techniques and the many processing methods involved were highly influential in the use of calcium fluoride as a substrate material. The material grown via vapor phase techniques is reasonably hard (although not as hard as the hot press polycrystalline material) which makes it capable of being polished to a good surface quality. This point is important when you are laying down sub-micrometer patterns. In addition, the  $\text{CaF}_2$  chemical bond is quite strong resulting in a material which is practically insoluble in water and is not attacked by most solvents. Many different solvents are used in micro electronics for substrate cleaning as well as in the liftoff process.  $\text{CaF}_2$  is also quite resistant to most acids and bases which are used in wet etching aluminum and chrome. Due to the strong  $\text{CaF}_2$  chemical bond, we did not expect the material to be attacked by the reactive species used for plasma etching or RIE. Lastly, the mechanical hardness of  $\text{CaF}_2$  (about the same as a penny for the polycrystalline IRTRAN 3) makes it resistant to the mechanical erosion process of ion-milling. These points are critical since after processing to leave the desired metal shapes, we desire the substrate to be optically transmitting and not diffuse.

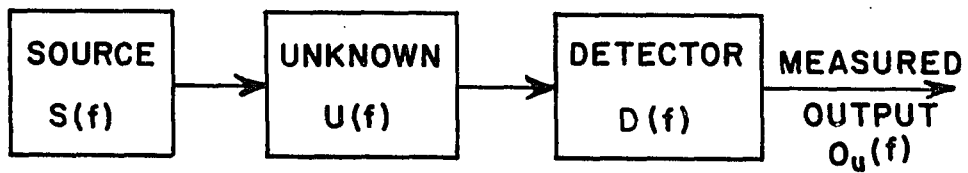
## APPENDIX B

### MID-INFRARED MEASUREMENTS

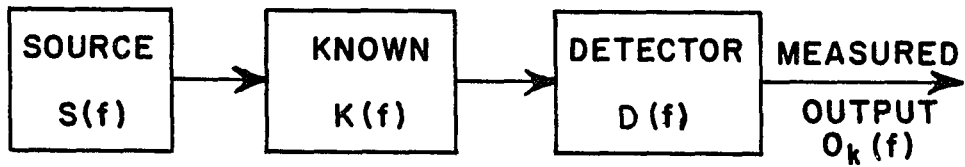
The periodic surfaces described and built during this study are resonant at wavelengths shorter than 10  $\mu\text{m}$ , which corresponds to frequencies greater than 1000  $\text{cm}^{-1}$  or 30,000 Ghz. Thus, the frequency range of interest is much too high to allow measurement of the filter characteristics by standard microwave techniques. However, this frequency range (approximately 700  $\text{cm}^{-1}$  to 2700  $\text{cm}^{-1}$ ) is easily within the capabilities of an infrared Fourier transform spectroscopy (FTS) system available at The Ohio State University ElectroScience Laboratory. In fact, the use of this system was highly influential in the choice of  $\text{CaF}_2$  as a substrate material which further influenced the choice of desired resonant frequencies. The reason for this was that the best available detector for the FTS system at the start of this study was a liquid nitrogen cooled Mercury-Cadmium-Tellurium (MCT), photo-conductive device, doped for maximum sensitivity near 8  $\mu\text{m}$ . The sensitivity of this MCT detector drops off rapidly at wavelengths greater than 12  $\mu\text{m}$  and therefore it is fairly well matched to the infrared sharp cutoff of

CaF<sub>2</sub>. In addition, the use of CaF<sub>2</sub> eased alignment of the measurement system due to its visible transparency. The MCT detector is also useful to wavelengths near 2  $\mu\text{m}$  although its output becomes rather noisy. In any event, these problems were avoided by making the resonant elements as large as possible to ease construction problems which pushed the region of interest into ranges where the detector output was satisfactory. This was also done to investigate the effects of dielectric loss on filter performance. The rest of this appendix will outline the important aspects of FTS spectroscopy which affected this study. In addition, two slightly different systems which were used to obtain transmission spectra of the mid-infrared filters will be presented.

FTS spectroscopy has its basis in linear system theory and the concept of a frequency dependent transfer function. The utility of the transfer function concept is that individual units may be strung together and the transfer function of the system is just the product of the individual transfer functions. This also provides a method for determining the transfer function of an individual unit by a ratio technique. This process consists of measuring the system output spectrum with and without the unknown element in the system. The resulting spectra are ratioed to obtain the transfer function of the unknown. This process is illustrated in Figure B.1. Note in Figure B.1 that when the unknown is taken out of the system it is replaced by a known object. Often it can be assumed that the known has unity transfer



(a)



(b)

Figure B.1. Illustration of two measurements required for FTS. System with unknown device in place and the system with the unknown replaced by a known.

function,  $k(f)$ , over the frequency range of interest, although this is not always possible. An example of the latter is when a reflected signal is desired and the known must also be a reflector. For the system in Figure B.1, the transfer function for the unknown is obtained from the ratio:

$$u(f) = \left[ \frac{O_u(f)}{O_k(f)} \right] k(f) \quad (\text{B.1})$$

where multiplication by the known function,  $k(f)$ , has been included for completeness. Note that for an accurate recovery of  $u(f)$ , Equation (B.1) implies that  $O_k(f)$  and  $k(f)$  have no zeroes within the frequency range of interest.

Figure B.2 shows a simplified optical FTS system which is similar to the systems actually used. This FTS system consists of five essential units which are: 1) a broadband optical source, 2) a Michelson interferometer, 3) the sample region, 4) an optical detector and 5) a digital computer. The computer is the only non-optical element of the FTS system and is responsible for system control, data collection and data processing. The data processing includes not only the simple process given by Equation (B.1) but also inversion of a Fourier transform which will be derived in the following discussion of the optical elements.

The source in the infrared FTS system is typically a broadband radiator such as a global made of silicon carbide. This global, which is electrically heated by conduction, radiates much like a blackbody



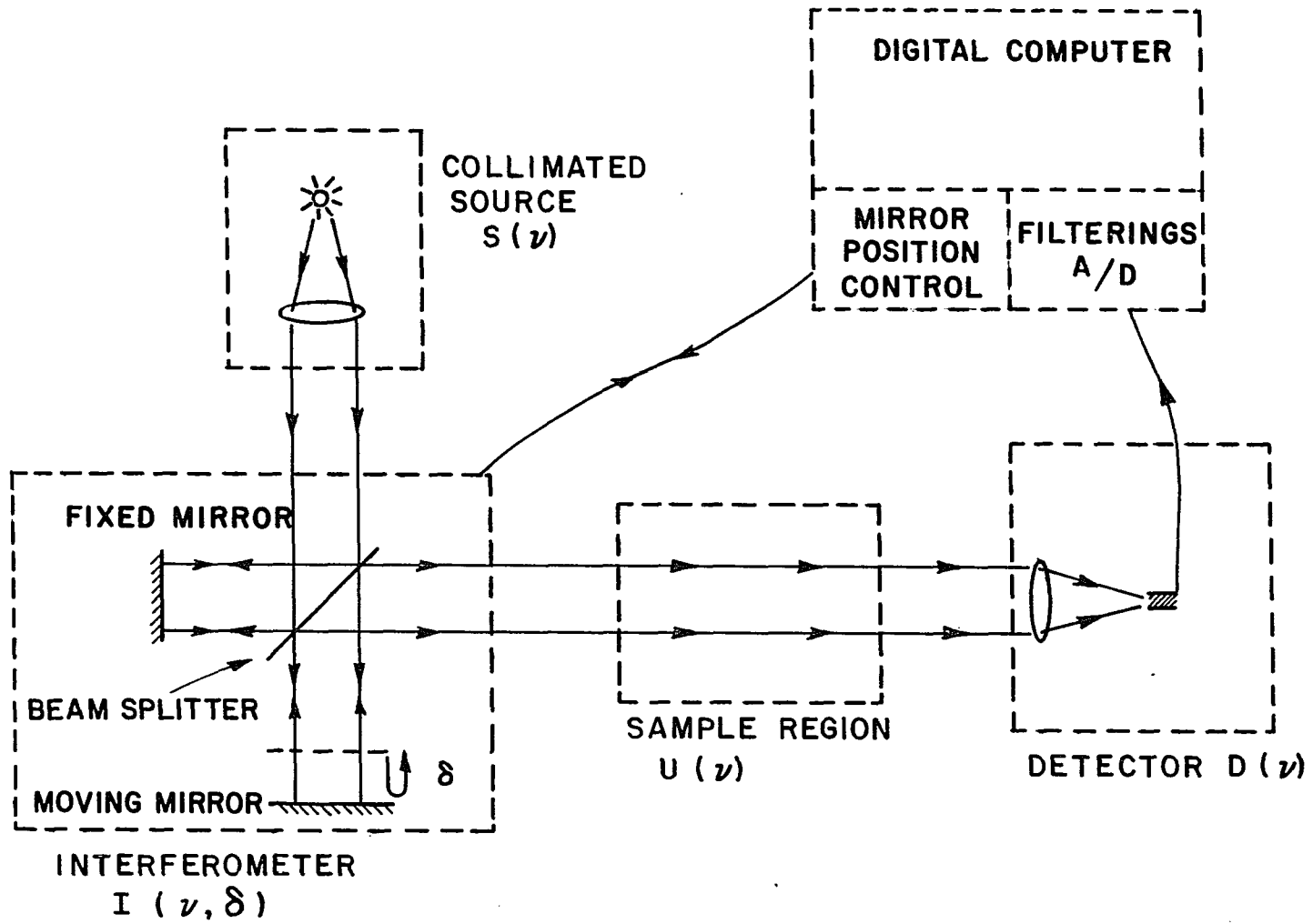


Figure B.2. Optical Fourier transform spectroscopy (FTS) system.

by the simple virtue that it is hot. It should be pointed out that the globar is a simple, high frequency, broadband noise generator and is quite analogous to the noise generators which are sometimes used at audio and microwave frequencies. Since the output spectrum of the source, SCF, varies with its temperature, it is essential that the source power supply be stable. The only other requirement for the source is that it not have any deep nulls within the frequency range of interest to satisfy the requirement on  $O_k(f)$  previously mentioned. For the globar source, it should be noted that the output is incoherent with random polarization.

The heart of the FTS system is the interferometer which is used to produce an output beam consisting of a reference beam added to a phase modulated beam. The phase modulation is obtained by altering the length of one of the interferometer legs by scanning a mirror in a direction parallel to the beam (see Figure B.2). The result is that the interferometer has a transfer function,  $I(f, \delta)$ , which depends on both the frequency (no specified units) and the directed displacement of the moving mirror from equilibrium. Equilibrium at a fixed frequency is defined as the mirror position where the optical path lengths through the two legs are identical. The resultant transfer function is

$$I(\nu, \delta) = I_F(\nu) + I_M(\nu) e^{-j\beta\delta} \quad (\text{B.2})$$

where

$$\beta = \frac{2\pi}{\lambda} = 2\pi\nu \quad , \quad (\text{B.3})$$

$\lambda$  is the free space wavelength,  $\nu$  is the frequency in inverse wavelengths, and  $\delta$  is path length difference from equilibrium which is twice the mirror displacement for this instrument. In the infrared,  $\nu$  is typically given in "wavenumbers" which has units  $\text{cm}^{-1}$ . In Equation (B.2),  $I_F(\nu)$  is the fixed mirror leg or reference beam transfer function and  $I_M(\nu)$  is the moving mirror leg or modulated beam transfer function at the equilibrium position. It would be desirable to have  $I_F(\nu)$  and  $I_M(\nu)$  equal since this would yield 100% modulation and a maximum output signal. It is relatively simple to make the mirrors alike to within experimental errors, but problems in beam splitter construction make differences in  $I_F(\nu)$  and  $I_M(\nu)$  inevitable. For reasons of stability and to obtain good optical surfaces, beam splitters in the infrared are typically made in a sandwich arrangement as in Figure B.3.

Unfortunately, it is impossible to make the support layers identical in terms of thickness which when coupled with the dispersive index of refraction of infrared materials results in a nonlinear phase error between the two legs. The process of "fixing" this inequity is called "phase correction" and will be discussed when we look at the detector output. For purposes of discussion in deriving the output of our simplified FTS system define,

$$I_F(\nu) \equiv I_0(\nu) , \quad (\text{B.4})$$

$$I_M(\nu) \equiv I_0(\nu)e^{-j\beta\Delta} \quad (\text{B.5})$$

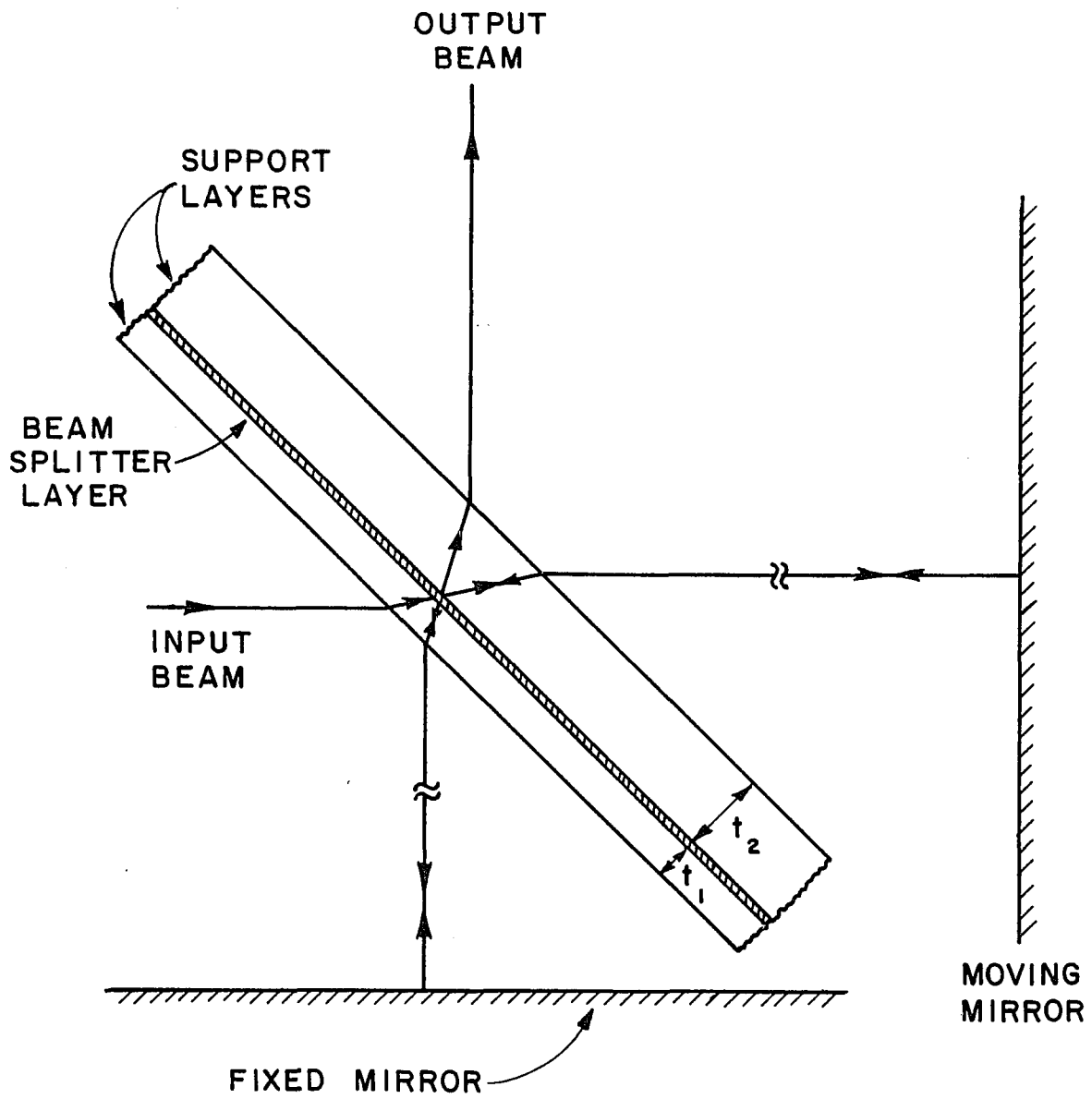


Figure B.3. Practical beam splitter construction. The difference in support layer thickness ( $t_1$  and  $t_2$ ) is exaggerated.

and

$$\Delta = 2(t_2 - t_1)n(\nu) \quad . \quad (B.6)$$

In Equation (B.6),  $\Delta$  is the differential optical distance through the interferometer beam splitter which will cause a nonlinear phase error if the index of the support layers,  $n(\nu)$ , is not constant and the layers are of different thicknesses. The thicknesses  $t_1$  and  $t_2$  are indicated in Figure B.3.

The next important section of the optical train is the sample or unknown region, which is assigned a transfer function,  $u(\nu)$ , that we wish to determine. As previously stated, it is assumed that the unknown may be replaced by a known without affecting the other elements in the system. For transmission measurements, the known may be a region of vacuum which has unity transmission (it is assumed that the sample is thin and does not walk the beam). Note that in the infrared, normal atmosphere will not usually suffice due to the strong infrared absorption lines of water vapor and carbon dioxide. In fact, due to these strong absorption lines, it is usually necessary to have most of the optical train in vacuum or in a region flushed with nitrogen. For reflection measurements, metallic mirrors may be used as knowns with the added problem of accurately repositioning the beam for both measurements. In addition, few mirrors have near perfect reflectance over broad frequency ranges so that the calibration procedure (multiplication by  $k(f)$  as in Equation (B.1)) must actually be done.

Thus, transmission measurements are inherently simpler and are the only type reported in this study.

The last major region of the optical train is the detector and any associated light gathering optics. This section of the system is assigned a transfer function,  $D(\nu)$ , which relates incident field strength to the detector output. Actually, the detector is a square-law device with an output which is linearly proportional to the incident power, integrated over all frequencies. Thus the voltage output may be written as

$$v(\delta) = \int_{-\infty}^{\infty} |S(\nu)I(\nu, \delta)U(\nu)D(\nu)|^2 d\nu \quad . \quad (\text{B.7})$$

Using Equations (B.1) through (B.6) this becomes

$$v(\delta) = 2 \int_{-\infty}^{\infty} M(\nu) d\nu + \text{Re} \left\{ \int_{-\infty}^{\infty} M(\nu) e^{-j2\pi\nu\Delta} e^{-j2\pi\nu\delta} d\nu \right\} \quad (\text{B.8})$$

where

$$M(\nu) \equiv |S(\nu)I_0(\nu)U(\nu)D(\nu)|^2 \quad . \quad (\text{B.9})$$

Since the mirror is usually scanned linearly with time, we may also think of  $v(\delta)$  as a simple function of time. With this reasoning, the first integral in Equation (B.8) may be recognized as a DC component which is usually removed by high pass filtering. The resulting filtered detector output is referred to as the "interferogram" and is given by

$$v_f(\delta) = \text{Re} \left\{ \int_{-\infty}^{\infty} [M(\nu)e^{-j2\pi\nu\Delta}]e^{-j2\pi\nu\delta}d\nu \right\} \quad (\text{B.10})$$

where any filter effects are included in the detector response. Note that the frequency function  $M(\nu)$  is the term we actually desire for use in our ratio technique. The result will then be a ratio of output to input power. Thus, for transmission and reflection measurements, we will obtain the sample transmittance and reflectance, respectively.

Due to well known restrictions on transfer functions for physical observables, the function  $M(\nu)$  is symmetric about  $\nu=0$ . Thus, for the ideal interferometer (i.e.,  $\Delta \equiv 0$ ), Equation (B.10) simplifies to

$$v_f(\delta) \Big|_{\Delta \equiv 0} = \int_{-\infty}^{\infty} M(\nu)e^{-j2\pi\nu\delta}d\nu \quad (\text{B.11})$$

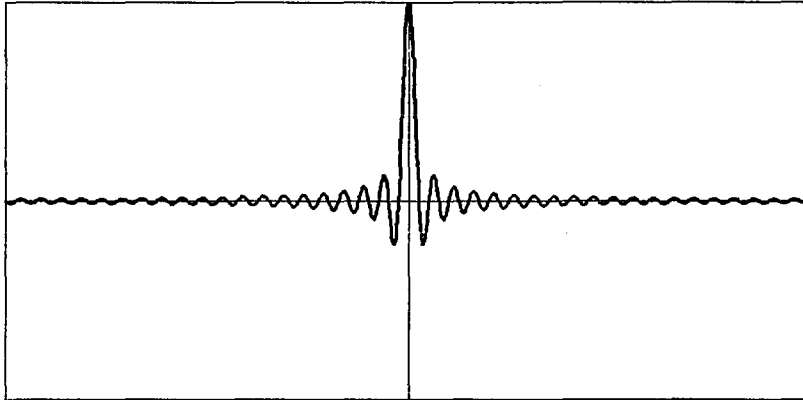
which may be recognized as a Fourier Transform (FT). Under this simplification, we can obtain  $M(\nu)$  directly using the Inverse Fourier Transform (IFT)

$$M(\nu) = \frac{1}{2\pi} \int_{-\infty}^{\infty} v_f(\delta) \Big|_{\Delta \equiv 0} e^{j2\pi\nu\delta}d\delta \quad (\text{B.12})$$

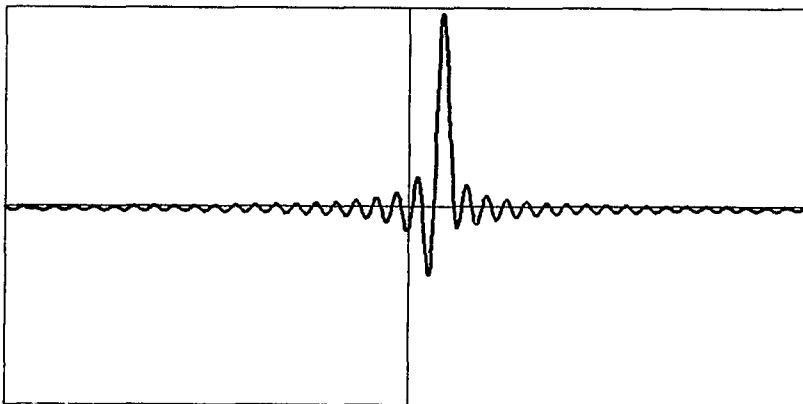
It is interesting to point out that for the ideal interferometer we would expect the interferogram to be symmetric about  $\delta=0$  which can be shown in Equation (B.11) by using a simple change of variable.

Unfortunately, the ideal interferometer is never encountered due to the aforementioned phase error (i.e.,  $\Delta \neq 0$ ). The effect of phase error is to produce an asymmetry in the interferogram. This effect is illustrated in Figure B.4 in which a synthetic interferogram (modelled as a simple  $\sin(x)/x$  function) and a distorted interferogram are presented. The distorted curve (Figure B.4(b)) was generated by transforming the undistorted curve (Figure B.4(a)), adding small amounts of phase shift to the spectrum and then taking the real part (per Equation (B.10)) of the inverse transform. If the phase shift is linear, then the distorted interferogram is simply a shifted version of the undistorted one. However, the asymmetry of the central maximum is caused by phase shifts which are non-linear in frequency (in Figure B.4(b), modelled by quadratic phase term due to a linearly decreasing index with frequency). This dispersive nature is characteristic of all dielectrics in the infrared. The result of all of this is that taking the IFT of  $v_f(\delta)$  does not yield  $M(\nu)$  but a distorted version of it. Several techniques have been developed to approximately correct for this error and all come under the term "phase correction". All these techniques rely on taking a spectrum of a narrow region about the interferogram maximum which is referred to as the centerburst. These techniques will not be discussed here since the details of FTS are beyond the scope of this work, however, the interested reader is directed to a review in [55].





(a). Synthetic interferogram  $(\sin(x)/x)$ .



(b). Distorted interferogram produced by adding linear and quadratic phase delay to the ideal interferogram spectrum.

Figure B.4. Effects of phase error.

Two additional aspects of FTS systems will now be briefly discussed since they affect the maximum allowable frequency and the frequency resolution. Since all FTS systems make use of sampled data, according to the sampling theorem [56] there is a maximum allowable optical frequency bandwidth. For ease in calculation, this bandwidth is assumed to run from  $0 \text{ cm}^{-1}$  to some maximum. This limit is well known as the Nyquist frequency which allows a maximum single-sided bandwidth of one-half the sampling frequency. In the system actually used, a Helium-Neon laser interferometer which is coaxial with the infrared interferometer is used to control the sampling. The output of the He-Ne interferometer is a simple sinusoid which triggers the sampling unit at each positive going zero crossing (i.e., each time the mirror travels one-half the He-Ne wavelength). Thus, the effective sampling rate is equal to the frequency of the stabilized He-Ne laser which yields a maximum frequency of approximately  $7899 \text{ cm}^{-1}$ . It is required that no frequencies above this propagate through the system or aliasing will result which irrecoverably corrupts the output spectrum. The system bandwidth is protected against aliasing by use of a germanium beam splitter layer sandwiched between potassium bromide layers. Since the germanium has a high frequency cutoff around  $7000 \text{ cm}^{-1}$ , no problems occur.

The other aspect of FTS systems relates a limit on the interferometer mirror travel or stroke to the spacing between frequency samples (since a Fast Fourier Transform (FFT) is used in processing).

This places an upper limit on the frequency resolution of the interferometer (high resolution implying small frequency spacing). An excellent description of this relation is given by Hawkins [55] with the result that resolution is inversely proportional to the interferometer stroke. For the system used, the limit is approximately  $0.04 \text{ cm}^{-1}$  [57], which is much greater than needed to observe the infrared filter characteristics (these spectral features are typically greater than several hundred wave numbers in width). Thus the effects of high resolution limits are not of great importance in this study. Data of high resolution was only taken in one instance to observe the etalon behavior of the  $\text{CaF}_2$  substrates which exhibit a ripple period of about  $3 \text{ cm}^{-1}$ . Each data run for high resolution typically required about 4 hours with two runs (known and unknown) required to obtain a filter spectra having adequate signal to noise ratios (improved by co-adding multiple interferograms). For typical low resolution data, usually only a few minutes per run were required.

#### A. f2 TRANSMISSION MEASUREMENT SYSTEM

Figure B.5 diagrams the first system (referred to as the "f2 system" or the low f# system) used to measure transmittance spectra of the infrared filters. As mentioned before, the light in this system is incoherent with random polarization. In Figure B.5, all spherical mirrors are labelled with their focal lengths ( $f_\lambda$ ) in centimeters. Flat mirrors are labelled with a capital "F". All lenses are labelled with f#, focal length and material.

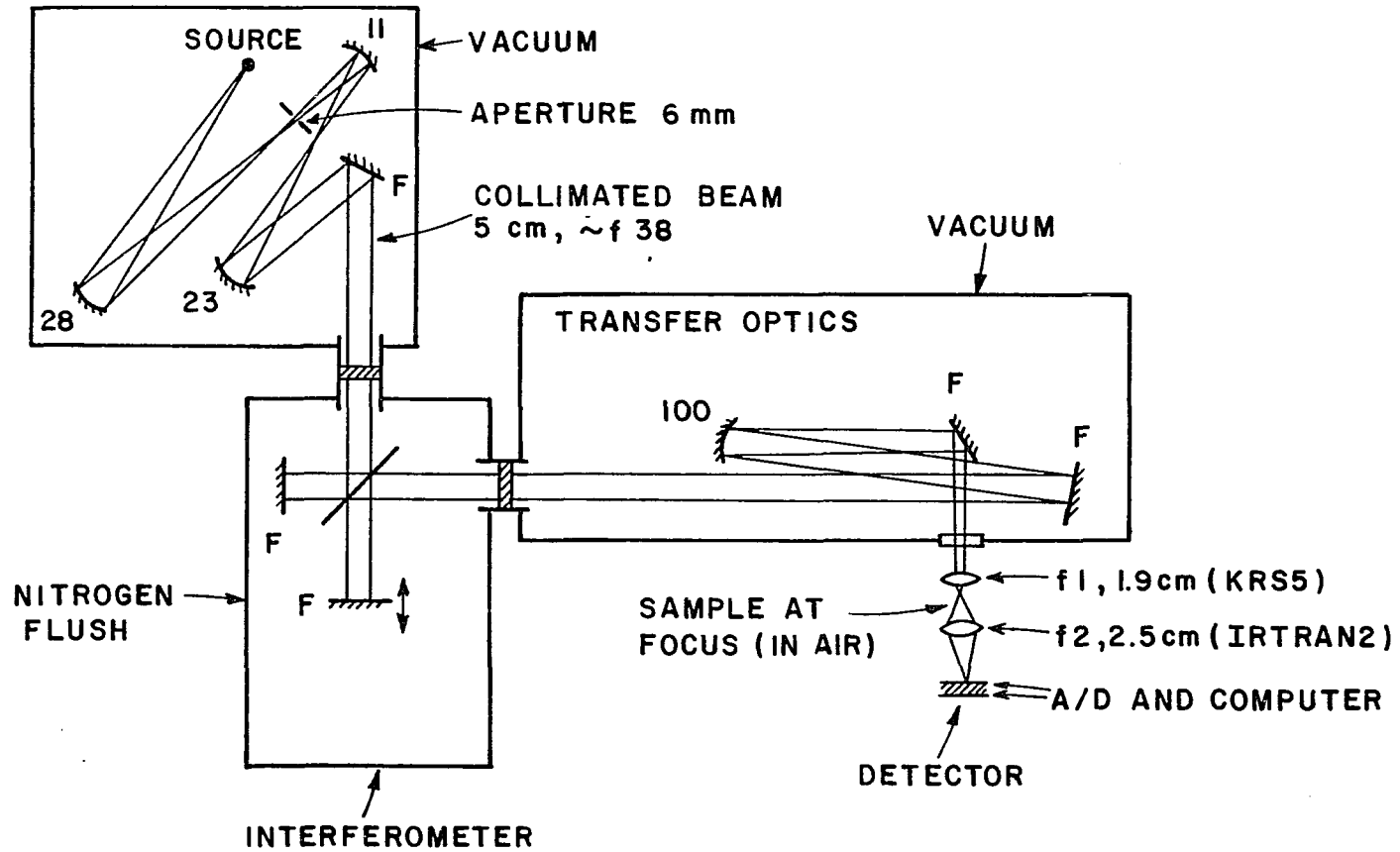


Figure B.5. f<sub>2</sub> transmission measurement system.

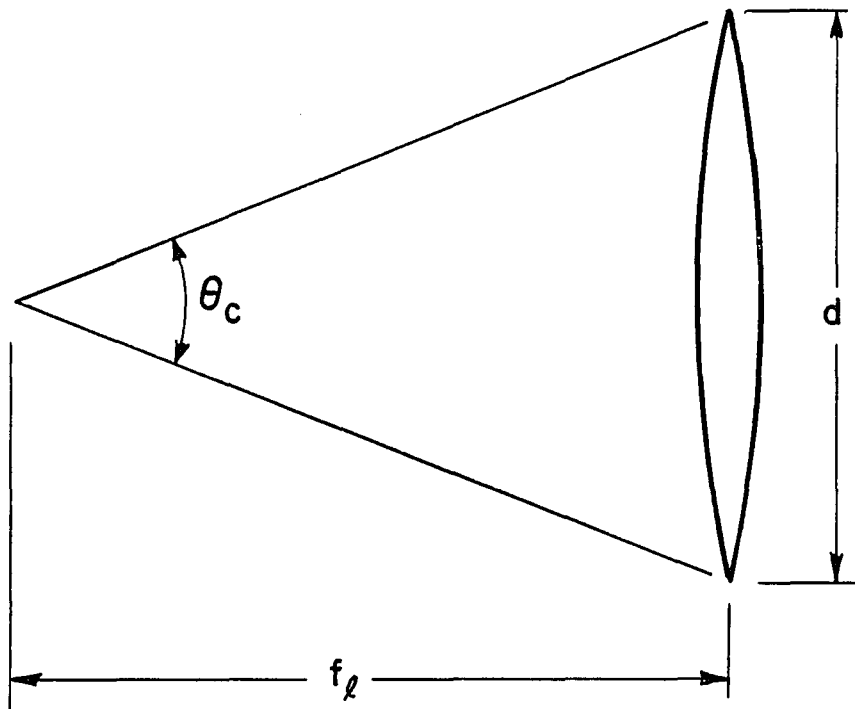
The source box in Figure B.5 was designed [58] specifically to feed the interferometer with a collimated, 5 cm diameter beam (the usable interferometer aperture). The beam diameter is defined by the 28 cm mirror which also serves as the aperture stop (10 cm diameter). The degree of beam collimation is given by its  $f\#$  which equals the ratio of the collimating mirror focal length to the field stop diameter. This is taken to be the physical aperture diameter indicated in Figure B.5 since this is where the source is imaged and it is re-imaged (1:1) in front of the collimating mirror. For the low resolution measurements, a 6 mm aperture (as indicated in Figure B.5) was used, yielding an output beam collimation of  $f38$ . For the few high resolution measurements, a 1 mm aperture was used yielding an  $f230$  beam. It should be pointed out that the source box was evacuated to eliminate absorption lines due to carbon dioxide and water vapor.

The interferometer and associated computer used in this system was a Nicolet Series 7000 system which is commercially available. This instrument has an inherent resolution limit of  $0.035\text{ cm}^{-1}$  although this capability was seldom used. Typically, data of  $1\text{ cm}^{-1}$  resolution was taken and then numerically averaged to lower the data noise level. Since this instrument uses nitrogen air bearings to support the moving mirror, it is not possible to evacuate the box containing it. Instead, the box is kept under a slight positive pressure with leakage from the air bearings to maintain a dry nitrogen flush. Again, this limits absorption by carbon dioxide and water vapor.

The last elements of the optical train prior to the sample are a mirror ( $f_e = 100$  cm) and a KRS-5 lens. These components were used to reduce the size of the interferometer output beam from 5 cm to something that would go through the samples (minimum sample diameter was approximately 2.8 mm). This was done to improve signal to noise in the measurements at the expense of a low  $f\#$  in the vicinity of the samples. Convergence of the rays in the sample region is estimated at  $f2$  (hence the reference to system name). The cone angle  $\theta_c$  as shown in Figure B.6 is given by

$$\theta_c = 2 \tan^{-1} \left( \frac{1}{2f\#} \right) . \quad (B.13)$$

For the  $f2$  estimate (best case), this yields an angle of  $28^\circ$ . As a result, many of the rays impinging on the surface are coming from well off normal (up to  $14^\circ$ ) yielding a poor approximation to a plane wave. Even though data were taken with this system and are reported herein and in a recent paper [59], a better system was desired in terms of approximating plane wave characteristics. This is done by increasing the  $f\#$  of the converging optics around the sample. In addition, it was desired to keep all the optics inside the transfer optics box which can be evacuated to minimize atmospheric absorption.



$$f \# = \frac{f_l}{d}, \theta_c = 2 \text{TAN}^{-1} \left( \frac{1}{2f \#} \right)$$

Figure B.6. Relation between cone angle and f#.

## B. f8 MEASUREMENT SYSTEM

A system which better approximates plane wave incidence on the sample is shown in Figure B.7. This system is referred to as the "f8 system" or the high f# system as a result of a nominal 5 cm diameter beam and a focusing mirror with a 40 cm focal length. Note that the f8 system results in a cone angle of approximately  $7.2^\circ$  which is reasonably good. Ideally, a higher f# would be desired but limitations on spot size at the focus prevented this. The focus spot size is given by the product of the source aperture size and the system magnification. System magnification is given by the ratio of focusing mirror focal length (here, 40 cm) to collimating mirror focal length (fixed at 23 cm) yielding a magnification of approximately 1.7. Thus, using the smallest source aperture of 1 mm diameter, we would ideally have a 1.7 mm focus spot. This is quite a bit smaller than the minimum sample diameter of 2.8 mm, however it allows some discrepancies in sample placement. In addition, aberrations in the optical system increase the actual spot size above the ideal 1.7 mm. Thus, the use of the f8 system is viewed as a good compromise between producing an accurate plane wave illumination and in putting maximum signal through the sample.



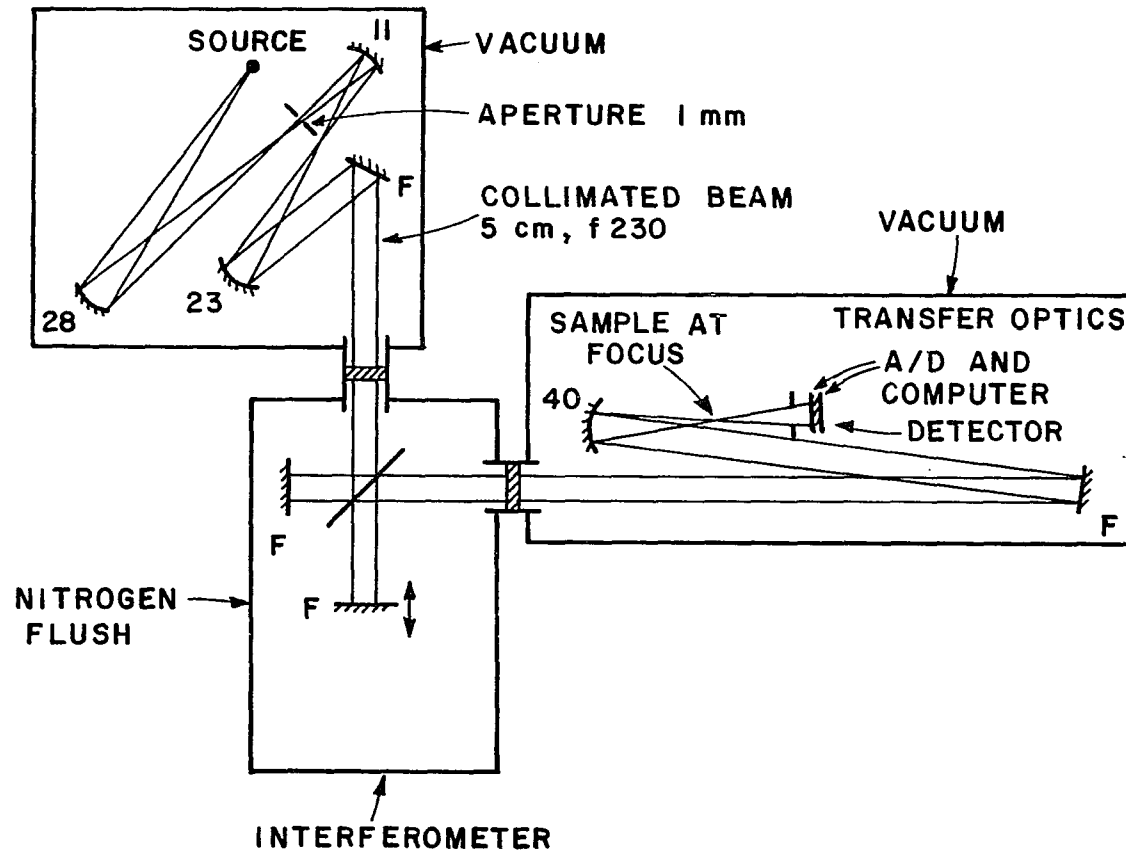


Figure B.7. f8 transmission measurement system.

## APPENDIX C

### MID-INFRARED PROPERTIES OF CALCIUM FLUORIDE

The primary reason for using calcium fluoride ( $\text{CaF}_2$ ) as the initial substrate material for the mid-infrared periodic surfaces is its excellent optical properties in this region of the electromagnetic spectrum.  $\text{CaF}_2$  has an optical passband which extends from the near-ultraviolet to the mid-infrared (infrared sharp cutoff at approximately  $12 \mu\text{m}$  [60,61]). Throughout this passband  $\text{CaF}_2$  has a high transmittance, typically exceeding 90%. This high transmittance is indicative of a low index of refraction which in this region varies between approximately 1.3 and 1.4 [60,61]. As explained elsewhere, a low index is advantageous for our designs since it allows the resonant elements to be as large as possible for a desired resonant frequency. Also, the extension of the passband from the infrared through the visible facilitates alignment of the substrates for measurement purposes. Alignment of visibly opaque substrates might be difficult for a finite sized interrogating beam and device patches kept small to minimize time on the electron beam microfabricator. In addition,  $\text{CaF}_2$

also has good mechanical strength and chemical properties which make it compatible with the techniques used in the construction of micro-electronic devices (see Section A on the construction of the resonant metallic elements).

In order to carry out an analysis of any periodic surface, we need to characterize the electromagnetic properties of any dielectrics involved. For a sometimes lossy (depending on frequency) nonmagnetic dielectric such as CaF<sub>2</sub>, this information is contained in the complex relative permittivity,  $\tilde{\epsilon}_r$ , or the complex index of refraction,  $\tilde{n}$ , which are related by

$$\tilde{\epsilon}_r = (\tilde{n})^2 . \quad (\text{C.1})$$

These parameters, which are not constant but vary slowly with frequency in the mid-infrared, are typically separated into real and imaginary parts as [62]:

$$\tilde{\epsilon}_r = \epsilon_r' - j\epsilon_r'' \quad (\text{C.2})$$

$$\tilde{n} = n - jk . \quad (\text{C.3})$$

In (C.3),  $n$  is the standard index of refraction (or just index) and  $k$  is the extinction coefficient which accounts for propagation loss. For a lossy material, both  $\epsilon_r''$  and  $k$  are positive. The rest of this section will be concerned with obtaining approximate models for  $n$  and  $k$  for CaF<sub>2</sub> in the mid-infrared.

From [61], a dispersion formula (after Sellmeier [63]) for the index of CaF<sub>2</sub> is given as:

$$n^2 + 1 = \frac{0.56788\lambda_0^2}{\lambda_0^2 - 0.0502306^2} + \frac{0.4710914\lambda_0^2}{\lambda_0^2 - 0.1003909^2} + \frac{3.8487723\lambda_0^2}{\lambda_0^2 - 34.649040^2} \quad (\text{C.4})$$

where  $\lambda_0$  is the free space wavelength in microns. Equation (C.4) is said to be valid to five significant figures in the range  $1.3 \mu\text{m} < \lambda_0 < 9.7 \mu\text{m}$ . In this dissertation, it is assumed that (C.4) is approximately valid in our range of interest down to a frequency of about  $750 \text{ cm}^{-1}$ . This corresponds to our frequency for the minimum detectable transmitted signal (about 1% or -20 dB) of a CaF<sub>2</sub> flat having a thickness of 1 mm (see Figure C.2). For clarity, note that the free space wavelength,  $\lambda_0$ , in micrometers and the frequency,  $f$ , in wave numbers ( $\text{cm}^{-1}$ ) are related by

$$f \times \lambda_0 = 10^4 \quad . \quad (\text{C.5})$$

Unfortunately, no expression or model for the extinction coefficient of CaF<sub>2</sub> could be found which is valid over our region of interest, although some limited data is available in the  $10 \mu\text{m}$  to  $80 \mu\text{m}$  region [64]. For our purposes, a highly exact model for the extinction coefficient is not necessary. Therefore, some rather simple approximations may be used to obtain a model for  $k$ . This may be done by using a model for the transmittance of a dielectric slab and measured data for two slab thicknesses.

For normal incidence, the transmitted field of a dielectric slab (see Figure C.1.) having thickness  $d$  is

$$E^0 = E^i \tau_1 \tau_2 e^{-\gamma d} \{ 1 + (\rho e^{-\gamma d})^2 + (\rho e^{-\gamma d})^4 + \dots \} \quad (C.6)$$

where the first term represents the directly transmitted field and succeeding terms represent internally reflected and then transmitted fields. For low index materials such as  $\text{CaF}_2$ , the reflected fields are relatively weak. Furthermore, if there is any appreciable loss, the reflected terms become even less significant and the transmitted field may be approximated using only the first term in Equation (C.6). Thus, to first order

$$E^0 \approx E^i \tau_1 \tau_2 e^{-\gamma d} \quad (C.7)$$

where the propagation constant,  $\gamma$ , is given by

$$\begin{aligned} \gamma &= j\omega \sqrt{\mu_0 \tilde{\epsilon}} \\ &= j \frac{2\pi}{\lambda_0} \tilde{n} \\ &= j \frac{2\pi}{\lambda_0} (n - jk) \quad . \end{aligned} \quad (C.8)$$

The transmittance of a slab is defined in terms of the ratio of output intensity to the incident intensity. Thus, to first order the transmittance may be approximated using (C.7) as

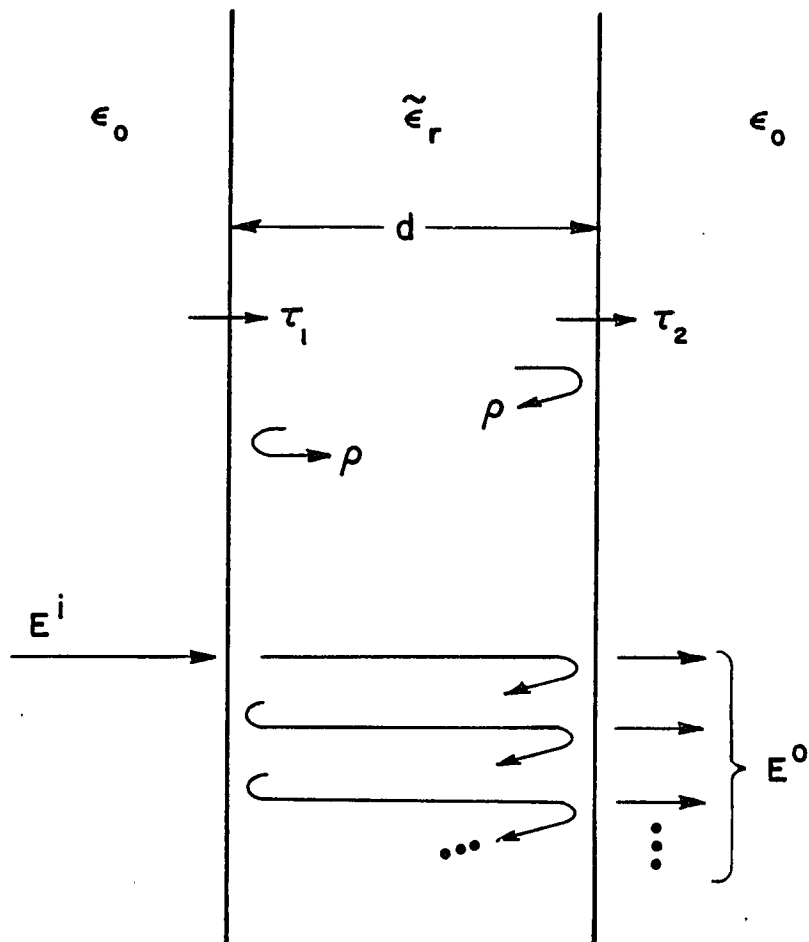


Figure C.1. Transmission by a dielectric slab in free space.

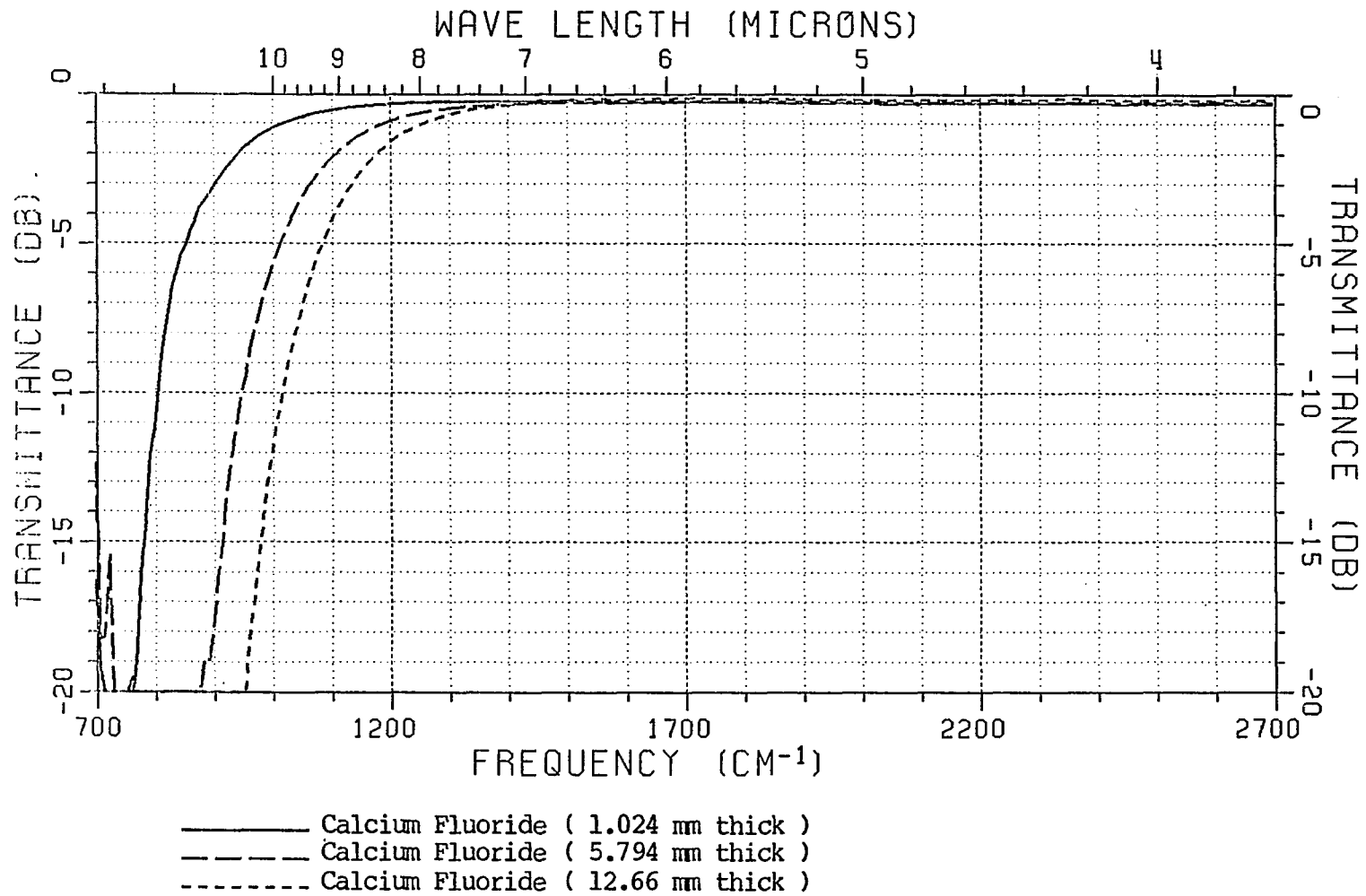


Figure C.2. Measured transmittance data for calcium fluoride.

$$\begin{aligned}
T &= \frac{|E^o|^2}{|E^i|^2} \\
&\approx |\tau_1|^2 |\tau_2|^2 |e^{-\gamma d}|^2 \\
&= |\tau_1|^2 |\tau_2|^2 e^{-(4\pi/\lambda_0) kd} \quad . \quad (C.9)
\end{aligned}$$

If we now know the transmittances  $T_1$  and  $T_2$  for two slabs of thicknesses  $d_1$  and  $d_2$  respectively, we can find an approximate value of  $k$  by taking ratios using Equation (C.9). This yields

$$k \approx - \frac{\lambda_0}{4\pi(d_1-d_2)} \ln (T_1/T_2) \quad . \quad (C.10)$$

Using the low  $f\#$  measurement system described in Appendix B, the transmittances of three  $\text{CaF}_2$  flats were measured. The results are shown in Figure C.2. The average value of each curve was found in the region from  $1700 \text{ cm}^{-1}$  to  $2700 \text{ cm}^{-1}$  to establish a lossless region value for each curve. The average of these three averages was then found. Each transmittance curve was then shifted so that each individual average value agreed with the single final average value. This was done to correct for any slight shifts in the measured data due to alignment errors, etc. Each set of data was processed against the other two using Equation (C.10) at each frequency sample point. The three values obtained at each frequency were then averaged with the results shown in Figure C.3. It can be seen that in the region from  $950 \text{ cm}^{-1}$  to



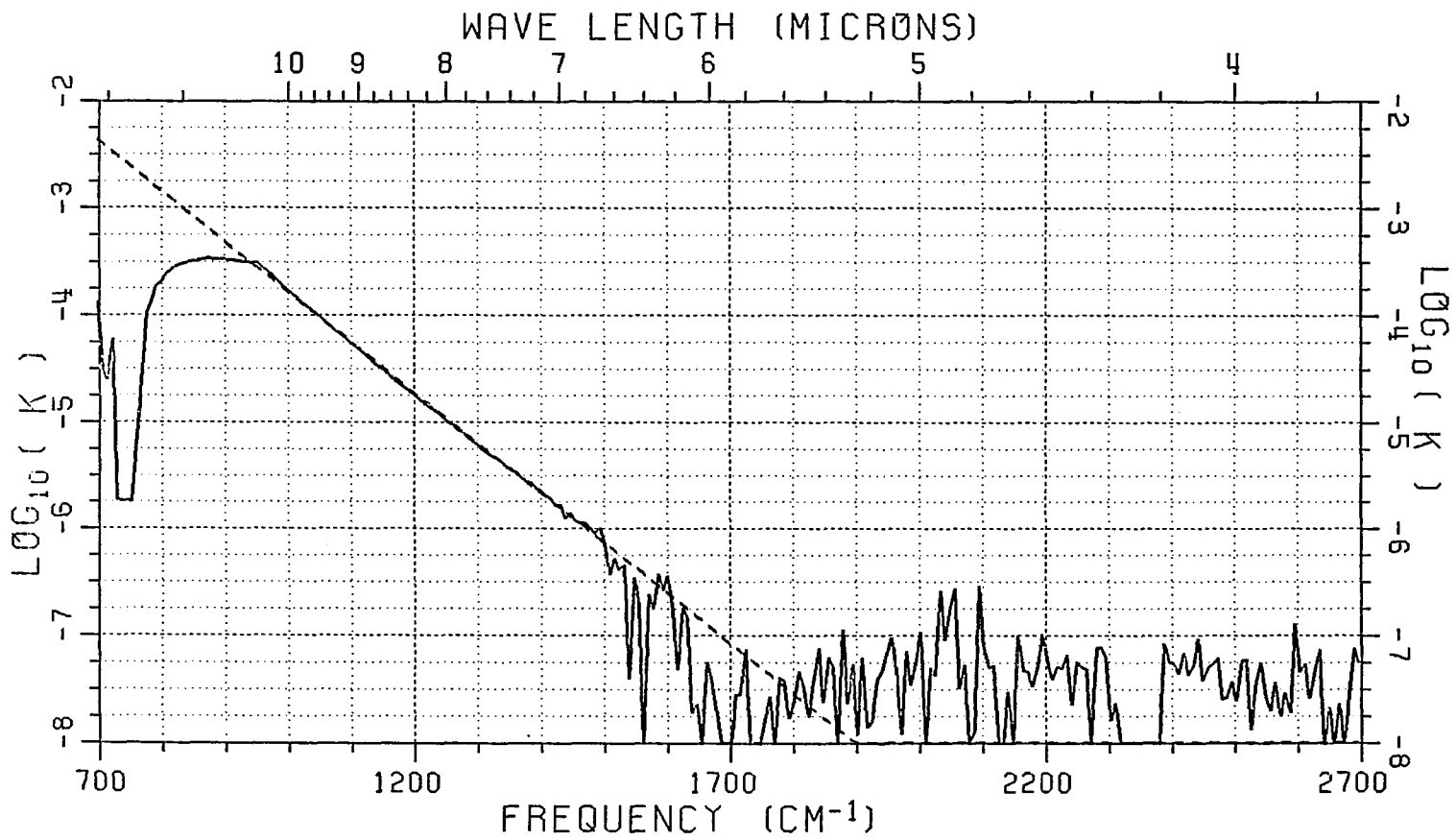


Figure C.3. Approximate extinction coefficient for CaF<sub>2</sub>. The linear, best fit model is for the 950 → 1500 cm<sup>-1</sup> data.

1500  $\text{cm}^{-1}$  this curve can be easily fit by a straight line. This was done in a least mean square (LMS) sense with the result being

$$\log_{10}(k) \approx 0.9360592 - 4.7146729 \times 10^{-3}f \quad (\text{C.11})$$

where  $f$  is the frequency in wave numbers. Note that a plot generated via Equation (C.11) is included in Figure C.3 for comparison. Above 1500  $\text{cm}^{-1}$ , the straight line fit and the actual plot differ but in this region, the data are essentially noise since we are in a region where any differences in transmission are due to noise in the measurement system. Below 950  $\text{cm}^{-1}$ , the actual data curve for  $k$  and the straight line again differ but in this region it is due to the fact that the measured signals for both of the thicker flats are below the measurement system noise level of about -20 dB.

Using Equations (C.4) and (C.11) as a model for the complex index of  $\text{CaF}_2$ , three calculated transmittance curves were generated for the slab thicknesses which were originally measured. The results are shown in Figure C.4. Comparing Figures C.2 and C.4, it can be seen that the agreement in the curves is reasonably good. For the thin flat curves, the measured and calculated data differ by only about one half dB at 900  $\text{cm}^{-1}$ . Below 900  $\text{cm}^{-1}$ , the agreement becomes steadily worse with indications that the values of the extinction coefficient are actually larger than those given by Equation (C.11).

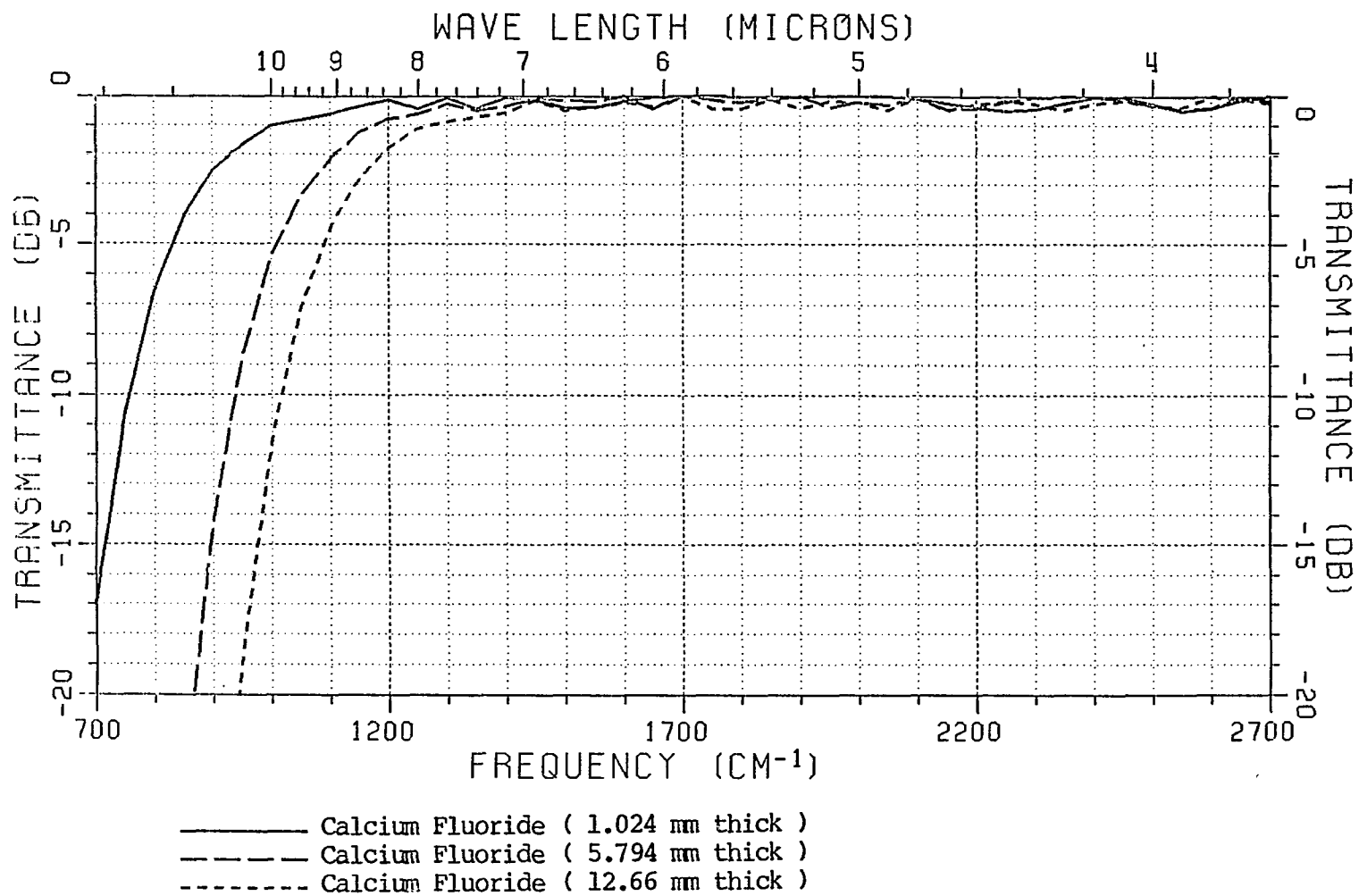


Figure C.4. Calculated transmittance data for calcium fluoride.

More precise models for the extinction coefficient could have been found in the region below  $900 \text{ cm}^{-1}$  but this would have required the addition of measured data on thinner slabs of  $\text{CaF}_2$ . This was not deemed necessary since the thrust of this work was not to develop an excellent model for  $\text{CaF}_2$ . Since all the periodic surfaces reported herein were designed to be resonant above  $1000 \text{ cm}^{-1}$ , it is felt that the model for  $\text{CaF}_2$  obtained using Equations (C.4) and (C.11) is sufficient.

## APPENDIX D

### OHMIC LOSS IN PERIODIC SURFACES

In this section, a technique is presented to model the effects of metallic loss in periodic surfaces. The basic assumptions involved are:

1. The loss does not significantly alter the assumed mode current distributions from the lossless case [65,66].
2. The radiators are 3-dimensional (length, width and thickness) but the patterns are unaffected by element thickness. The element widths may be appreciable.
3. The loss mechanism may be adequately modelled by a uniform surface resistance,  $R_s$ , and assumed surface current densities.

Given these assumptions, the procedure will be as follows:

1. Find the power loss in any metal surfaces due to the assumed scattering current (voltage) modes on the dipoles (slots).

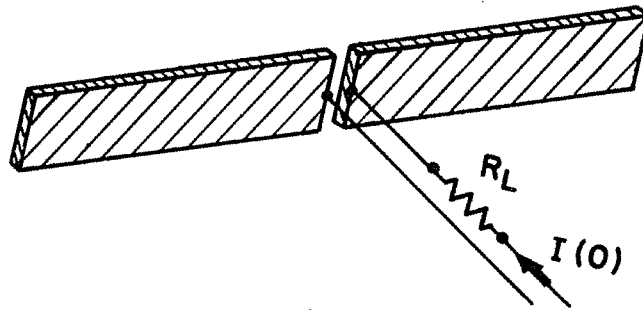
2. Equate the ohmic loss on the elements to the loss in an equivalent resistance (conductance) at the terminals of the dipole (slot) as shown in Figure D.1.
3. Solve for the equivalent loss component to be added to the self impedances (admittances) for the dipoles (slots).

#### A. LOSSY DIPOLES SURFACES

It is assumed that the elements are located in an array with coordinates defined in  $(\hat{x}, \hat{y}, \hat{z})$  space. Local to the elements, a set of coordinates  $(\hat{p}, \hat{p}')$  are used to describe the element current distribution as shown in Figure D.2. The unit vector,  $\hat{p}$ , is assumed along the major element axis. For typical planar arrays where the arrays are orthogonal to the  $\hat{y}$  direction, we will have  $\hat{x} \times \hat{z} = -\hat{y}$  and it is assumed that  $\hat{p} \times \hat{p}' = \hat{y}$ . It is further assumed that the surface current density is uniform around the element (i.e., constant in a plane  $p = \text{constant}$ ) and given by

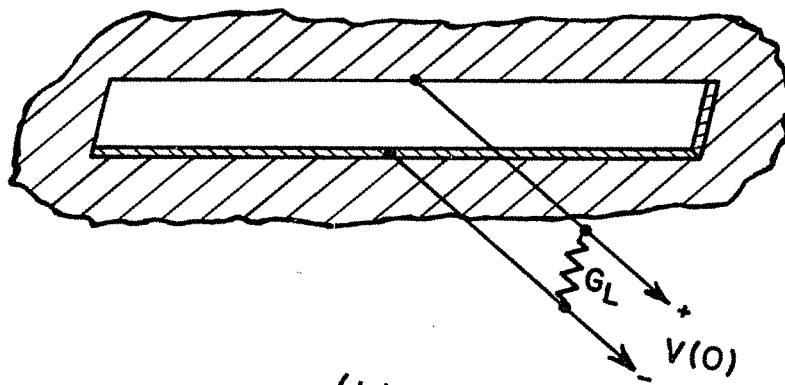
$$\vec{J}_s(p) = \hat{p} J_p \times D(p) \quad . \quad (D.1)$$

In Equation (D.1),  $J_p$  is the mode current amplitude and  $D(p)$  the mode current distribution. Note that the mode current terminals are at  $p=0$ . Two distributions [67,69] have been favored in moment methods and past



(a)

(a). Resistance,  $R_L$ , for a current excited dipole.



(b)

(b). Conductance,  $G_L$ , for a voltage excited slot.

Figure D.1. Placement of equivalent loss components.

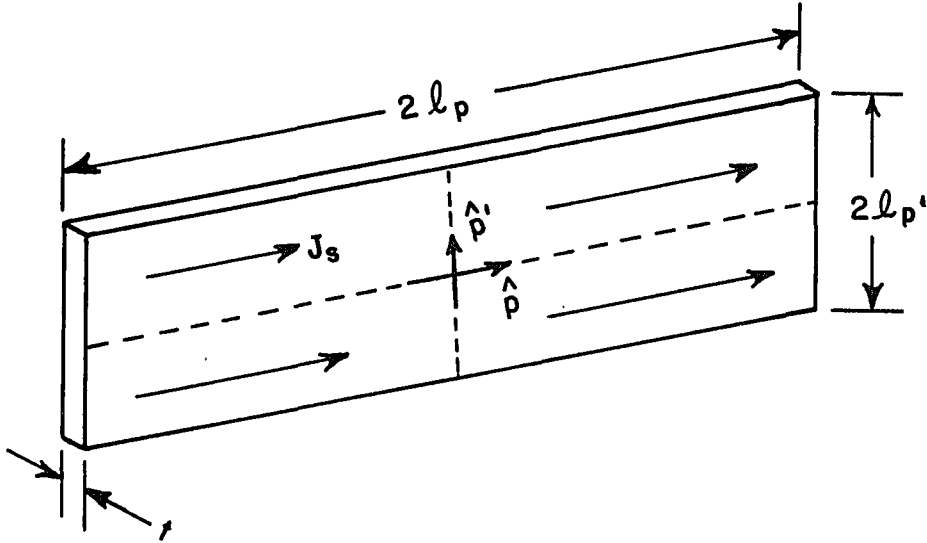


Figure D.2. Local element coordinate system geometry and dipole dimensions.

PST studies: the sine mode,  $D_S(p)$ , and the cosine mode,  $D_C(p)$ . These are given by

$$D_S(p) = \frac{\sinh(\gamma_e(l_{pe} - |p|))}{\sinh(\gamma_e l_{pe})}, \quad -l_p < p < l_p, \quad (D.2)$$

and

$$D_C(p) = \frac{\cosh(\gamma_e l_{pe}) - \cosh(\gamma_e p)}{\cosh(\gamma_e l_{pe}) - 1}, \quad -l_p < p < l_p. \quad (D.3)$$

In Equations (D.2) and (D.3),  $\gamma_e$  is the effective propagation constant along the elements which depends on the surrounding media parameters and possibly on effects due to the lossy metal itself. In addition,



$l_{pe}$  is the effective length of the element [68] used to account for charge buildup at the end of the elements due to width and thickness effects. This effect is illustrated in Figure D.3. Note that  $l_{pe}$  is always greater than  $l_p$ . Typically, this is written as

$$l_{pe} = l_p + \Delta l_p \quad (D.4)$$

where  $\Delta l_p$  is always greater than zero. Furthermore, note that the current distributions are normalized such that

$$D_S(0) = 1 = D_C(0) \quad (D.5)$$

Given a uniform surface resistance,  $R_S$ , the ohmic power loss in an element is

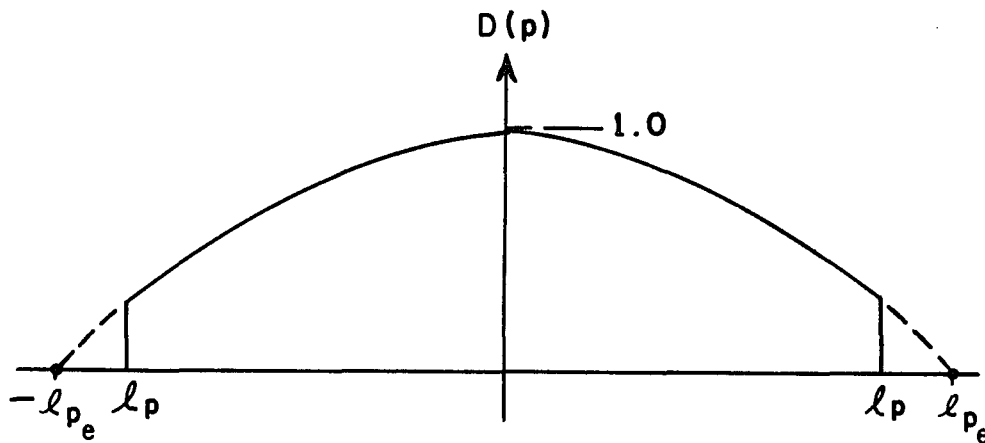


Figure D.3. Example of a sine or cosine mode showing effect of effective length on the distribution.  $l_{pe} < l_p$ .

$$\begin{aligned}
P_L &= \frac{R_S}{2} \int_S |J(S)|^2 dS \\
&= \frac{R_S}{2} \left\{ 2 \int_{-\ell_p}^{\ell_p} dp \int_{-\ell_{p'}}^{\ell_{p'}} dp' |J_p|^2 |D(p)|^2 \right. \\
&\quad \left. + 2 \int_{-\ell_p}^{\ell_p} dp \int_0^t dt |J_p|^2 |D(p)|^2 \right\} \\
&= \frac{R_S}{2} \left\{ 2(2\ell_{p'} + t) |J_p|^2 \int_{-\ell_p}^{\ell_p} |D(p)|^2 dp \right\} . \tag{D.6}
\end{aligned}$$

This result assumes a negligible power loss on the ends of the dipole. The input current to the dipole (assuming no variation of the current orthogonal to  $\hat{p}$ ) is given by

$$I(0) = J_p \times D(0) \times 2(2\ell_{p'} + t) \tag{D.7}$$

which results in a power loss in the equivalent loss resistance,  $R_L$ , of

$$\begin{aligned}
P_L &= \frac{R_L}{2} |I(0)|^2 \\
&= \frac{R_L}{2} |J_p|^2 |D(0)|^2 (2(2\ell_{p'} + t))^2 . \tag{D.8}
\end{aligned}$$

Equating the results of Equations (D.5) and (D.7) yields

$$R_L = \frac{R_S}{2(2\ell_{p'} + t)} \int_{-\ell_p}^{\ell_p} \frac{|D(p)|^2}{|D(0)|^2} dp . \tag{D.9}$$

Thus, the value of  $R_L$  depends on the form of  $D(p)$  and not on  $D(0)$  due to the normalization.

1.  $R_L$  for the Sine Mode,  $R_L^S$

Substituting  $D_S(p)$  for  $D(p)$  in Equation (D.8), yields a sine mode loss resistance,  $R_L^S$ , of

$$\begin{aligned} R_L^S &= \frac{R_S}{2(2\ell_p + t)} \int_{-\ell_p}^{\ell_p} \frac{|D_S(p)|^2}{|D_S(0)|^2} dp \\ &= \frac{R_S}{2(2\ell_p + t)} \int_{-\ell_p}^{\ell_p} |D_S(p)|^2 dp \quad . \end{aligned} \quad (D.10)$$

To evaluate this integral we must break it up into real and imaginary parts. Thus, define as usual

$$\gamma_e = \alpha_e + j\beta_e \quad . \quad (D.11)$$

Noticing the obvious symmetry in the integrand in Equation (D.10) and using Equation (D.11), we have

$$\begin{aligned} \int_{-\ell_p}^{\ell_p} |D_S(p)|^2 dp &= 2 \int_0^{\ell_p} \left| \frac{\sinh((\alpha_e + j\beta_e)(\ell_{pe} - p))}{\sinh(\gamma_e \ell_{pe})} \right|^2 dp \\ &= \frac{2}{|\sinh(\gamma_e \ell_{pe})|^2} \int_0^{\ell_p} \frac{1}{2} \left[ \cosh(2\alpha_e(\ell_{pe} - p)) - \cos(2\beta_e(\ell_{pe} - p)) \right] dp \quad . \end{aligned} \quad (D.12)$$

Evaluating this integral and using Equation (D.4), yields

$$\int_{-l_p}^{l_p} |D_S(p)|^2 dp = \frac{1}{|\sinh(\gamma_e l_{pe})|^2} \left[ \frac{\sinh(2\alpha_e l_{pe}) - \sinh(2\alpha_e \Delta l_p)}{2\alpha_e} - \frac{\sinh(2\beta_e l_{pe}) - \sinh(2\beta_e \Delta l_p)}{2\beta_e} \right] \quad (D.13)$$

Substituting into Equation (D.10), we obtain for the sine mode

$$R_L^S = \frac{R_S l_p}{2(2l_p + t) |\sinh(\gamma_e l_{pe})|^2} \left[ \frac{\sinh(2\alpha_e l_{pe}) - \sinh(2\alpha_e \Delta l_p)}{2\alpha_e l_p} - \frac{\sinh(2\beta_e l_{pe}) - \sinh(2\beta_e \Delta l_p)}{2\beta_e l_p} \right] \quad (D.14)$$

For the case  $\alpha_e=0$ , this reduces to Munk's Equation (A.119), [68].

2.  $R_L$  for the Cosine Mode,  $R_L^C$

As with the sine mode, we obtain

$$R_L^C = \frac{R_S}{2(l_p + t)} \times \frac{2}{|\cosh(\gamma_e l_{pe}) - 1|^2} \int_0^{l_p} |\cosh(\gamma_e l_{pe}) - \cosh(\gamma_e p)|^2 dp \quad (D.15)$$

Expanding the integrand we have

$$\begin{aligned}
& \int_0^{\lambda_p} |\cosh(\gamma_e \lambda_{pe}) - \cosh(\gamma_e p)|^2 dp \\
&= \int_0^{\lambda_p} [|\cosh(\gamma_e \lambda_{pe}) + \cosh(\gamma_e p)|^2 - \cosh(\gamma_e \lambda_{pe}) + \cosh(\gamma_e^* p) \\
&\quad - \cosh(\gamma_e^* \lambda_{pe}) + \cosh(\gamma_e p)] dp \tag{D.16}
\end{aligned}$$

where the notation  $A^*$  denotes the complex conjugate of  $A$ . The first term and the last two terms are very simple to integrate and the second term may be expanded and integrated as was done to obtain  $R_L^S$ . The final result is

$$\begin{aligned}
R_L^C &= \frac{R_S \lambda_p}{2(2\lambda_p + t) |\cosh(\gamma_e \lambda_{pe}) - 1|^2} \{2|\cosh(\gamma_e \lambda_{pe})|^2 \\
&\quad + \frac{\sinh(2\alpha_e \lambda_p)}{2\alpha_e \lambda_p} + \frac{\sin(2\beta_e \lambda_p)}{2\beta_e \lambda_p} - 4R_e \left[ \frac{\cosh(\gamma_e \lambda_{pe}) \sinh(\gamma_e^* \lambda_p)}{\gamma_e^* \lambda_p} \right] \} . \tag{D.17}
\end{aligned}$$

As a final comment concerning the use of the sine or cosine mode loss terms, it should be stated that the term corresponding to the scattering current mode should be used. This is because in the reaction formulation used in periodic surface theory to find the mutual impedance terms, it is the scattering current which actually radiates and thus will be responsible for any loss. The transmitting current mode is only used for testing purposes and is not excited to find a radiated field.

## B. THIN, LOSSY SLOTS

In this case, it is assumed that straight slots have been formed in some lossy metal. The geometry and dimensions of a single slot are shown in Figure D.4. To find the equivalent loss conductance (see Figure D.1) to be added to the self admittance terms, it is assumed that the slot supports a voltage distribution

$$V(p) = V_p D(p) \quad (D.18)$$

along the slot length. The sense of the voltage and the direction of the resulting induced electric field is also shown in Figure D.4. The length, width and thickness of the slot are given respectively by  $2l_p$ ,  $2l_p'$  and  $t$ . This yields an electric field in the slot given by

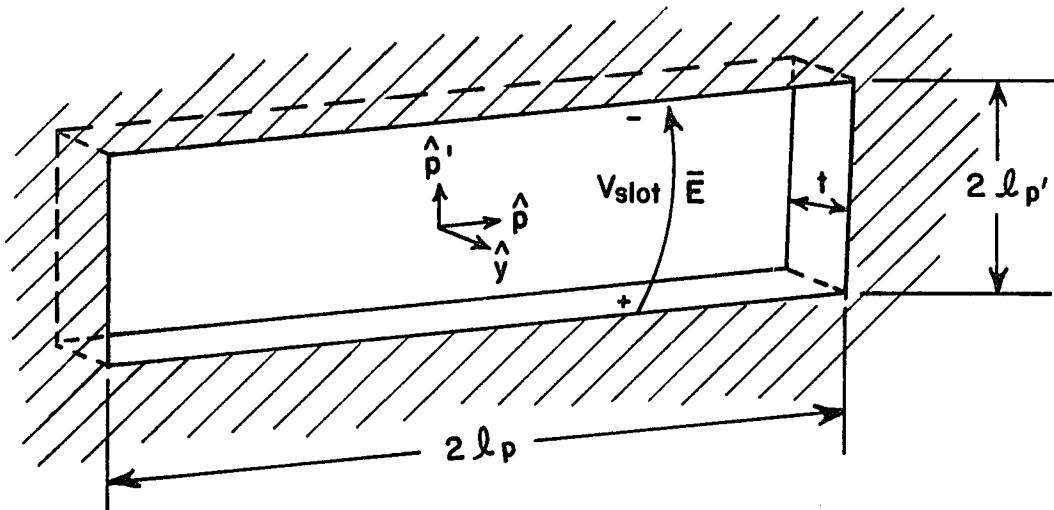


Figure D.4. Slot geometry and electric field direction.

$$\bar{E}(p) = \hat{p}' \frac{V_p}{2\ell_p} D(p) , \quad (D.19)$$

where  $V_p$  is the voltage mode amplitude and  $D(p)$  is the mode distribution. Again, it is assumed that  $D(p)$  is defined by Equations (D.2) and (D.3) [69,70].

The slot case is more complicated since it is necessary to find the power loss due to the fields radiated by the assumed voltage excitation. This will require a knowledge of the relationship between the two coordinate systems (i.e.,  $\hat{x}, \hat{y}, \hat{z}$  and  $\hat{p}, \hat{p}', \hat{y}$ ). Since we are only looking at a single array, we are free to choose the origins of the two systems to be coincident as shown in Figure D.5. Thus, we can relate the local and global coordinates via the single parameter,  $\theta$ , which is the angle from the x-axis to the p-axis in the direction of the z-axis. It can be seen that the coordinates are related by

$$\begin{aligned} \hat{p} &= \hat{x} \cdot \cos \theta + \hat{z} \cdot \sin \theta \\ \hat{p}' &= \hat{x} \cdot \sin \theta - \hat{z} \cdot \cos \theta \end{aligned} \quad (D.20)$$

and

$$\begin{aligned} \hat{x} &= \hat{p} \cdot \cos \theta + \hat{p}' \cdot \sin \theta \\ \hat{z} &= \hat{p} \cdot \sin \theta + \hat{p}' \cdot \cos \theta \end{aligned} \quad (D.21)$$

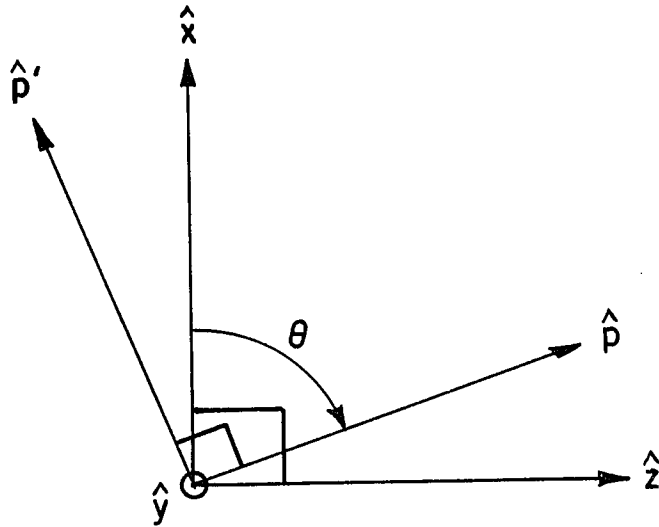


Figure D.5. Relationship between the local slot coordinates  $\hat{p}$ ,  $\hat{p}'$ ,  $\hat{y}$  and the array coordinates  $\hat{x}$ ,  $\hat{y}$ ,  $\hat{z}$ .

These relationships will be necessary when subtracting out the loss terms across the actual slot areas. Since there is no metal in the slot areas, there can be no loss.

It is further necessary to separate the slot loss analysis into two cases. The first is for thin slots in which one mode satisfactorily models the slot. The second case is for thick slots in which a mode is placed on each side of the slot surface.

### 1. Thin Slots ( $t \ll \lambda$ )

For thin slots, the single voltage mode radiates into both of the regions on each side of the slot. This is shown in Figure D.6, with the three loss regions indicated. Note that it will be necessary to find



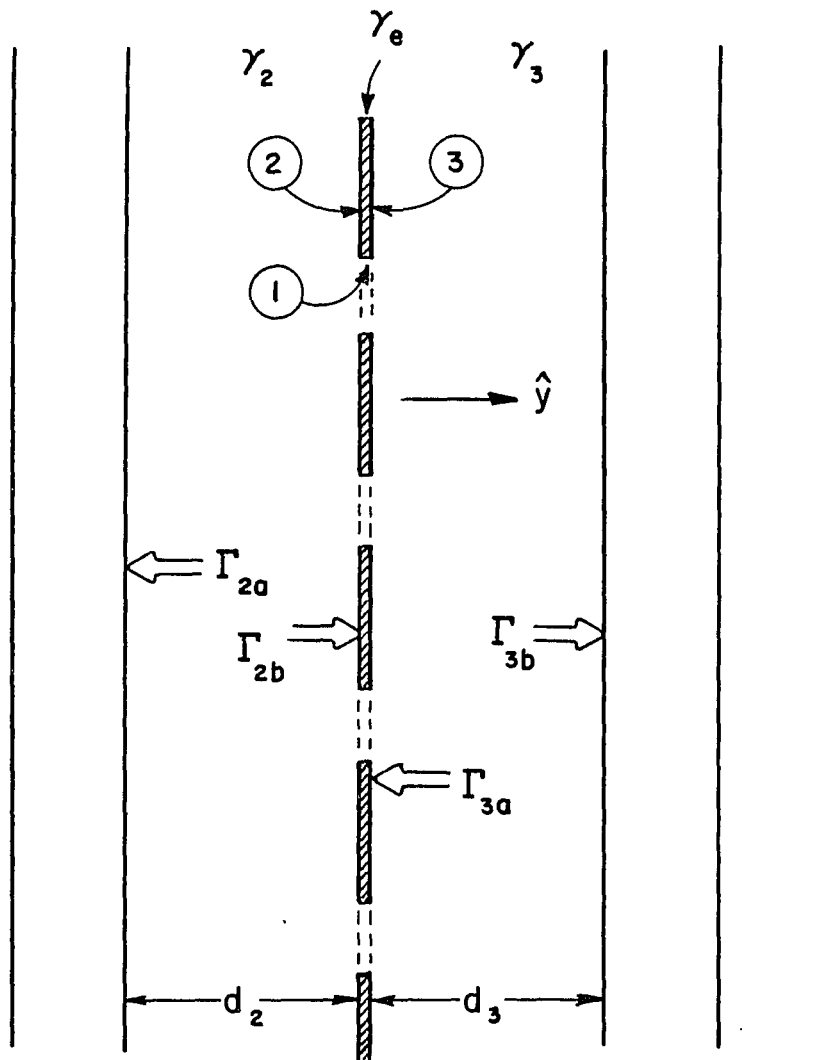


Figure D.6. Loss regions for thin slots, showing dimensions and effective reflection coefficients.

the interior loss and add to that the exterior loss on both sides found by integrating over one array cell (i.e.,  $X \rightarrow X+D_x$  and  $Z \rightarrow Z+D_z$ ). In addition, an equivalent integral over the area of the slot on each side must be subtracted. Thus, the cell integration is done in global coordinates and the slot integrals are done in the local coordinates.

The surface currents which cause the loss are found from the magnetic fields evaluated at the surfaces as

$$\vec{J}(\vec{S}) = \hat{n} \times \vec{H} \Big|_S \quad (D.22)$$

where  $\hat{n}$  is the outward pointing unit normal from the surface.

In region 1, the thin slot interior region, the magnetic field,  $H_1$ , can be easily found from Equation (D.18) as

$$\begin{aligned} H_1 &= \frac{1}{-j\omega\mu_1} \nabla \times E_1 \\ &= \frac{1}{-j\omega\mu_1} \begin{vmatrix} \hat{p} & \hat{p}' & \hat{y} \\ \frac{\partial}{\partial p} & \frac{\partial}{\partial p'} & \frac{\partial}{\partial y} \\ 0 & \frac{V_p}{2\ell_{p'}} D(p) & 0 \end{vmatrix} \\ &= \frac{1}{-j\omega\mu_1} \times \frac{V_p}{2\ell_{p'}} \times \frac{\partial D(p)}{\partial p} \hat{y} \end{aligned} \quad (D.23)$$

where  $\mu_1$  is the permeability of the material in the slot. From Figure (D.4) it can be seen that inside the slot the surface normals are

either in the  $\hat{p}$  or  $\hat{p}'$  directions. As a consequence of this and the forms of Equations (D.22) and (D.23) it can be seen that the magnitude of the surface current in region 1 equals the magnitude of the magnetic field evaluated at the surface. Thus the power loss in region 1 is given by

$$P_{L1} = \frac{R_S}{2} \left[ 2 \int_{-\ell_p}^{\ell_p} dp \int_0^t dt |H_1(p)|^2 + \right. \\ \left. + 2 \int_{-\ell_{p'}}^{\ell_{p'}} dp' \int_0^t dt |H_1(p)| \Big|_{p=\ell_p} \right]^2 \quad (D.24)$$

where the factors of 2 account for the symmetry between the left and right sides (see Figure D.4) and the top and bottom sides. Using Equation (D.23) yields,

$$P_{L1} = \frac{R_S}{2} \left[ 2(t) \left| \frac{1}{j\omega\mu_1} \frac{V_p}{2\ell_{p'}} \right|^2 \int_{-\ell_p}^{\ell_p} \left| \frac{\partial D(p)}{\partial p} \right|^2 dp \right. \\ \left. + 2(t)(2\ell_{p'}) \left| \frac{1}{j\omega\mu_1} \frac{V_p}{2\ell_{p'}} \right|^2 \left| \frac{\partial D(p)}{\partial p} \right| \Big|_{p=\ell_p} \right]^2 \\ = \frac{R_S}{2} |V_p|^2 \left[ \frac{2t}{(2\ell_{p'})} \times \frac{1}{|j\omega\mu_1|^2} \right] \times \left[ \int_{-\ell_p}^{\ell_p} \left| \frac{\partial D(p)}{\partial p} \right|^2 dp \right. \\ \left. + 2\ell_{p'} \left| \frac{\partial D(p)}{\partial p} \right| \Big|_{p=\ell_p} \right]^2 \quad (D.25)$$

To find the loss in the exterior regions, 2 and 3 in Figure D.6, it is necessary to know the fields radiated by a set of periodic elements in a general stratified medium. Such a medium is shown in Figure D.7, for which we define

$$\bar{R} = x\hat{x} + y\hat{y} + z\hat{z} \quad (D.26)$$

and

$$\bar{R}' = x'\hat{x} + y'\hat{y} + z'\hat{z} \quad (D.27)$$

as the field and source points, respectively. For this analysis, some simplification is allowed since we actually will only need to know the fields at the plane of the elements. In addition, we are free to choose the reference point at  $X'=0, Z'=0$ . If the radiators are electric currents, the total electric field in the plane of the array is

$$\bar{E}(X,Z) \Big|_{\text{array}} = J(0,0) \frac{Z_c}{2D_x D_z} \sum_k \sum_n \frac{e^{-\gamma(Xr_x + Zr_z)}}{r_y} \bar{R}(k,n) \quad (D.28)$$

where  $r_x, r_y$  and  $r_z$  are defined by Equation (2.9) both sums run from  $-\infty$  to  $\infty$ , and

$$\bar{R}(k,n) = - \left[ \frac{[\perp\hat{n}_+ - \perp\hat{n}_- \perp\Gamma_b e^{-\gamma 2y^2 r_y}][\perp P_+ - \perp P_- e^{-\gamma 2y' r_y}]}{1 - \perp\Gamma_a \perp\Gamma_b e^{-\gamma 2d r_y}} + \frac{[\parallel\hat{n}_+ - \parallel\hat{n}_- \parallel\Gamma_b e^{-\gamma 2y^2 r_y}][\parallel P_+ - \parallel P_- e^{-\gamma 2y' r_y}]}{1 - \parallel\Gamma_a \parallel\Gamma_b e^{-\gamma 2d r_y}} \right] \quad (D.29)$$

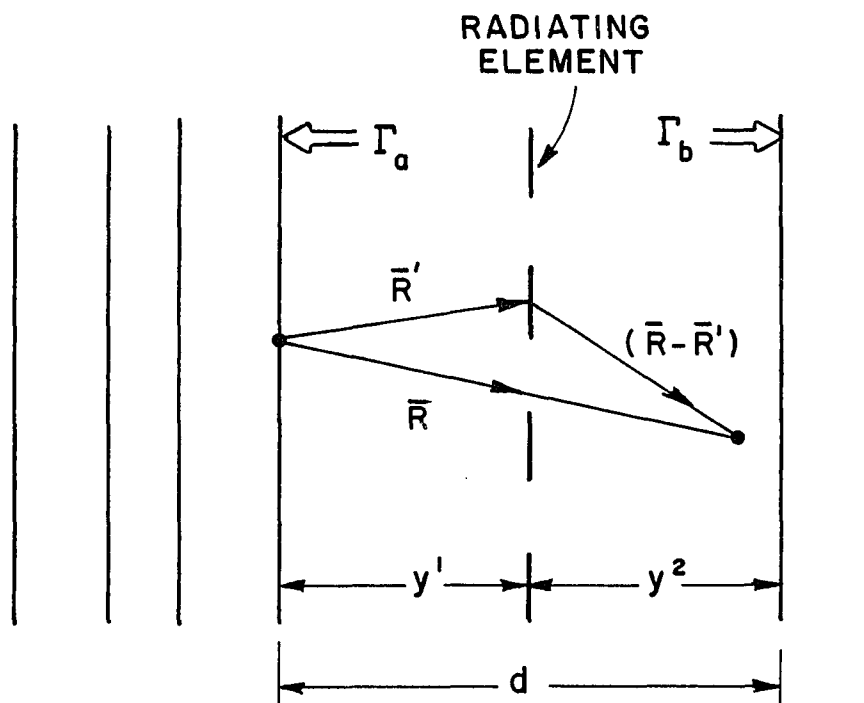


Figure D.7. Radiating elements in a stratified media.

All terms in Equations (D.28) and (D.29) are defined as in [71] except  $r_x$ , which is obtained from [72] so that skewed grid geometries may be evaluated. In addition, the pattern factors,  $P_{\pm}$ , are defined for two dimensional elements [73] as

$$P_{\pm} = \frac{1}{J(0,0)} \int_{-\ell_p}^{\ell_p} dp \int_{-\ell_{p'}}^{\ell_{p'}} dp' J(p, p') e^{+\gamma(\hat{p}\hat{p} + \hat{p}'\hat{p}') \cdot \hat{r}_{\pm}} \quad (D.30)$$

It should also be pointed out that in Equation (D.29),  $\Gamma_a$  and  $\Gamma_b$  are the effective E-field reflection coefficients which account for multiple reflections and stratified dielectrics. Note that  $\Gamma_a$  and  $\Gamma_b$  depend on the summation indices,  $k$  and  $n$ .

To find the field from an array of slots modelled as magnetic current dipoles on a ground plane, we use the duals [74] of Equations (D.28) through (D.30) and allow the array to approach either the left or right interface. Note that the interface will be a conducting wall. Thus, in the plane of the magnetic radiators

$$H(x,y) \Big|_{\text{array}} = K(0,0) \frac{Y_c}{2D_x D_z} \sum_k \sum_n \frac{e^{-\gamma(xr_x + zr_z)}}{r_y} \bar{R}(k,n) \quad (D.31)$$

and

$$\bar{R}(k,n) = - \left[ \frac{[\hat{n}_+ - \hat{n}_- \Gamma_b e^{-\gamma 2y^2 r_y}][\hat{p}_+ - \hat{p}_- e^{-\gamma 2y' r_y}]}{1 - \Gamma_a \Gamma_b e^{-\gamma 2d r_y}} + \frac{[\hat{n}_+ - \hat{n}_- \Gamma_b e^{-\gamma 2y^2 r_y}][\hat{p}_+ - \hat{p}_- e^{-\gamma 2y' r_y}]}{1 - \Gamma_a \Gamma_b e^{-\gamma 2d r_y}} \right] \cdot \quad (D.32)$$

In Equation (D.26), the fact that  $\hat{p}$  and  $\hat{p}'$  have no  $y$  component has been used to obtain

$$P_{\pm} = P = \frac{1}{K(0,0)} \int_{-l_p}^{l_p} dp \int_{-l_{p'}}^{l_{p'}} dp' K(p,p') e^{\gamma(p r_p + p' r_{p'})} \quad (D.33)$$

where  $r_p$  and  $r_{p'}$  are obtained from Equations (D.20) and (D.21) as

$$\begin{aligned} r_p &= \hat{p} \cdot \hat{r}_{\pm} \\ &= \hat{p} \cdot (\hat{x} r_x \pm \hat{y} r_y + \hat{z} r_z) \\ &= \hat{p} \cdot ((\hat{p} \cos \theta + \hat{p}' \sin \theta) r_x + \hat{y} r_y + (\hat{p} \sin \theta - \hat{p}' \cos \theta) r_z) \\ &= r_x \cos \theta + r_z \sin \theta \end{aligned} \quad (D.34)$$

and similarly,

$$r_{p'} = r_x \sin \theta - r_z \cos \theta. \quad (D.35)$$

The last necessary piece of information is the form of the magnetic current distribution,  $\bar{K}(p,p')$ . This can be obtained from the aperture E-field distribution of Equation (D.19) using the equivalence principle [75]. This yields

$$\begin{aligned}\bar{K}(p,p') &= -\hat{n} \times \bar{E}(p,p') \Big|_{\text{aperture}} \\ &= -(\pm \hat{y}) \times \left[ \hat{p}' \frac{V_p}{2\ell_{p'}} D(p) \right] \\ &= \pm \hat{p} \frac{V_p}{2\ell_{p'}} D(p)\end{aligned}\tag{D.36}$$

where the minus sign is used in region 2 and the plus sign in region 3.

The necessary terms to evaluate the power loss in region 2 can now be defined (see Figure D.6 for the dimensions and illustration of the reflection coefficients). For region 2 we have

$$\bar{K}(p,p') = -\hat{p} \frac{V_p}{2\ell_{p'}} D(p) \quad ,\tag{D.37}$$

and

$$\begin{aligned}y^1 &\rightarrow d_2 \\ y^2 &\rightarrow 0 \quad .\end{aligned}\tag{D.38}$$

Using these expressions yields,

$$\bar{H}_2(x,z) \Big|_{\text{surface 2}} = \left[ -\frac{V_p}{2\ell_{p'}} D(0) \right] \frac{\gamma_{2c}}{2D_x D_z} \sum_k \sum_n \frac{e^{-\gamma_2(xr_{2x} + zr_{2z})}}{r_{2y}} \bar{R}_2(k,n)\tag{D.39}$$



where  $Y_{2c}$  is the admittance of the dielectric to the left (see Figure D.6) of the slotted surface. In addition,

$$\begin{aligned} \bar{R}_2(k, n) = & - \left| \frac{[\hat{n}_{2+} - \hat{n}_{2-} \times \Gamma_{2b}] [\Gamma_{2a} P_{2+} - \Gamma_{2a} P_{2-} \times e^{-\gamma_2 2d_2 r_{2y}}]}{1 - \Gamma_{2a} \Gamma_{2b} e^{-\gamma_2 2d_2 r_{2y}}} \right. \\ & + \left. \frac{[\hat{n}_{2+} - \hat{n}_{2-} \times \Gamma_{2b}] [\Gamma_{2a} P_{2+} - \Gamma_{2a} P_{2-} \times e^{-\gamma_2 2d_2 r_{2y}}]}{1 - \Gamma_{2a} \Gamma_{2b} e^{-\gamma_2 2d_2 r_{2y}}} \right| \end{aligned} \quad (D.40)$$

and

$$\begin{aligned} P_{2\pm} = & \frac{1}{\left[ \frac{V_p}{2\ell_{p'}} D(0) \right]} \int_{-\ell_p}^{\ell_p} dp \int_{-\ell_{p'}}^{\ell_{p'}} dp' \left[ -\frac{V_p}{2\ell_{p'}} D(p) \right] e^{\gamma_2 (pr_{2p} + p'r_{2p}')} \\ & \int_{-\ell_p}^{\ell_p} dp \int_{-\ell_{p'}}^{\ell_{p'}} dp' \left[ \frac{V_p D(p)}{V_p D(0)} \right] e^{\gamma_2 (pr_{2p} + p'r_{2p}')} , \end{aligned} \quad (D.41)$$

where

$$\begin{aligned} r_{2p} &= r_{2x} \cos \theta + r_{2z} \sin \theta \\ r_{2p'} &= r_{2x} \sin \theta - r_{2z} \cos \theta . \end{aligned} \quad (D.42)$$

The surface current in region 2 is thus,

$$\begin{aligned} \bar{J}_{2s}(x, z) &= -\hat{y} \times \bar{H}_2(x, z) \Big|_{\text{surface}} \\ &= \left[ \frac{V_p}{2\ell_{p'}} D(0) \right] \frac{Y_{2c}}{2D_x D_z} \sum_k \sum_n \frac{e^{-\gamma_2 (x r_{2x} + z r_{2z})}}{r_{2y}} \left[ \hat{y} \times \bar{R}_2(k, n) \right] \end{aligned} \quad (D.43)$$

where it is important to remember that  $r_{2x}$ ,  $r_{2y}$  and  $r_{2z}$  depend on the summation indices  $k$  and  $n$ .

Equations (D.40) through (D.43) can be slightly rearranged by shifting the factor  $(1/2 \ell p')$  from Equation (D.43) to (D.41) yielding

$$\bar{J}_{2s}(x,z) = [V_p \cdot D(0)] \frac{\gamma_{2c}}{2D_x D_z} \sum_k \sum_n \frac{e^{-\gamma_2(xr_{2x} + zr_{2z})}}{r_{2y}} \bar{Q}_z(k,n), \quad (D.44)$$

$$\bar{Q}_z(k,n) = \hat{y} \times \bar{R}_z(k,n), \quad (D.45)$$

$$\begin{aligned} P_{2\pm} &= \frac{1}{2\ell p'} \int_{-\ell_p}^{\ell_p} dp \int_{-\ell_{p'}}^{\ell_{p'}} dp' \left[ \frac{V_p D(p)}{V_p D(0)} \right] e^{\gamma_2(p r_{2p} + p' r_{2p'})} \\ &= \left[ \frac{e^{\gamma_2 \ell_p r_{2p'}} - e^{-\gamma_2 \ell_p r_{2p'}}}{2\gamma_2 \ell_p r_{2p'}} \right] \int_{-\ell_p}^{\ell_p} \left[ \frac{V_p D(p)}{V_p D(0)} \right] e^{\gamma_2 p r_{2p}} dp \\ &= \text{Sinc}(\gamma_2 \ell_p r_{2p'}) \int_{-\ell_p}^{\ell_p} \left[ \frac{V_p D(p)}{V_p D(0)} \right] e^{\gamma_2 p r_{2p}} dp, \quad (D.46) \end{aligned}$$

where we define

$$\text{Sinc}(x) = \frac{\sinh(x)}{x} \quad (D.47)$$

and  $\sinh(x)$  is the standard hyperbolic sine function. It is also fairly easily seen that

$$\bar{J}_{2s}(p,p') = [V_p \cdot D(0)] \frac{Y_{2c}}{2D_x D_z} \sum_k \sum_n \frac{e^{-\gamma_2(p r_{2p} + p' r_{2p'})}}{r_{2y}} \bar{Q}_2(k,n). \quad (D.48)$$

The power loss in region 2 may now be easily written as

$$P_{L2} = \frac{R_s}{2} \left[ \int_{-D_x/2}^{D_x/2} dx \int_{-D_z/2}^{D_z/2} dz |\bar{J}_{2s}(x,z)|^2 - \int_{-\ell_p}^{\ell_p} dp \int_{-\ell_{p'}}^{\ell_{p'}} dp' |\bar{J}_{2s}(p,p')|^2 \right]. \quad (D.49)$$

For the first integral, we have

$$\begin{aligned} \int_{-D_x/2}^{D_x/2} dx \int_{-D_z/2}^{D_z/2} dz |\bar{J}_{2s}(x,z)|^2 &= \int_{-D_x/2}^{D_x/2} dx \int_{-D_z/2}^{D_z/2} dz \bar{J}_{2s}(x,z) \cdot \bar{J}_{2s}(x,z) \\ &= |V_p \cdot D(0)|^2 \frac{|Y_{2c}|^2}{4D_x^2 D_z^2} \sum_k \sum_n \sum_m \sum_i \frac{\bar{Q}_2(k,n) \cdot \bar{Q}_2^*(m,i)}{r_{2y}(k,n) r_{2y}^*(m,i)} \\ &\cdot \int_{-D_x/2}^{D_x/2} e^{-[\gamma_2 r_{2x}(k,n) - \gamma_2^* r_{2x}^*(m,i)] x} dx \int_{-D_z/2}^{D_z/2} e^{-[\gamma_2 r_{2z}(k,n) - \gamma_2^* r_{2z}^*(m,i)] z} dz \\ &= |V_p \cdot D(0)|^2 \frac{|Y_{2c}|^2}{4D_x^2 D_z^2} \sum_k \sum_n \sum_m \sum_i \frac{\bar{Q}_2(k,n) \cdot \bar{Q}_2^*(m,i)}{r_{2y}(k,n) r_{2y}^*(m,i)} \\ &\cdot D_x \text{Sinc} \left[ \frac{D_x}{2} (\gamma_2 r_{2x}(k,n) - \gamma_2^* r_{2x}^*(m,i)) \right] \\ &\cdot D_z \text{Sinc} \left[ \frac{D_z}{2} (\gamma_2 r_{2z}(k,n) - \gamma_2^* r_{2z}^*(m,i)) \right]. \quad (D.50) \end{aligned}$$

Similarly for the second integral

$$\begin{aligned}
 & \int_{-\ell_p}^{\ell_p} dp \int_{-\ell_{p'}}^{\ell_{p'}} dp' |\bar{J}_{2s}(p, p')|^2 |V_p \cdot D(0)|^2 \frac{|Y_{2c}|^2}{4D_x^2 D_z^2} \sum_k \sum_n \sum_m \sum_i \frac{\bar{Q}_2(k, n) \cdot \bar{Q}_2^*(m, i)}{r_{2y}(k, n) r_{2y}^*(m, i)} \\
 & \cdot \int_{-\ell_p}^{\ell_p} e^{-[\gamma_2 r_{2p}(k, n) - \gamma_2^* r_{2y}^*(m, i)] p} dp \int_{-\ell_{p'}}^{\ell_{p'}} e^{-[\gamma_2 r_{2p'}(k, n) - \gamma_2^* r_{2y}^*(m, i)] p'} dp' \\
 & = |V_p|^2 \frac{|Y_{2c}|^2}{4D_x^2 D_z^2} \sum_k \sum_n \sum_m \sum_i \frac{\bar{Q}_2(k, n) \cdot \bar{Q}_2^*(m, i)}{r_{2y}(k, n) r_{2y}^*(m, i)} \\
 & \cdot 2\ell_p \text{Sinc} \left[ \ell_p (\gamma_2 r_{2p}(k, n) - \gamma_2^* r_{2y}^*(m, i)) \right] \\
 & \cdot 2\ell_{p'} \text{Sinc} \left[ \ell_{p'} (\gamma_2 r_{2p'}(k, n) - \gamma_2^* r_{2y}^*(m, i)) \right] \quad \cdot \quad (D.51)
 \end{aligned}$$

Thus the power loss in region 2 is given by:

$$\begin{aligned}
P_{L2} = & \frac{R_s}{2} |V_p D(0)|^2 \left\{ \frac{|Y_{2c}|^2}{4D_x^2 D_z^2} \sum_k \sum_n \sum_m \sum_i \frac{\bar{Q}_2(k,n) \cdot \bar{Q}_2^*(m,i)}{r_{2y}(k,n) r_{2y}^*(m,i)} \right. \\
& \cdot \left[ D_x D_z \text{Sinc} \left( \frac{D_x}{2} (\gamma_2 r_{2x}(k,n) - \gamma_2^* r_{2x}^*(m,i)) \right) \text{Sinc} \left( \frac{D_z}{2} (\gamma_2 r_{2z}(k,n) - \gamma_2^* r_{2z}^*(m,i)) \right) \right. \\
& \cdot -4\ell_p \ell_p \cdot \text{Sinc} \left( \ell_p (\gamma_2 r_{2p}(k,n) - \gamma_2^* r_{2p}^*(m,i)) \right) \\
& \left. \left. \left. \text{Sinc} \left( \ell_p (\gamma_2 r_{2p}(k,n) - \gamma_2^* r_{2p}^*(m,i)) \right) \right] \right\} \cdot \quad (D.52)
\end{aligned}$$

Note that in region 2, the reflection coefficient on the right boundary,  $\Gamma_{2b}$ , will be approximately unity since this is a metal wall.

A similar analysis in region 3 yields

$$\begin{aligned}
P_{L3} = & \frac{R_s}{2} |V_p D(0)|^2 \left\{ \frac{|Y_{3c}|^2}{4D_x^2 D_z^2} \sum_k \sum_n \sum_m \sum_i \frac{\bar{Q}_3(k,n) \cdot \bar{Q}_3^*(m,i)}{r_{3y}(k,n) r_{3y}^*(m,i)} \right. \\
& \cdot \left[ D_x D_z \text{Sinc} \left( \frac{D_x}{2} (\gamma_3 r_{3x}(k,n) - \gamma_3^* r_{3x}^*(m,i)) \right) \text{Sinc} \left( \frac{D_z}{2} (\gamma_3 r_{3z}(k,n) - \gamma_3^* r_{3z}^*(m,i)) \right) \right. \\
& \cdot -4\ell_p \ell_p \cdot \text{Sinc} \left( \ell_p (\gamma_3 r_{3p}(k,n) - \gamma_3^* r_{3p}^*(m,i)) \right) \\
& \left. \left. \left. \text{Sinc} \left( \ell_p (\gamma_3 r_{3p}(k,n) - \gamma_3^* r_{3p}^*(m,i)) \right) \right] \right\} \quad (D.53)
\end{aligned}$$

where

$$\bar{Q}_3(k, n) = -\hat{y} \times \bar{R}_3(k, n) , \quad (D.54)$$

$$\begin{aligned} \bar{R}_3(k, n) = & \frac{[\hat{\Gamma}_{3+} - \hat{\Gamma}_{3-} \Gamma_{3b} e^{-\gamma_3^2 d_3 r_{3y}}][\Gamma_{3+} - \Gamma_{3-} \Gamma_{3a}]}{1 - \Gamma_{3a} \Gamma_{3b} e^{-\gamma_3^2 d_3 r_{3y}}} \\ & + \frac{[\hat{\Gamma}_{3+} - \hat{\Gamma}_{3-} \Gamma_{3b} e^{-\gamma_3^2 d_3 r_{3y}}][\Gamma_{3+} - \Gamma_{3-} \Gamma_{3a}]}{1 - \Gamma_{3a} \Gamma_{3b} e^{-\gamma_3^2 d_3 r_{3y}}} , \end{aligned} \quad (D.55)$$

$$P_{3\pm} = \text{Sinc}(\gamma_3 \ell_p, r_{3p}) \int_{-\ell_p}^{\ell_p} \left[ \frac{V_p \cdot D(p)}{V_p \cdot D(0)} \right] e^{\gamma_2 p r_{3p}} dp . \quad (D.56)$$

Note that for region 3, the lefthand boundary reflection coefficient,  $\Gamma_{3a}$ , will be nearly unity since now this wall is a metal.

The total power loss is found by summing Equations (D.25), (D.52) and (D.53), the result of which is equated to the equivalent loss power to yield

$$\begin{aligned} P_{L1} + P_{L2} + P_{L3} &= \frac{G_L}{2} |V(0)|^2 \\ &= \frac{G_L}{2} |V_p \cdot D(0)|^2 . \end{aligned} \quad (D.57)$$

Solving for the equivalent loss conductance yields

$$\begin{aligned}
G_L = R_S & \left\{ \frac{1}{|D(0)|^2} \frac{2t}{(2\ell_{p'})^2} \left| \frac{\gamma_2}{j\omega\mu_1} \right|^2 \left\{ (2\ell_{p'}) \left| \frac{1}{\gamma_e} \frac{\partial D(p)}{\partial p} \right|^2 \right\}_{p=\ell_p} \right. \\
& \left. + \int_{-\ell_p}^{\ell_p} \left| \frac{1}{\gamma_e} \frac{\partial D(p)}{\partial p} \right|^2 dp \right\} \\
& + \frac{1}{4D_x^2 D_z^2} \sum_k \sum_n \sum_m \sum_i \left\{ |\gamma_{2c}|^2 \frac{\bar{Q}_2(k,n) \cdot \bar{Q}_2^*(m,i)}{r_{2y}(k,n) r_{2y}^*(m,i)} \right. \\
& \cdot \left[ D_x D_z \text{Sinc} \left( \frac{D_x}{2} (\gamma_2 r_{2x}(k,n) - \gamma_2^* r_{2x}^*(m,i)) \right) \text{Sinc} \left( \frac{D_z}{2} (\gamma_2 r_{2z}(k,n) - \gamma_2^* r_{2z}^*(m,i)) \right) \right. \\
& \cdot -4\ell_p \ell_{p'} \text{Sinc} \left( \ell_p (\gamma_2 r_{2p}(k,n) - \gamma_2^* r_{2p}^*(m,i)) \right) \\
& \left. \left. \text{Sinc} \left( \ell_{p'} (\gamma_2 r_{2p'}(k,n) - \gamma_2^* r_{2p'}^*(m,i)) \right) \right] \right. \\
& \left. + |\gamma_{3c}|^2 \frac{\bar{Q}_3(k,n) \cdot \bar{Q}_3^*(m,i)}{r_{3y}(k,n) r_{3y}^*(m,i)} \right. \\
& \cdot \left[ D_x D_z \text{Sinc} \left( \frac{D_x}{2} (\gamma_3 r_{3x}(k,n) - \gamma_3^* r_{3x}^*(m,i)) \right) \text{Sinc} \left( \frac{D_z}{2} (\gamma_3 r_{3z}(k,n) - \gamma_3^* r_{3z}^*(m,i)) \right) \right. \\
& \cdot -4\ell_p \ell_{p'} \text{Sinc} \left( \ell_p (\gamma_3 r_{3p}(k,n) - \gamma_3^* r_{3p}^*(m,i)) \right) \\
& \left. \left. \left. \text{Sinc} \left( \ell_{p'} (\gamma_3 r_{3p'}(k,n) - \gamma_3^* r_{3p'}^*(m,i)) \right) \right] \right\} \cdot \quad (D.58)
\end{aligned}$$

It is important to note that when evaluating the first two terms in Equation (D.58) involving the distribution  $D(p)$  it is necessary to use the effective propagation constant,  $\gamma_e$ .  $\gamma_e$  should also be used when evaluating the pattern factors given by Equations (D.46) and (D.56).

As mentioned previously, the two favored choices for the distribution  $D(p)$  have been the sine mode,  $D_S(p)$ , and the cosine mode,  $D_C(p)$ , given by Equations (D.2) and (D.3), respectively. Using these distributions, several of the terms required for evaluation of Equation (D.58) may be obtained. These terms will now be presented for each distribution. Since the mathematics involved are fairly straightforward only the results are presented.

For the sine mode,  $D_S(p)$

$$\left| \frac{1}{\gamma_e} \frac{\partial D_S(p)}{\partial p} \right|^2 \Big|_{p=\pm l_p} = \left| \frac{\cosh(\gamma_e \Delta l_p)}{\sinh(\gamma_e l_{pe})} \right|^2, \quad (D.59)$$

$$\int_{-l_p}^{l_p} \left| \frac{1}{\gamma_e} \frac{\partial D_S(p)}{\partial p} \right|^2 dp = \frac{l_p}{|\sinh(\gamma_e l_{pe})|^2} \left[ \frac{\sinh(2\alpha_e l_{pe}) - \sinh(2\alpha_e \Delta l_p)}{2\alpha_e l_p} + \frac{\sin(2\beta_e l_{pe}) - \sin(2\beta_e \Delta l_p)}{2\beta_e l_p} \right], \quad (D.60)$$



$$p_{2\pm}^S = \frac{\{\text{sinc}(\gamma_2 r_{2p} \ell_p)\}}{\sinh(\gamma_e \ell_{pe})} \left[ \frac{\cosh(\gamma_e \ell_{pe}) - \cosh(\gamma_e \Delta \ell_p - \gamma_2 r_{2p} \ell_p)}{(\gamma_2 r_{2p} + \gamma_e)} \right. \\ \left. - \frac{\cosh(\gamma_e \ell_{pe}) - \cosh(\gamma_e \Delta \ell_p + \gamma_2 r_{2p} \ell_p)}{(\gamma_2 r_{2p} - \gamma_e)} \right], \quad (\text{D.61})$$

and lastly,

$$p_{3\pm}^S = \frac{\{\text{sinc}(\gamma_3 r_{3p} \ell_p)\}}{\sinh(\gamma_e \ell_{pe})} \left[ \frac{\cosh(\gamma_e \ell_{pe}) - \cosh(\gamma_e \Delta \ell_p - \gamma_3 r_{3p} \ell_p)}{(\gamma_3 r_{3p} + \gamma_e)} \right. \\ \left. - \frac{\cosh(\gamma_e \ell_{pe}) - \cosh(\gamma_e \Delta \ell_p + \gamma_3 r_{3p} \ell_p)}{(\gamma_3 r_{3p} - \gamma_e)} \right]. \quad (\text{D.62})$$

Similarly for the cosine mode,  $D_C(p)$ :

$$\left| \frac{1}{\gamma_e} \frac{\partial D_C(p)}{\partial p} \right|_{p=\pm \ell_p}^2 = \left| \frac{\sinh(\gamma_e \ell_p)}{\cosh(\gamma_e \ell_{pe}) - 1} \right|^2, \quad (\text{D.63})$$

$$\int_{-\ell_p}^{\ell_p} \left| \frac{1}{\gamma_e} \frac{\partial D_C(p)}{\partial p} \right|^2 dp = \frac{\ell_p}{|\cosh(\gamma_e \ell_{pe}) - 1|^2} \left[ \frac{\sinh(2\alpha_e \ell_p)}{2\alpha_e \ell_p} - \frac{\sin(2\beta_e \ell_{pe})}{2\beta_e \ell_p} \right] \quad (\text{D.64})$$

$$P_{2\pm}^c = \frac{\{\text{sinc}(\gamma_2 r_{2p}, \lambda_p)\}}{\sinh(\gamma_e \lambda_{pe})} \cdot \left[ \begin{array}{l} 2\cosh(\gamma_e \lambda_{pe}) \text{sinc}(\gamma_2 r_{2p}, \lambda_p) \\ - \text{sinc}((\gamma_2 r_{2p} + \gamma_e) \lambda_p) - \text{sinc}((\gamma_2 r_{2p} - \gamma_e) \lambda_p) \end{array} \right], \quad (\text{D.65})$$

and

$$P_{3\pm}^c = \frac{\{\text{sinc}(\gamma_3 r_{3p}, \lambda_p)\}}{\sinh(\gamma_e \lambda_{pe})} \cdot \left[ \begin{array}{l} 2\cosh(\gamma_e \lambda_{pe}) \text{sinc}(\gamma_3 r_{3p}, \lambda_p) \\ - \text{sinc}((\gamma_3 r_{3p} + \gamma_e) \lambda_p) - \text{sinc}((\gamma_3 r_{3p} - \gamma_e) \lambda_p) \end{array} \right]. \quad (\text{D.66})$$

## 2. Thick Lossy Slots

The geometry is the same as that shown in Figure D.4 but now the restrictions on  $t$  (the slot thickness or depth) are relaxed. If  $t$  becomes appreciable, then the slot voltages on each side of the surface may be different. Thus, it is necessary to place a different voltage mode on each side of the slot (possibly several modes for long slots) for which a mutual admittance must be determined. When finding the equivalent loss conductance for this case it is necessary to find values for the left ( $-y$  side) and right ( $+y$  side) sides. For the thin slot we had an interior region and two exterior regions for one mode. For the thick slot, the "left and right" modes will each have one exterior region and one interior region. Note that for the left mode exterior

region, the loss term is identical to that found for region 2 of Section 2. For the right mode, the exterior loss term is the same as for region 3. To simplify the analysis, note that the power loss for the interior region is the same for the left and right modes except for the magnitude squared of the mode amplitude. Thus we need find only one new term: the interior loss term.

The geometry and dimensions of a thick slot are shown in Figure D.8. Note that the magnetic current mode is still in the  $\hat{p}$  direction. To find the interior loss we must find the magnetic fields in the interior region radiated by the assumed magnetic current (voltage) mode in the presence of the four conducting walls. The effects of the walls can be modelled using image theory [76] to obtain an infinite array of magnetic current sources as shown in Figure D.9. This technique has been previously used to evaluate the mutual coupling terms for the modes on each side of the slot [77]. Note that all the images seen in Figure D.9 are in phase. Thus we can look at all these images as an infinite array of currents excited by a field incident normal to the surface. Thus  $S_x$  and  $S_z$  defined by Equation (2.4) are both zero for this array. The field in the interior region can now be found using the results from the previous section for the region 3 loss. The model geometry is shown in Figure D.10. For this situation, both the reflection coefficients,  $\Gamma_L$  and  $\Gamma_R$  will be approximately unity. From Figure D.10 it can also be seen that we must make the following substitutions to obtain the interior fields from the region 3 analysis:

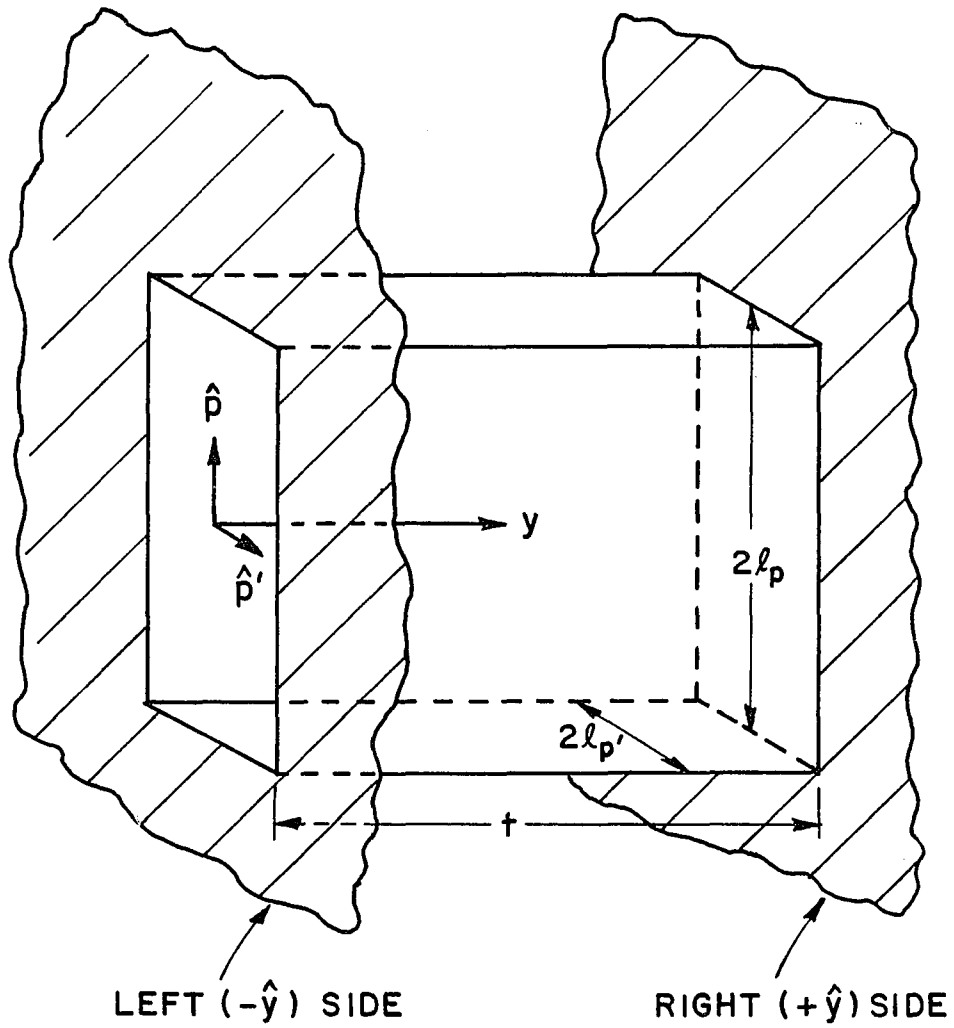
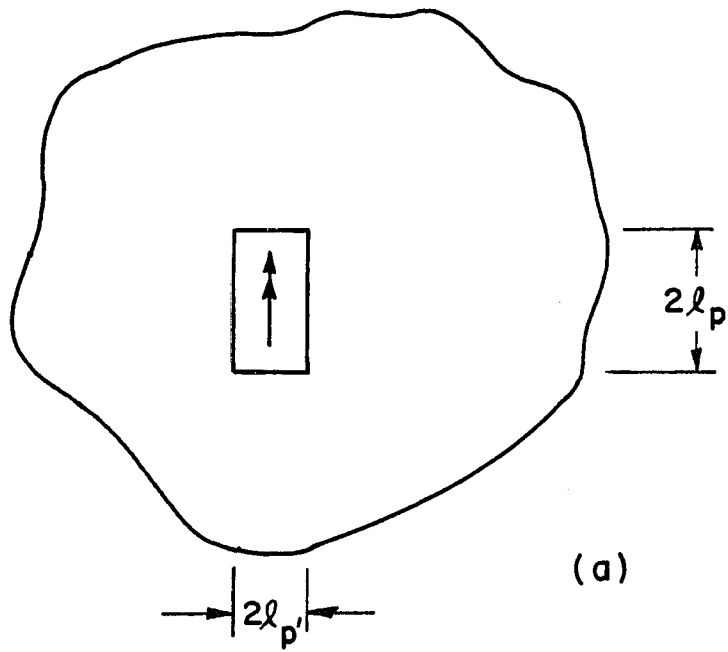
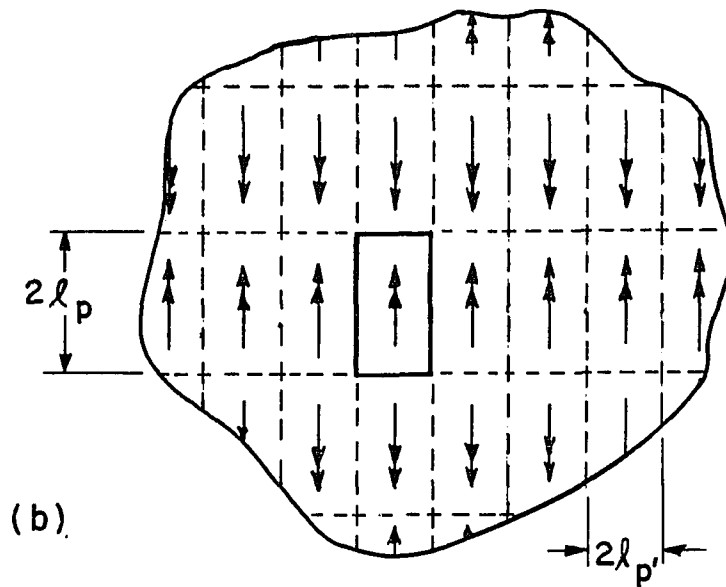


Figure D.8. Geometry of a thick slot.



(a). The single mode with the slot walls.



(b). The magnetic mode and its images.

Figure D.9. Modelling the effect of the thick slot walls using image theory.

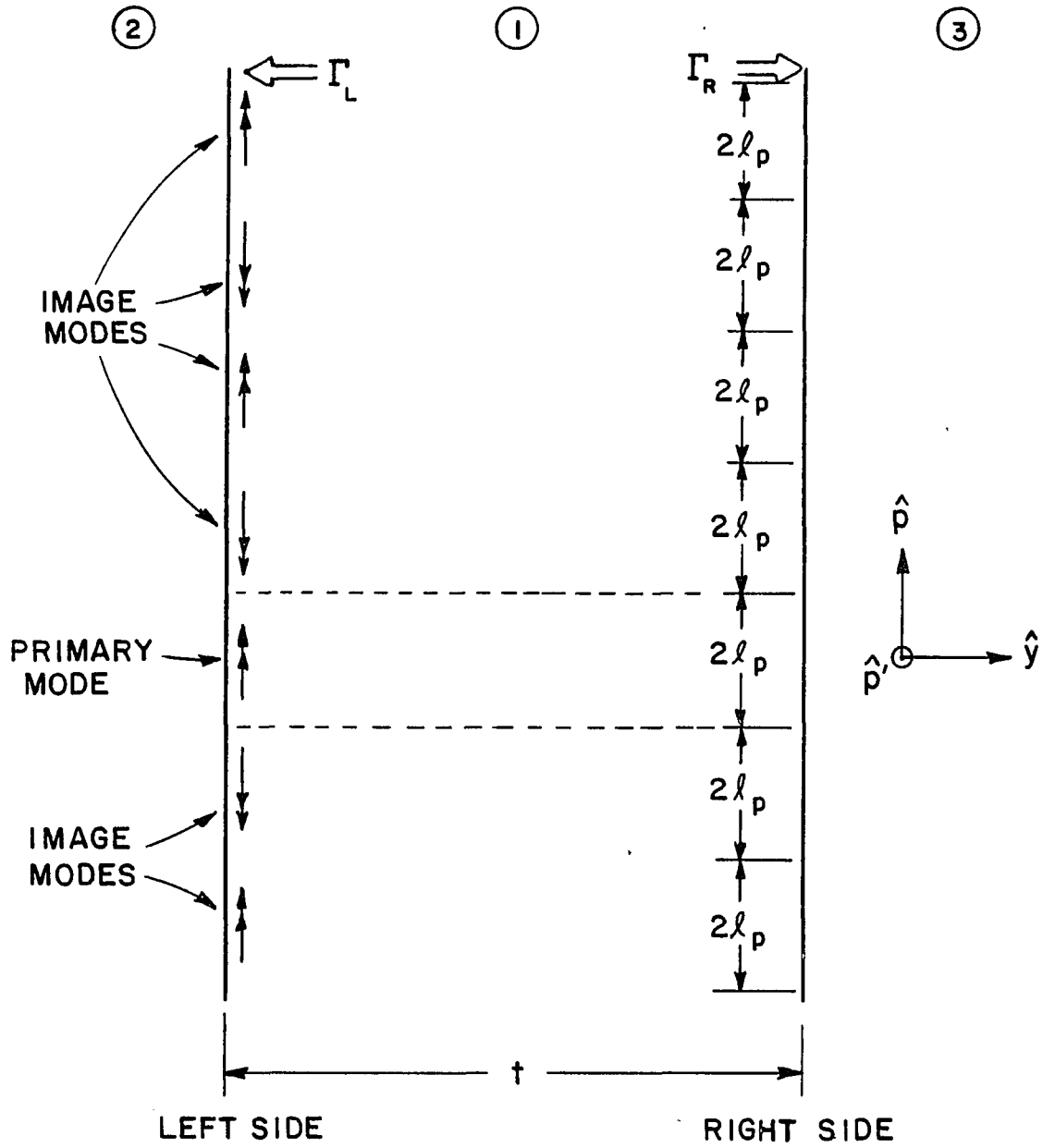


Figure D.10. Model geometry to obtain the interior slot fields. The slot walls have been removed via image theory (magnetic dipoles).

$$(\bar{R} - \bar{R}') = x\hat{x} + y\hat{y} + z\hat{z} \quad (D.67)$$

and

$$\begin{aligned} \theta &= \pi/2 \\ x &= p' \\ z &= p \\ D_x &= 4\ell_{p'} \\ D_z &= 4\ell_p \\ d_3 &= t \end{aligned} \quad (D.68)$$

Equation (D.67) has assumed that the reference point of the reference element is at the coordinate origin. In Equations (D.68) it has been assumed that the basic element or voltage mode covers the region  $[-\ell_p \leq p \leq 3\ell_p, -2\ell_{p'} \leq p' \leq 2\ell_{p'}]$ . If this was not done then we would have to look at the sum of fields radiated by two overlapping infinite arrays. Instead, this effect is taken into account in the pattern factor for this region with a mode distribution given by  $D(p)$  for  $[-\ell_p \leq p \leq \ell_p]$  and by  $-D(p-2\ell_p)$  for  $[\ell_p \leq p \leq 3\ell_p]$ .

The resulting field inside the slot is given by

$$H_1(x,y,z) = [V_p \cdot D(0)] \frac{\gamma_{1c}}{2(4\ell_{p'})(4\ell_p)} \sum_k \sum_n \frac{e^{-\gamma_1(xr_{1x} + yr_{1y} + zr_{1z})}}{r_{1y}} R_1(k,n) \quad (D.69)$$

where

$$\bar{R}_1(k,n) = \frac{[\hat{\Gamma}_{1+} - \hat{\Gamma}_{1-} \Gamma_R e^{-\gamma_1 2tr_1 y}][\Gamma_{1+} - \Gamma_{1-} \Gamma_L]}{1 - \Gamma_L \Gamma_R e^{-\gamma_1 2tr_1 y}} + \frac{[\hat{\Gamma}_{1+} - \hat{\Gamma}_{1-} \Gamma_R e^{-\gamma_1 2tr_1 y}][\Gamma_{1+} - \Gamma_{1-} \Gamma_L]}{1 - \Gamma_L \Gamma_R e^{-\gamma_1 2tr_1 y}} \quad (D.70)$$

and the pattern factor is defined over the region shown in Figure D.11 as

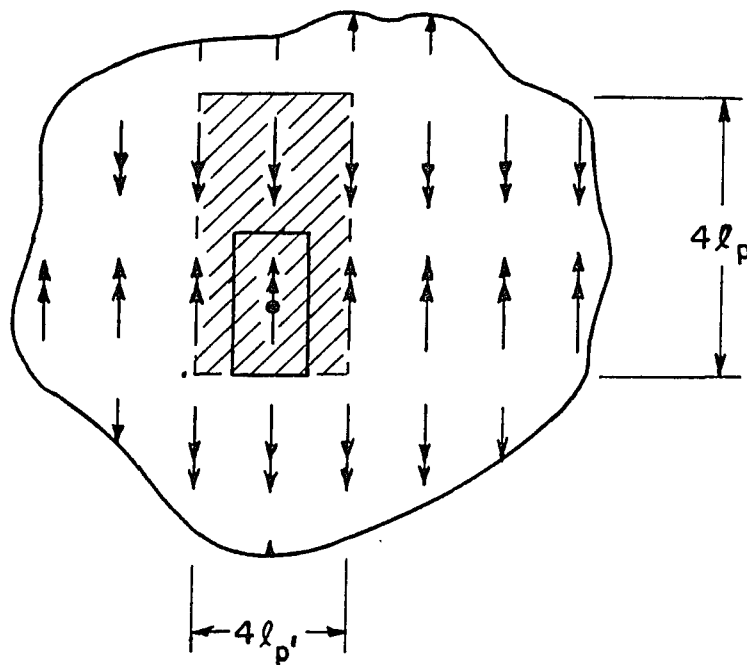


Figure D.11. Definition of the region for the interior pattern factor. The shaded region defines the reference element  $[-l_p \leq p \leq 3l_p, -2l_{p'} \leq p' \leq 2l_{p'}]$ . The box is the original slot position.



$$\begin{aligned}
P_{1\pm} &= \frac{1}{[V_p \cdot D(0)]} \int_{-2\ell_p}^{2\ell_p} e^{\gamma_1 p' r_{1p'}} dp' \left[ \int_{-\ell_p}^{\ell_p} V_p \cdot D(0) e^{\gamma_1 p r_{1p}} dp \right. \\
&\quad \left. - \int_{\ell_p}^{3\ell_p} V_p \cdot D(p-2\ell_p) e^{\gamma_1 p r_{1p}} dp \right] \\
&= \frac{4\ell_p \cdot \text{sinc}(\gamma_1 2\ell_p, r_{1p'})}{[V_p \cdot D(0)]} \left[ 1 - e^{\gamma_1 2\ell_p r_{1p}} \right] \int_{-\ell_p}^{\ell_p} [V_p \cdot D(p) e^{\gamma_1 p r_{1p}} dp] .
\end{aligned}
\tag{D.71}$$

Due to the symmetry in the image sources (see Figure D.9), the magnetic fields along the slot walls are everywhere parallel to the walls. Thus, the magnitude of the wall currents is equal to the magnitude of the magnetic fields evaluated at the walls. Also, due to symmetry, the magnitude of the current on the top wall equals that on the bottom and the magnitudes of the currents on the side walls are equal. Thus, the region 1 resistive power loss may be written as

$$\begin{aligned}
P_{L1} = & \left(\frac{R_s}{2}\right) |V_p \cdot D(0)|^2 \frac{|Y_{1c}|^2}{4(4\ell_p)^2(4\ell_p)^2} \sum_k \sum_n \sum_m \sum_i \frac{\bar{R}_1(k,n) \cdot \bar{R}_1^*(m,i)}{r_{1y}(k,n) r_{1y}^*(k,n)} \\
& \cdot \left[ \int_{-l_p}^{l_p} dx \int_0^t dy \left[ e^{-[\gamma_1 r_{1x}(k,n) - \gamma_1^* r_{1x}^*(m,i)]x} \right] \left[ e^{-[\gamma_1 r_{1y}(k,n) - \gamma_1^* r_{1y}^*(m,i)]y} \right] \right] \\
& \cdot \left[ e^{-[\gamma_1 r_{1z}(k,n) - \gamma_1^* r_{1z}^*(m,i)]z} \right] \\
& + 2 \int_{-l_p}^{l_p} dz \int_0^t dy \left[ e^{-[\gamma_1 r_{1x}(k,n) - \gamma_1^* r_{1x}^*(m,i)]z} \right] \left[ e^{-[\gamma_1 r_{1y}(k,n) - \gamma_1^* r_{1y}^*(m,i)]y} \right] \\
& \cdot \left[ e^{-[\gamma_1 r_{1z}(k,n) - \gamma_1^* r_{1z}^*(m,i)]z} \right] \cdot \tag{D.72}
\end{aligned}$$

The integrals in Equation (D.72) are fairly simple and may be evaluated to yield:

$$\begin{aligned}
P_{L1} = & \left(\frac{R_s}{2}\right) |V_p \cdot D(0)|^2 \left\{ \frac{|Y_{1c}|^2}{256 \ell_p^2 \ell_p^2} \sum_k \sum_n \sum_m \sum_i \left\{ \frac{\bar{R}_1(k,n) \cdot \bar{R}_1^*(m,i)}{r_{1y}(k,n) r_{1y}^*(m,i)} \right. \right. \\
& \cdot \left[ \frac{1 - e^{-[\gamma_1 r_{1y}(k,n) - \gamma_1^* r_{1y}^*(m,i)]t}}{[\gamma_1 r_{1y}(k,n) - \gamma_1^* r_{1y}^*(m,i)]} \right] \\
& \left[ \ell_p \cdot \text{Sinc} \left( \ell_p (\gamma_1 r_{1x}(k,n) - \gamma_1^* r_{1x}^*(m,i)) \right) \right. \\
& \left. \left. + \ell_p \cdot \text{Sinc} \left( \ell_p (\gamma_1 r_{1z}(k,n) - \gamma_1^* r_{1z}^*(m,i)) \right) \right] \right\} \cdot (D.73)
\end{aligned}$$

Combining this result with Equation (D.52) for the region 2 power loss and equating the sum to the equivalent power loss in the left mode loss conductance we have

$$P_{L1} + P_{L2} = \frac{G_{\text{left}}}{2} |V_p \cdot D(0)|^2 \cdot (D.74)$$

Solving for  $G_{\text{left}}$  yields,

$$\begin{aligned}
G_{\text{left}} = R_s & \left\{ \frac{|Y_{1c}|^2}{256 \ell_p^2 \ell_p^2} \sum_k \sum_n \sum_m \sum_i \left\{ \frac{\bar{R}_1(k,n) \cdot \bar{R}_1^*(m,i)}{r_{1y}(k,n) r_{1y}^*(m,i)} \right. \right. \\
& \cdot \left[ \frac{1 - e^{-[\gamma_1 r_{1y}(k,n) - \gamma_1^* r_{1y}^*(m,i)] t}}{[\gamma_1 r_{1y}(k,n) - \gamma_1^* r_{1y}^*(m,i)]} \right] \\
& \cdot \left[ \ell_p \cdot \text{Sinc} \left( \ell_p (\gamma_1 r_{1x}(k,n) - \gamma_1^* r_{1x}^*(m,i)) \right) \right. \\
& \quad \left. + \ell_p \cdot \text{Sinc} \left( \ell_p (\gamma_1 r_{1z}(k,n) - \gamma_1^* r_{1z}^*(m,i)) \right) \right] \\
& \frac{|Y_{2c}|^2}{4 D_x^2 D_z^2} \sum_k \sum_n \sum_m \sum_i \left\{ \frac{\bar{Q}_2(k,n) \cdot \bar{Q}_2^*(m,i)}{r_{2y}(k,n) r_{2y}^*(m,i)} \right. \\
& \cdot \left[ D_x D_z \text{Sinc} \left( \frac{D_x}{2} (\gamma_2 r_{2x}(k,n) - \gamma_2^* r_{2x}^*(m,i)) \right) \text{Sinc} \left( \frac{D_z}{2} (\gamma_2 r_{2z}(k,n) - \gamma_2^* r_{2z}^*(m,i)) \right) \right] \\
& \cdot -4 \ell_p \ell_p \cdot \text{Sinc} \left( \ell_p (\gamma_2 r_{2p}(k,n) - \gamma_2^* r_{2p}^*(m,i)) \right) \\
& \quad \left. \text{Sinc} \left( \ell_p (\gamma_2 r_{2p}(k,n) - \gamma_2^* r_{2p}^*(m,i)) \right) \right\} \cdot \quad (D.75)
\end{aligned}$$

Note that when evaluating the pattern factors (Equations (D.46) and (D.73) associated with Equation (D.75) it is important to use the effective propagation constant,  $\gamma_e$ , associated with the voltage mode on

the left side of the slot. Similarly for the right side of the slot, the conductance to be added to the self admittance is given by

$$\begin{aligned}
 G_{\text{right}} = R_s & \left\{ \frac{|Y_{1c}|^2}{256 \ell_p^2 \ell_p^2} \sum_k \sum_n \sum_m \sum_i \left\{ \frac{\bar{R}_1(k,n) \cdot \bar{R}_1^*(m,i)}{r_{1y}(k,n) r_{1y}^*(m,i)} \right. \right. \\
 & \cdot \left[ \frac{1 - e^{-[\gamma_1 r_{1y}(k,n) - \gamma_1^* r_{1y}^*(m,i)] t}}{[\gamma_1 r_{1y}(k,n) - \gamma_1^* r_{1y}^*(m,i)]} \right] \\
 & \cdot \left[ \ell_p \cdot \text{Sinc} \left( \ell_p (\gamma_1 r_{1x}(k,n) - \gamma_1^* r_{1x}^*(m,i)) \right) \right. \\
 & \quad \left. + \ell_p \cdot \text{Sinc} \left( \ell_p (\gamma_1 r_{1z}(k,n) - \gamma_1^* r_{1z}^*(m,i)) \right) \right] \\
 & \left. \frac{|Y_{3c}|^2}{4D_x^2 D_z^2} \sum_k \sum_n \sum_m \sum_i \left\{ \frac{\bar{Q}_3(k,n) \cdot \bar{Q}_3^*(m,i)}{r_{3y}(k,n) r_{3y}^*(m,i)} \right. \right. \\
 & \cdot \left[ D_x D_z \text{Sinc} \left( \frac{D_x}{2} (\gamma_3 r_{3x}(k,n) - \gamma_3^* r_{3x}^*(m,i)) \right) \text{Sinc} \left( \frac{D_z}{2} (\gamma_3 r_{3z}(k,n) - \gamma_3^* r_{3z}^*(m,i)) \right) \right] \\
 & \cdot -4 \ell_p \ell_p \cdot \text{Sinc} \left( \ell_p (\gamma_3 r_{3p}(k,n) - \gamma_3^* r_{3p}^*(m,i)) \right) \\
 & \quad \left. \text{Sinc} \left( \ell_p (\gamma_3 r_{3p'}(k,n) - \gamma_3^* r_{3p'}^*(m,i)) \right) \right\} \left. \right\} \quad (D.76)
 \end{aligned}$$

where now the effective propagation constant for the right side must be used when evaluating the appropriate pattern factors.

Again, the region 1 pattern factors may be evaluated for the sine and cosine modes. For the sine mode we have

$$\begin{aligned}
 \int_{-\ell_p}^{\ell_p} \left[ \frac{V_p D_S(p)}{V_p D(0)} \right] e^{\gamma_1 r_1 p} dp &= \int_{-\ell_p}^{\ell_p} \frac{\sinh(\gamma_e (\ell_{pe} - |p|))}{\sin(\gamma_e \ell_{pe})} e^{\gamma_1 r_1 p} dp \\
 &= \frac{1}{\sinh(\gamma_e \ell_{pe})} \left[ \frac{\cosh(\gamma_e \ell_{pe}) - \cosh(\gamma_e \Delta \ell_p - \gamma_1 r_1 \ell_p)}{(\gamma_1 r_1 + \gamma_e)} \right. \\
 &\quad \left. - \frac{\cosh(\gamma_e \ell_{pe}) - \cosh(\gamma_e \Delta \ell_p + \gamma_1 r_1 \ell_p)}{(\gamma_1 r_1 - \gamma_e)} \right] \tag{D.78}
 \end{aligned}$$

which yields

$$\begin{aligned}
 P_{1\pm}^S &= \frac{4\ell_p \cdot \text{Sinc}(\gamma_1 2\ell_p r_1)}{\sinh(\gamma_e \ell_{pe})} \left[ 1 - e^{\gamma_1 2\ell_p r_1} \right] \\
 &\quad \left[ \frac{\cosh(\gamma_e \ell_{pe}) - \cosh(\gamma_e \Delta \ell_p - \gamma_1 r_1 \ell_p)}{(\gamma_1 r_1 + \gamma_e)} \right. \\
 &\quad \left. - \frac{\cosh(\gamma_e \ell_{pe}) - \cosh(\gamma_e \Delta \ell_p + \gamma_1 r_1 \ell_p)}{(\gamma_1 r_1 - \gamma_e)} \right] . \tag{D.79}
 \end{aligned}$$

Similarly for the cosine mode

$$\begin{aligned}
\int_{-\ell_p}^{\ell_p} \left[ \frac{V_p D_C(p)}{V_p D(0)} \right] e^{\gamma_1 r_{1p} p} dp &= \int_{-\ell_p}^{\ell_p} \left[ \frac{\cosh(\gamma_e \ell_{pe}) - \cosh(\gamma_e p)}{\cosh(\gamma_e \ell_{pe}) - 1} \right] e^{\gamma_1 r_{1p} p} dp \\
&= \frac{\ell_p}{[\cosh(\gamma_e \ell_{pe}) - 1]} \left[ 2 \cosh(\gamma_e \ell_{pe}) \text{Sinc}(\gamma_1 r_{1p} \ell_p) \right. \\
&\quad \left. \text{Sinc}((\gamma_1 r_{1p} + \gamma_e) \ell_p) - \text{Sinc}((\gamma_1 r_{1p} - \gamma_e) \ell_p) \right], \tag{D.80}
\end{aligned}$$

and we have

$$\begin{aligned}
P_{1\pm}^C &= \frac{4 \ell_p \ell_{p'} \text{Sinc}(\gamma_1 2 \ell_p, r_{1p'})}{[\cosh(\gamma_e \ell_{pe}) - 1]} \left[ 1 - e^{\gamma_1 2 \ell_p r_{1p}} \right] \\
&\cdot \left[ 2 \cosh(\gamma_1 \ell_{pe}) \text{Sinc}(\gamma_1 r_{1p} \ell_p) - \text{Sinc}((\gamma_1 r_{1p} + \gamma_e) \ell_p) \right. \\
&\quad \left. - \text{Sinc}((\gamma_1 r_{1p} - \gamma_e) \ell_p) \right]. \tag{D.81}
\end{aligned}$$

## APPENDIX E

### MID-INFRARED DATA FOR ALUMINUM AND GOLD

In this section, data for the metals aluminum and gold are presented. Both metals are typically used for mirrors in the mid-infrared since they have high reflectivity which is indicative of a good conductivity. Unfortunately, data for chrome was not readily available and even though it was used to build periodic surfaces, the specific attributes of this metal in the mid-infrared are not known. However, from the measured periodic surface transmittance data in Chapter IV, it can be inferred that the mid-infrared properties of chrome are not greatly different from those of aluminum.

Figures E.1 and E.2 present extinction coefficient data and reflectance data [78], respectively. Using the reflectance data and Equation (2.28), the surface resistance data of Figure E.3 was obtained. The skin depth data of Figure E.4 was obtained using the extinction coefficient data as follows. It is assumed that propagation is of the form

$$E(x) \sim e^{-\gamma x} \tag{E.1}$$



given by

$$\begin{aligned}\gamma &= j\omega \sqrt{\mu_0 \tilde{\epsilon}} \\ &= j \frac{2\pi k}{\lambda_0} + j \frac{2\pi n}{\lambda_0} \quad ,\end{aligned}\tag{E.2}$$

using the results in Appendix C. Since the skin depth,  $\delta$ , is defined to be the distance required for  $e^{-1}$  field strength [79] decay we have

$$e^{-1} = e^{-\left(\frac{2\pi k}{\lambda_0}\right)\delta} \quad .\tag{E.3}$$

Thus we obtain

$$\delta = \frac{\lambda_0}{2\pi k}\tag{E.4}$$

where  $k$  is the extinction coefficient.

It should be pointed out that the data in [78] are somewhat out of date. More recent data are now available [80] but have not been included since the metal films obtained during this study are probably not of the quality of those in [78] yet alone [80].

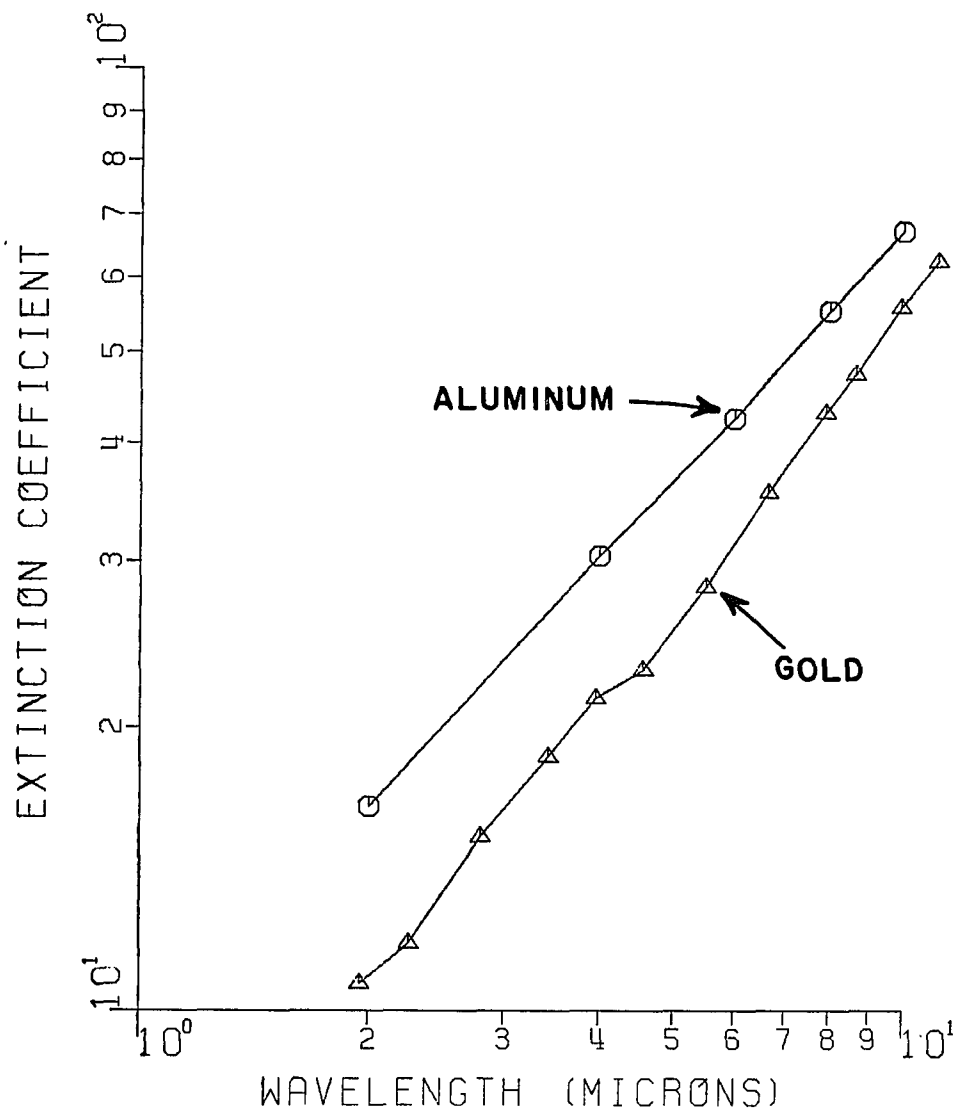


Figure E.1. Extinction coefficient data for aluminum.

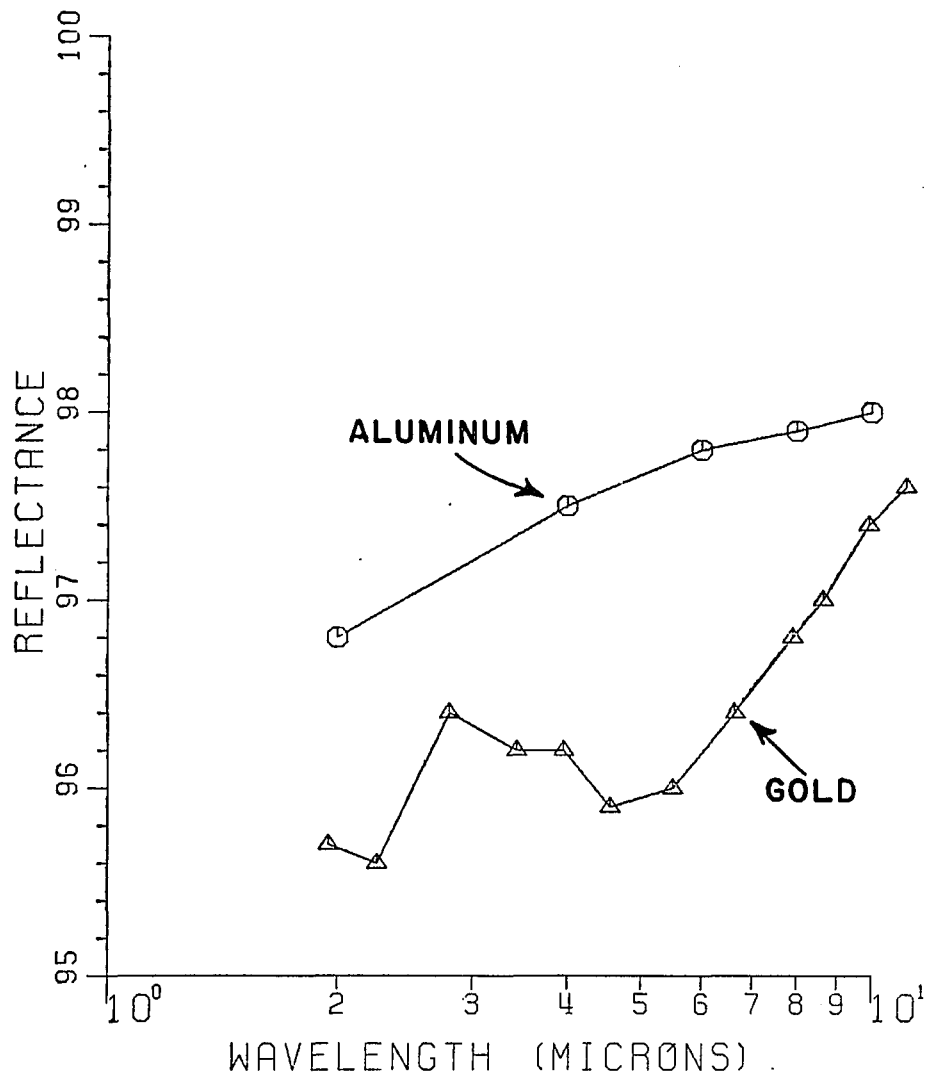


Figure E.2. Reflectance data for aluminum and gold [79].

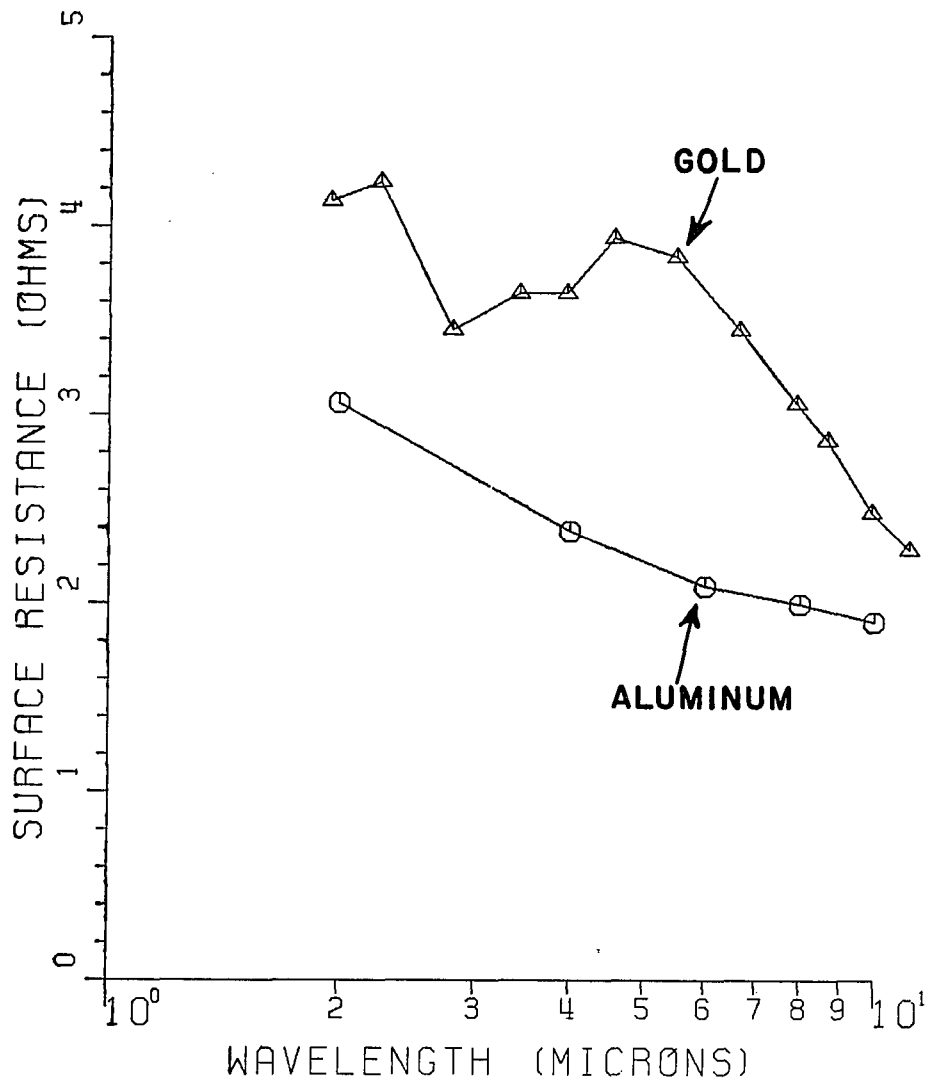


Figure E.3. Calculated surface resistance of aluminum and gold.

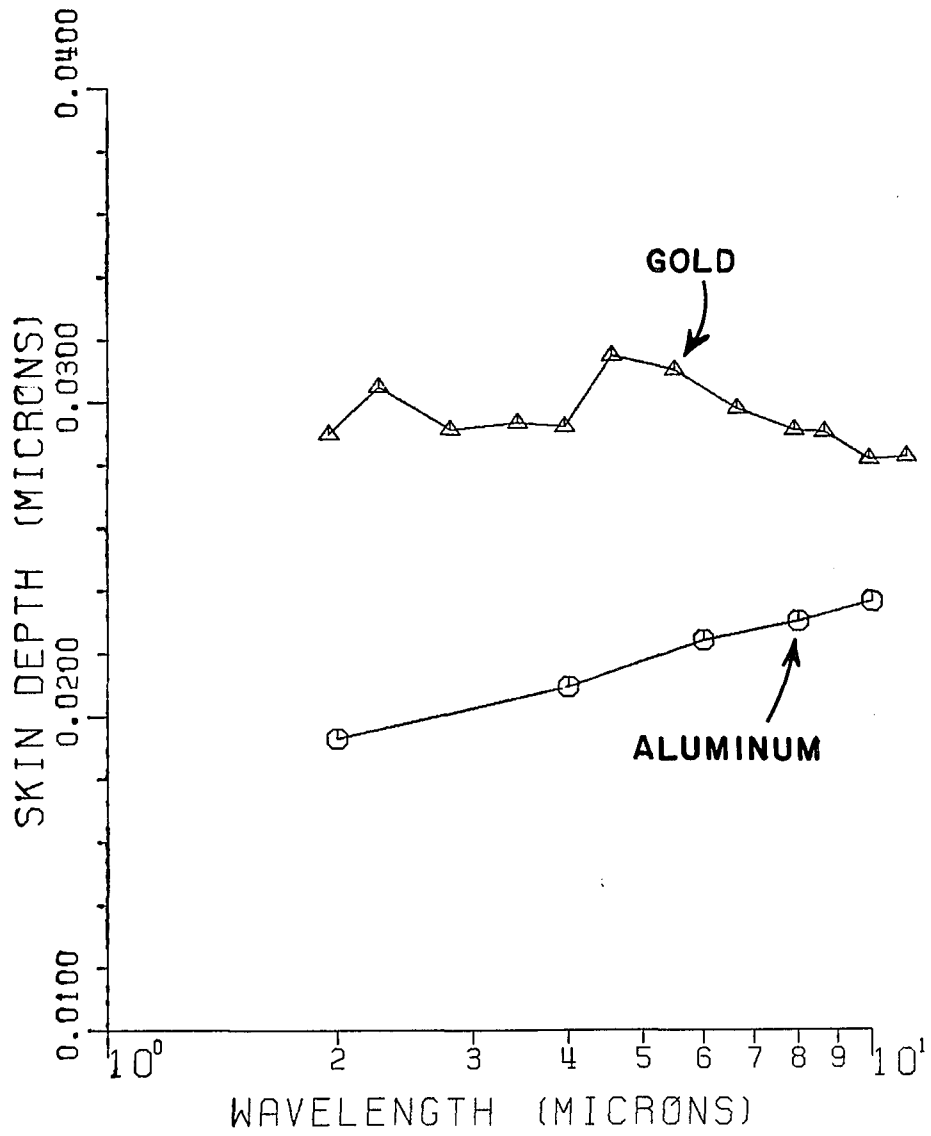


Figure E.4. Calculated skin depths of aluminum and gold.

## REFERENCES

- [1] R. Ulrich, K.F. Renk and L. Genzel, "Tunable Submillimeter Interferometers of the Fabry-Perot Type", IEEE Transactions on Microwave Theory and Techniques, pp. 363-371, September, 1963.
- [2] R. Ulrich, "Far Infrared Properties of Metallic Mesh and Its Complementary Structure", Infrared Physics, Vol. 7, pp. 37-55, 1967, Pergamon Press.
- [3] R. Ulrich, "Effective Low-Pass Filters for Far Infrared Frequencies", Infrared Physics, Vol. 7, 1967, pp. 65-74, Pergamon Press.
- [4] R. Ulrich, "Interference Filters for the Far Infrared", Applied Optics, Vol. 7, No. 10, October, 1968, pp. 1987-1996.
- [5] N. Marcuvitz, Waveguide Handbook, MIT Radiation Lab Series, Vol. 10, p. 280, 1964.
- [6] C.C. Chen, "Transmission Through a Conducting Screen Perforated Periodically with Apertures", IEEE Trans., v. MTT-18, No. 9, pp. 637-630, 1970.
- [7] B.A. Panchenko and I.P. Solovyanova, "Anomalous Reflections of EM Waves from Diffraction Gratings", Transactions of the Institute of Radiophysics, 1970.
- [8] I.P. Solovyanova, "The Influence of a Two-sided, Multilayered Dielectric Coating on the Radiotransparency of Perforated Metallic Screens", Manuscript received, Technical Society, V.I.M.I., 1978.
- [9] B.A. Munk, G.W. Burrell and T.W. Kornbau, "A General Theory of Periodic Surfaces in Stratified Dielectric Media", Technical Report 784346-1, November 1977, The Ohio State University, ElectroScience Laboratory, Department of Electrical Engineering; prepared under Contract #F33615-76-C-1024 for Air Force Systems Command, Aeronautical Systems Division, Wright-Patterson Air Force Base, Ohio.

- [10] J.S. Ernst, "Broadband Metallic Radome", Thesis and Technical Report 784346-11, September 1979, The Ohio State University, ElectroScience Laboratory, Department of Electrical Engineering; prepared under Contract #F33615-76-C-1024 for Air Force Systems Command, Aeronautical Systems Division, Wright-Patterson Air Force Base, Ohio.
- [11] B.A. Munk and G.A. Burrell, "Plane-Wave Expansion for Arrays of Arbitrarily Oriented Piecewise Linear Elements and Its Application in Determining the Impedance of a Single Linear Antenna in a Lossy Half-Space", IEEE Transactions on Antennas and Propagation, Vol. AP-27, No. 3, May 1979, pp. 331-343.
- [12] E.L. Pelton and B.A. Munk, "Scattering from Periodic Arrays of Crossed Dipoles", IEEE Transactions on Antennas and Propagation, Vol. AP-27, No. 3, May 1979, pp. 323-330.
- [13] B.A. Panchenko and I.P. Solovyanova, "Numerical Analysis of Radio Transparency of Perforated Metal Structures", Antenny (Moscow), 81, No. 29, 1980, pp. 170-175.
- [14] R.F. Miller, "Scattering by a Grating. I", Canadian Journal of Physics, Vol. 39, 1961, pp. 81-103.
- [15] R.F. Miller, "Scattering by a Grating. II", Canadian Journal of Physics, Vol. 39, 1961, pp. 104-118.
- [16] A. Yariv, Introduction to Optical Electronics, Chap. 4, 1976, Holt, Rinehart and Winston.
- [17] R. Ulrich, T.J. Bridges and M.A. Pollack, "Variable Metal Mesh Coupler for Far Infrared Lasers", Applied Optics, Vol. 9, No. 11, November 1970, pp. 2511-2516.
- [18] D. Muehlner and R. Weiss, "Balloon Measurements of the Far-Infrared Background Radiation", Physical Review, Vol. 7, No. 2, January 15, 1973, pp. 326-344.
- [19] S.E. Whitcomb and J. Keene, "Low-Pass Interference Filters for Submillimeter Astronomy", Applied Optics, Vol. 19, No. 2, January 15, 1980, pp. 197-198.

- [20] T. Timusk and P.L. Richards, "Near Millimeter Wave Bandpass Filters", *Applied Optics*, Vol. 20, No. 8, April 15, 1981, pp. 1355-1360.
- [21] V.P. Tomaselli, D.C. Edewald, P. Gillan and K.D. Moller, "Far-Infrared Bandpass Filters From Cross-Shaped Grids", *Applied Optics*, Vol. 20, No. 8, April 15, 1981, pp. 1361-1366.
- [22] R.F. Harrington, Time-harmonic Electromagnetic Fields, pp. 98-100, McGraw-Hill, 1961.
- [23] T.W. Kornbau, "Application of the Plane Wave Expansion Method to Periodic Arrays Having a Skewed Grid Geometry", Thesis and Technical Report 784346-3, June 1977, The Ohio State University, ElectroScience Laboratory, Department of Electrical Engineering; prepared under Contract #F33615-76-C-1024 for Air Force Systems Command, Aeronautical Systems Division, Wright-Patterson Air Force Base, Ohio.
- [24] B.A. Munk, G.W. Burrell and T.W. Kornbau, "A General Theory of Periodic Surfaces in Stratified Dielectric Media", Technical Report 784346-1, op. cit., pp. 45-47.
- [25] Ibid., pp. 10-13.
- [26] R.F. Harrington, Field Computation by Moment Methods, reprinted by Roger F. Harrington, R.D.2, West Lake Road, Cazenovia, New York 13035.
- [27] V.H. Rumsey, "Reaction Concept in Electromagnetic Theory", *Physical Review*, Vol. 94, June 15, 1954, pp. 1483-1491.
- [28] J.H. Richmond, "Radiation and Scattering by Thin Wire Structures in the Complex Frequency Domain", Technical Report 2902-10, July 1973, The Ohio State University ElectroScience Laboratory, Department of Electrical Engineering; prepared under Grant No. NGL 36-008-138 for National Aeronautics and Space Administration, Washington, D.C.
- [29] B.A. Munk, G.W. Burrell and T.W. Kornbau, "A General Theory of Periodic Surfaces in Stratified Dielectric Media", Technical Report 784346-1, op. cit., pp. 14-19.
- [30] S.A. Schelkunoff and H.T. Friss, Antennas Theory and Practice, p. 366, 1952, T. Wiley and Sons.
- [31] Ibid., p. 403.



- [32] B.A. Munk, "The Backscattering from a Tuned Resonant Surface Made of an Array of Short Loaded Dipoles, Technical Report 2148-6, March 1967, The Ohio State University ElectroScience Laboratory, Department of Electrical Engineering; prepared under Contract No. AF 33(615)-3461 for Air Force Avionics Laboratory, Wright-Patterson Air Force Base, Ohio.
- [33] B.A. Munk, "Scattering by Periodic Arrays of Loaded Elements", Dissertation, The Ohio State University, 1968.
- [34] J.S. Ernst, "Broadband Metallic Radome", op. cit.
- [35] B.A. Munk and G.A. Burrell, "Plane-Wave Expansion for Arrays of Arbitrarily Oriented Piecewise Linear Elements and Its Application in Determining the Impedance of a Single Linear Antenna in a Lossy Half-Space", op. cit.
- [36] B.A. Munk, Burrell and Kornbau, "A General Theory of Periodic Surfaces in Stratified Dielectric Media", op. cit., Appendix E.
- [37] The Microwave Engineers Handbook and Buyers Guide, Horizon House Publishers, Dedham, Massachusetts, 1966, p. 126.
- [38] B.A. Munk, "Scattering by Periodic Arrays of Loaded Elements", Dissertation, The Ohio State University, 1968, Appendix IX.
- [39] B.A. Munk, Burrell and Kornbau, "A General Theory of Periodic Surfaces in Stratified Dielectric Media", op. cit.
- [40] T.W. Kornbau, "Application of the Plane Wave Expansion Method to Periodic Arrays Having a Skewed Grid Geometry", Thesis and Technical Report 784346-3, op. cit.
- [41] B.A. Munk, Burrell and Kornbau, "A General Theory of Periodic Surfaces in Stratified Dielectric Media", op. cit.
- [42] Private discussions with Lee Henderson of The Ohio State University ElectroScience Laboratory.
- [43] Private discussions with Benedikt Munk of The Ohio State University ElectroScience Laboratory.
- [44] B.A. Munk, "Scattering by Periodic Arrays of Loaded Elements", Dissertation, The Ohio State University, 1968, op. cit.

- [45] B.A. Munk, "Scattering by Periodic Arrays of Loaded Elements", Dissertation, The Ohio State University, 1968, op. cit.
- [46] J.S. Ernst, "Broadband Metallic Radome", op. cit.
- [47] "'Turn Key Focused-Ion Beam Lithography System", Commerce Business Daily, September 17, 1982, p. 31.
- [48] Private discussions with Benedikt Munk of The Ohio State University ElectroScience Laboratory.
- [49] R. Ulrich, "Preparation of Grids for Far Infrared Filters", Applied Optics, Vol. 8, No. 2, February 1969.
- [50] National Research and Resource Facility for Submicron Structures", NRFSS Introductory Pamphlet, available from: Director, NRFSS, Cornell University, Phillips Hall, Ithaca, New York 14853.
- [51] G. Brewer, Electron-Beam Technology in Microelectronic Fabrication, 1980, Academic Press.
- [52] Ibid., p. 11.
- [53] N.G. Einspruch, VLSI Electronics Microstructure Science, Vol. 1, 1981, Academic Press.
- [54] N.G. Einspruch, VLSI Electronics Microstructure Science, Vol. 2, 1981, Academic Press.
- [55] R.L. Hawkins, "Whole Band Analysis of Infrared Spectra of  $^{14}\text{N}_2$ - $^{16}\text{O}$  Broadened by Nitrogen, Oxygen and Air", Dissertation, The Ohio State University, 1982.
- [56] A. Papoullis, The Fourier Integral and Its Applications, 1962, pp. 52, McGraw-Hill.
- [57] R.L. Hawkins, "Whole Band Analysis of Infrared Spectra of  $^{14}\text{N}_2$ - $^{16}\text{O}$  Broadened by Nitrogen, Oxygen and Air", op. cit., Chapter 5.
- [58] R. Nordstrom and E.K. Damon, "Optical Techniques in Long-path, High-resolution Fourier Transform Spectroscopy", Internal Report, The Ohio State University ElectroScience Laboratory. Also see, Jenkins and White, Fundamentals of Optics, McGraw-Hill.
- [59] C.M. Rhoads, E.K. Damon and B.A. Munk, "Mid-Infrared Filters Using Conducting Elements", Applied Optics, Vol. 21, No. 15, August 1, 1982, pp. 2814-2816.

- [60] "Laser Focus Buyer's Guide", 1980, p. 307, Advanced Technology Publications, Inc.
- [61] "Harshaw Optical Crystals", 1967, p. 22, The Harshaw Chemical Company.
- [62] M. Born and E. Wolf, Principles of Optics, section 13.4, 1964.
- [63] Ibid., p. 96.
- [64] Kaiser, Spitzer and Kaiser, "Infrared Properties of CaF<sub>2</sub>, SrF<sub>2</sub> and BaF<sub>2</sub>", Physical Review, Vol. 127, No. 6, September 1962, pp. 1950-1954.
- [65] R.N. Ghose, Microwave Circuit Theory and Analysis, McGraw-Hill, 1966, pp. 125-130.
- [66] R.E. Collin, Foundations for Microwave Engineering, McGraw-Hill, 1966, pp. 124-132.
- [67] S.A. Schelkunoff and H.T. Friss, Antennas Theory and Practice, op. cit., Chapter 8.
- [68] B.A. Munk, "Scattering by Periodic Arrays of Loaded Elements", op. cit., Appendix II.
- [69] J.H. Richmond, "Radiation and Scattering by Thin Wire Structures in the Complex Frequency Domain", Technical Report 2802-10, op. cit.
- [70] R.F. Harrington, Time-Harmonic Electromagnetic Fields, op.cit., p. 138, problem 317.
- [71] B.A. Munk, Burrell and Kornbau, "A General Theory of Periodic Surfaces in Stratified Dielectric Media", op. cit., Appendix D, Equations D11 and D12.
- [72] T.W. Kornbau, "Application of the Plane Wave Expansion Method to Periodic Arrays Having a Skewed Grid Geometry", Thesis and Technical Report 784346-3, op. cit.
- [73] B.A. Munk, Burrell and Kornbau, "A General Theory of Periodic Surfaces in Stratified Dielectric Media", op. cit., Appendix G.

- [74] R.F. Harrington, Time-Harmonic Electromagnetic Fields, op. cit., pp. 98-100.
- [75] Ibid., pp. 106-110.
- [76] Ibid., pp. 103-106.
- [77] A.J. Fenn, G.A. Thiele and B.A. Munk, "Moment Method Calculation of Reflection Coefficient for Waveguide Elements in a Finite Planar Phased Antenna Array", Technical Report 784372-7, September 1978, The Ohio State University ElectroScience Laboratory, Department of Electrical Engineering; prepared under Contract N00014-76-C-0573 for Office of Naval Research, Arlington, Virginia.
- [78] American Institute of Physics Handbook, Chapter 6, 1957, McGraw-Hill.
- [79] R.F. Harrington, Time-Harmonic Electromagnetic Fields, op. cit., Chapter 2.
- [80] M.A. Ordal, L.L. Long, R.J. Bell, S.E. Bell, R.R. Bell, R.W. Alexander, Jr. and C.A. Ward, "Optical Properties of the Metals Al, Co, Cu, Au, Fe, Pb, Ni, Pd, Pt, Ag, Ti, and W in the Infrared and Far Infrared", Applied Optics, Vol. 22, No. 7, April 1, 1983, pp. 1099-1119.